FERROCENE AS FUNCTIONAL SUBUNITS IN MACROCYCLES

Inauguraldissertation

zur

Erlangung der Würde eines Doktors der Philosophie

vorgelegt der

Philosophisch-Naturwissenschaftlichen Fakultät

der Universität Basel

von

Viktor Hoffmann

aus Lörrach (BW), Deutschland

Basel, 2017

Genehmigt von der Philosophisch-Naturwissenschaftlichen Fakultät
auf Antrag von

Prof. Dr. Marcel Mayor
Prof. Dr. Thomas Ward

Basel, den 21. März 2017

Prof. Dr. Martin Spiess
Dekan

ABSTRACT

Viktor Hoffmann

Ferrocene as Functional Subunits in Macrocycles

University of Basel, PhD thesis 2017, 159 pages, 73 figures, 47 schemes, 16 tables.

The interdisciplinary field of molecular electronics, describes the use of molecules in electronic devices and deals with the central question of how electrons move through a single molecule. The research spans chemistry, physics and material science and is focused on the investigation of the structure-property relationship of functional molecules as well as their implementation in an electrical circuit. Thereby, the chemists' role is to synthesize tailormade compounds at a molecular level of control that mimic the features of conventional electronic components such as rectifiers, switches or transistors.

This PhD thesis is mainly focused on the design and syntheses of ferrocene grafted phenylethynyl backbones that are rotationally restricted through cyclization. The redox-active ferrocene unit acts as decisive functional entity in the construct. Alteration in the oxidation state of ferrocene has a direct influence on the molecular energy level and thus the electronic properties of the molecule. The ability to externally address and control the energy level of the molecule is a central feature and of great importance for the construction of components for single molecule electronics.

The thesis is segmented into 4 chapters, whereat chapter 1 - 3 discuss the synthesis and characterization of the functional molecules and chapter 4 provides the experimental details of all compounds described throughout the thesis. Each chapter is introduced individually and the projects are put into the scientific context which is relevant to the described work and illustrated with a few examples.
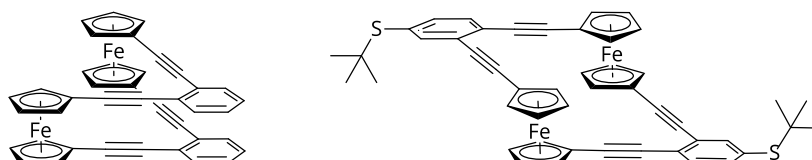
INDIVIDUAL PROJECTS

In Chapter 1, a new synthetic route for three macrocycles comprising a 1,1'-bis(phenylethynyl)-ferrocene subunit was developed in order to increase the structural control over the spatial arrangement of the two cyclopentadienyl arms of the ferrocene. The target structures were obtained through a modular strategy that enables the assembly of varying ring sizes from a common precursor. In particular, macrocycles were either formed by an ether formation reaction or by ring-closing metathesis reactions.
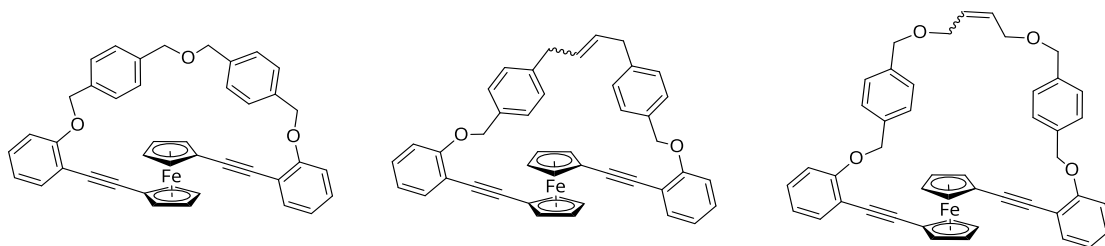
In chapter 2, the synthesis of three interlinked molecular wires (IMWs) comprising a central ferrocene unit is presented. The molecular wires have been assembled by *Sonogashira* cross-coupling and intramolecular ring-closing reaction. The macrocyclic structures share a common precursor that gives access to a variety of new cyclisation approaches. The quantum mechanical properties of the compounds have been evaluated. Two of the synthesized interlinked molecular wires have been probed in break junction experiments in order to assess structure and oxidation state related conductance dependences.
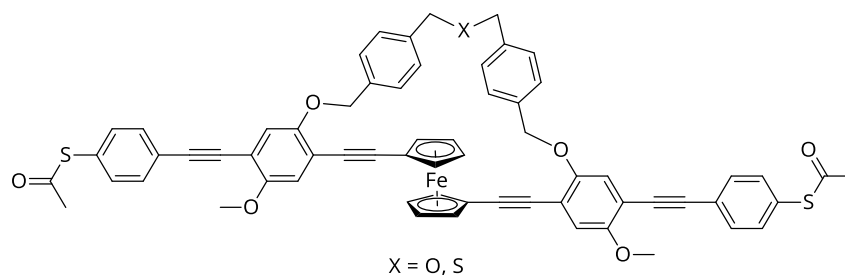
In chapter 3, we describe the syntheses, full characterization, and electrochemical investigation of two complementary shaped bis-ferrocene macrocycles build up via *Sonogashira* cross coupling and intramolecular ring closing reaction. The conformation of the bis-ferrocene macrocycles can be controlled by the peripheric phenyl substituents. The voltammograms of the macrocycles reveal that electronic communication between both ferrocenyl groups can be neglected, while the electrostatic through space coupling is significant.

ACKNOWLEDGMENTS

Meiner Familie

"Experience is what you get when you didn't get what you wanted"

Randy Pausch

CHAPTER 1

ROTATIONALLY RESTRICTED 1,1′-BIS-(PHENYLETHYNYL)FERROCENE SUBUNITS IN MACROCYCLES

INTRODUCTION

FERROCENE

In 1973, Ernst Otto Fischer and Geoffrey Wilkinson were awarded the Nobel Prize in chemistry "for their pioneering work, performed independently, on the chemistry of the organometallic, so called sandwich compounds"[1]. Among those sandwich compounds, Ferrocene (Fc) (**FIGURE 1**) is the protopypic and most protruding. Fc was first isolated in 1951, by T. Kealy and P. Pauson[2] in the attempt to synthesize fulvalene from cyclopentadienyl magnesium bromide and iron(III) chloride. At the same time, Miller and coworkers[3] synthesized Fc, from the reaction of gaseous cyclopentadienyl and reduced iron at 300 °C. Pauson deduced the structure as bivalent iron that forms σ-bonds with cyclopentadienyl (**FIGURE 1**, left). The extraordinary stability and aromaticity of ferrocene led Fischer, Pfab[4] and Wilkinson[5] to the assumption that a sandwich structure of the form bis(η^5-cyclopentadienyl)iron (**FIGURE 1**, middle and right) would be the only correct possibility. Shortly after, the 3-dimensional shape was confirmed by crystal structure analysis[6,7] stating the beginning of a renaissance in organometallic chemistry with ferrocene as figurehead.[8]
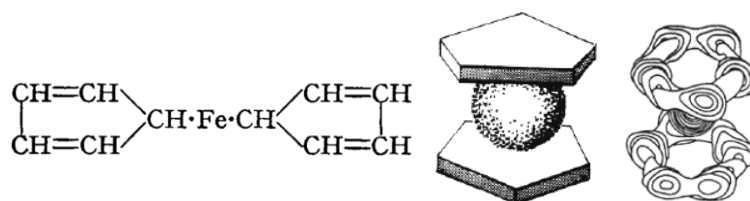
FIGURE 1 left) σ-bound iron cyclopentadienyl as suggested by Pauson. middle) Fc (staggered) as it was proposed by Wilkinson and Woodward. right) Fischer's proposal.

Owing to its aromaticity, Robert B. Woodward proposed the appropriate terminology as a combination of ferrum + benzene = ferrocene.[5] The most striking peculiarity of this archetypal sandwich complex, is the 3-dimensional structure and the accompanied conformational diversity. This is possible because the ferrocene molecule is a η^5 coordination complex that allows rotational reorientation of the cyclopentadienyl (Cp) rings around the vertical 5-fold symmetry axis. Interestingly, the equilibrium conformation was found to be eclipsed (D_{5h}) in the gas phase and the rotational barrier was estimated by Haaland and Nilsson to be 3.8 ± 1.3 kJ mol^{-1} which implies that this rotation is fast.[9] The molecular conformation of ferrocene in crystalline phases, are highly depending on packing forces, so that a monoclinal unit cell crystallized at room temperature, shows fully staggered (D_{5d}) conformation, while the triclinic unit cell (T < 164 °K) shows a slightly twisted from eclipsed D_5 symmetry. At temperatures below 110 °K the ferrocene conformation is fully eclipsed (D_{5h}) in an orthorhombic unit cell.[10]

Due to its partial negatively charged cyclopentadienyl ligands, ferrocene shows strong affinity towards electrophiles when comparable with other aromatic systems (**SCHEME 1**). For instance, electrophilic aromatic substitution reactions are readily performed at the Cp ring, while typical aromatic-type reactions such as nitration or direct halogenation leads to decomposition of ferrocene, presumably through oxidation of the iron.[11] However, formylation and carboxylation reactions only afford the mono-

functionalized ferrocene, as electron withdrawing functional groups strongly deactivate the second Cp-ring through an electronic effect. In contrast, metalation and acylation reactions can be performed in a consecutive manner, leading to 1,1'-disubstituted derivatives.[12]
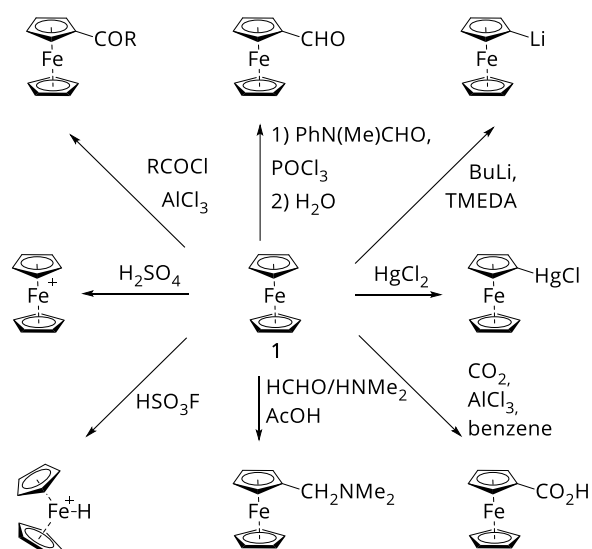
SCHEME 1 Selection of ferrocene functionalization reactions.

Due to its closed-shell, low spin 18 valence electron structure, neutral ferrocene is an air- and temperature-stable orange solid with a magnetic moment of zero. However, ferrocene also exists in various oxidation states that can be generated chemically and electrochemically (**SCHEME 2**).[12] Thereof, cationic ferrocenium salts are stable as solids, but slightly air- and light-sensitive when in solution.[13] The thermal stability and electrochemical reversibility of the Fe^{II}/Fe^{III} redox couple renders ferrocene as electrochemical antenna and transmitter in a broad field of applications.[14,15]
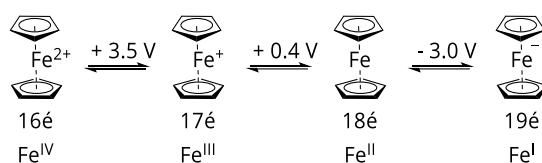
SCHEME 2 Extreme oxidation states of ferrocene Fe^{I} and Fe^{IV}. The potentials characterized by cyclic voltammetry and are given against the saturated calomel reference electrode (SCE).[12]

CHIRALITY IN FERROCENE

Owing to its 3-dimensionality, not only the hetero-annularly heterodisubstituted ferrocenes can be chiral in a common way, but also the homo-annularly 1,2- and 1,3-hetrodisubstituded ferrocenes inherit a planar-chirality (**FIGURE 2**). The CIP convention for planar-chiral metallocenes was proposed by Schlögel[16] in 1967, and is denoted by subscribing the p for planar chirality.
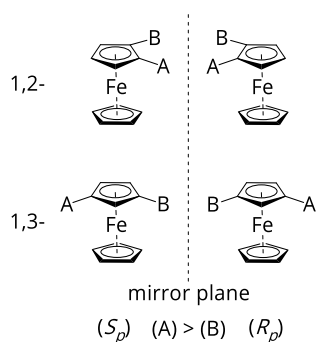
FIGURE 2 Planar metallocenic chirality for 1,2- and 1,3-heterodisubstituted ferrocenes.

This feature becomes significant, when tailor-made ligands for catalysis are required. The difficulty in the generation of enantiomerically pure ferrocenes for catalysis can be solved through diastereoselective *ortho*-functionalization. A very popular system that exploit the *ortho*-directing ability of *N,N*-dimethyl-1-ferrocenylethylamine **2** (Ugi's amine) in lithiation and subsequent electrophilic addition, was developed by Ivar Ugi in the 1970s.[17,18] The diastereoselectivity arises from unfavorable methyl-Cp interactions that come along with *ortho*-complexation of one intermediate (**SCHEME 3**).
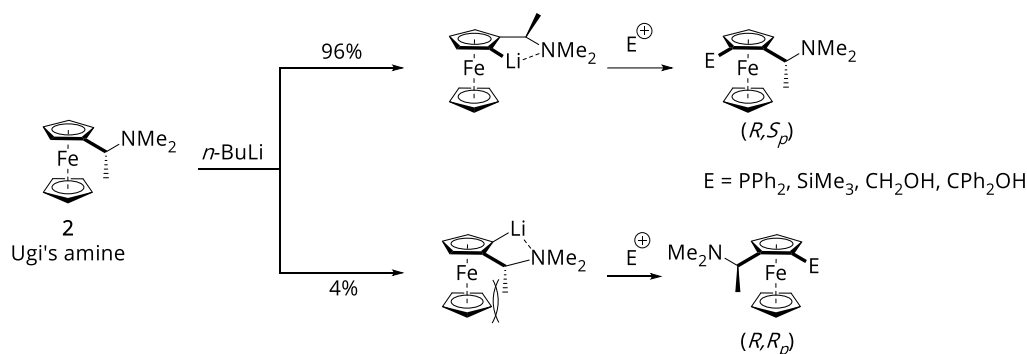
SCHEME 3 Lithiation of Ugi's amine followed by electrophilic substitution.

Upon quaternization of the dimethylamine moiety, a nucleophilic substitution under retention of configuration can give access to a vast number of compounds with planar chirality. This can be rationalized as, during the course of the reaction, the carbo-cationic species is being stabilized by the iron center before it is exo- attacked by a nucleophile (**SCHEME 4**).[19]
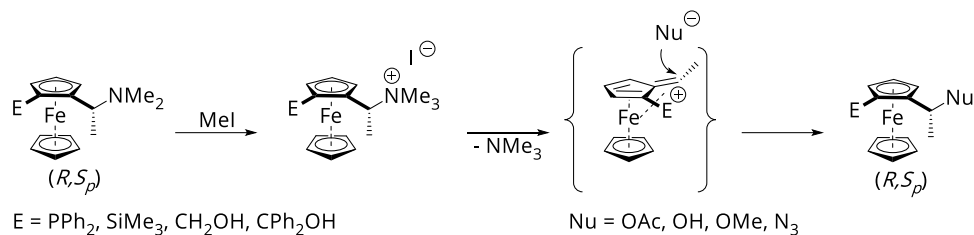
SCHEME 4 Substitution of nucleophiles under full retention of configuration.

The significance of enantiomeric pure ferrocene ligands is by far not limited to small scale academic applications as it has been demonstrated extensively with Xyliphos (**5**). Xyliphos is a 1,2-heterodisubstituted ferrocene used as phosphine chelate ligand in the Ir/Xyliphos catalyzed enantioselective imine hydrogenation of the *(S)*-metachlor precursor **4** (**SCHEME 5**). *(S)*-metachlor, only active in its *(S)*-configuration, is an herbicide that is produced by Ciba-Geigy/Syngenta in a 10000-ton scale annually.
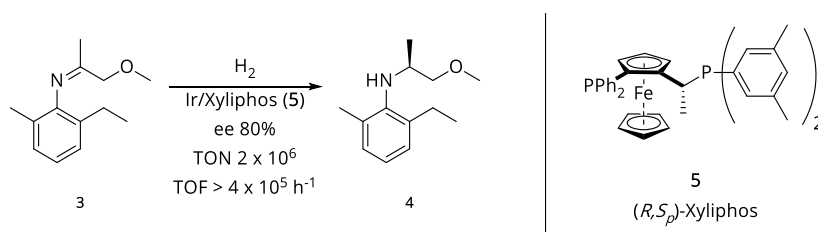
SCHEME 5 Enantioselective hydrogenation of **3** with Ir/Xyliphos(**5**) by Ciba-Geigy/Syngenta.[20]

FERROCENE IN FUNCTIONAL MATERIALS

The characteristics of functional materials can be altered decisively, when ferrocene is incorporated either as part of the molecular backbone or as pendant unit. This tendency becomes particularly pronounced when the neutral ferrocene is oxidized and the polarity inverted.

Much attention was drawn on ferrocene grafted molecules and polymers with nonlinear optical (NLO) properties which are arranged in a linear donor-π-acceptor sequence. These compounds showed an increased hyperpolarizability and were dealt as promising materials for opto-electronic applications such as frequency doubling of laser pulses.[21–29] The tunable oxidation state of ferrocene and the accompanied change of d-electron configuration allows further for the study of the differences between diamagnetic and paramagnetic complexes in respect to NLO polarizabilities.[30] In 2014, Wang et al.[31] constructed a molecular NLO switch based on 1,1-di-(4,4'-bipyridinium) ferrocene, by exploiting the natural hinge structure of ferrocene and its NLO properties (**FIGURE 3**). They demonstrated the *'on'* function upon reduction of the "closed" complex, where the ferrocene arms formed a stacked structure,

while oxidation repelled the arms and forced the *'off'* state with "open" conformation. In the centro-symmetric *'off'*-state, the hyperpolarizability was zero due to the symmetry criteria.
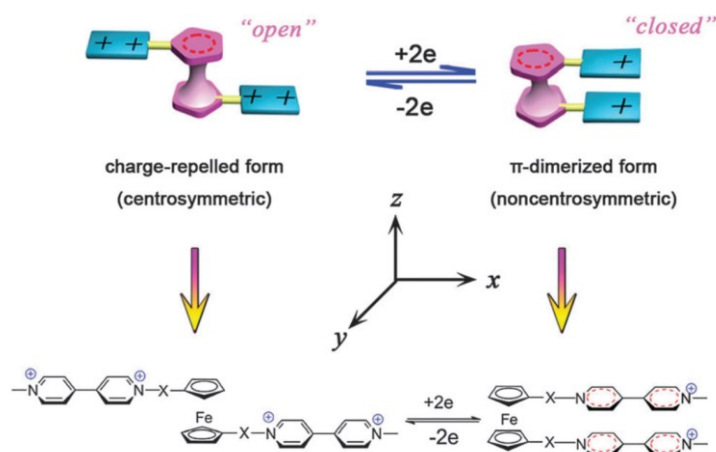
FIGURE 3 Reversible conversion between charge-repelled and π-dimerized form. Reprinted with permission from ref. [31] Royal Society of Chemistry.

The intrinsic mild and reversible redox capability of Fc is an excellent actuator for external responsive applications. Switching from neutral to cationic ferrocene species changes the polarity of the ferrocene embodied compounds dramatically. This effect is intensified in ferrocene grafted polymers, where the polarization, morphology and reactivity is dominated by the nature of the ferrocenyl units. That principle was applied to modify the wettability of a polyvinylferrocene (PVFc) functionalized silicon wafer surface (**FIGURE 4**). Upon oxidation with $FeCl_3$ or tris(4-bromophenyl)ammoniumyl hexachloroantimonate, the PVFc grafted surface became hydrophilic and the contact angle of a water droplet was decreased, whereat the reduction of the ferrocenium units with L-ascorbic acid leads to an hydrophobic response of the surface.[32] Such materials can be envisioned as surface adaptive materials that may be triggered electrochemically in future and are of great interest for e.g. microfluidic applications.
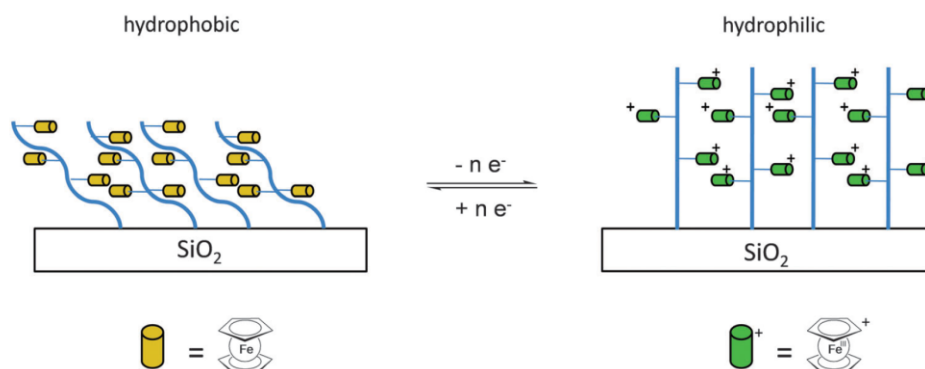
FIGURE 4 Ferrocene grafted polymers switch the polarity upon oxidation. Reprinted from Pietschnig.[33]

Other smart surface systems rely on supramolecular host-guest interactions that become reversible with the redox responsive ferrocene functionality.[34−36] Ahn et al. described a molecular Velcro adhesive, based on a cucurbit[7]uril functionalized silicon surface as host and a aminomethylferrocene functionalized silicon surface as guest, and showed the reversible adhesion initiated when the functionalized areas are immersed in an oxidizing/reducing solution.[37]

Macrocyclic and supramolecular host-systems with appendant ferrocenyl units enable the amperometric detection/sensing of bound anion guests. This becomes particularly interesting in environmental applications to detect pollutants such as phosphate and nitrate which usually lead to disruption of aquatic life cycles. Ferrocene is preferably used because of its initial neutrality and absence of electrostatic interactions with anions. However, this can be "switched on" by oxidation of ferrocene and thereby the increase in affinity for anion binding. The group of Paul Beer developed various host-system for the selective recognition of anions which are shown in **FIGURE 5**.[38,39]
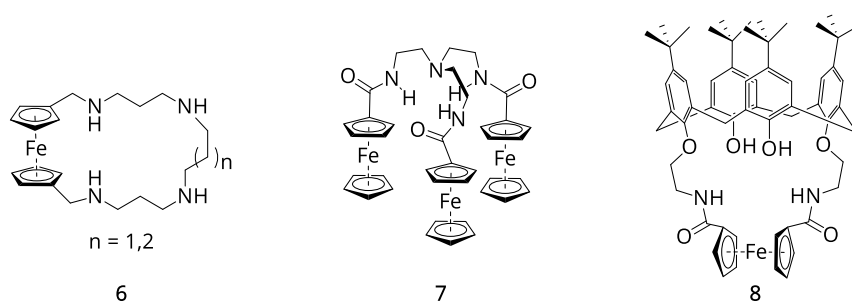
FIGURE 5 Polyaza-ferrocene **6**,[39] ferrocene amide **7** and calix[4]arene **8**[38]. Synthesized ferrocene-decorated host-systmes for selective phosphate sensing.

Ferrocene grafted polymers with partially oxidized entities are envisaged in applications for low-dimensional conductors.[40,41] Not surprisingly, ferrocene containing polymers have recently drawn a lot of attention in the scientific community as battery components. The polymers were in particular suitable as air-stable cathode materials in Li-ion batteries while delivering high capacity, excellent cycling stability and power densities comparable to state of the art systmes.[42−46] In 2015, Ding et al.[47] designed a ferrocene-based membrane-free Li-ion battery that has a stable capacity retention of up to 94% of its theoretical capacity, while having high power density of 1400 W L^{-1}, delivering the next generation of sustainable energy storage devices.

The aromaticity and redox activity of ferrocene is the reason it drew attention as prospect functionality in molecular electronics. The possibility to reversibly change the oxidation state and ultimately the energy level of the molecule, opens the access to potential molecular transistors and switches, which are of great interest for the device miniaturizing semiconductor industry.[48,49] Both theoretical and experimental studies point out that ferrocene can address the requirement as functional unit in molecular wires and exceed the performance of all organic molecular analogues.[50,51] In 2012, Lu et al. reported that the incorporation of ferrocene into oligo(*p*-phenylethynylene) (OPE) backbone enhances

the molecular conductance in both the tunneling and hopping regimes, due to lowering of the LUMO energy levels that matches the Fermi level of the electrodes (**FIGURE 6**).[52]
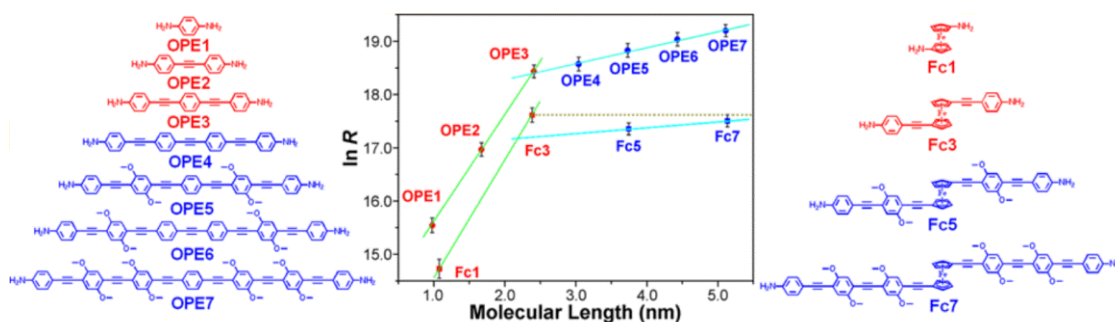
FIGURE 6 Incorporation ferrocene units reduced the molecular resistance of analogues ferrocene OPEs. Reprinted with permission from ref.[52] Copyright © 2012 American Chemical Society.

Over the past few decades, fascinating macrocycles comprising ferrocenes as functional units have been reported such as a molecular scissors,[53] tweezers[54] and springs.[55] Chiral structures resembling Escher's endless staircase[56] or ferrocene terminated helicene[57] are remarkable examples of how the 3D scaffold of ferrocene is used as structure providing "shaping" synthon. Moreover, the stable and reversible redox chemistry of ferrocene has been exploited in molecular wires,[52] sensors,[58] and switches.[59]

An increasing number of new functional materials with ferrocene as decisive entity are delivered by the scientific community. Ferrocenes exceptional ease of functionalization, the chemical and thermal stability of both, ferrocene and ferrocenium are the reason for the ubiquitous and widespread application in virtually any field of applied science, and hence it stands as synonym for an organometallic Swiss army knife.

AIM OF THIS WORK

Nanocircuits made from single-molecular devices are envisioned to replace traditional CMOS-based circuits in the near future. Molecular wires play an integral role in connecting the components of such nanocircuits. Oligo-(phenylethynylene) (OPE) molecular wires are dealt as prospect molecules for this task. Furthermore, OPEs showed reasonable charge transfer properties when redox active ferrocene subunits were integrated in the molecular backbone.[52] However, the inherent problem is the unpredictable rotational mobility of these three-dimensional units. Hence, this project arose as an imperative to find a suitable methodology to restrict the rotational freedom of trans-annularly disubstituted 1,1'-ferrocene wires. In previous studies, numerus unsuccessful experiments have been conducted to form biphenyl and terphenyl bridges that span oligo-phenylethynylene ferrocene arms.[60] We therefore designed a model-system that resembles the cyclization relevant molecular geometry of the parent compound, while omitting the uninvolved periphery (red in **SCHEME 6**). For this purpose, we chose 1,1'-diphenylene-ethynyl ferrocene as a simplified plug & play model. The major advantage of this approach is the ability to investigate the cyclization reaction and study the properties that come along with this new functionality. The results described in this chapter were published in a full article in "*The European Journal of Organic Chemistry*"[61].
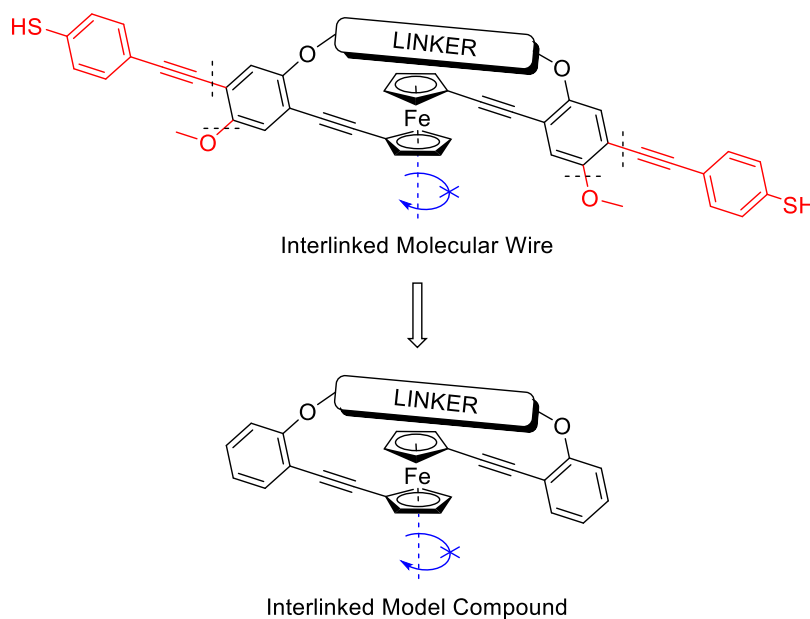
SCHEME 6 Sketch of the model approach.

STRATEGY

Preceding studies on bridging the Fc-OPE wire **9** were conducted by our former group member Nicholas Jenny and represent the starting point of our investigation.[60] In his work, the assembly of the symmetric 1,1'-functionalized ferrocene rod exposing two phenol groups as potential nucleophiles to form bridges with various di-halides was studied. With the phenol precursor, numerous attempts to bridge the ferrocene subunit with more or less rigid biphenyl and terphenyl di-halides (**10** - **12**) were performed. A representative collection of investigated reaction conditions (i-iv) and di-halides is displayed in **SCHEME 7**. In all investigated nucleophilic reaction conditions, the bridging of the ferrocene junction was not observed, but the formation of the 1,1'-di(5-methoxy-6-tris(isopropyl)silylethinylbenzofuran-2-yl)ferrocene **13** was detected as the main product instead. The formation of a double 5-*Endo-Dig* cyclization, clearly shows that the deprotonated phenols undergo an intramolecular nucleophilic attack at the *β*-carbon of the ethynyl moiety adjacent to the ferrocene and in accordance with *Baldwins* rules[62]. The observed cyclisation of 2-ethynyl substituted phenols to the corresponding benzofuran derivatives, has been proposed as versatile synthetic access to the heterobicyclic motive[63] and was already reported by Babin et. al before.[64]
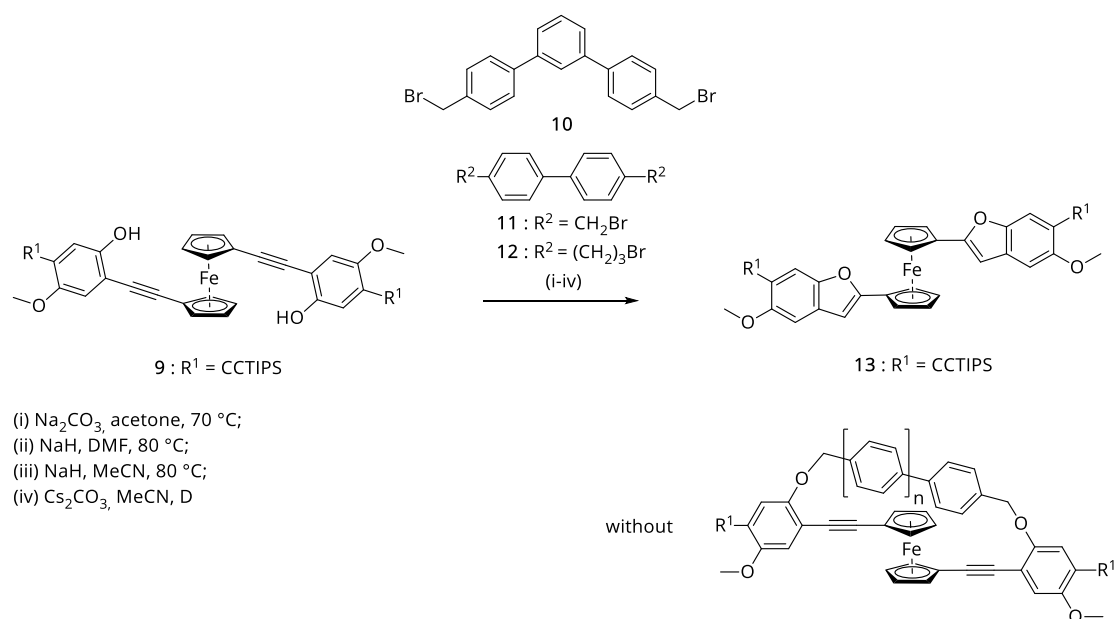
SCHEME 7 Unsuccessful *"capping"* attempts with the bis-phenol **9**, which exclusively forms the bis-benzofuran-2-yl ferrocene derivative **13** under basic reaction conditions conducted by Nicholas Jenny.

The closing of a macrocycle is usually a late step in a synthetic strategy and is often performed in diluted or pseudo diluted conditions to favor the desired intramolecular macrocyclization over intermolecular oligomer- and polymer formation. Exceptions are synthetic strategies profiting either from templates or from particular pre-folded precursors. Here we considered two conceptually different strategies, namely the *"Capping"* approach and the *"Drawbridge"* strategy, displayed in **SCHEME 8**. While the *"Capping"* strategy (as shown at top of **SCHEME 8**), is

considerably more appealing due to the large variety of different bridging structures that can be introduced in a single step, we did not succeed in the macrocycle closing by following this strategy. However, after all attempts demonstrated that the phenolate anion in *ortho*-position of the ethynyl group (**A**) is unacceptable, we considered the *"Drawbridge"* strategy (bottom path in **SCHEME 8**) that has a twofold intrinsic beauty.
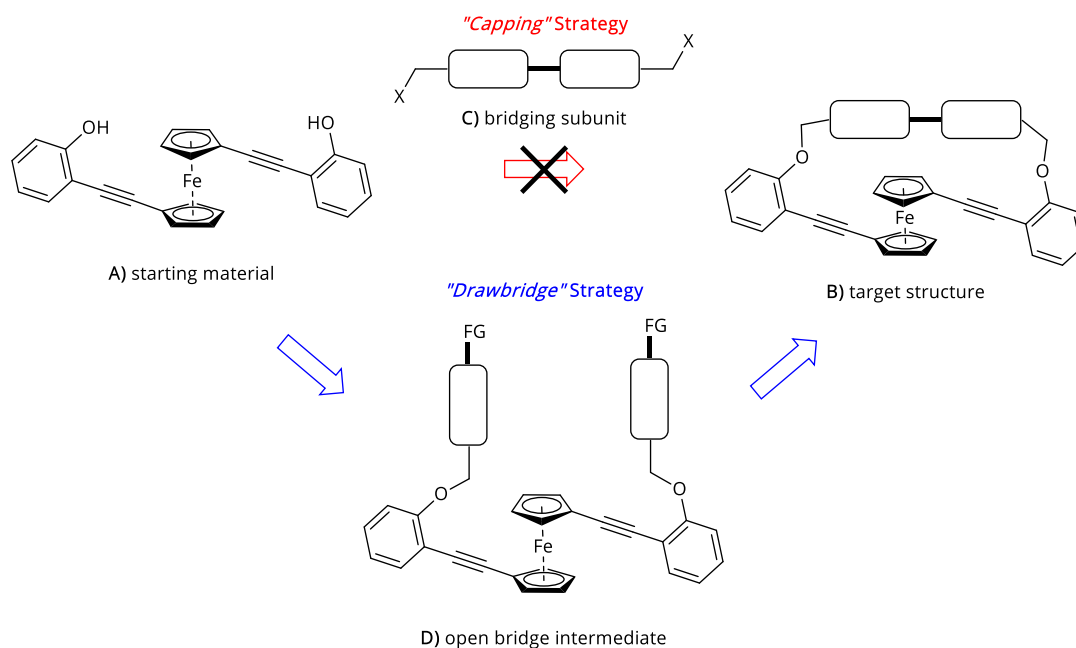
SCHEME 8 Assembly of the 1,1'-bis-(phenylethynyl)-ferrocene macrocycle based on a disconnection approach following either the *"Capping"* strategy (top: red arrow) or the *"Drawbridge"* strategy (bottom: blue arrows).

In the *"Drawbridge"* approach, not only is the phenol masked, but also the masking group itself serves as the building block for the assembly of the bridging structure in a later step. We aimed for a masking group exposing a benzaldehyde function as promising precursors of a variety of potential macro-cyclization reactions. Furthermore, the *"Drawbridge"* strategy might offer modular diversity in the bridging structure depending on the chemistry selected for the bridge formation. Particularly interesting would be an open bridge intermediate (D in **SCHEME 8**) exposing functional groups giving access to different types of coupling reactions to close the bridge. The appealing feature of this strategy would be its modularity, giving in principle access to structures with various opening angle α (**FIGURE 7**) at the ferrocene joint. Therefore, a variety of bi-functional small molecules with various spacing between both functional groups could be introduced as linker.

Top view:
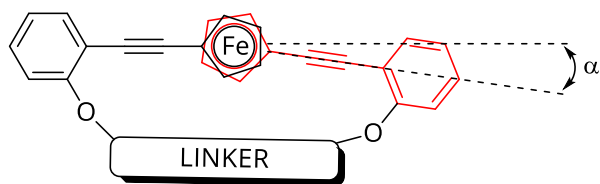
FIGURE 7 Top view representation of the target structure showing how the various length of the linker will define the opening angle α of the molecular wire.

As mentioned before, while the rotational freedom between both Cp units usually is an attractive feature of the structure and has been used e.g. as mechanical joint in scissor-type architectures,[53] in molecular rods this flexibility results in a large variety of possible conformations and consequently in a poor structural control. Thus, here we focused on locking the elsewhere appealing rotational freedom of the 3-dimensional ferrocene. As strategy to gain control over the subunits spatial arrangement, we focused on the integration of 1,1'-diphenylene-ethynylene ferrocene subunits into a macrocyclic structure.

Guided by these rationales, we chose the benzylic aldehyde **14** as precursor, giving access to a broad variety of potential ring closing reactions as displayed in **SCHEME 9**. For instance, the building block **14** might be closed directly to **30** through an intramolecular *McMurry* type reaction catalyzed by low-valent titanium species.[65] The reduction of the benzaldehydes to benzylic alcohols **15**, giving access to nucleophilic substitution chemistry. So that either closing with an ether type bridge can be accomplished or introduction of low molecular weight extensions comprising alternative functional groups like e.g. terminal olefins, which would offer ring-closing olefin metathesis (RCM) chemistry as bridging option. In an alternative approach, the bridge might also be closed using suitable bi-functional small molecules, like e.g. a bis-*Wittig* salt or a bis-amine (R in **SCHEME 9**). The first one would result in a bis-olefin bridged macrocycle while the second, upon double *Schiff*-base formation would close the bridge with a bis-imine structure.
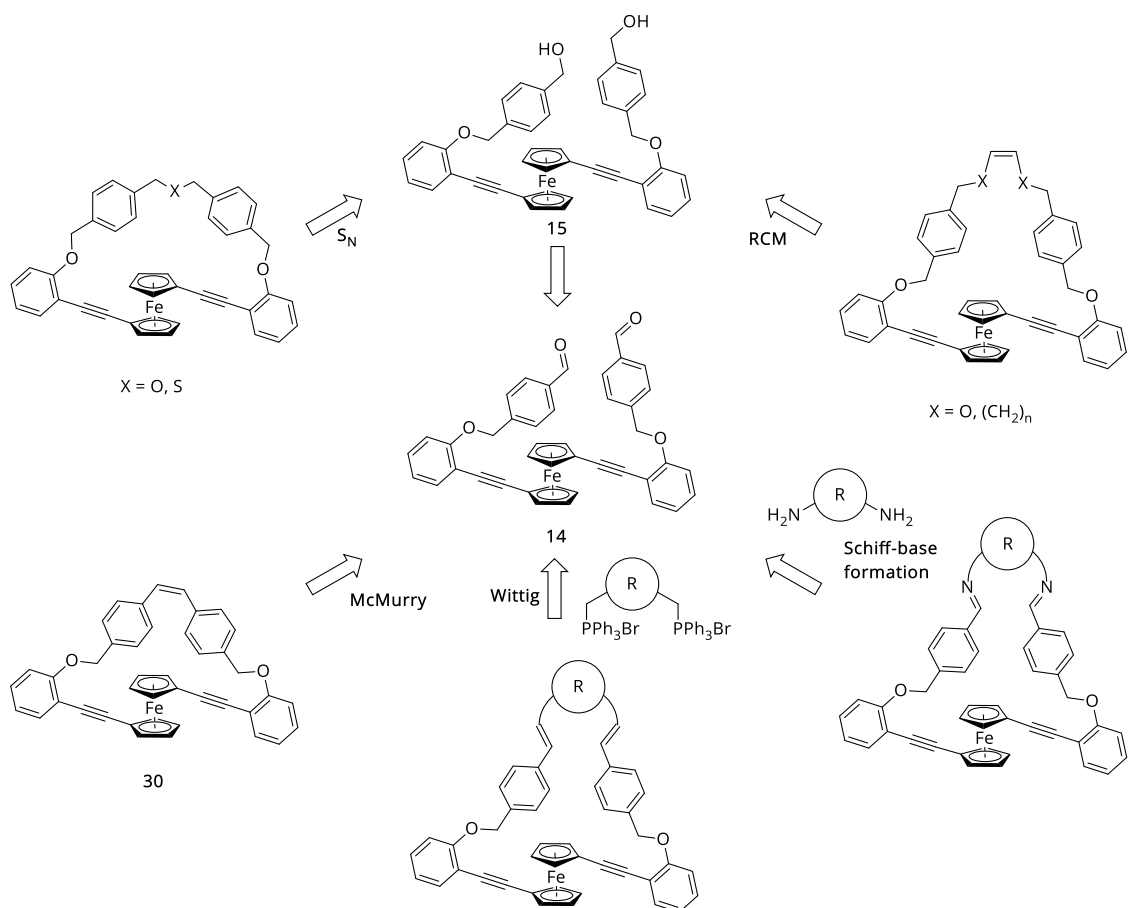
SCHEME 9 Different ring closing strategies with bis-benzaldehyde **14** as precursor.

RESULTS AND DISCUSSION

SYNTHESIS

SYNTHESIS OF ETHER BRIDGED FERROCENE

Synthesis of benzaldehyde **14** starts with the preparation of the benzyl moiety. Therefore, 2-(4(bromomethyl)phenyl)1,3-dioxolane **16** was prepared in two steps according to standard protocols (**SCHEME 10**).[66,67] Commercially available 4-bromomethyl benzonitrile was first reduced using one equivalent DIBAL-H in methylene chloride at -70 °C. After the mixture was allowed to warm up to 0 °C during one hour, the crude was purified by chromatography on silica gel yielding **16** in satisfying 84% yield. Excess use of DIBAL-H or elevated temperatures lead to the competitive formation of the amine via the intermediate iminoalane species. Benzaldehyde **16** was then transformed into dioxolane **17**, by acid-catalyzed acetalization in refluxing toluene with the aid of a Dean Stark trap. The *O,O*-acetal is compatible with the subsequent basic cross-coupling conditions, while is readily cleaved in acidic media.
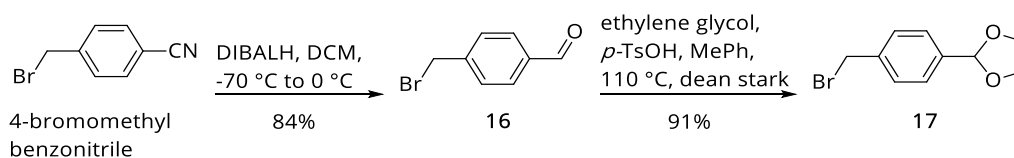
SCHEME 10 Synthesis of Dioxolane **17** in two steps.

The benzylation of 2-bromophenol was performed under basic conditions using K_2CO_3 in DMF at 80 °C (**SCHEME 11**). Palladium-catalyzed *Sonogashira* coupling of aryl bromide **18** with a slight excess of 2-methyl-3-butyn-2-ol was performed in a 1:3 mixture of DIPA/THF, using 6 mol-% of $PdCl_2(PPh_3)_2$ and 10 mol-% copper(I) iodide. The unprotected aldehyde analogue of **18** was also tested, but afforded the coupling product in low yields only. The use of 2-methyl-3-butyn-2-ol was preferred over silyl protected acetylenes, since the polarity introduced by the propargyl alcohol in **19** that enabled easy chromatographic purification.[68] Removal of hydroxypropyl with sodium hydride in refluxing toluene yielded the building block **20** in 72%. Deprotection of **19** was also accomplished, yet incomplete, using a 1 M solution of TBAOH in methanol at 75 °C, following Huang's protocol[69].
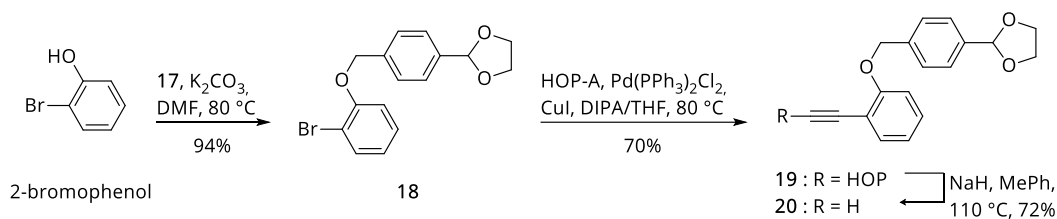
SCHEME 11 Synthesis of building block **18.**

Since 1,1'-diethynyleneferrocene readily undergoes cyclization reactions upon treatment with nucleophilic species[70], 1,1'-diiodoferrocene (FcI$_2$) **22** was selected as ferrocene source. Initially, we tried to use the solid bis-*tri*-phenylstannylferrocene as reactive precursor of FcI$_2$.

However, it rendered to be unreactive towards treatment with I$_2$ or ICl. Therefore, we followed a described protocol by Butler et al.[71] to synthesize FcI$_2$ in two reaction steps (**SCHEME 12**). Lithiation with 2.5 equivalents of *n*-BuLi and TMEDA at 0 °C and subsequent treatment with a slight excess of *tri-n*-butyltin chloride gave the corresponding bis-stannylferrocene **21**. We first washed the crude bis-stannylferrocene **21** with 1 M solution of KF in methanol, so that not con-verted *tri-n*-butyltin chloride was crushed out, and then the product was purified via column chromatography over aluminum oxide eluting with pure hexane. Additionally, we performed a vacuum Kugelrohr-distillation of the brown oil, since the formed mono-stannylferrocene could not be removed by chromatography. The pure bis-stannylferrocene **21** was then cleanly trans-formed into 1,1'-diiodoferrocene **22**, by addition of iodine to a cooled solution of **21** in CH$_2$Cl$_2$.
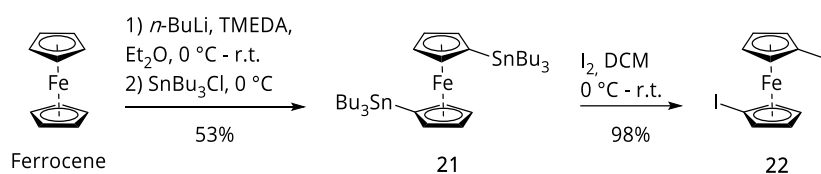
SCHEME 12 Synthesis of 1,1'-diiodoferrocene.

With acetylene **20** in hand, we were able to perform the twofold *Sonogashira* cross coupling reaction shown in **SCHEME 13**. The reaction conditions developed by Buchwald[72] and cowork-ers, and further optimized for FcI$_2$ by Inkpen et al.[73] were applied. Thus, Pd(MeCN)$_2$Cl$_2$/P(^{t}Bu)$_3$ with copper(I) iodide in a DIPA/THF mixture was kept at 60 °C, while 3 equivalents of the acetylene **20** were added to FcI$_2$. The desired symmetric product **23** was iso-lated after flash column chromatography on silica gel as an orange-red solid in 90% yield. Sub-sequent cleavage of the acid labile dioxolane was accomplished with pyridinium *p*-toluenesulfonate (PPTS), by trans-acetalization in an acetone/water mixture.[66,74] The deprotec-tion was performed in a sealed microwave tube and completion was observed after 10 minutes of irradiation at 80 °C. Reduction of the corresponding aldehyde **14** worked in nearly quantitative

yields when treated with $NaBH_4$ in THF at room temperature for 30 minutes, forming the Fc derivative **15** exposing two benzylic alcohol groups. Thus, starting from 2-bromophenol and FcI_2, the molecular rod **15** comprising a ferrocene junction and exposing on both sides a benzylic alcohol was available in 6 steps and in an over-all yield of 56%.

(i) PPTS, acetone/water, mW, 80 °C, 10 min, 96%
(ii) $NaBH_4$, THF, r.t., 30 min, 99%
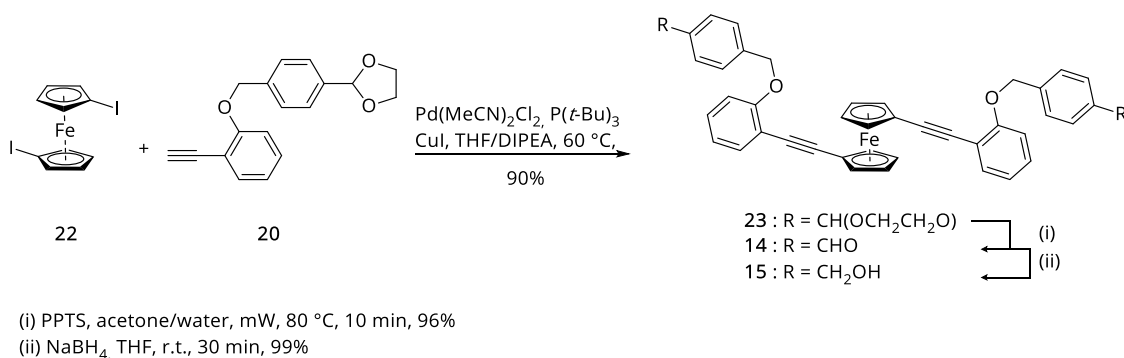
SCHEME 13 *Sonogashira* cross coupling of FcI_2 and acetylene **20**, subsequent treatment formed dibenzyl alcohol **15**.

With the bis-benzylic alcohol **15** we first tried to form the ether-bridge via an intramolecular cyclization reaction. Thereby, one of the benzylic alcohols of **15** should be converted in a good leaving group, in order to be attacked intramolecularly by the other alcohol. Efforts to trigger the formation by activating one benzylic alcohol in an intramolecular *Mitsunobu*-Type reaction (**TABLE 1**, entry 1) as well as in an intramolecular S_N2-type reaction (entry 2), failed at first. The *in-situ* formation of mono-mesylate and consequent substitution reaction gave the cyclic product **24** in poor yields.
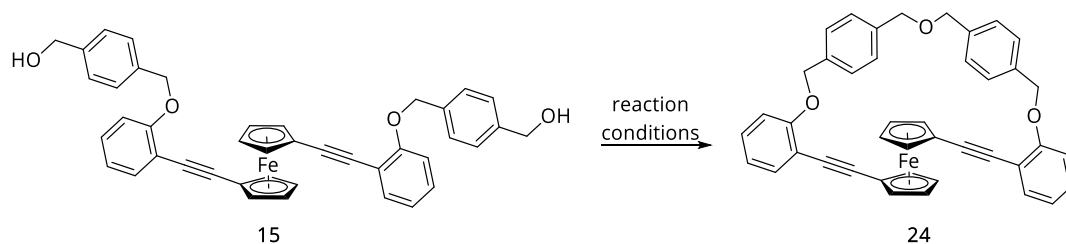
TABLE 1 Reaction conditions used for the direct cyclization of diol **15**.

entry	reagent	base	solvent	temperature in (°C)	duration in (h)	yield
1	PPh_3 (0.6 eq.), DIAD (0.6 eq.)	-	THF (12 mM)	0 − 25	24	-
2	Tf_2O (0.6 eq.)	pyridine (1 mL)	DCM (30 μM)	25	12	
3	MsCl (1.0 eq.)	NaH (2 eq.)	THF (6 mM)	0	1	15%

When the reaction mixture of mono-mesylated intermediate was heated to 50 °C, intermolecular reaction products of open and closed structures in varying ring sizes were formed and detected by MALDI ToF spectrometry as shown in **FIGURE 8**.
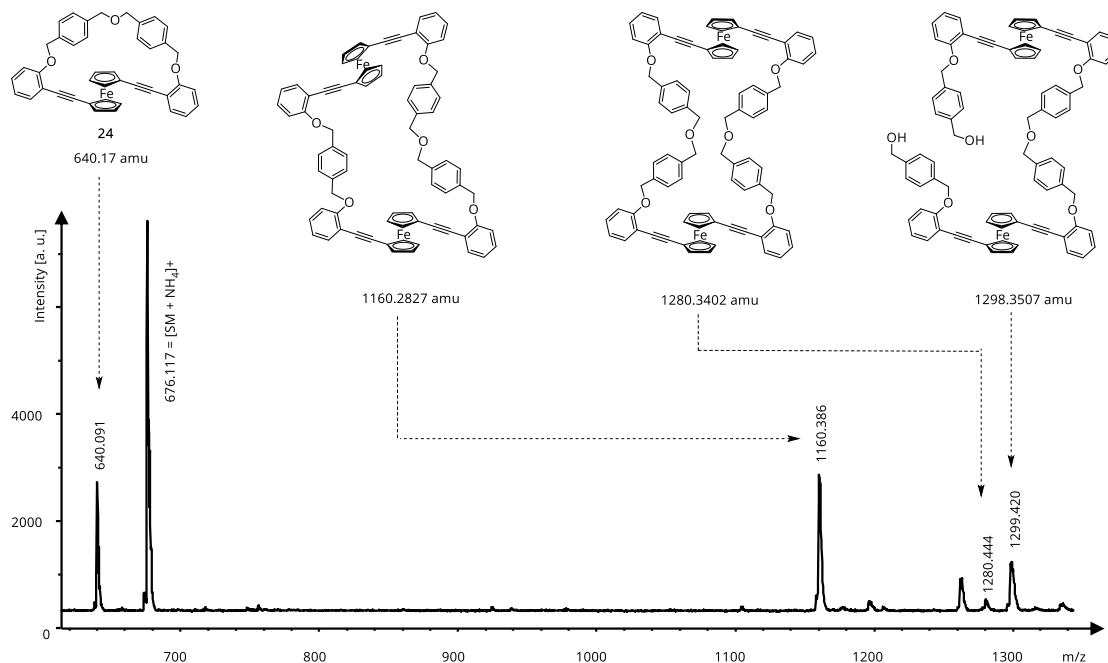
FIGURE 8 MALDI-ToF MS reaction control of mesylation after heating to 50 °C.

This motivated us to further investigate the mesylation reaction with regard to mono- and bis-mesylate formation. Therefore, an oven-dried Schlenk flask was purged with argon and charged with a 1.5 mM solution of diol **15** in dry and deoxygenated THF or DCM. The reaction mixture was cooled down and the resulting bright orange solution was treated with base under a positive pressure of argon. The mixture was stirred for 20 minutes, before methanesulfonyl chloride was added via a Hamilton syringe and the reaction progress was monitored by MALDI-ToF MS.

The MALDI-ToF MS reaction control showed that the mesylate was formed statistically when one equivalent methansulfonyl chloride was used (**TABLE 2**, entry 4 & 5). Full conversion could be monitored when an excess of reagent was used. Mesylate, started to decompose at elongated reaction times and at room temperature as depicted in **FIGURE 9**. Attempts to isolate the reactive mesylate intermediate resulted in loss of compound and formation of poorly soluble, tar-like substance when the crude was concentrated rendering the isolated yields to be poor.
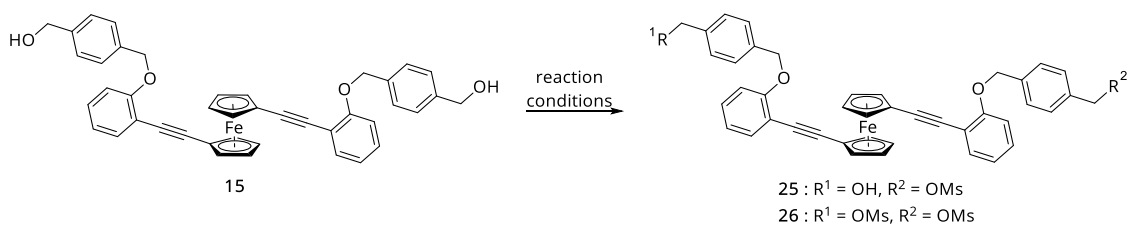
TABLE 2 Mesylation of bis- alcohol **15** with varying reaction conditions and isolated yields.

entry	reagent	base	solvent	temperature in (°C)	duration in (h)	**25**	**26**
1	MsCl (1.0 eq.)	Et$_3$N (1 mL)	DCM	0 − 25	1	-	-
2	MsCl (4.0 eq.)	NaH (4 eq.)	THF	0 − 25	12	-	-
3	MsCl (10 eq.)	NaH (50 eq.)	THF	-10 − 25	64	-	-
4	MsCl (0.6 eq.)	NaH (5 eq.)	THF	0	24	13%	12%
5	MsCl (1.0 eq.)	NaH (2 eq.)	THF	-10	1	20%	36%
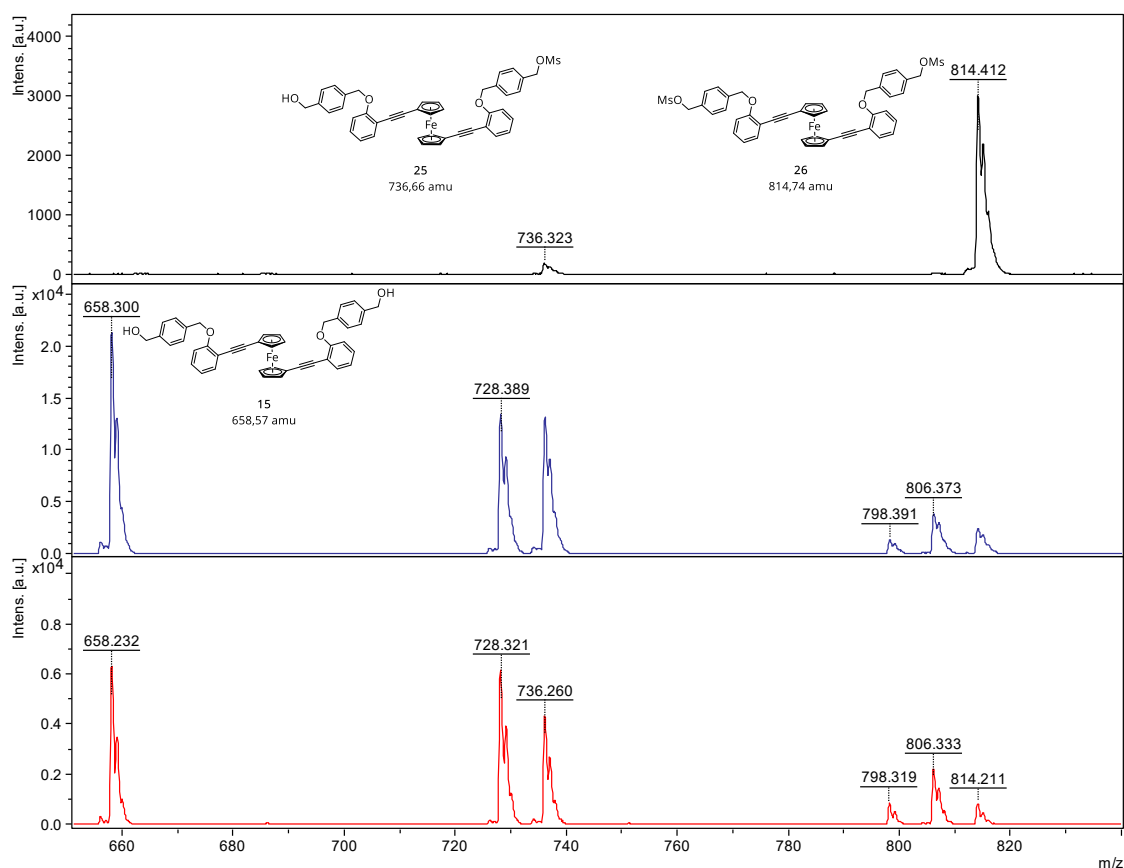
FIGURE 9 MALDI-ToF MS reaction control of the cooled solution after 2 h (top), 24 h (middle) and 48 h (bottom) at room temperature.

Hence, we decided to convert the mesylate intermediates *in-situ* into the less reactive bromo derivate, by addition of lithium bromide to the reaction mixture of mesylated intermediates

(**SCHEME 14**).[75] The two-fold statistical reaction cleanly transformed the bis-alcohol into mono-bromo **27** and bis-bromo **28** after 2 h and the products showed different polarities on silica gel. It was possible to isolate the products from the remaining starting material by FCC in 33% and 40% respectively. We found this stepwise procedure inevitable, since alternative Appel reactions turned out to be too acidic, as several side products arise from cleavage of the benzyl moiety and subsequent benzofuran formation upon treatment.
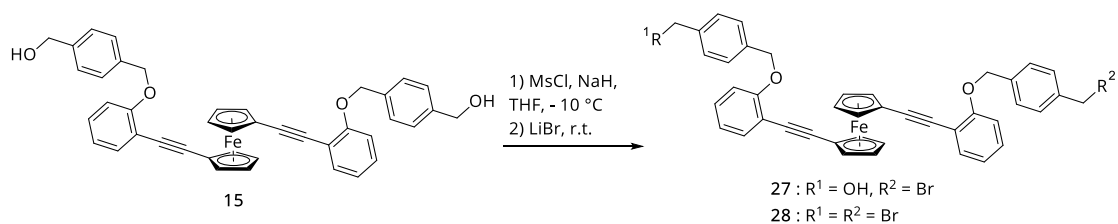
SCHEME 14 Mesylation and subsequent bromination of diol to the statistical mono-bromo **27** and bis-bromo **28** derivate.

Due to the high reactivity of the mesylated intermediate and the accompanied cyclization problems we were facing, we chose the ether formation to conduct with mono-bromo ferrocene **27** (**SCHEME 15**). Therefore, a 0.5 mM solution of mono-bromo **27** in dry and deoxygenated tetrahydrofuran was treated with an excess of sodium hydride. To our delight, the reaction gave cleanly the desired ether bridged macrocycle **24** in excellent 70% yield after 2 hours at 70 °C.
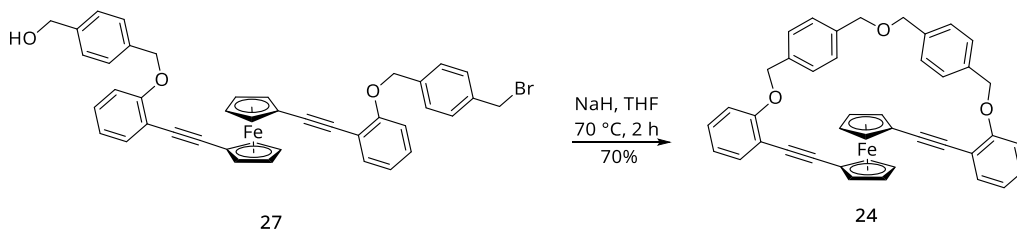
SCHEME 15 Intramolecular S_N2-type macro-cyclisation of mono-bromo ferrocene **27** with NaH in THF at 70 °C.

The successful macrocyclization was confirmed by the mass of the isolated compound recorded by MALDI-ToF-MS, and further corroborated by ^{1}H NMR spectroscopy.

We noticed significant difference in the chemical shifts for the benzylic-CH_2 protons and the ferrocene-CH signals. As depicted in **FIGURE 10**, compound **27** nicely shows two separate signals for its methylene protons H^c at 4.63 ppm (s, 2H) (geminally located to OH) and H^e at 4.44 ppm (s, 2H) (CH_2 next to Br), while in symmetric compound **24**, CH_2-protons merge into a common benzyl ether signal $H^{c'}$ at 4.58 ppm (s, 4H). The benzylic protons H^a and H^b in compound **27** are found as two overlapping singlets, and likewise culminate as $H^{a'}$ in macrocycle **24**. More profound, the ferrocene protons of open structure **27** are seen as four pseudo-triplets with α protons H^d at 4.49 ppm (pseudo-t, "J" = 1.9 Hz, 2H) and 4.46 ppm (pseudo-t, "J" = 1.9 Hz,

2H) respectively, and two upfield shifted and overlapping β protons as pseudo-triplets H^f at 4.25 ppm (pseudo-t, "J" = 1.9 Hz, 2H) and 4.24 ppm (pseudo-t, "J" = 1.9 Hz, 2H). This splitting can be explained by the magnetic inequivalence of the two α- and two β-protons of each Cp ring. Hence the ferrocene protons of compound **27** are shown as two high-order AA'MM' and BB'XX' spin systems with four signals in total. In contrast, the spectra of fully symmetric macrocycle **24** shows only two pseudo-triplets $H^{d'}$ at 4.61 ppm (pseudo-t, "J" = 1.8 Hz, 4H) and $H^{f'}$ at 4.30 ppm (pseudo-t, "J" = 1.8 Hz, 4H) as one AA'MM' high-order spin system.
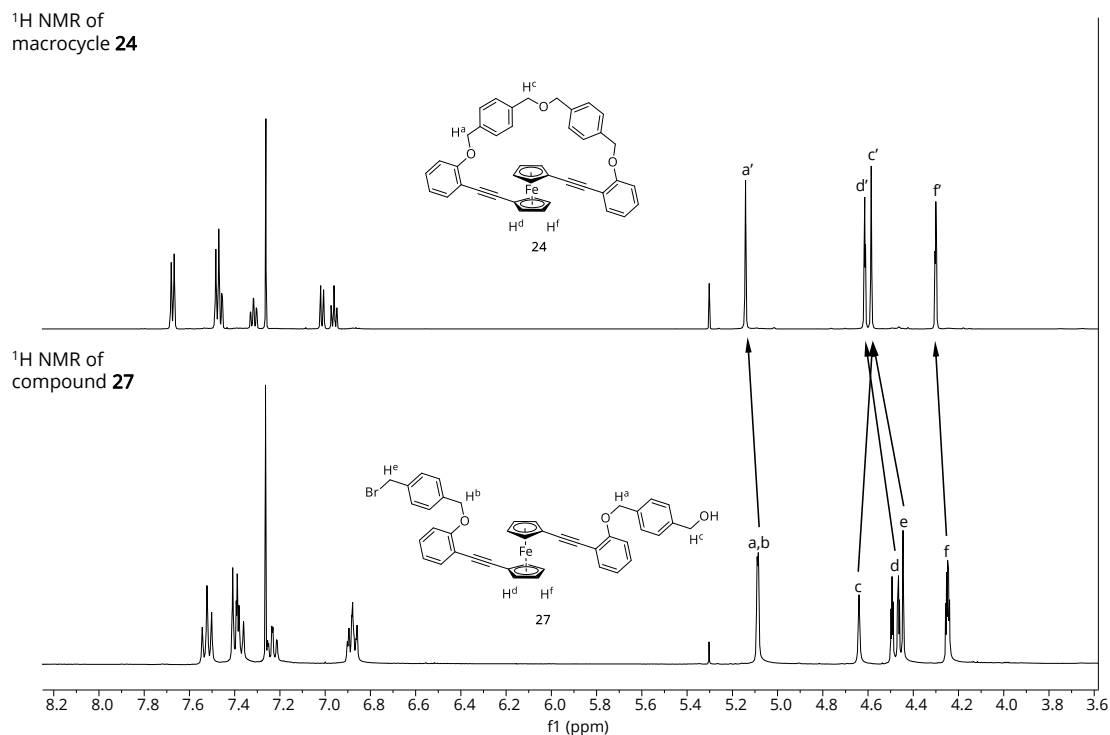
FIGURE 10 ¹H NMR spectra of compound **24** and **27** in CDCl₃ at 25 °C.

SYNTHESIS OF BUTENE BRIDGED FERROCENE

In order to obtain a heteroatom free bridging structure, we focused on the RCM as potential ring closing reaction (**SCHEME 9**). Our efforts to bridge the bis-styrene decorated ferrocene rod **29** were unsuccessful. RCM reactions were conducted in dry solvent over 12 h. The open precursor **29** was treated with varying catalysts (see Table 3), however not even traces of a cyclic stilbene ferrocene **30** were found. At first, the RCM of the styrene units that are categorized as type II olefins (moderate reactivity, found by Grubbs[76]), appeared to be accomplishable as styrene cross metathesis (CM) is reported[77]. Yet, the demanding steric effects that are accompanied with a stilbene bridged cycle, probably outbalance the entropic benefits of the RCM reaction.
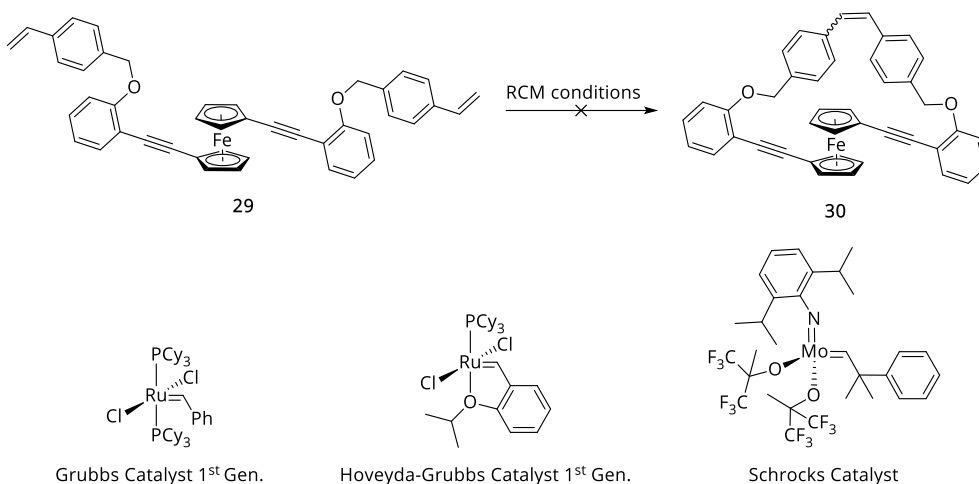
TABLE 3 Ring closing metathesis reaction to form a stilbene bridged ferrocene.

entry	catalyst	concentration	solvent	solvent	temp
1	Grubbs catalyst 1st gen.	DCM	1.2 mM	1.2 mM	25 °C
2	Hoveyda-Grubbs cat. 2nd Gen.	DCM	1.2 mM	1.2 mM	40 °C
3	Schrocks catalyst	toluene	4.6 mM	4.6 mM	40 °C

It became clear that the formation of a stilbene bridge is very challenging. Hence, we decided to further allocate the terminal olefin from the benzyl moiety, in order to increase the olefin reactivity (allyl groups are categorized as type I in Grubbs reactivity chart) and facilitate a larger reaction cavity on the cycle side.

As promising precursor we identified the ferrocene rod **31** exposing two (4-allylbenzyl)oxy substituents. Thus, the diol **15** was converted to the bis-bromo derivate **28** (**SCHEME 14**), this time by excessive use of methanesulfonyl chloride and subsequent addition of 20 equiv. of LiBr. The product was isolated in 69% yield after a short column on silica gel, as a red oil that crystalized upon standing. Then, bis-bromo compound **28** was treated with 20 equiv. of a 1 M solution of vinylmagnesium bromide in THF in the presence of 1.0 equiv. copper(I) iodide at -70 °C (**SCHEME 16**).[78]
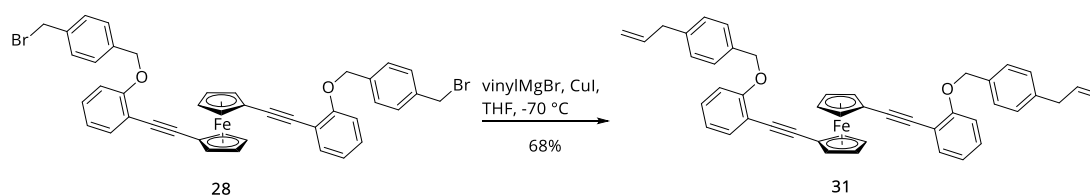
SCHEME 16 *Grignard* reaction to generate the RCM precursor bis-allylbenzyl **31**.

The reaction mixture was allowed to warm up to room temperature over 15 h when the control reaction by MALDI-ToF mass spectrometry showed full consumption of the starting material. The black reaction mixture was quenched by pouring onto a saturated aqueous solution of NH_4Cl. After aqueous workup and extraction, the crude was purified by FCC on silica gel and bis-allylbenzyl **31** was isolated as a red/orange oil in 68% yield. Additional side products were eluted by gradually increasing the polarity of the eluent. Interestingly, the analysis by mass spectrometry of these isolated side products revealed the formation of an ethane-bridged monomeric macrocycle and a di- and tri-meric open structures (**FIGURE 11**), pointing at an intra- and intermolecular *Grignard* reaction of bis-bromobenzyl **28** under these reaction conditions.
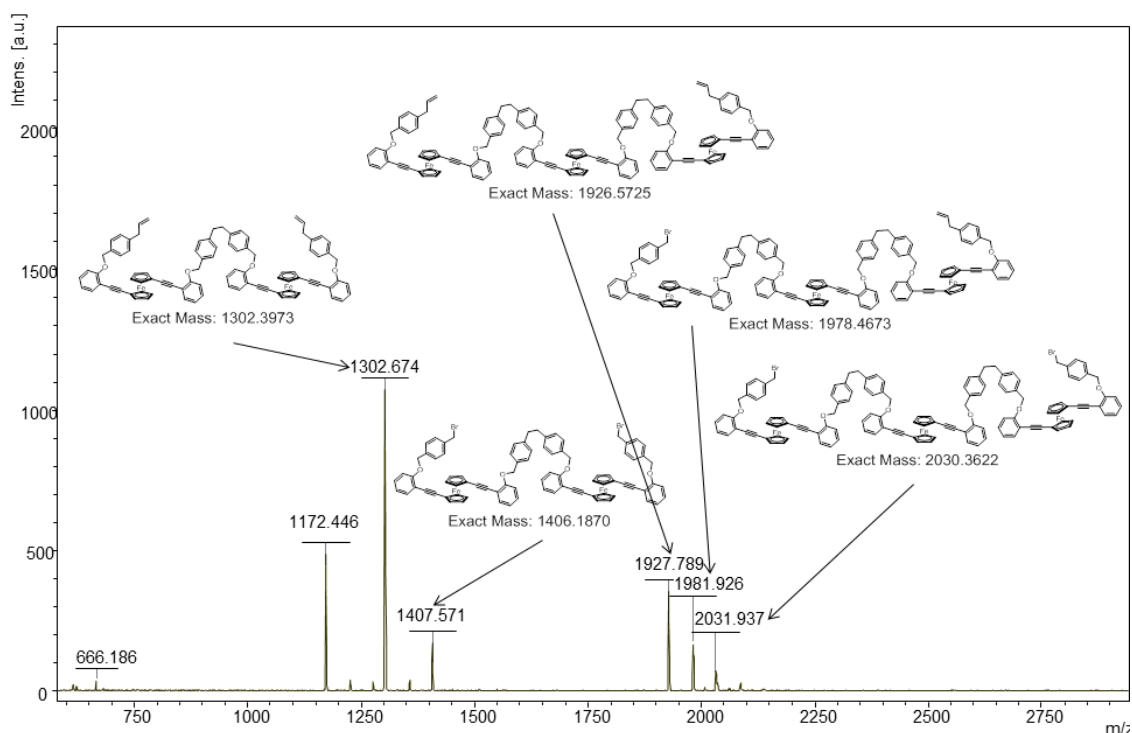
FIGURE 11 MALDI-ToF spectrum of the mixture of side products obtained in the intramolecular Grignard reaction.

With the bis-olefin **31** in hand, we were able to investigate the RCM reaction (**SCHEME 17**). Therefore, a 1.0 mM solution of divinyl **31** in freshly distilled dichloroethane was prepared and heated together with 15 mol-% of Grubbs' catalyst 1st gen. for 16 hours at 70 °C. Butene-bridged macrocycle **32** was isolated after column chromatography in 57% yield as an inseparable mixture of *E/Z* isomers.
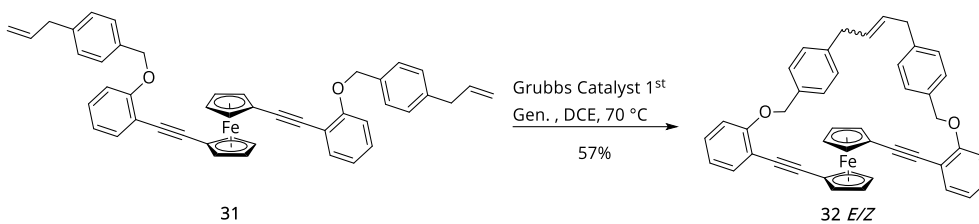
SCHEME 17 Ring Closing Metathesis of allyl benzyl moiety using Grubbs' catalyst 1st gen.

The formation of an **E/Z** mixture was not surprising as neither an **E-** or **Z**-selective RCM catalyst was used, nor the starting material bears structural determinants. The macrocycle was characterized by mass analysis and identified as the target compound **32E/Z** by one- and two-dimensional NMR experiments.

Unambiguous determination of the **E** and **Z** isomer is hampered by the symmetry of the two stereoisomeric compounds. The two vinyl protons $H^a_{E/Z}$ in **32E/Z** are symmetry equivalent and isochronous in both cases. However, the coupling to the two adjacent $H^f_{E/Z}$ methylene groups results in magnetically inequivalent protons that show high-order spectra that cannot be analyzed directly. Consequently, we recorded a 2D-HSQC spectrum (**FIGURE 12**) that showed a chemical shift difference of $\Delta\delta = 5.3$ ppm for the allylic carbons. It allows unambiguous assignment of the major species as the **E-** isomer with $\delta = 38.7$ ppm, whereas the minor **Z-** isomer resonates at $\delta = 33.4$ ppm.
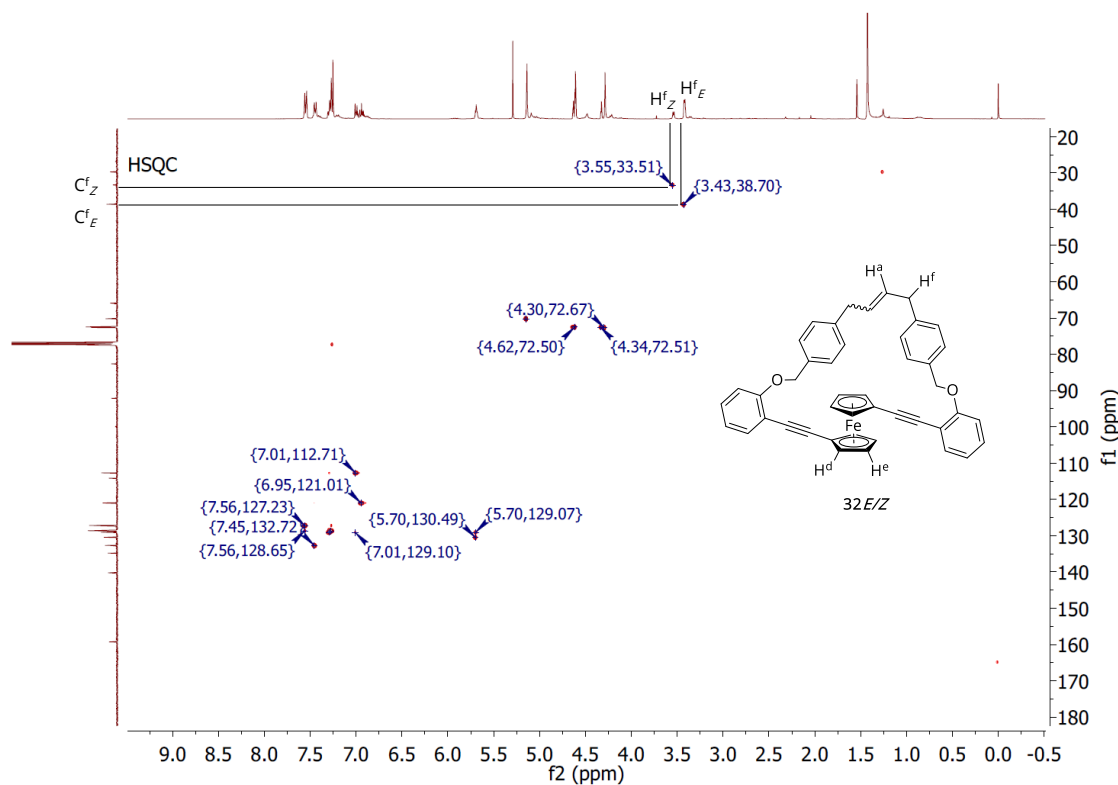
FIGURE 12 2D HSQC NMR shows a chemical shift difference for the allylic carbons of 5.3 ppm, whereas the *E* isomer resonates at lower field.

FIGURE 13 shows the ¹H NMR spectra of macrocycle **32** and its precursor **31**. Structural transformation is most commandingly pronounced by the H^f allyl- and H^a vinyl proton signals. The characteristic vinylic methine protons H^a in **31**, merge from 5.93 ppm (ddt, J = 16.9 Hz, 10.2 Hz, 6.7 Hz, 2H) to an overlapping signal for both isomers as $H^a_{E/Z}$ at 5.69 ppm (m, 2H). Allylic protons H^f in compound **31** diverge in two for the **E-** and **Z-** isomer corresponding doublets with H^f_Z at 3.54 ppm (d, J = 5.1 Hz, 2H) and H^f_E at 3.42 ppm (d, J = 4.9 Hz, 2H). The terminal olefin protons H^c in **31**, completely disappear in the macrocycle. The structural change affects the benzylic protons H^b slightly, as the change is only $\Delta\delta$ = 0.047 ppm. Finally, the ferrocene signals draw a coherent picture of the formed macrocycle **32**. We recorded H^d_Z ferrocene protons at 4.63 ppm (pseudo-t, "J" = 1.8 Hz, 4H) and H^e_Z at 4.33 ppm (pseudo-t, "J" = 1.8 Hz, 4H) respectively H^d_E at 4.61 ppm (pseudo-t, "J" = 1.8 Hz, 4H) and H^e_E at 4.29 ppm (pseudo-t, "J" = 1.8 Hz, 4H) in accordance with the above stated splitting system for symmetric substituted ferrocenes. The **E/Z** ratio was calculated by comparing the integrals for allylic protons H^f_E and H^f_Z and was found to be [2.8:1].
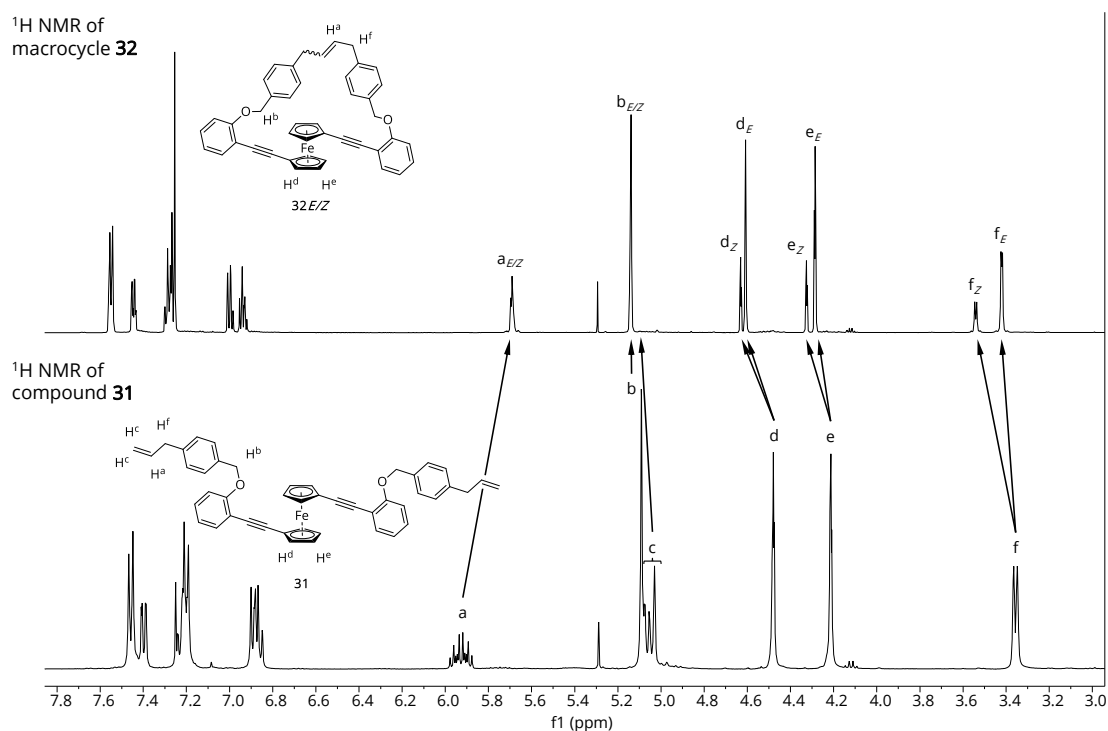
FIGURE 13 ¹H NMR spectra of compound **31** and **32** in CDCl$_3$ at 25 °C.

Synthesis of a (benzyloxy)but-2-ene bridged ferrocene

To further elongate the bridging unit, we planned to connect the benzyl moieties via an allyl ether bridge. For this, diol **15** was treated in a dry and deoxygenated THF solution with 4.0 eq. of sodium hydride at room temperature, followed by the addition of 4.0 eq. allyl bromide and heating at 60 °C for 5 hours (**SCHEME 18**).
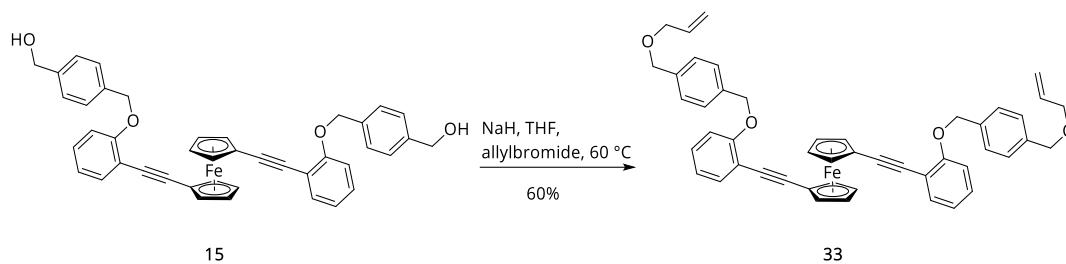
SCHEME 18 S$_N$2 reaction of bis-benzyl alcohol 20 and allylbromide in THF at 60 °C.

The product **33** was isolated after column chromatography on silica as an orange solid in 60% yield. For the final ring closing reaction, diallyl ether **33** was heated to 60 °C in a 1.3 mM solution of dichloroethane and 7.5 mol-% of Grubbs' catalyst 1st gen (**SCHEME 19**). Full conversion was observed after 20 hours and macrocycle **34** was isolated after column chromatography on silica gel in 57% yield as a mixture of **E/Z** isomers. The mixture was separated on semi-preparative HPLC eluting with a DCM/2-propanol (95/5) mixture to give 73% of **E-** and 27% of the **Z-** isomer.
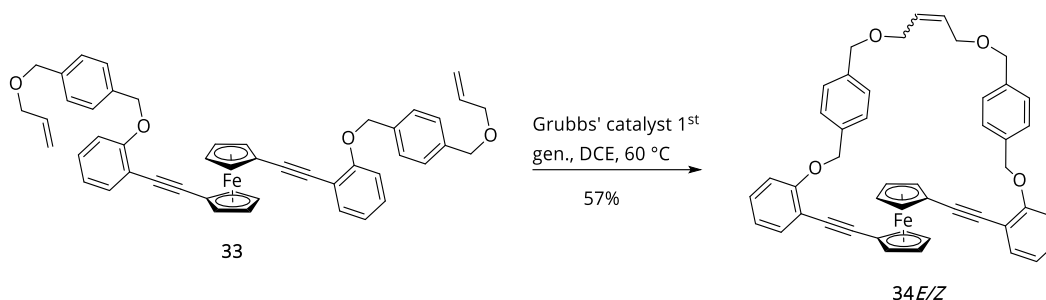
SCHEME 19 Ring Closing Metathesis of allyl ether **33** using Grubbs' catalyst 1st gen. in DCE and 60 °C.

We identified the two isomers by recording a double-quantum filtered, carbon-coupled 1D HMQC type spectra, where only protons bound to a ^{13}C-nucleus give a detectable signal. The coupling to the carbon-13 results in a large doublet splitting and thus, leads to anisochronous olefinic protons that now couple in a first order spectrum with each other. The differences in proton-proton coupling constants clearly allow the assignment of the **Z-** ($^3J_{HH}$ = 11.5 Hz) and the **E-** isomer ($^3J_{HH}$ = 15.8 Hz) shown in **FIGURE 14**.
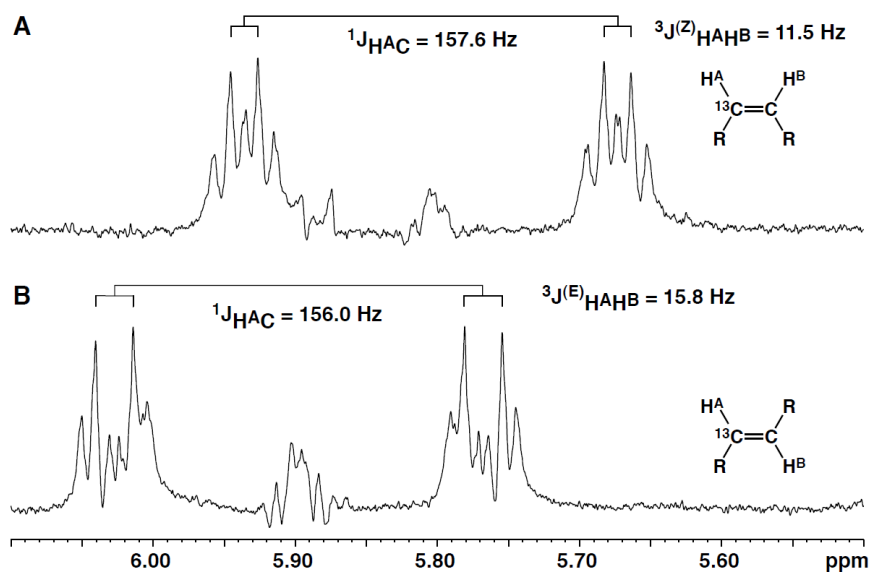
FIGURE 14 Double-quantum filtered, carbon-coupled 1D HMQC type spectra of both compounds. Proton-proton coupling constants unambiguously allow the assignment of the A) **34Z**- ($^3J_{HH}$ = 11.5 Hz) and the B) **34E**-isomer ($^3J_{HH}$ = 15.8 Hz).

Furthermore, the ^{13}C-chemical shift difference for the adjacent CH_2-group additionally validates these findings (**34E** at 69.9 ppm and **34Z** isomer at 65.0 ppm), displaying the well-known gamma-effect.[79] The structural change can be tracked with the help of ^{1}H NMR spectra shown in **FIGURE 15**. Vinylic methine protons H^a in **33** at 5.93 ppm (ddt, J = 17.2 Hz, 10.4 Hz, 5.6 Hz, 2H) diverge into H^a_E at 5.88 ppm (m, 2H) in **34E** and H^a_Z at 5.78 ppm (m, 2H) in **34Z**. The olefin protons H^b and H^c in compound **33** disappear for the **E** and **Z** isomers of the macrocycle **34**. The benzylic protons H^d are both shifted slightly highfield in the macrocycles while methylene protons H^f show an inverse trend for the **E-** and **Z-** isomer as H^f_E at 5.09 ppm (s, 4H) is slightly shifted downfield and H^f_Z at 4.43 ppm (s, 4H) shifts highfield. More connotatively is the strong downfield shift for the α ferrocene protons going from the open structure in **33** to the closed macrocycle **34E** with $\Delta\delta$ = 0.31 ppm for $H^{g'}_E$ and $\Delta\delta$ = 0.26 ppm for H^g_Z in **34Z**. Less explicit is the change in the β ferrocene protons for **34E** with $\Delta\delta$ = 0.22 ppm in H^h_E and $\Delta\delta$ = 0.22 ppm for H^h_Z in **34Z**. We attribute this variation to local magnetic anisotropic effects that arise from *"edge"* pointing aromatic bridging rings that are forced into the ferrocene space. On the other hand, allylic protons H^e in **33** are strongly deshielded, while in the macrocyclic compounds the protons H^e_E and H^e_Z are twisted out of the olefinic plane and are strongly highfield shifted as depicted in **FIGURE 15**.
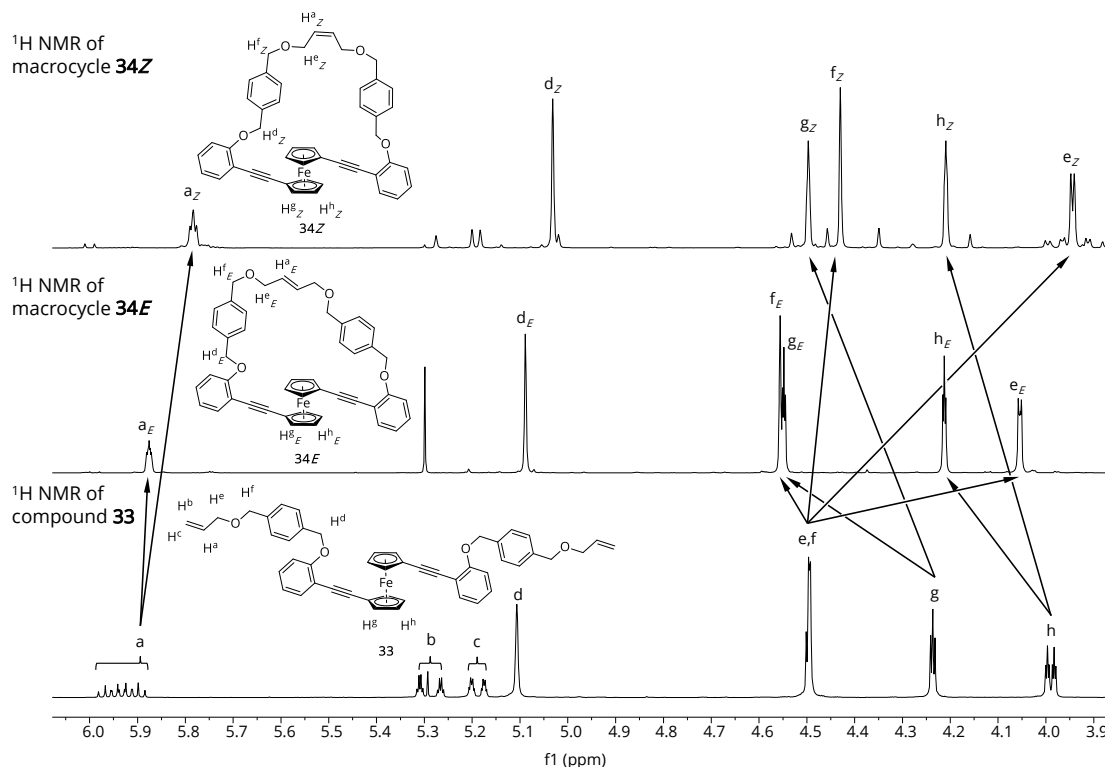
FIGURE 15 ¹H NMR spectra of compound **33E**, **33Z** and **32** in CDCl₃ at 25 °C.

Numerous attempts to grow single crystals of the macrocycles **24**, **32** and **34** failed, what we initially attributed to a too large flexibility of the bridging structure. This hypothesis was not correct as first single crystals suitable for X-ray diffraction analysis were obtained of the macrocycle **34Z**, comprising a particular long and flexible bridging structure. The crystals were obtained by solvent diffusion crystallization in a CH₂Cl₂/2-propanol system. The solid-state structure is displayed in **FIGURE 16** and corroborated both, the identity of compound **34Z** and our assignment to the structures based on the NMR spectra. While the structural affirmation is pleasing, the solid-state structure challenges our molecular design. Obviously, the bridging structure is too flexible to enforce a stretched arrangement of the phenyl-ethynyl-Fc-ethynyl-phenyl substructure, at least in the solid-state. Instead, **34Z** crystallizes in a hook shaped arrangement, with nearly parallel-orientated phenylethynyl moieties and a dihedral angle of 9.95° enclosed by both ethynyl groups. The interplanar distance of 3.723 Å measured between both centers of the phenyl rings (d_1 in **FIGURE 16**), suggests considerable π-π interactions between the OPE subunits. Due to this stacked confirmation, the Z-allyl ether bridge forms a loop that is tilted to one side of the macrocycle and causes an O-atom distance of only 3.551 Å between O_1 and O_4 (d_2 in **FIGURE 16**). Another eye-catching structural feature is the proximity of the ferrocene hydrogen atoms and the phenyl rings of the bridging linker. The ferrocene α and β hydrogen atoms next to the linking loop are both located in the periphery of the phenyl rings, what agrees with the strong downfield proton shift observed for the α and β ferrocene protons upon forming both, the macrocycles **34Z** and **34E** (**FIGURE 15**). The hook shaped arrangement of **34Z** is mainly present in the solid-state structure due to crystal packing forces and the dissolved

molecule must have a structural flexibility resulting in a single signal for all α and β ferrocene protons respectively, as observed in the ^{1}H NMR spectrum (**FIGURE 15**). Attempts to freeze out the molecular motion were not successful, as the ^{1}H NMR experiments at -80 °C in CD_2Cl_2 still displayed a single signal for all 4 α ferrocene protons. The averaging flexibility of the dissolved molecule must comprise rotational motion around the ferrocene as well as along the CC-Cp axis.
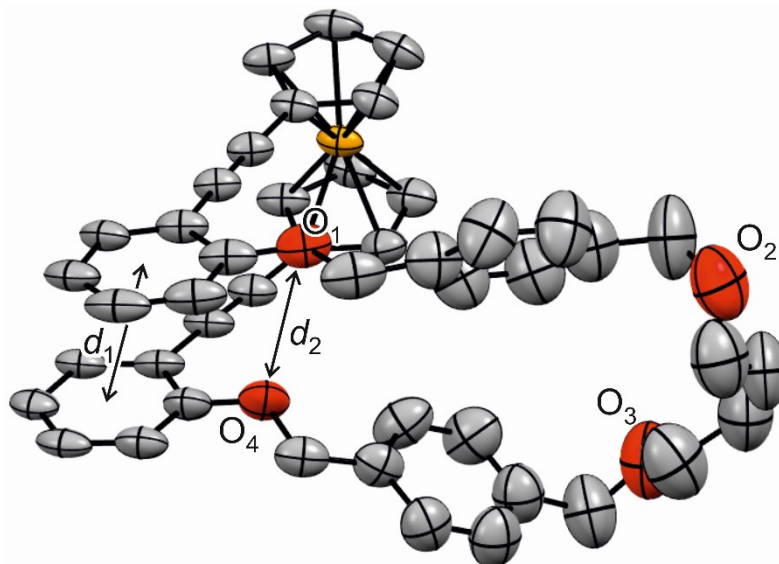
FIGURE 16 ORTEP plots of the solid-state structure of **34Z** with ellipsoids plotted at the 50% probability level.

It is noteworthy that only the macrocycles **34Z** and **34E** display a pronounced downfield shift of the ferrocene protons, pointing at a to some extent coplanar arrangement of the phenyl rings in the bridging structure and the cyclopentadienyl rings of the ferrocene subunit. For the cyclization reaction to form macrocycles **24**, **32E** and **32Z** only little effect on the chemical shift of the α and β ferrocene protons was observed (**FIGURE 10** and **FIGURE 13**). This does not exclude a rotation of the ferrocene joint, but implies that the bridge rings are at least less frequently located in plane with the cyclopentadienyl rings when in solution.

DFT-CALCULATIONS

In the previous section, it was described that the chemical shift of the α and β ferrocene protons of the macrocycles **24**, **32E** and **32Z** showed to be influenced only marginally, when the cycles were formed, while the α and β ferrocene protons of **34E/Z** showed significant downfield shift, pointing at stacked phenylethynyl arms. In order to assess the likeability of forming stacked conformers, of the otherwise dynamic geometry, the quantum mechanically optimized structures might suggest the preferred orientation. In addition, the preferred orientation of either bridging unit is an important criterion for choosing the linker moiety in the parent interlinked molecular wires.

Therefore, the *O-O* spanning distance of the introduced bridge, the *O-O* distance of macrocycles (stacked and elongated) and the *O-O* distance in fully extended Fc-OPE-OH were compared (**TABLE 4**). For this task, DFT geometry optimization calculations in gas phase were performed, utilizing the quantum mechanical program Spartan '10 (Wavefunction, Inc., USA) with the B3LYP method and mixed basis set (6-31G** for C, H, O and LANL2DZ for Fe). The results are summarized in **TABLE 4**.

In general, the significance of this theoretical approach is at best, limited by the conformity of the *O-O* distance in the crystal structure of **34Z** and its corresponding calculated *O-O* distance in stacked Fc-DPE-*Z*-allyl-ether and that of the free bridge (**TABLE 4**, entry 8 & 9). However, matching values of bridge and macrocycle suggest tentatively the rightness of what the *O-O* distance might be in the respective compound.

In Fc-DPE-OH the free hydroxy groups span a *O-O* distance of 11.212 Å, when the Cp arms are fully elongated and oriented coplanar (**TABLE 4**, entry 1). This value is best reproduced by the ether bridge with a calculated distance of 11.770 Å (**TABLE 4**, entry 2). The calculated *O-O* distance in elongated Fc-DPE-ether is 11.035 Å (**TABLE 4**, entry 2), while that of the stacked structure is 4.175 Å only (**TABLE 4**, entry 3). In this scenario, the calculation supports an elongated orientation of the ferrocene arms. In contrast, the longer butane and allyl-ether bridges show *O-O* distances much longer than the maximum *O-O* distance in Fc-DPE-OH that is 12.265 Å. This points out that any formed macrocycle of the butane- and allylether-bridges has to distort the Fc-DPE-OH from elongated orientation and hence would favor a stacked structure by spanning greater angles than 180°.

In summary, the comparison of the linker spanning distances and the macrocyclic spanning distances showed matching results for the ether bridged macrocycle **24** and the *Z*-allyl-ether macrocycle **34**, only. However, only the ether bridge linker shows the advantageous elongated orientation preference. The remaining structures show distance discrepancies that do not suggest a preference orientation for an elongated over a stacked structure.
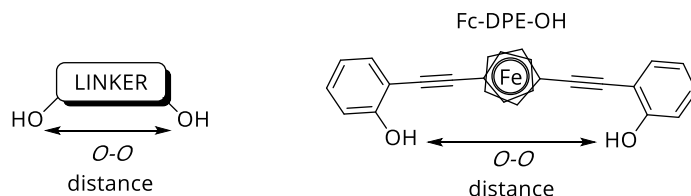
TABLE 4 DFT calculated *O-O* distances of geometry optimized bridges, stacked and elongated macrocycles.

entry	linker	calc. *O-O* distance in Å	macrocycle	calc. *O-O* distance in Å
1			Fc-DPE-OH	11.212
2	ether bridge	11.770	Fc-DPE-ether	11.035
3			stacked Fc-DPE-ether	4.175

4	*Z*-butene bridge	15.407	Fc-DPE-*Z*-butene	10.971
5			stacked Fc-DPE-*Z*-butene	4.795
6	*E*-butene bridge	15.163	Fc-DPE-*E*-butene	11.141
7			stacked Fc-DPE-*E*-butene	5.900
8	*Z*-allyl-ether bridge	6.013	stacked Fc-DPE-*Z*-allyl-ether	4.624
9			**34*Z***	3.551[a]
10	*E*-allyl-ether bridge	16.509	Fc-DPE-*E*-allyl-ether	10.971
11			stacked Fc-DPE-*E*-allyl-ether	5.612

[a]*O-O* distance obtained from crystal structure.

OUTLOOK AND CONCLUSION

We showed the syntheses of three macrocyclic model compounds **24**, **32E/Z**, **34E/Z** comprising 1,1'-diphenylene-ethynylene ferrocene subunits (**FIGURE 17**). Their syntheses are all based on ring closing reactions forming the second parallel bridge and all three have as common precursor the parent 1,1'-diphenylene-ethylene ferrocene structure **14** that comprises an oxybenzyl-4-benzaldehyde substituent in *ortho*-position of the phenylene ring on both sides. Due to the intramolecular nature of the ring closing reaction, these macrocycles were isolated in acceptable yields ranging from 57 to 70%.
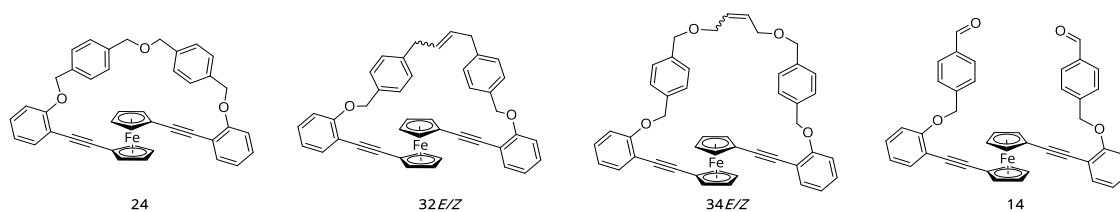
FIGURE 17 Macrocyclic model compounds and their precursor **14**.

While the integration of the 1,1'-diphenylene-ethynylene ferrocene subunits in a macrocycle restricts the rotation of the ferrocene axis, the intended "total" fixation in the stretched arrangement could not be realized with the macrocycles described in this chapter. In contrary, the solid-state structure analysis of **34Z** revealed a stacked arrangement of the two OPE subunits, pointing at unhindered rotation about the Fc-axis. These macrocyclic structures display a dynamic behavior in solution with a large variety of angles between the Fc-interlinked OPE subunits. However, DFT models suggest that the ether bridged ferrocene **24** favors the elongated orientation in the gas phase and hence is considered as most promising bridging strategy towards an elongated interlinked molecular wire (IMW) which is discussed in the next chapter.

CHAPTER 2

INTERLINKED MOLECULAR WIRES
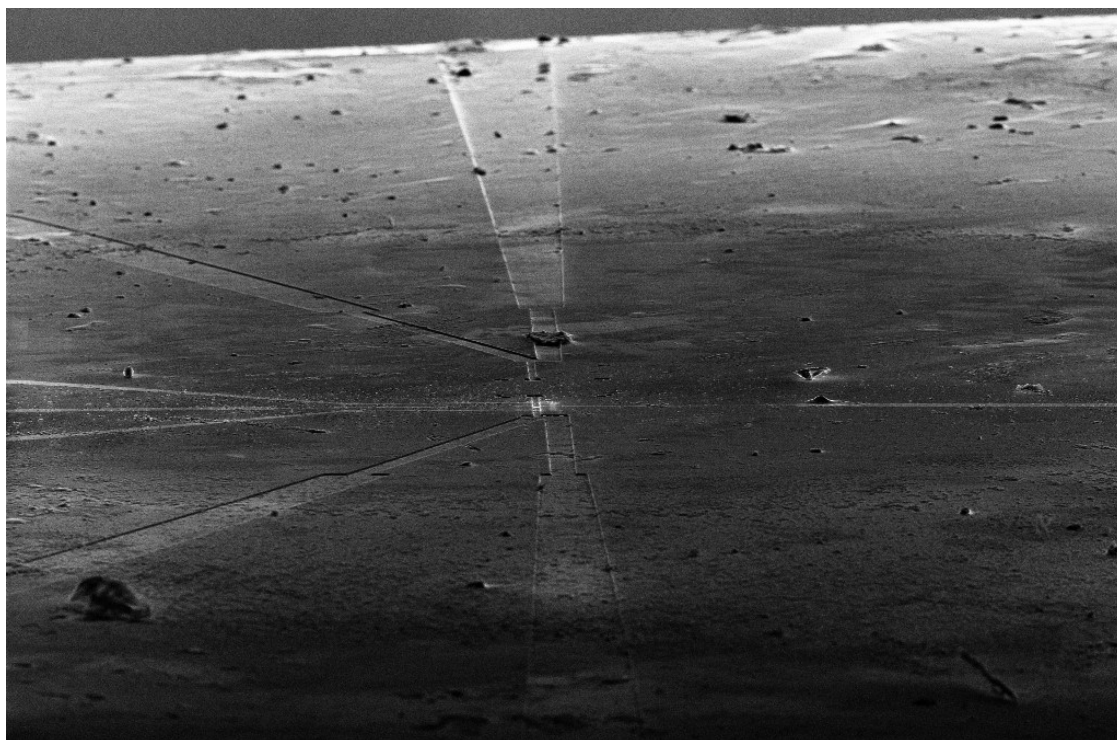
INTRODUCTION

MOLECULAR SIZED ELECTRONICS

In 1904, John Ambrose Fleming invented the vacuum tube that became the basic component of any electronic device of that time. The fundamental working principle of a vacuum tube is that the current flow between two electrodes can be controlled by an applied voltage. This function has facilitated many purposes, including rectification, switching and amplification and culminated in the invention of new technologies and their practical and widespread application in radars, radios, sound reinforcement systems and television. These technologies quickly became essential not only to military but also in domestic use. With the invention of solid-state semiconductors in the late 1940s the cornerstone of an industrial revolution was laid and it became possible to produce components such as transistors that facilitate the production of much smaller, more efficient and more reliable devices that eventually led to an almost complete replacement of vacuum tubes. Transistors had a huge impact on the technological development of integrated circuits (ICs) and the contineous reduction in transistor size and cost is responsible for its use in virtually any electronic device (**FIGURE 18**). The increasing number of transistors that can be placed on a postal-stamp sized silicon plate spurred the functional density of ICs and are the reason for the incredible computing power of today's computers and mobile phones. It was Richard Feynman realizing at the beginning of the semiconductor technology that the miniaturization of electronic devices will ultimately lead to a change in manufacturing paradigm towards atomic scales.[80] However, it took another 12 years until Kuhn and Bernhard reported that monolayers of cadmium salts of fatty acids showed tunneling current with exponential decrease of conductivity, which was predicted by the tunneling theory.[81]
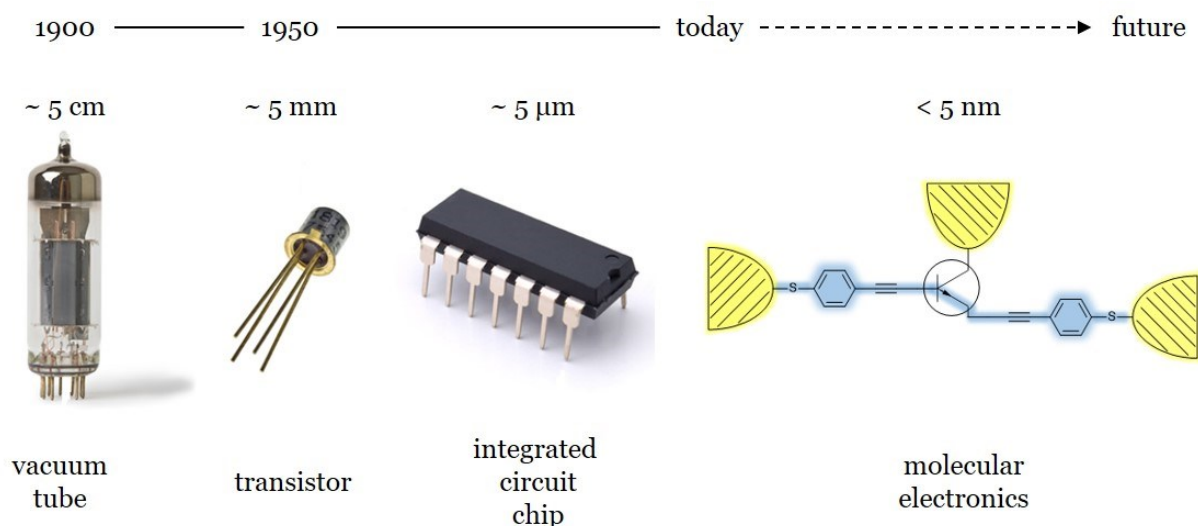
FIGURE 18 Size reduction of electronic components which might culminate in circuits made of molecular components in the future.

In 1974, Aviram and Ratner postulated a theoretical approach towards the mechanism of electron transport through a single molecule and implemented the idea of a molecular rectifier that consists of a Donor-π and an Acceptor-π (D-A) system, separated by a σ-bonded methylene bridge that represents a tunneling barrier.[82] After the first experimental and theoretical achievements that state the beginning of this age, it was the development of the scanning tunneling microscope (STM), in 1986, and later that of the atomic force microscope (AFM) that spurred the progress in molecular electronics.[83,84] Significant advances in techniques provided insight in the understanding on transport mechanisms in single molecules that ignited the international interest in molecular electronics.[85]

Molecular electronics deal with the fundamental question of how electrons move through a single molecule. The experimental and theoretical challenge to address the question is exceptional. The problem is on one hand to connect a single molecule in an appropriate experiment and on the other hand, to establish a valid theoretical description of the transport mechanism. Beside these challenges there are substantial benefits from dealing with single molecules. First of all, molecules are smaller (few nm) by an order of magnitude than the currently existing microelectronic devices. Secondly, they can be chemically synthesized with atomically precession and designed to the desired function. These advantages validate the tremendous efforts that have been put in the investigation of molecular electronics and perhaps pave the way for further miniaturization of electronics.

MOLECULAR JUNCTIONS

In bulk material, the conductance G obeys the classical Ohm's law ($G = I/V$) that is defined as the ratio between the current I passing through the conductor and the applied voltage V. Atomic-sized conductors with a contact width of a few nanometers only, enter the quantum limit. In this regime, the *Landauer* Formula $G_0 = \frac{2e^2}{h}$ where e is the electron charge and h is Planck's constant, describes the quantum conductance G_o, where the current flow is considered as transmission process with a certain probability of the charge carriers to reach the other end of the conductor.[86,87] For one dimensional systems, where only one conduction channel exists, the conductance is quantized. The number of conductance channels is determined by the valence orbital of the conducting material. The preferred materials for metallic electrodes are gold and platinum, because of their robustness against oxidation and degradation. Gold as a s-metal, only has one conducting channel that gives a quantum conductance of G_o= 77.5 μS for a single gold atom contact.[88] The quantization of conductance was experimentally confirmed by Ohnishi et al. using a STM gold tip in ultrahigh vacuum. By pulling the STM tip off the gold surface (**FIGURE 19** a) the group could demonstrate that the conductance of a single strand thick gold contact is G_o, and that of a double strand showed twice the conductance (**FIGURE 19** b). Further displacement of the tip caused breaking the contact and drops the conductance.[89] Hence, conduction histograms scale conductivity as logarithmic fractions of G/G_o and molecular conduction is always a referred as integers of G_o.
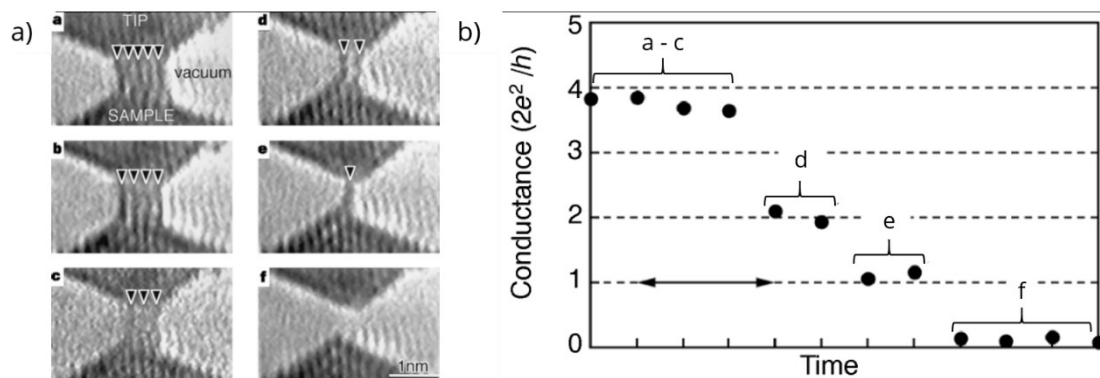
FIGURE 19 a) TEM image of a Au-STM break junction being withdrawn until it breaks b) Conductance change is quantized and depending on the channel number. Reprinted with permission from ref.[89] the Nature publishing group.

The generally accepted process for the formation of a molecular junction is depicted in **FIGURE 20** a)[90]. If a gold constriction breaks by slow displacement of the electrodes, atomically sharp tips are formed (stage a – c, **FIGURE 20** a) and these tips can be used as electrical contacts in a break junction. At the same time, the conductance drops exponentially (conductance from b – d, **FIGURE 20** b) until adequately designed molecules with terminal anchor groups slip into the junction, forming a covalent electrode-molecule-electrode contact (stage d – f, **FIGURE 20** a). A current flow through the molecular junction can be recorded as a molecular conductance plateau of a certain length, depending on the assembly and the length of the molecule (conductance d – f, **FIGURE 20** b).
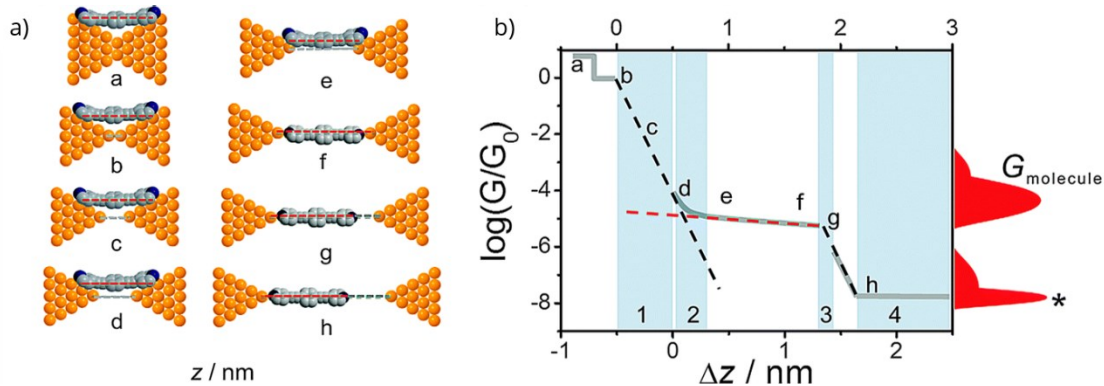
FIGURE 20 a) The formation of a molecular junction. b) simplified schematic representation of a conductance trace (gray line), molecular conductance contribution (red dashed line) and conductance contribution from tunneling. The 1D conductance histogram is displayed in red, on the right vertical axis. Reprinted with permission from ref. [91] the Royal Society of Chemistry.

Further displacement of the contacts cause a breaking of the molecule-electrode contact at one end (stage g, **FIGURE 20** a) generating a sharp decrease in conductance (conductance g, **FIGURE 20** b). Finally, a tunneling channel of the molecule-electrode assembly can be formed that shows tunneling conductance until the detection limit is reached (stage and conductance h, **FIGURE 20** a and b).

The shape of these conductance traces can vary dramatically due to variations in the structure and geometry of the junctions and the mechanical instability of the assembly.[92] Therefore, it is inevitable to generate a large data set and to treat the experimental data collection of thousands individual conductance traces with statistical analysis and to extract the conductance characteristics thereof. For this purpose, STM-BJ and mechanically controlled break junction (MCBJ) techniques are preferred, as they rapidly provide a high number of conductance traces. The logarithmic-scale histograms of the data collection allow to easily distinguish between the different conductance features such as high or low conductance regions (**FIGURE 21** b). 2D conductance-distance histograms (**FIGURE 21** c) help to understand the molecular junction related characteristics and give information about the junction evolution during the displacement. The plateau length distribution histograms (**FIGURE 21** d) provide information about the molecular junction formation probability and the molecular length.[91]
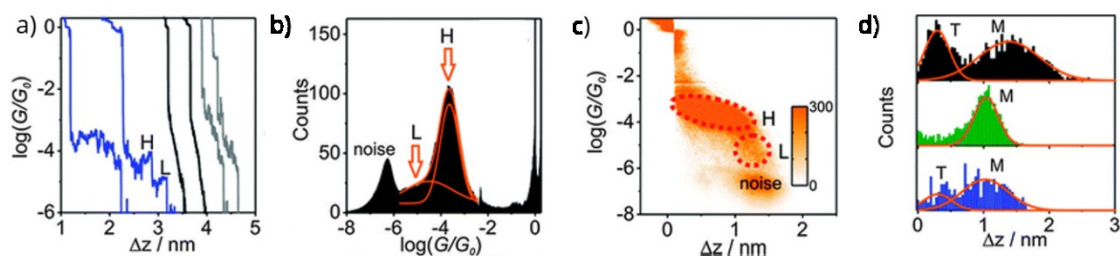
FIGURE 21 a) individual conductance trace as a function of displacement with molecular plateaus b) 1D conductance histograms c) 2D conductance histograms d) characteristic length distributions for the formed molecular junctions with different stretching rates. Reprinted with permission from ref.[93] Copyright © 2012 American Chemical Society.

ELECTRODE-MOLECULE CONTACT

The anchoring groups are responsible for the efficient contact formation between electrode and molecular wire. The nature of the anchoring group needs to be considered regarding its affinity to the electrode material, its electronic coupling ability and its thermal stability. Along with the different break junction techniques and apparatuses, different electrode materials such as gold, silver, platinum, palladium and carbon have been employed.[94–96] It was demonstrated that combinations of electrode material and anchor groups display great variations in their bond strength and electronic coupling ability.[95] Hence, the electrode-anchor pair is of great importance to the experiment robustness and the conductivity performance. For charge transport experiments, the thiol/Au couple is the most widely used due to their good electronic coupling and strong binding. Electron transport depends decisively on the coupling strength Γ, and on the energy barrier E_{mol}, given by the energy difference between the molecular orbital (HOMO/LUMO) and the electrode Fermi level E_F (**FIGURE 22**). When an electrode-molecule contact is formed, the discrete molecular orbitals and the electronic states of the electrode can overlap, which leads to a broadening and a shift of the molecular energy levels. Large orbital overlap indicates strong coupling and large Γ values. The hybridization of the electronic states leads to a

delocalization of the electronic wave function over the whole junction. A poor coupling of electrode and molecule leads to incoherent transport and effects like Coulomb blockade and the Kondo effect.
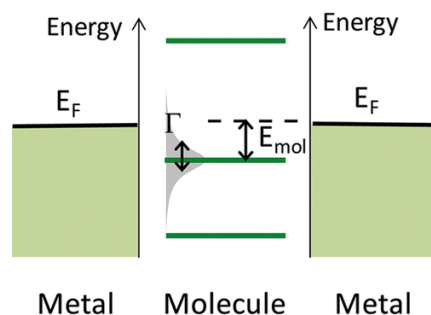
FIGURE 22 Coupling of the molecular orbitals with the electrodes, causes a broadening of the electronic energy levels with respect to the Fermi energy E_F of the electrodes. Reprinted with permission from ref. [97] Copyright © 2014 American Chemical Society.

Therefore, the anchoring group affects the energy-level alignment of the molecule relative to the metal Fermi energy, and consequently the conductance. In addition, the binding geometry of a given anchoring group decisively impacts the degree of coupling strength, which can cause considerable fluctuations in a conductance measurement. Beside thiol as the most commonly used anchor group, other functionalities (**FIGURE 23**) have shown good affinity to gold contacts.[98–112] The challenge is to find the appropriate anchoring group that woulde facilitate a strong and uniform binding geometry, while having a good chemical accessibility and stability.
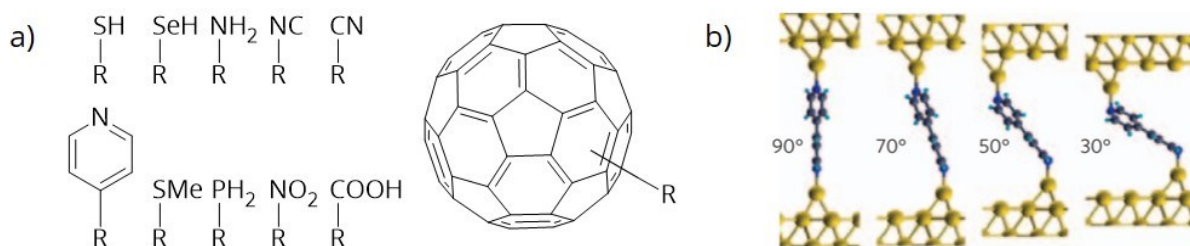
FIGURE 23 a) Typically used anchoring groups for single-molecule electronics. b) Various junction geometries of bipyridine. Reprinted with permission from ref.[113] Copyright © 2009 Nature Publishing Group.

STRUCTURE-PROPERTY RELATIONSHIP IN MOLECULAR ELECTRONICS

Iteratively performed conductance experiments provide an ideal testbed for describing the electronic properties of a molecule. However, the intrinsic conduction capabilities of a molecule rely on the electrode-molecule coupling and the molecular structure. Both parameters can be influenced independently by the choice of the anchor group and by the design of the molecular back-

bone. In addition, functional entities such as redox active units that can be triggered externally, have a tremendous influence on the charge transport characteristics of the whole molecule.

Understanding of how the structure determines the molecular conductance is of great interest for experimentalist and theorists. Conductivity experiments can be run systematically in order to obtain results that obey or test the underlying transport theory.

For instance, the length dependence of the electron transfer has been observed experimentally and was theoretically treated by two distinct charge transport models: coherent transport by non-resonant tunneling[114] and incoherent hopping. In the tunneling approach, the molecule acts as tunneling barrier for electrons where a length depending exponential decay of the wave function is predicted by the theory. Hence, the charge transport depends mainly on the height and width of the energy barrier and on the electrode coupling.[115] The molecular conductance G is then described as $G = Ae^{-\beta L}$, where L is the length of the molecule, β is the tunneling constant and the factor A depends on the electrode-molecule coupling. In literature, different β values are found for various molecular wires. For instance, non-conjugated alkanes have a rather high tunneling constant ($\beta = 6 - 10$ nm^{-1}),[116] while highly conjugated systems like oligothiophenes have low tunneling constants ($\beta = 0.01$ nm^{-1}). Chen et al. could demonstrated that by increasing chain length of alkene dithiols and oligopeptide dithiols the conductance decays exponentially (**FIGURE 24**).[117] Interestingly, when a certain chain length was exceeded, the conductance had a linear dependence.
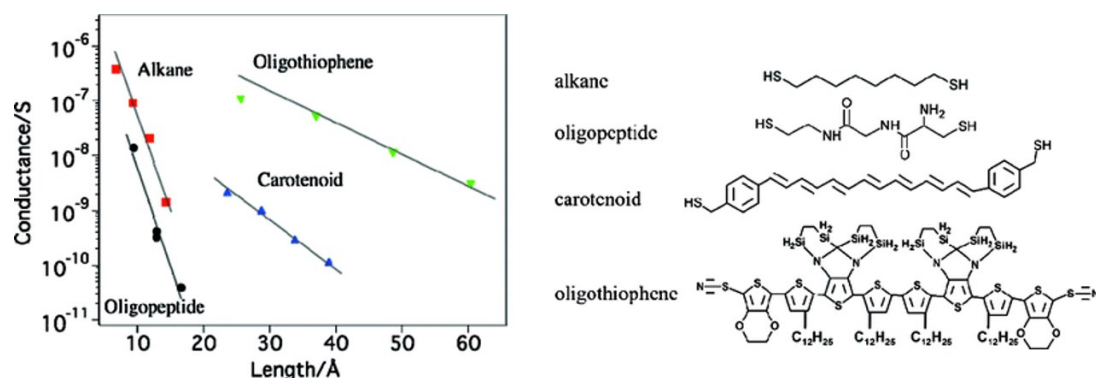
FIGURE 24 Length dependence of conductance for saturated chains and conjugated molecules. Change from tunneling to hopping transport mechanism for conjugated molecules with a length of ~ 3 nm. Reprinted with permission from ref. [117] Copyright © 2009 American Chemical Society.

The reason for this is the transition from tunneling to incoherent thermally activated hopping transport.[115] In recent studies, the transition for the dominating transport mechanism was found at a molecular length of $3 - 7$ nm depending on the conjugation and anchoring groups of the molecules.[118]

Molecular conductance is considerably affected by the length of the wire but also strongly relies on the orbital overlap of the molecule. Different approaches have been devised to provide useful

theoretical models to understand the transfer rates. A more sophisticated one, is the quantum interference (QI) concept that is based on the intramolecular interference of electron pathways and their contribution to the current flow.[119] The QI effect is dominated by the molecular conformation, charge distribution and energies of the frontier orbitals.[120] Accordingly, the higher conductance of *para*-phenyl-bis(ethynyl-thiol) over the *meta*- substituted analog[119] is due to constructive phase shifts of transmission channels. Empirical studies on conductance dependence based on π-conjugation patterns[121], HOMO-LUMO spacing[93] and the torsion angle[122], helped to evaluate rules of thumb for the structure-property relationship. However, these criteria are a function of the degree of orbital overlap that is dominated by the QI effect.[120]

Kaliginedi et al. summarized the influence of the molecular structure on the charge transport characteristics in a series of dithiol terminated OPEs with varying central units (**FIGURE 25**).[93] The OPE wires were tested in a STM-BJ and a MCBJ respectively, according to length, interference, conjugation and HOMO-LUMO spacing. In general, an increase in the HOMO-LUMO gap as well as an increase in length of the molecular wire leads to a conductance decrease. In particular, destructive quantum interference phenomenon leads to lowered conductance values as shown for the cross-conjugated anthraquinone molecule when compared with linear π-conjugated (anthracene) or broken π-conjugated (dihydroanthracene) molecules.
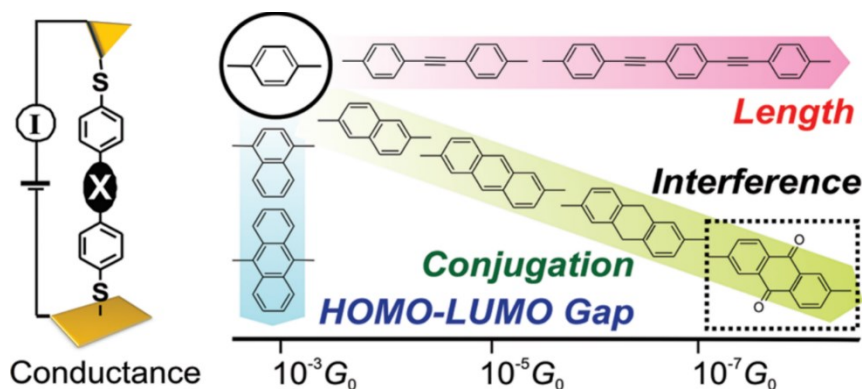
FIGURE 25 Conductance as a function of the molecular structure. Reprinted with permission from ref. [93] Copyright © 2012 American Chemical Society.

JUNCTION GATING

Molecular junction experiments, weather produced by a driving tip, mechanical bending, electromigration or self-assembly, allow to investigate the conductance characteristics of molecules as a function of the applied bias, in order to gain current-voltage diagrams. Changing the source-drain potential V_{sd} is effectively manipulating the Fermi level gap of the electrodes with respect to the molecular orbital energy. Break junction setups can be equipped with an additional electrode pair that allows to shift the energy levels of the molecule with respect to the Fermi level, by an externally applied gating voltage V_g. The gating electrodes, consisting of a reference electrode (RE) and a counter electrode (CE), can affect the molecule via an applied

electrochemical or electrostatic potential and lift or lower the HOMO/LUMO energy of the molecule. In this scenario, the source and drain electrode act as the working electrodes (WE) and the setup is called a "three-terminal junction". In order to achieve a sufficient gating field, the gating electrode has to be placed in close proximity to the molecule, when a solid-state device is used (**FIGURE 26** a). In liquid cells, the gating electrode can be immersed in an electrolyte containing solution and the molecular junction is triggered electrochemically (**FIGURE 26** b). Yet, both techniques aim to modulate the molecular energy level in order to facilitate a switch in the conductance profile. Switching between high and low conducting states is a key function for the construction of molecular switches and field effective transistors (FETs).
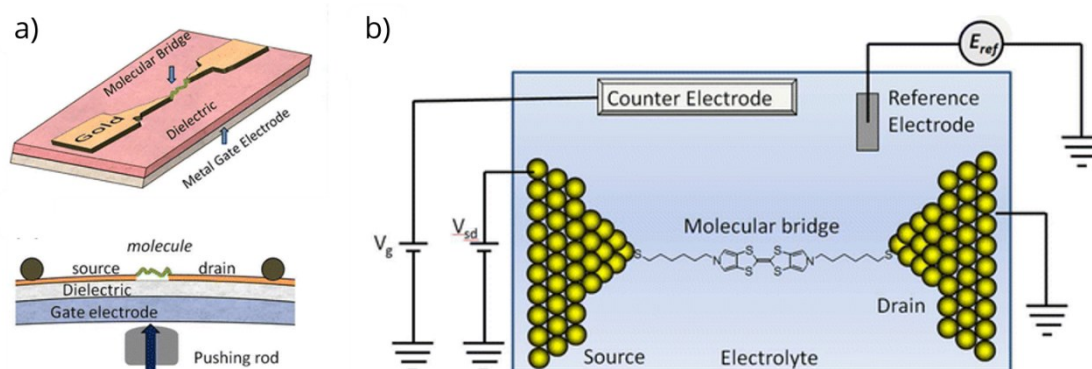
FIGURE 26 a) Solid-state gating in a MCBJ setup. b) Electrochemical gating of pTTF by a third electrode in a liquid cell. Reprinted with permission from ref.[123] Copyright © 2012 American Chemical Society.

In recent studies, the switching behavior of different classes of redox-active molecules has been investigated. Thereby, a high ratio between conductance in ON and OFF state is desirable. In 2012, Kay et al. demonstrated the consecutive "OFF" - "ON" - "OFF" - "ON" - "OFF" conductance switch with a ratio of ~ 4, for pyrrolo-tetrathiafulvalene (pTTF) dihexanethiol by sweeping the gate potential to the positive and oxidizing the pTTF unit (**FIGURE 26** b)[123]. Molecular conductance as a function of the gate voltage V_g was observed at the oxidation potentials of pTTF and attributed to outer-sphere reorganization of charge transfer. Darwish et al. describes the conductance switch based on destructive quantum interference when the linear π-conjugated dihydroanthraquinone (ON state) is oxidized to the cross-conjugated anthraquinone (OFF state).[124] An EC-STM setup was used as testbed for the electrochemically controlled QI switch of based on AQ-norbornylogous tetrathiol wires.

In 2006, Xiao et al. exploited cysteamine-terminated 1,1'-disubstituted ferrocene wires to perform conductance switching in an EC-STM break junction. The authors conducted the measurements by fixing the source-drain bias V_{sd} to 0.1 V, while sweeping the gate electrode to positive potential. They could observe an 8-10 fold increase in conductance associated with the oxidation of the ferrocene moiety (**FIGURE 27**). One possible explanation is that the charge is

transferred by a coherent process, in which an electron tunnels through the junction so fast that the oxidized ferrocene has no time to relax to the reduced state.^
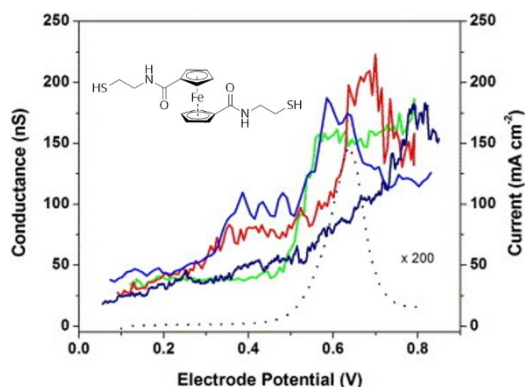
FIGURE 27 Current through a cysteamine-terminated ferrocene vs. substrate potential in 0.1 HClO$_4$. Reprinted with permission from ref. [48] Copyright © 2006 Elsevier.

A related approach was proposed by the group of Sita in 2005.[51] The authors proposed high conductance values for the ferrocene comprising OPE **35** that was integrated in a solid-state gold junction crafted by electromigration (**SCHEME 20** a). The gating field was applied via an electrode under the dielectric substrate at cryogenic temperatures with T = 1.3 K. The group recorded significant fractions of the quantum conductance (up to 70%) by no applied gating voltage. The authors admitted that the precise configuration of the molecular wire is unknown, however, the rotation about the five-fold ferrocene axis allows a double-stranded coplanar orientation of the wire arms (**SCHEME 20** b, **35'**) that could facilitate the high conductance value. In fact, 1,1',3,3'-tetrasubstituded ferrocenes experience low energy rotation barriers in solution[125] and due to close packing a stacked conformation is adopted in solid state for several Fc-OPEs.[126–128]
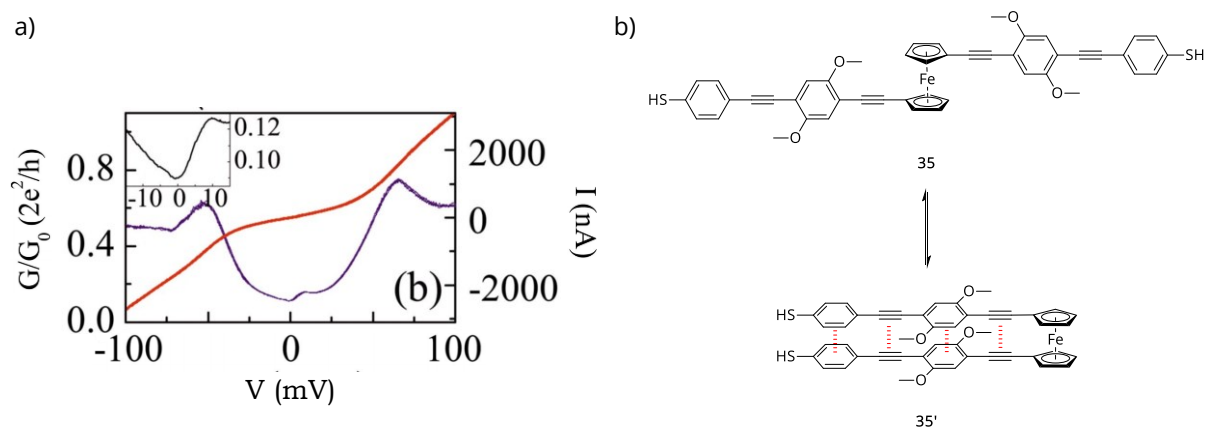
SCHEME 20 a) High conductance value for **35** in an electromigration junction. Reprinted with permission from ref. [51] Copyright © 2005, American Physical Society.

In addition, the conductance performance of a double-stranded conformer **35'** could profit from intermolecular π - π interaction that a fully conjugated aromatic backbone might facilitate. Such behavior was observed for OPE-monothiol molecules in MCBJ experiments as reported by Wu et al. (depicted in **FIGURE 28**).[129] In this regard, Fc-OPEs could act as a monothiol functionalized molecular wire whereat both anchoring groups are contacting opposing electrodes, giving higher conduction values.
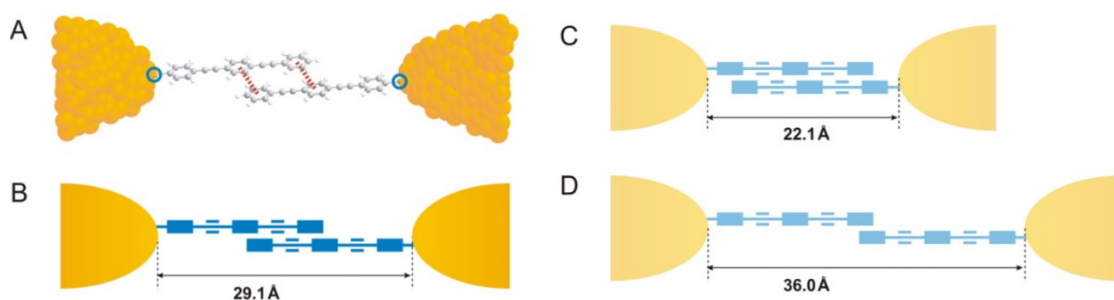
FIGURE 28 Different π – π stacking configurations of a pair of OPE–monothiol molecules that show current flow through aromatic interaction. Reprinted with permission from the Nature publishing group.[129]

Finally, Fc itself can act as an electrode anchoring group, especially when in terminal position. Karmakar et al. observed single-electron tunneling behavior for nanoparticle hybrids with terminal Fc groups, whereat the authors assign the electrode contacting and electron transport through the ferrocene units.[130]

In contrast, a Fc-OPE with limited rotational freedom would meet the requirement of a rigid molecular wire, capable of contacting opposing electrodes.

AIM OF THIS WORK

Ferrocene grafted OPEs have shown a dramatic impact to enhance the molecular conductance.[131] Moreover, these classes of molecules are dealt as field effect transistors, due to the addressable ferrocene redox center.[132] However, the current approaches suffer from flexible molecular backbones that are likely to form double-strand conformers that could discredit the conductance experiment. In the preceding chapter, we developed a strategy to bridge the OPE scaffold with a suitable linker (right panel, **SCHEME 21**). In this regard, we planned to integrate the bridging moiety and build an interlinked molecular wire (IMW) that is equipped with phenylethynyl thiol anchor groups (blue) and solubilizing methoxy features (red). In a second stage, the interlinked molecular wire would be subjected to a molecular junction experiment in order to assess its conductance. In the final part of the project, the interlinked molecular wire should be tested in a three-terminal EC-STM break junction, so that the conductance as function of the applied gating voltage can be plotted. The ideal result would show molecular conductance which can be switched with a high conductance ratio by the gating voltage. The electronic function of such a molecule would mimic transistor-linke behavior.

Interlinked Model Compound

Interlinked Molecular Wire
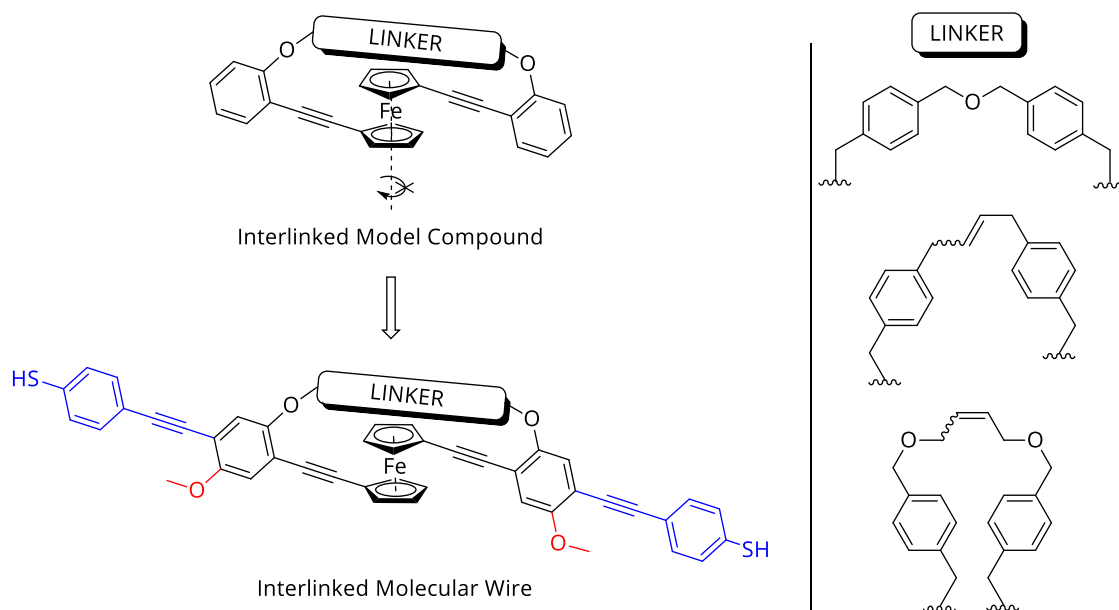
LINKER

SCHEME 21 Within the previous chapter developed linker moieties, a molecular wire design can be adapted.

STRATEGY

The linker is considered as the structure determining part of the wire, which should be decoupled of the conjugated wire backbone, as potential bypass events might take place in a fully conjugated bridge. We envisaged to adapt the ether bridge strategy, as DFT models of the structure showed preference for the elongated conformation. In the preceding chapter, we could demonstrate the reliable formation of the macrocycle and wish to adapt its synthesis. The retrosynthetic analysis of the benzylether bridged molecular wire **36** suggests a consecutive 12 step synthesis and is displayed in **SCHEME 22**.
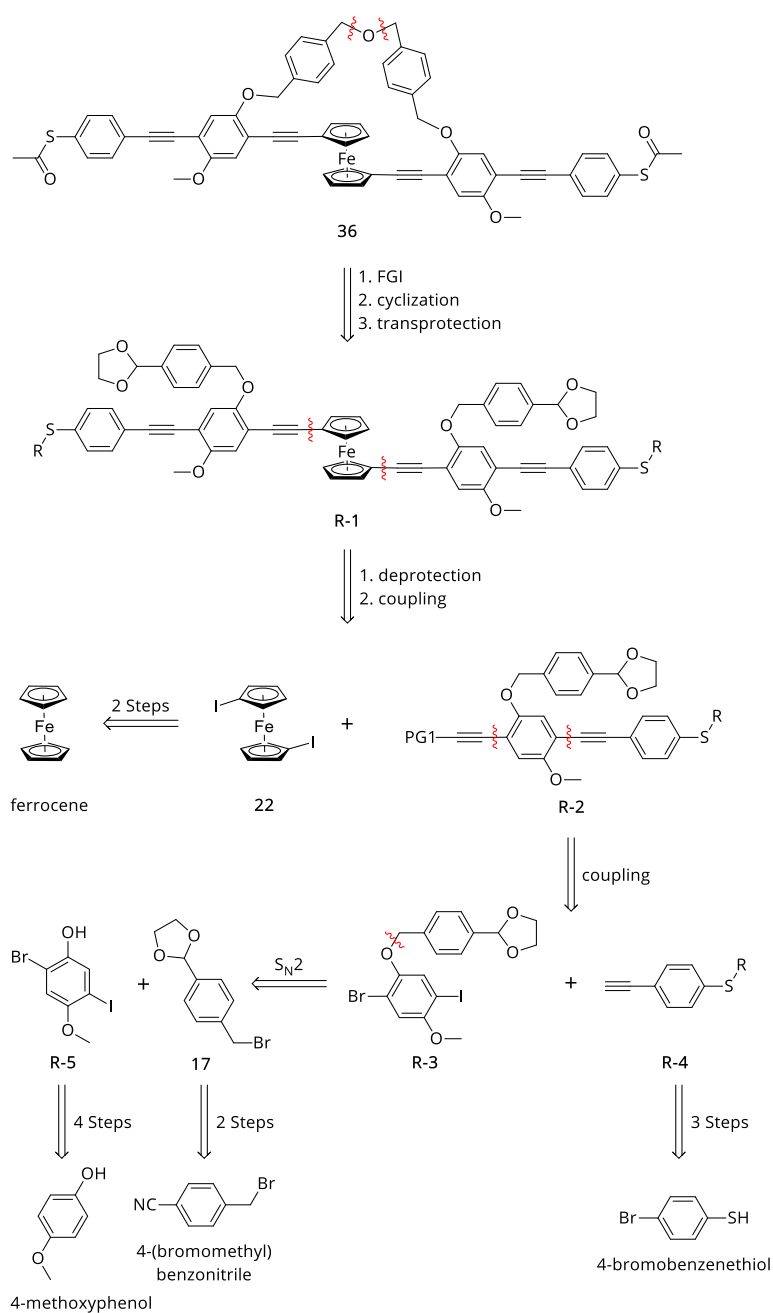
SCHEME 22 Retrosynthetic analysis of the proposed structure.

The first disconnection can be made at the macrocycle forming ether bridge, from a bis-alcohol functionality. Although the ether bridge formation has been successfully examined in the model compound, the cyclization is considered as the most challenging reaction step in the synthesis. The bis-alcohol, is interconverted from the respective 1,3-dioxolane masked aldehyde **R-1**. Thio-acetate groups are base labile thiol protecting groups that are introduced, to be cleaved readily in the contact experiments. For the synthesis, a robust sulfur protecting group is needed that is replaced with thioacetate prior to the contact experiment. Twofold *Sonogasihra* cross coupling from 1,1'-diiodoferrocene **22** and the corresponding acetylene **R-2** will give the transannularly disubstituted ferrocene **R-1**. 1,1'-diiodoferrocene is synthesized within two reaction steps from ferrocene and the main building block **R-2**, can be assembled from the respective 2-bromo-5-iodo benzene **R-3**, a thiol protected phenylacetylene **R-4** and an orthogonally protected low-molecular weight acetylene. The anchoring group bearing phenylacetylene **R-4** is available in 3 reaction steps form *para*-bromo-thiophenol. 2-bromo-5-iodo benzene **R-3** can be assembled from the previously introduced 1,3-dioxolane **17** and the phenol **R-5** in a bimolecular substitution reaction. The synthesis of **R-5** from 4-methoxyphenol was demonstrated by Sigurd Höger and is accomplished within 4 steps.

RESULTS AND DISCUSSION

SYNTHESIS

SYNTHESIS OF THE ACETYLENE BUILDING BLOCK

In order to functionalize the benzene building block asymmetrically, it was necessary to introduce the acetylenes sequentially. Therefore, the order of reactivity towards Pd(0) catalyzed reactions, had to be introduced within halide functions of the building block. The group of Höger[133] demonstrated an efficient procedure to exploit *ortho*-selectivity for the introduction of halides in their synthesis of **40**, within 4 reaction steps, starting from symmetric 4-methoxyphenol. Likewise, we started our efforts with the tosylation of the phenol function, using *p*-toluenesulfonyl chloride and pyridine in THF at room temperature (**SCHEME 23**). The tosylated (Ts) anisole **37** directs the aromatic electrophilic iodination through its electron-withdrawing Ts-group and electron-donating methoxy substituent into the *ortho*-position of the methoxy group. After aqueous workup and recrystallization from methanol, **38** was isolated as a white solid in 83% yield. Then, the tosyl-group was cleaved by using sodium hydroxide in refluxing *t*-butyl alcohol for 12 h. After aqueous acidic workup and recrystallization from chloroform, phenol **39** was isolated as colorless needles in 70%. Bromination was accomplished via dropwise addition of bromine to a cooled solution of **39** in DCM. The crude product could be purified by FCC and **40** was isolated as a white solid in 96% yield.
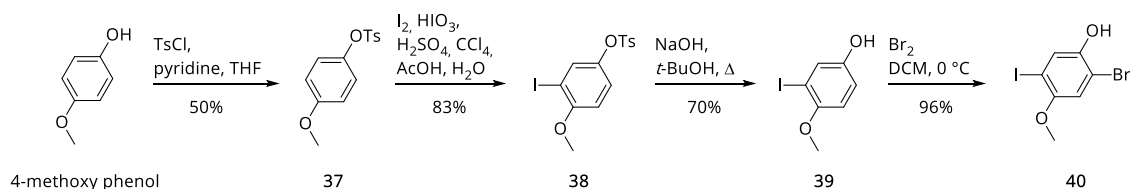
SCHEME 23 Synthesis of 2-bromo-5-iodo-4-methoxyphenol **40** in 4 steps.

As outlined in the strategy, it was planned to introduce the bridging unit via the masked aldehyde. The synthesis of 2-(4(bromomethyl)-phenyl)1,3-dioxolane **17** is described in the previous chapter. Hence, benzylation with **17** was performed with dried potassium carbonate in DMF at 80 °C and gave the benzyl decorated building block **41** in excellent 99% yield (**SCHEME 24**).
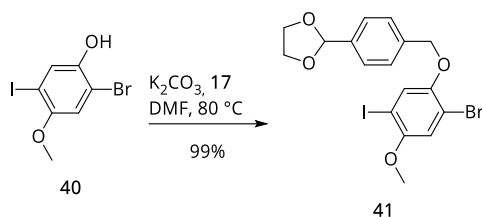
SCHEME 24 Benzylation of phenol building block **40**.

The introduction of S-acetyl aryl-halides via Pd catalyzed *Sonogashira* coupling at a late stage, showed to be inefficient (~30%). Hence, we decided to introduce the anchor group containing phenylethynyl building block via *Sonogashira* reaction, before the bridge is closed.

The choice of the masking group is crucial, as the protecting group has to be orthogonal to the later used HOP or TMS protecting groups, while being cleaved readily in the last step. Alkyl-thioethers bind too strongly, while the S-acetyl group bind too weakly. In addition, trimeric structures (**42**) are formed from 4-ethynylphenyl-thioacetate via cyclo-oligomerization and isomeric conjugates (**43**) of the mono-functionalized analogues are formed when *Sonogashira* conditions are applied as reported by Inkpen et al. [73] (shown in **SCHEME 25**).
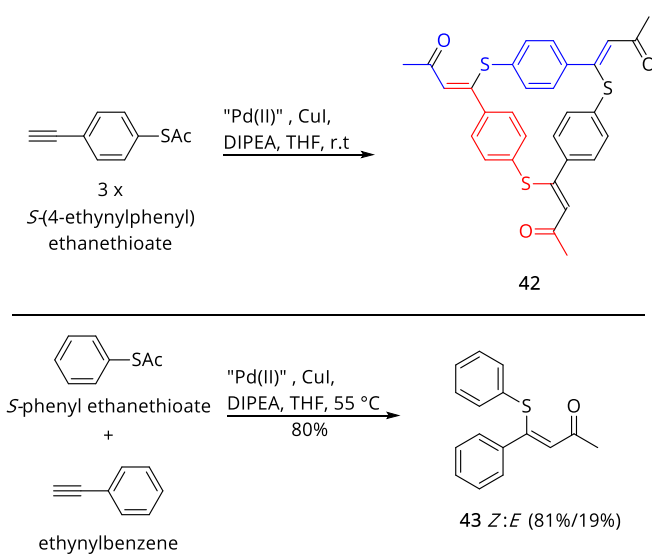
SCHEME 25 Top) trimeric structure is formed via cyclo-oligomerization of 4-ethynylphenyl-thioacetate under *Sonogashira* conditions. Bottom) mono-functionalized analogues forming a mixture of *Z* and *E* isomers.[73]

Ideally, the best protecting group should be stable under a variety of many experimental conditions as well as being easily removed under mild conditions. Creager et al.[134] used 2-(trimethylsilyl)ethyl for masking ferrocene aryl thiols, prepared via *Sonogashira* coupling and was able to remove these by treatment with tetrabutylammonium fluoride at room temperature.

Following the protocol of Yu et al.,[135] the protecting group was introduced by the reaction of neat trimethylvinyl silane and 4-bromothiophenol in the presence of a catalytic amount of *tert*-butyl peroxide as free radical initiator to afford the *β*-addition product **44** (**SCHEME 26**). Then, TMS-acetylene was introduced via *Sonogashira* coupling, using $Pd(PPh_3)_2Cl_2$ and copper iodide in a mixture of THF/Et_3N, 3:1 that was heated to 80 °C for 5 h and gave compound **45** after silica column chromatography in 97% yield. While the TMS-acetylene deprotection afforded the acetylene **46** in excellent yield, the HOP-protected analog revealed substantial loss of compound during removal.
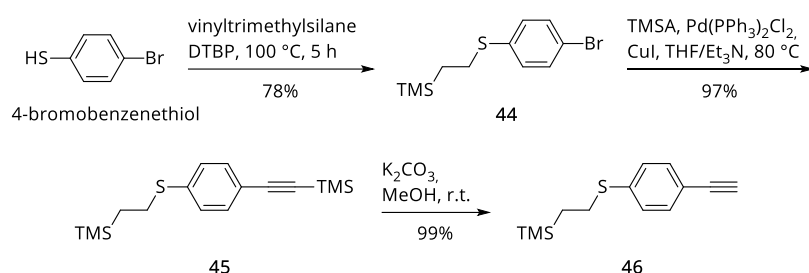
SCHEME 26 Synthesis of the anchoring group bearing phenylethynyl building block **44**.

With the building blocks **41** and **46** in hand, we had the tools to build up the asymmetric arms of the molecular wire. As displayed in **SCHEME 27**, first the anchoring unit was introduced in a chemoselective *Sonogashira* reaction, using 1.05 eq. of acetylene **46** at room temperature. After the acetylene **46** was consumed, a 3-fold excess of TMS-acetylene was added to the reaction and the mixture was heated to 60 °C over night. The TMS-terminated acetylene **47** was isolated in a good yield of 72% after column chromatography on silica gel.
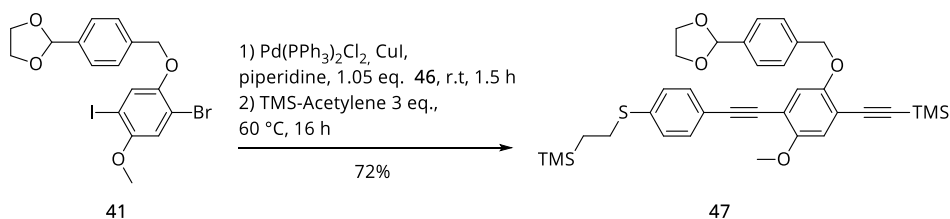
SCHEME 27 Twofold *Sonogashira* reaction of bromo-iodo arene **41** with **46** and TMS-acetylene.

TMS removal was accomplished smoothly, for that, **47** was dissolved in a small volume of CH_2Cl_2 and added to a degassed suspension of K_2CO_3 in MeOH (**SCHEME 28**). After aqueous workup, the free acetylene **48** was isolated in 79% as colorless solid. It is worth mentioning that it was necessary that all glassware was washed with concentrated sulfuric acid and aq. 1 M NaOH solution prior of use. Apparently, trace metal contamination might have facilitated intermolecular oxidative homocoupling of the terminal acetylenes. This became particularly substantial in a

series of deprotection attempts of compound **49** (compare **TABLE 5**). In those cases, where the reactions were performed without precautionary washings, homocoupling adducts were observed. In one case, the isolated terminal acetylene was placed in an untreated flask and stored at 4 °C for two days, when GC-MS analysis showed that the homocoupling adduct was formed during the storage.
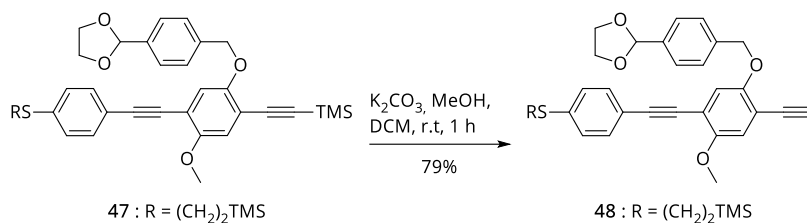
SCHEME 28 Deprotection of TMS-acetylene using K_2CO_3 in MeOH.
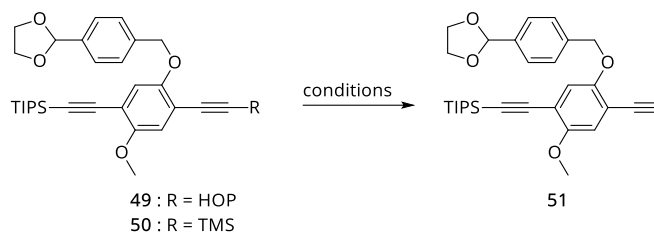
TABLE 5 Deprotection of **49** and **50** using respective protocols.[a]

R	eq. base	solvent	duration	temp.	**51**	side product
TMS	2 eq. K_2CO_3	MeOH/DCM	2 h	r.t	29%	homocoupling
TMS	2 eq. K_2CO_3	MeOH/DCM	12 h	r.t	47%	36% homocoupling
HOP	0.8 eq. NaH	PhMe	12 h	110 °C	42%	decomposition
HOP	1 eq. NaH	PhMe	12 h	50 -80 °C	11%	starting material
HOP	2 eq. NaH	PhMe	1 h	140 °C[a]	-	homocoupling

[a]reaction conducted in the microwave reactor.

SYNTHESIS OF INTERLINKED MOLECULAR WIRES

After we were able to synthesize the terminal acetylene in reasonable quantities, we focused on the wire assembly. As discussed in the former chapter, the twofold *Sonogashira* coupling reaction is a crucial step in the synthesis of the wire (**SCHEME 13**). We could benefit from the established procedure evaluated for the reaction of the model compound **23**. For that, usually a pretreated reaction vessel was used, carefully dried in vacuum and then charged with 10 mol-% of freshly prepared $Pd(MeCN)_2Cl_2$ and 10 mol-% copper iodide under positive pressure of argon. Then, 1,1'-diiodoferrocene **22** dissolved in freshly distilled and deoxygenated THF was added

together with 20 mol-% of tri-*tert*-butylphosphine as a stock solution in THF. To the mixture, freshly distilled and deoxygenated DIPEA was added and the mixture was degassed for further 15 min with a stream of argon. The reaction mixture was heated to 60 °C before a 3-fold excess of acetylene **48**, dissolved in freshly distilled and deoxygenated THF was added. The reaction progress was controlled via MALDI-ToF and stopped after 12 h, when no more starting material was observed. After column chromatography on silica gel, the di-substituted product **52** could be isolated in excellent yields. The formed side products were usually the mono-substituted adduct and a neglectable percentage of dehalogenated mono-substituted adduct. The isolated mono-substituted adduct could be used in the next reaction cycle. In analogy to the model compound **23**, the 1,3-dioxolane was transformed via trans-acetalization into the corresponding aldehyde using PPTS in a 10:1 acetone/water mixture. Subsequent reduction of the aldehyde **53** using sodium borohydride in THF at room temperature, gave the bis-alcohol **54** in excellent 98% yield (**SCHEME 29**).
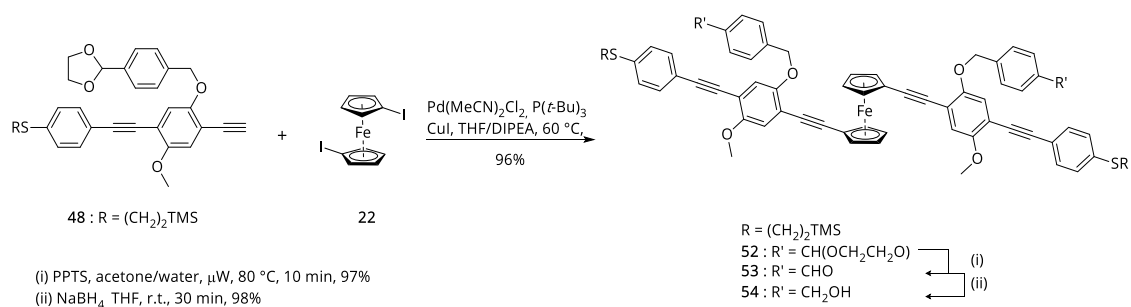
SCHEME 29 Synthesis of the ferrocene wire with terminal acetylenes.

Following the outlined strategy, bis-alcohol **54** was closed by intramolecular substitution reaction. Two successful routes were found to form the ether bridged macrocycle **55**. Ring closure without intermediate isolation was accomplished by treating a 2.1 mM solution of the bis-alcohol in THF with 1.0 equivalent methanesulfonyl chloride in the presence of excess base at -10 °C (**SCHEME 30**). The formation of the sulfonate was monitored by MALDI-ToF and revealed to be a slow process. When the reaction mixture was allowed to warm to room temperature overnight all reagent was consumed. Addition of another equivalent of methanesulfonyl chloride did not led to further mesylate formation.
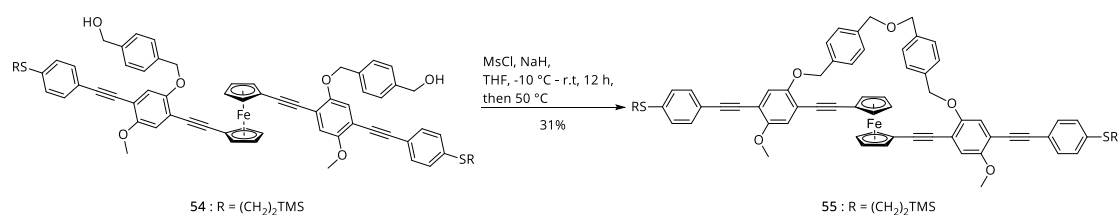
SCHEME 30 Macrocyclization without intermediate mesylate isolation.

The mixture was then heated to 50 °C and the consecutive intramolecular cyclization product was formed within one hour. As a side product, dimeric bis-alcohol and a dimeric macrocycle were formed and observed by MALDI-ToF (**FIGURE 29**). Ether bridged macrocycle **55** was then purified by column chromatography on silica gel and size exclusion chromatography to isolate the orange solid in 31% yield.
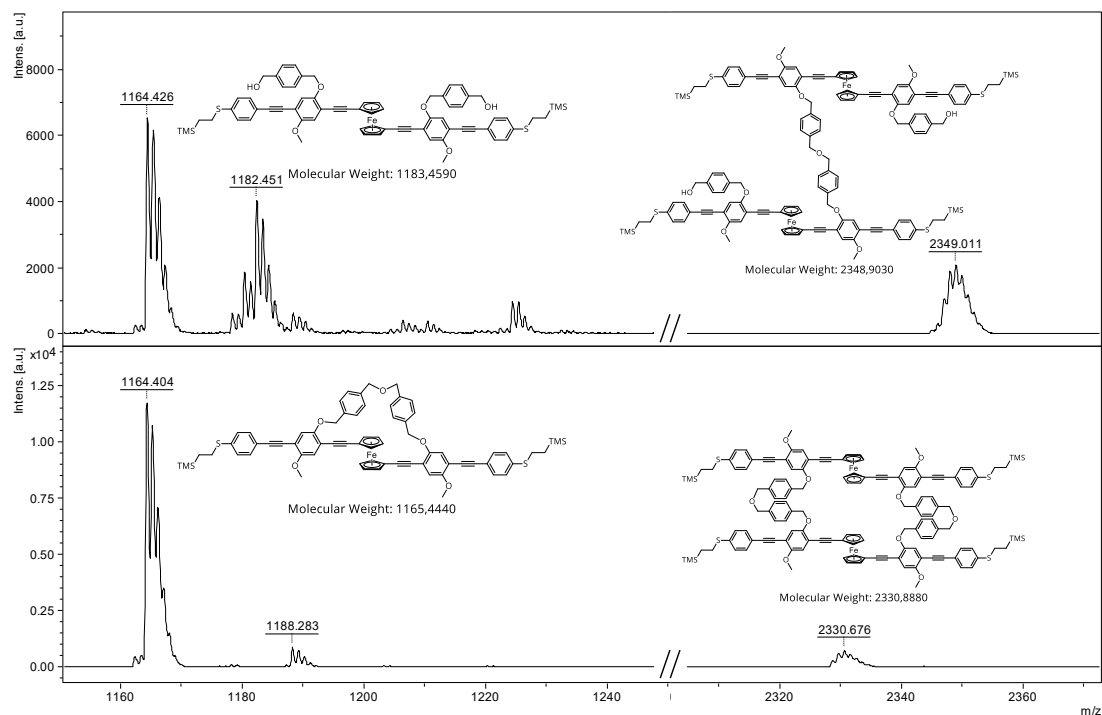
FIGURE 29 Top) MALDI-ToF reaction control of one step cyclization reaction. Bottom) MALDI-ToF after FCC.

When bis-alcohol **54** was treated with 10 eq. of methanesulfonyl chloride, disubstituted bis-mesylate **57** could be isolated after FCC in 23% yield (**SCHEME 31**). Attempts to isolate the formed mono-mesylate **56** were not successful, as the compound was unstable. The same inaccessibility was found for the model compound **25** described in the previous chapter.
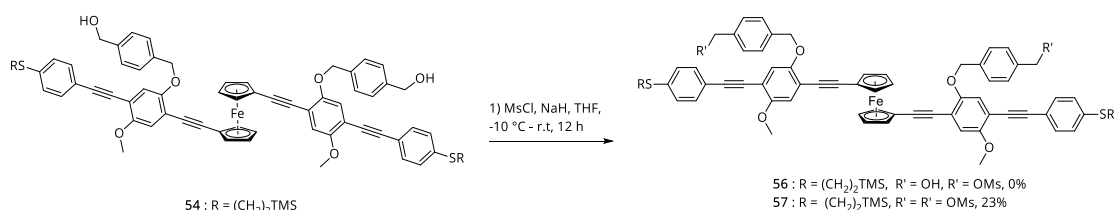
SCHEME 31 Synthesis of mesylated analogs **57** in 23% yield. Mono-mesylate **56** could not be isolated.

Hence, we changed the strategy to afford the bromo-analog (**SCHEME 32**). Therefore, bis-alcohol **54** was treated with a large excess of NaH in previously distilled and degassed THF. The suspension was cooled to approx. − 10 °C before 3.0 eq. of methanesulfonyl chloride were added dropwise. The reaction mixture was allowed to warm slowly to room temperature, when the statistical formation of reaction products was monitored by MALDI-ToF. To the reaction mixture, a large excess of LiBr was added, in order to transform all reactive mesylate. After aqueous workup and purification via column chromatography, the mono-bromo **58** and bis-bromo **59** were isolated in 42% and 24%, respectively. The use of 1.0 eq. methanesulfonyl chloride afforded the mono-bromo **58** in 30% only.
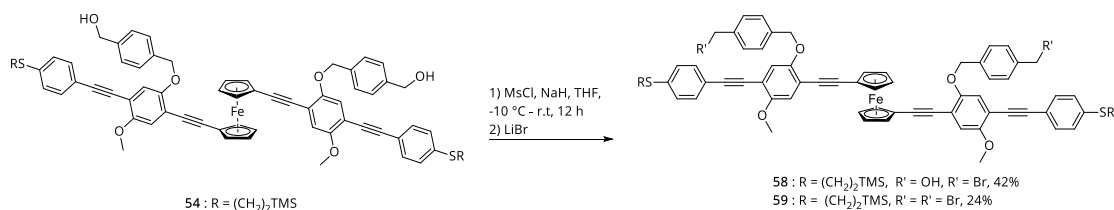
SCHEME 32 Synthesis of mono- and bis-bromo functionalized ferrocene **54** and **55**, respectively.

In order to probe the interlinked molecular wire in an electrode contact experiment, the sulfur anchoring group had to be transprotected to -SAc. Studies on the transportection of aryl(ethynyl)ferrocenes (**60**) with TBAF and acetylchloride showed that hydrochlorigenation forms the Markovnikov addition product (**61**, **SCHEME 33**)[128]. The same outcome, in particular when electron rich acetylenes are present, was observed when BBr_3 and AcCl were used for instance as transprotection agents for -S^{t}Bu protecting groups.

To favor the intramolecular over the intermolecular cyclization reaction (**SCHEME 34**), a diluted, 1 mM solution of **58** in freshly distilled and degassed THF was prepared. A 50-fold excess of sodium hydride was suspended in the solution and after gas evolution has stopped, the mixture was heated to 50 °C for 1 h. MALDI-ToF analysis confirmed the clean and exclusive formation of the intramolecular cyclization product. After acidic aqueous workup, the crude was subjected to column chromatography and the product **55** was isolated as orange solid in 45% yield.
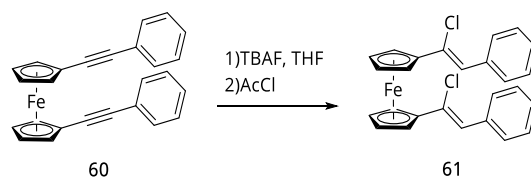
SCHEME 33 Treatment with TBAF and AcCl provide a 'H-Cl' addition forming the *Z*- Markovnikov product **61**, with anti-stereoselectivity.[128]

Hence, macrocycle **55** was dissolved in degassed THF and treated with 10 eq. TBAF at room temperature. After 45 min., a large excess of acetic anhydride was added to the mixture at 0 °C and stirred for further 15 min when the reaction was stopped by adding ice. After aqueous workup, the crude was filtered over silica, to give the target compound **36** in 72% yield as orange solid (**SCHEME 34**).
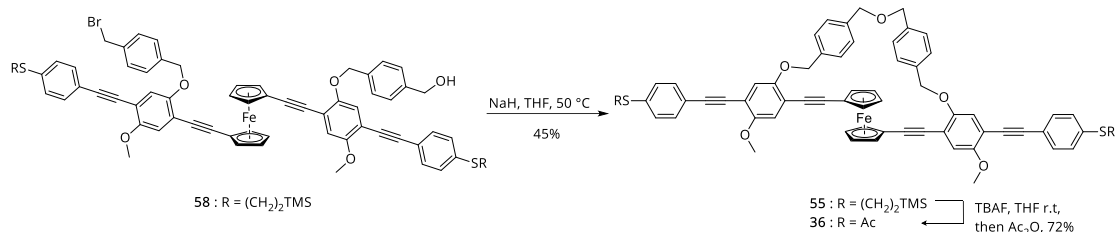
SCHEME 34 Intramolecular cyclization reaction, followed by a transprotection gave the target compound **36**

Bis-mesylate **57**, isolated as side product in the statistical mesylation of **52**, bears two excellent leaving groups in the bridging unit, which makes it accessible to nucleophilic substitution. As shown in literature, sodium sulfide readily forms cyclic sulfides with appropriate leaving groups in aprotic solvents.[136–138] In order to extent the repertoire of interlinked molecular wires, bis-mesylate **57** dissolved in dry toluene, was slowly added to a mixture of sodium sulfide nonahydrate in 1:1 ethanol/toluene, to form the macrocyclic sulfide **62** (**SCHEME 35**). The reaction mixture was stirred for 5 h at room temperature, before the solvent was evaporated and the crude material subjected to column chromatography. The orange solid was isolated in 49% and subsequently transprotected to the acetyl terminated wire **63** in 25% yield. One-pot cyclization attempts without isolating the reactive mesylate **57,** gave cyclic sulfide **62** in 34% yield only.

SCHEME 35 Formation of the macrocyclic sulfide, using sodium sulfide in a 0.7 mM toluene/ethanol mixture.

Another very interesting approach, in terms of bridge rigidity, is based on the oxidative acetylene homocoupling of terminal acetylenes to form super stiff macrocycles. Such a bis-ethynyl precursor can be accessed by Seyferth-Gilbert homologation from bis-aldehyde **53** (displayed in **SCHEME 36**). For that, aldehyde **53** was treated with the Bestmann-Ohira Reagent (B-O-R) in a THF/MeOH mixture and Cs_2CO_3 as base.[139] The bis-acetylene **64** was isolated as red-orange

solid in 71% yield after FCC on silica gel. The compound showed limited stability, as its decomposition was detected after 14 days of storage at 4 °C.
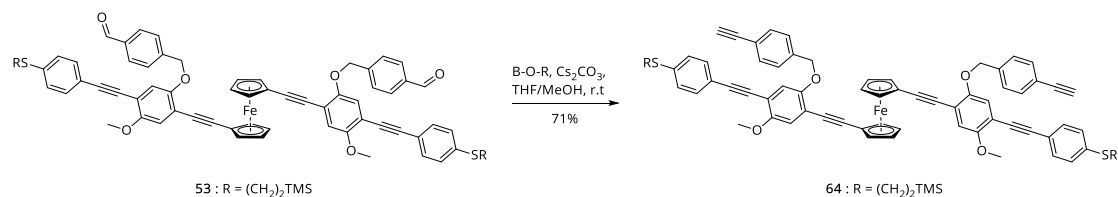
SCHEME 36 Seyferth-Gilbert homologation using the Bestmann-Ohira reagent.

The subsequent cyclization reaction was tested with several methods (**TABLE 6**). The cyclization product **65** was exclusively observed in the reaction control MALDI-ToF (**FIGURE 30**) by utilizing Glaser-Hay conditions[140] (**TABLE 6**, entry 1) in an open Erlenmeyer flask and aerated solvent. However, the product could not be isolated in sufficient quantities for spectroscopic analysis. Unfortunately, the reaction outcome could not be reproduced with these conditions (**TABLE 6**, entry 1). Applying common oxidative homocoupling conditions did not facilitate product formation (**TABLE 6**, entry 2). For those reactions where the coupling was supported by a Pd catalyst (**TABLE 6**, entry 3 & 4), excessive dimer formation was observed.
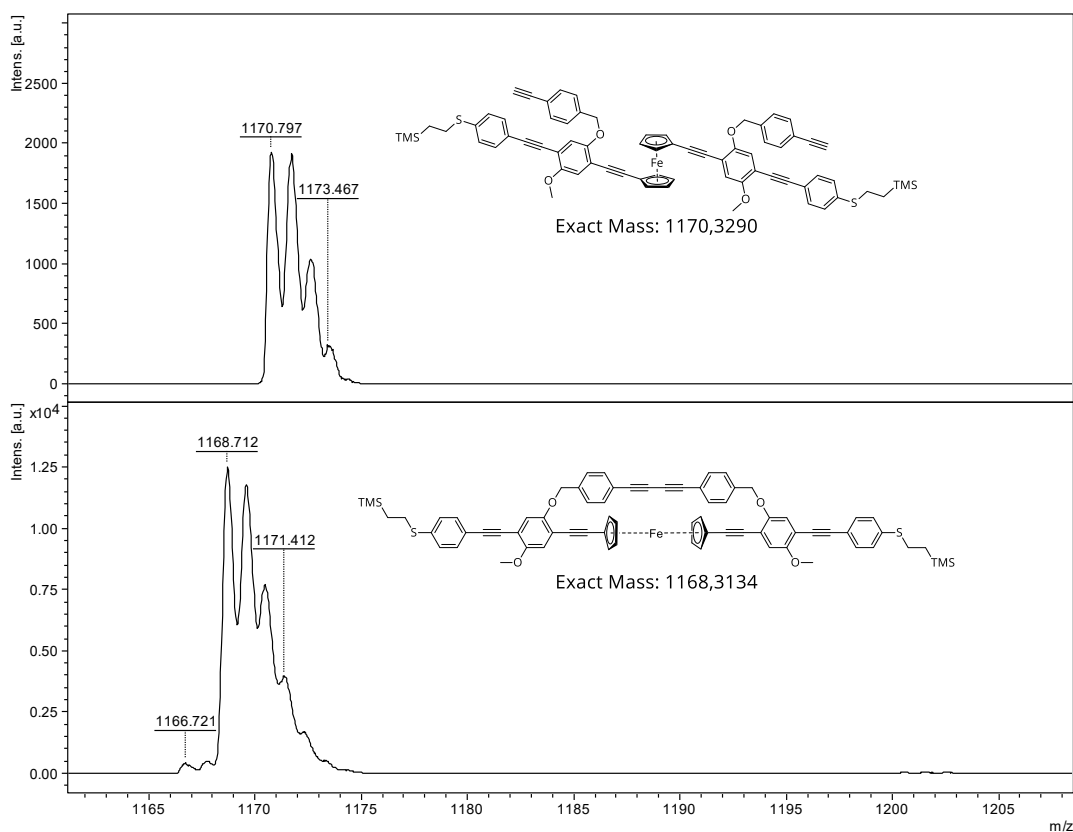
FIGURE 30 1,3-diyne bridged macrocycle **65** was exclusively observed in MALDI-ToF of reaction **TABLE 6**, entry 1.

64 : R = (CH₂)₂TMS

65 : R = (CH₂)₂TMS
66 : R = Ac
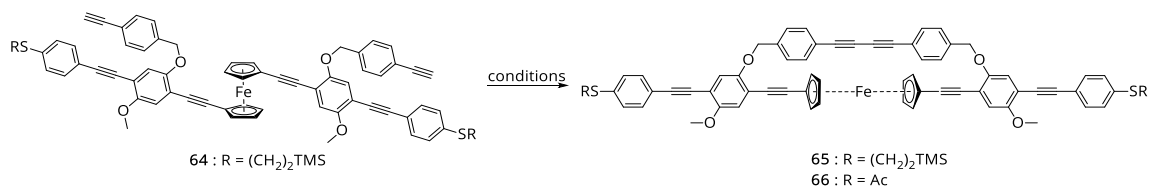
TABLE 6 Macrocyclization reaction conditions employed following protocols. [a,b,c]

entry	solvent	catalyst	base	temperature	conc.	result
1	DCM	CuI/TMEDA	-	r.t.	0.3 mM	traces of **65**
2	DCM	[a]Cu(OAc)$_2$	piperidine	r.t	0.26 mM	SM & dimer
3	THF	[b]Pd(PPh$_3$)$_4$, Ag$_2$O	-	60 °C	0.5 mM	SM & dimer
4	THF	[c]Pd(PPh$_3$)$_2$Cl$_2$, CuI, DIB	Et$_3$N	60 °C	1.3 mM	dimer

[a,]Blaraman et al.,[141] [b]Feng et al.,[142] and [c]Yan et al. [143] respectively.

UV-VIS SPECTROSCOPY

The electronic absorption spectrum of the bis-alcohol **54**, ether bridged macrocycle **55** and sulfide bridged macrocycle **62** was recorded and compared. Therefore, a 10⁻⁵ M solution of each compound was measured at room temperature and the wavelength was plotted against the normalized absorbance. **FIGURE 31** and **TABLE 7** show the details of the acquired data.

The three ferrocene structures showed two strong absorptions in the near UV and a common onset absorption of λ_{onset} = 520 nm. The absorbance in the visible region between 430 and 500 nm was found as responsible for the red-orange colorization of the compounds. The change from the open structure in compound **54** to the close cycle in **55** and **62** does affect the strong transition between 350−400 nm that most likely can be attributed to π-d* transitions that can be classified as Ligand-Metal Charge Transfer (LMCT). The bathochromic shift upon cyclization is probably due to the increased conjugation of the phenylethynyl backbone by planarization. In case of ether **54,** a bathochromic shift of 12 nm and for the sulfide macrocycle **62** a shift of 13 nm was observed. Interestingly, the shorter wavelength transition between 300−350 nm is not affected from cyclization. The transition is most likely a metal centered Metal-Ligand Charge Transfer (MLCT), arising from the d-π* absorption.
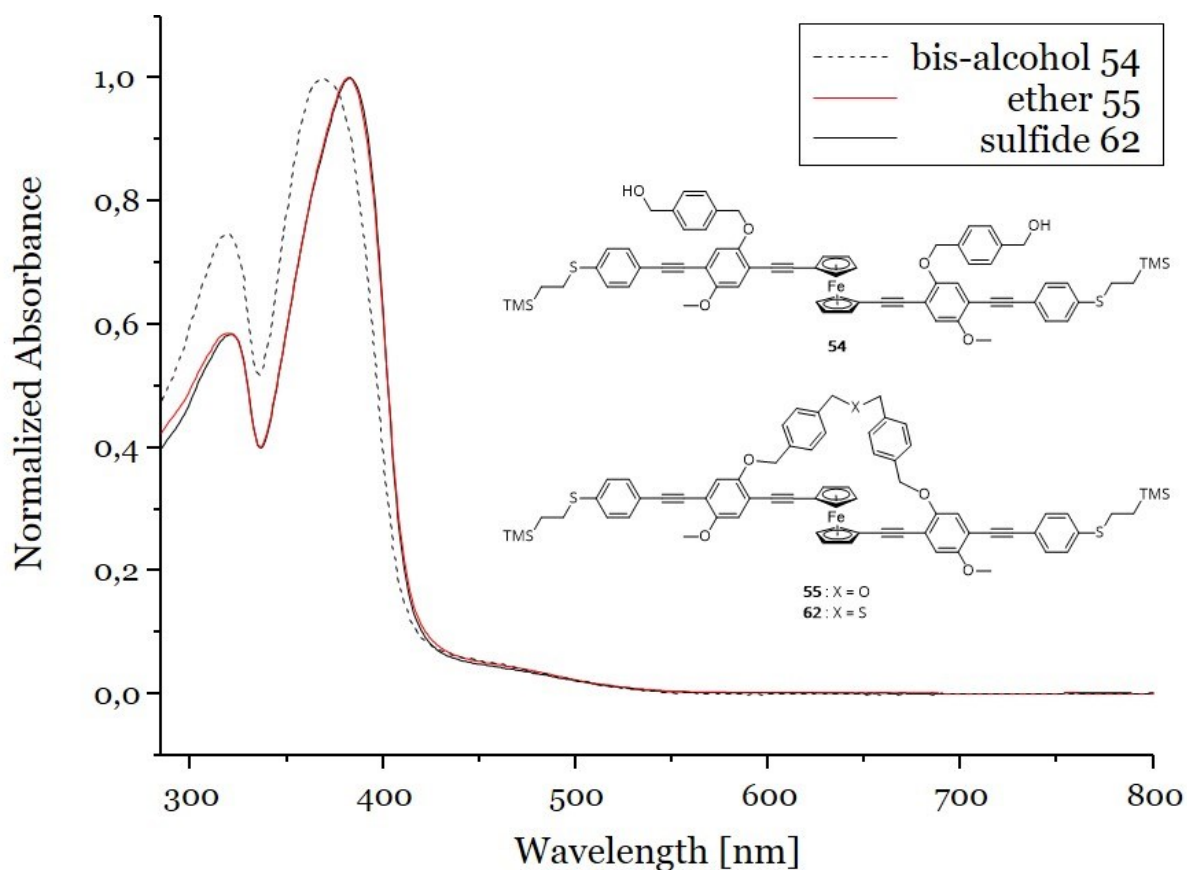
FIGURE 31 Normalized absorbance electronic spectra of bis-alcohol **54** and macrocycles **55** and **62** in CHCl$_3$ at room temperature.

TABLE 7 Electronic absorption spectra of macrocycles **55** and **62** and its precursor **54** in CHCl3 at room temperature.[a]

compound	MLCT λ_{max}	LMCT λ_{max}
bis-alcohol **54**	320(0.59)	370(0.79)
ether **55**	320(0.54)	382(0.92)
sulfide **62**	322(0.55)	383(0.94)

[a]Absorbance in parenthesis of a 10^{-5} M solution.

DFT-CALCULATIONS

The structural information relying on the DFT-calculations, give an important insight in the orientation of the wire arms, since no crystal structure information is available. This is in particular interesting, as the spanning angle of the arms defines the S-S anchoring group distance. From a different point of view, the spanning angle is a function of the bridging unit which is incorporated into the wire. Further, DFT-calculations help to evaluate the energy levels of the frontier orbitals with respect to the Fermi-level of the electrodes, which is useful for the inter-

pretation of conductance measurements. Although these calculations give an accurate trend for the frontier energies, the absolute values from these calculations are not reliable.

The ground state equilibrium geometry and the molecular orbital representation of the thioacetyl terminated ether **36**, sulfide **63** and buta-1,3-diyne **66** bridged interlinked molecular wires in gas phase as obtained by the DFT calculations using B3LYP functional with mixed basis set (6-31G** for C, H, S and LANL2DZ for Fe) within the SPARTAN'10 software package (Wavefunction, Inc., USA) are summarized in **TABLE 8** DFT calculations gave structure and energies of the ground state.

TABLE 8 DFT calculations gave structure and energies of the ground state.

macrocycle	spanning angle[a]	length[b]	E_{HOMO} (eV)	E_{LUMO} (eV)	$\Delta E_{LUMO-HOMO}$ (eV)
ether **36**	168°	33.5 Å	-5.05	-1.72	3.33
sulfide **63**	167°	33.4 Å	-5.10	-1.75	3.35
1,3-butadiyne **66**	175°	33.6 Å	-5.46	-2.02	3.44

[a]spanning angles were determined between S-Fe-S atoms. [b]The distance from S to S atom was measured.

The interlinked molecular wire frontier orbitals are shown in **FIGURE 32**. Ether **36** has two, nearly degenerate HOMO orbitals, which are obtained from a symmetric combination of two parts, each of which is mostly localized on one side of the wire arm, whereby the orbitals are on the ferrocene adjacent phenyl ring with little contribution on the outer phenyl ring. The same holds for the two LUMO orbitals of ether **36**. The nearly degeneracy of these orbitals shows only little electronic coupling between both parts of the molecule, reflecting its broken conjugation probably caused by phenyl torsions.

Likewise, the sulfide **63** has a HOMO and HOMO[-1] orbital of nearly identical energy and of symmetric and complementary localization. In contrast to the former, the HOMO orbitals of compound **63** are distributed over the molecular backbone of both arms, but leaving the anchor groups uninvolved. The LUMO and LUMO[+1] lobes are almost even distributed over the molecule with little contribution of the ferrocene and of very similar energy.

Finally, buta-1,3-diyne **66** does not feature the degeneracy of HOMO and HOMO[-1] orbitals, but rather shows a lobe localization of on one arm in HOMO and more a ferrocene centered localization in HOMO[-1]. Interestingly, the LUMO and LUMO[+1] and very close in energy and complementary in localization. The lobes are distributed over one arm and also show a significant proportion over the 1,3-diyne bridge.
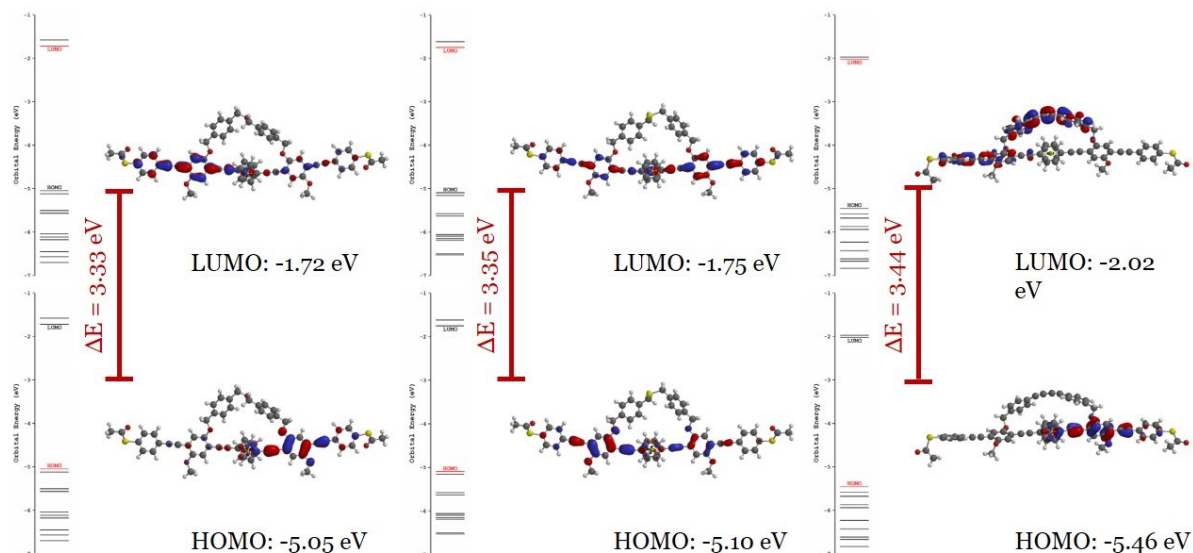
FIGURE 32 DFT calculated HOMO-LUMO energies of the three macrocycles.

The DFT calculations show that the HOMO energies for the ether **36** and the sulfide **63** are very similar and being the closest molecular energy levels to the fermi level of the gold contacts (E_F = - 5.0 eV, determined by Trouborst et al.[144]). The buta-1,3-diyne bridged **66** showed to have the lowest HOMO energy of -5.46 eV. This result suggests that electron transport in a gold-gold junction would involve the HOMO orbitals of the molecular wires. The molecular length of the wires suggests a tunneling mechanism according to the literature.[117] The critical distance for a transition from temperature independent non-resonant tunneling to the thermally activated hopping mechanism was observed for OPE wires at a length of ~4 nm.[131,145]

MCBJ MEASUREMENTS

In order to obtain electron transport characteristics, the interlinked molecular wires were tested first for their electrode contact ability. For this purpose, interlinked molecular wires (IMWs) **36** and **63** were probed in a *Mechanically Controlled Break-Junction* (MCBJ) setup within a liquid cell environment (**FIGURE 33**). The experiments have been performed by Jan Overbeck from the research group of PD Dr. Michel Calame.

The gold junctions were lithographically fabricated on a polished bronze substrate that was spin-coated with a 2-3 μm thick polyimide layer (**FIGURE 34**). The substrate contained three in parallel fabricated junctions that had a central constriction of 80 - 150 nm. On top of the substrate a Viton tube was mounted that contained a total volume of 250 μL.[146] When the substrate is suspended in a three-point bending apparatus, the vertical displacement of the pushing rod would elongate the central gold wire, eventually breaking it. Ideally, the originated atomically sharp electrode gap is bridged by the solute molecules. At the same time, the junction conductance as a function of rod displacement Δz is recorded. A conductance trace, usually shows a conductance plateau at 1 G_o (G_o = $2e^2/h$), signaling the monoatomic gold contact. Further elon-

gation breaks the contact and is accompanied with exponential drop of conductance. Conductance plateaus in the individual curves are then attributed to molecular conductance. By opening and closing the junction iteratively, numerous conductance traces can be recorded and displayed in histograms that help to statistically validate the molecule junction formation.
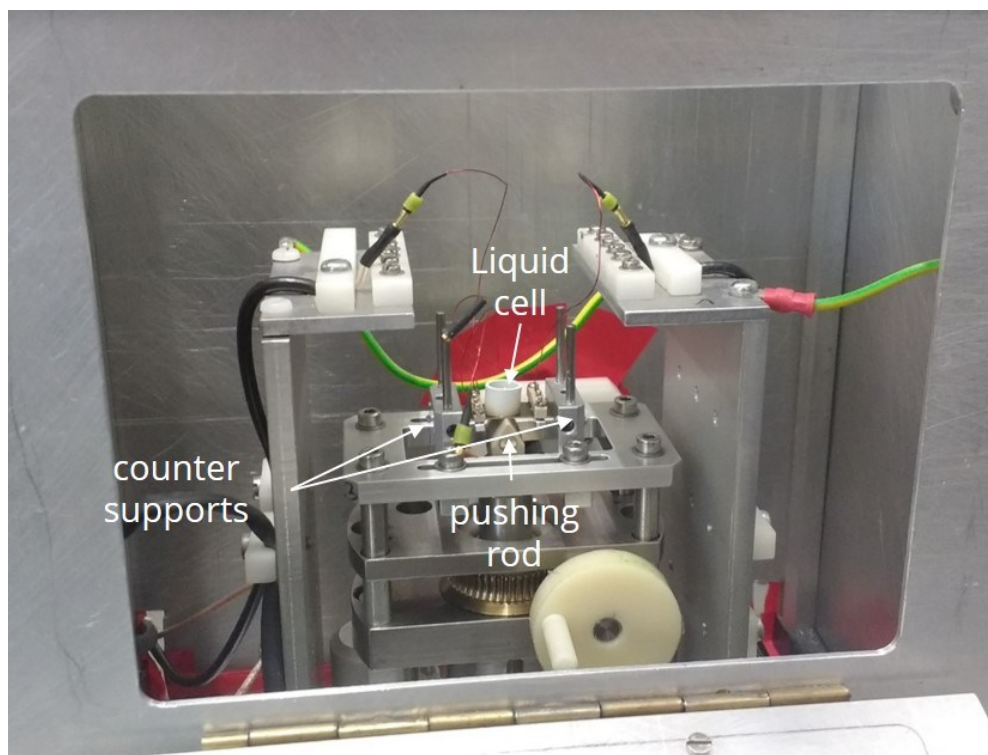
FIGURE 33 MCBJ setup of the measurements performed in the Calame group.
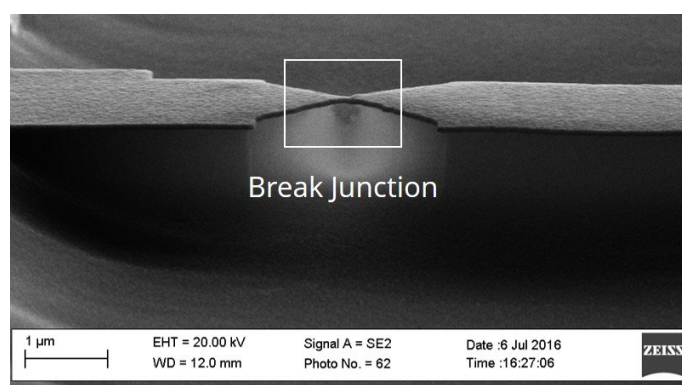
FIGURE 34 SEM image of a fabricated gold structure, before performing contact experiments.

In order to immobilize molecules in the junction, the liquid cell was filled with a 100 μM solution of the respective IMW, in degassed mesitylene or in a mixture of THF/mesitylene (1:4). The acetyl protection groups of the thiophenol anchor groups were removed *in situ* by adding a 200 μM solution of tetrabutylammonium hydroxide (TBAOH) in THF or tetrabutylammonium fluo-

ride (TBAF) in THF and conductance histograms have been recorded (**FIGURE 35** & **FIGURE 36**).

First, about 70 open-close cycles with the solvent only were performed, in order to assess the junction stability. Then, 100 µL of ether bridged macrocycle **36** in THF/Mesitylene were injected in the cell and again several open-close cycles were performed (**FIGURE 35** a). No molecular signature could be detected for the acetyl protected compound **36**. After adding 2.0 eq. of TBAOH in THF solution, about 350 open-close cycles were made (**FIGURE 35** b), and showed a non-exponential decay of conductance ranging from 10^{-2} - 10^{-5} G_0. The shallow decay of conductance plateau results in no clear conductance peak in the 1D histograms. A possible explanation for this shape is the length of the molecule and the accompanied different molecular configuration that can obtained within the junction during the stretching process. Thereby, different dominant charge transport contributions might lead to the observed conductance traces. However, this exceptional conductance "plateau" was not observed for the majority of traces, but for the very last recorded (**FIGURE 35** c), indicating the delayed anchor group liberation with a weak molecular conductance signal at best. Unfortunately, we could not exceed 350 junction formation with the employed constriction as it reached its lifetime.
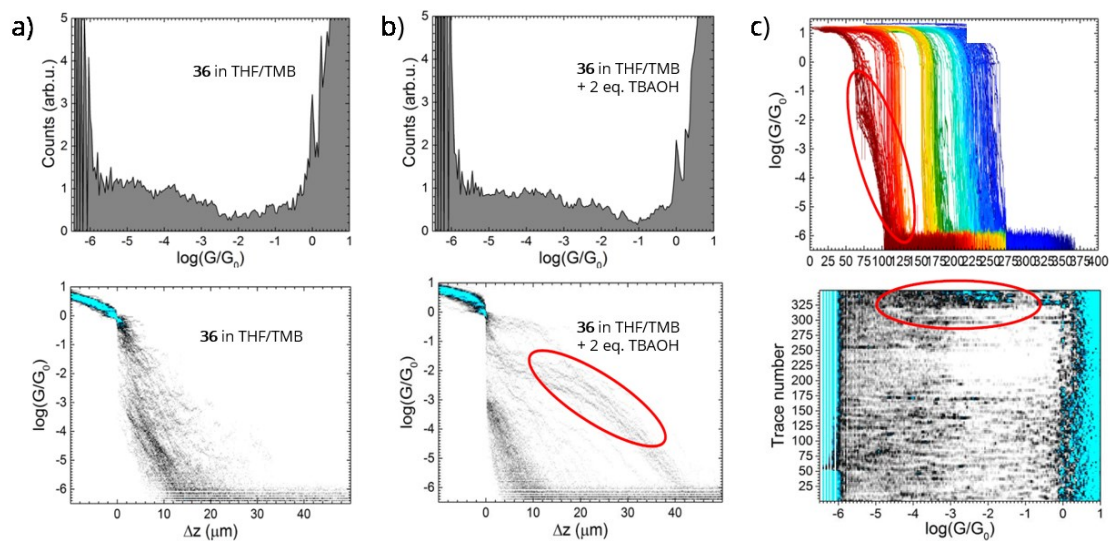
FIGURE 35 a) top: Logarithmic conductance histogram of **36** in THF/mesitylene; bottom: 2D Conductance traces of **36** in THF/mesitylene. b) top: Logarithmic conductance histogram of **36** in THF/mesitylene + 2 eq. TBAOH; bottom: 2D conductance traces of **36** in THF/mesitylene + 2 eq. TBAOH. c) All conductance traces of **36** in THF/mesitylene + 2 eq. TBAOH; bottom: 2D plot of conductance histogram of **36** in THF/mesitylene+ 2 eq. TBAOH.

In order to ensure the S-acetyl cleavage, the experiment was repeated with the use of TBAF as deprotection agent. This time, 2 eq. of a 200 µM TBAF solution in THF was added to the liquid cell and the experiment was monitored (**FIGURE 36**).
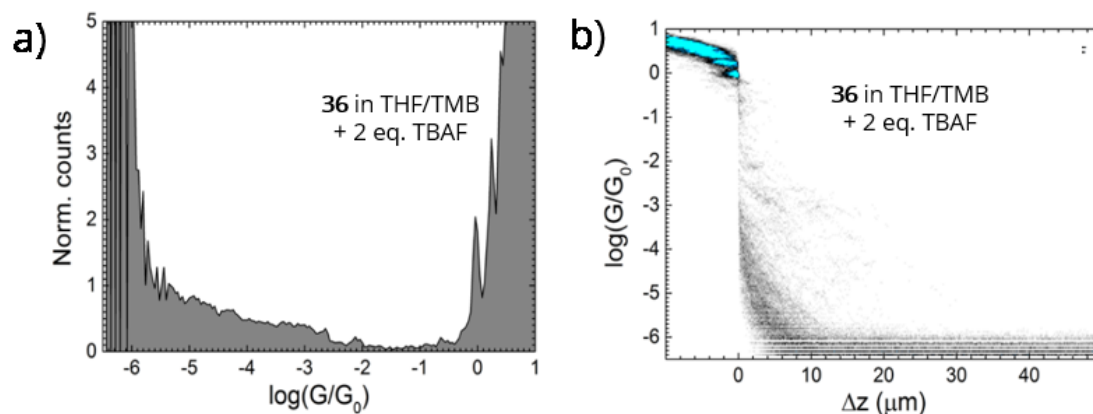
FIGURE 36 a) 1D conductance histogram of **36** in THF/mesitylene + 2 eq. TBAF. b) 2D representation of the conductance histogram.

No molecular conductance signature in the observed repeating cycles was detected for macrocyclic ether **36**, when TBAF was used as deprotecting agent. Instead, a decolorization of the solution and an orange precipitation in the liquid cell was observed after the measurements. A post measurement SEM of the metallic substrate and the free-standing gold constrictions revealed that an agglomerate was dispersed on the surface of the substrate (**FIGURE 37**). The missing conductance plateau implies that the molecular wire **36** has been precipitated from the solution before molecular junctions could be formed.
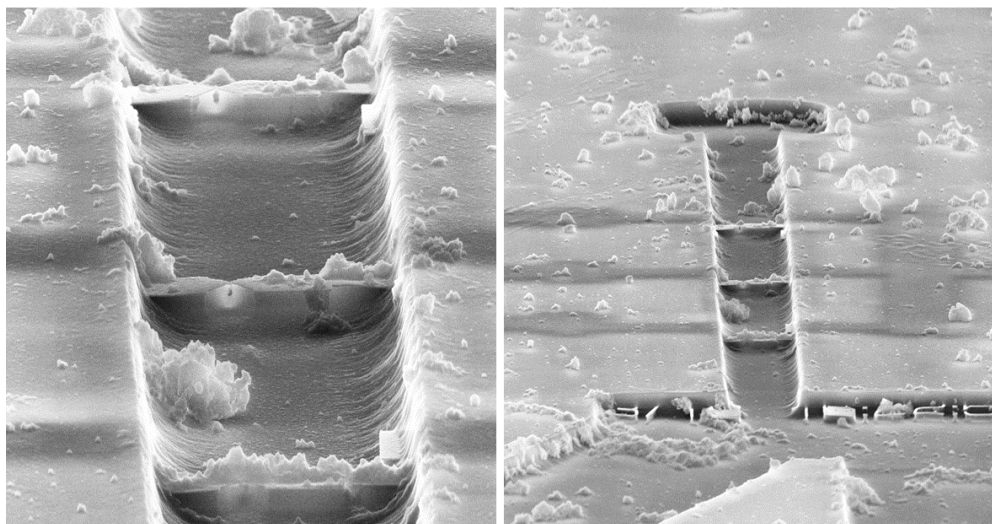
FIGURE 37 The MCBJ cell was filled with a THF/TMB solution of compound **36** and TBAF was added. The figure shows post measurement SEM images of the substrate and the constrictions.

The sulfide bridged molecular wire **63** has been probed on a newly fabricated substrate and the junctions have been tested prior of measurement in the same manner as described for the ether bridged wire **36**. After the stability of the junction was verified, 100 μL of **63** in a 100 μM solution in mesitylene was injected in the cell and several open-close cycles were performed. Then, 4

eq. of TBAOH were added and the conductance traces recorded (**FIGURE 38** a). No molecular signature was detected. To ensure that all acetyl protecting group is cleaved off and the molecular wire available for junction formation, **63** was treated with 2 eq. TBAF in THF. However, this did not result in junction formation or corresponding plateau recording (**FIGURE 38** b). The experiment was terminated after about 320 open-close cycles. The sum of all conductance traces indicated that no junction formation was detected (**FIGURE 38** c). Again, decolorization and precipitation was observed after measurement, indicating that the compound formed aggregates that were insoluble and hence no molecular conductance was recorded.
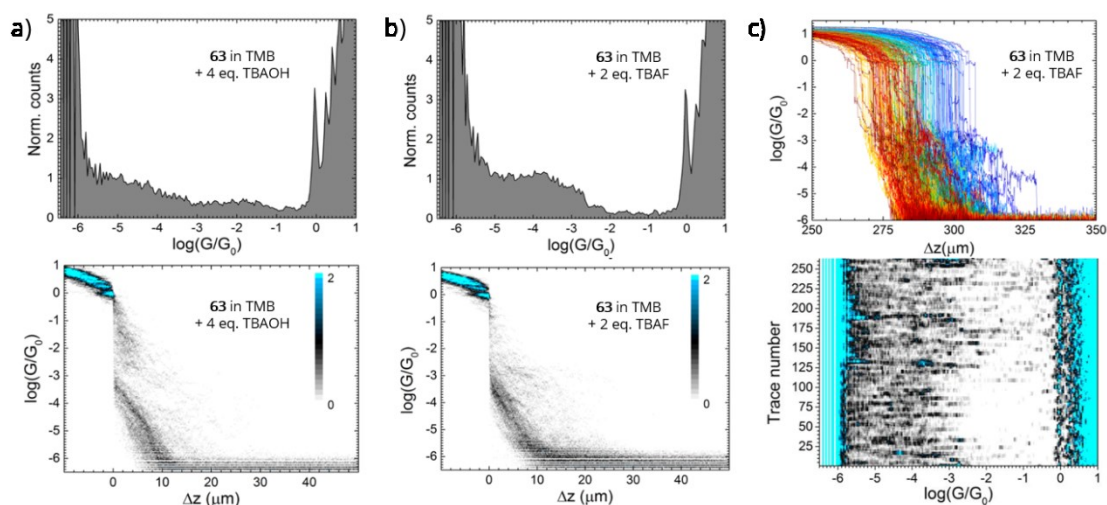
FIGURE 38 a) top: Logarithmic conductance histogram of **63** in mesitylene + 4 eq. TBAOH; bottom: 2D Conductance traces of **63** in mesitylene + 4 eq. TBAOH. b) top: Logarithmic conductance histogram of **63** in mesitylene + 2 eq. TBAF; bottom: 2D conductance traces of **63** in mesitylene + 4 eq. TBAOH. c) All conductance traces of **63** in mesitylene + 2 eq. TBAF; bottom: 2D plot of conductance histogram of **63** in mesitylene+ 2 eq. TBAF.

To conclude the MCBJ experiments performed in solution, the ether bridged molecular wire **36** showed shallow conductance plateaus at best for the late open-close cycles of the experiment, when dissolved in a THF/mesitylene mixture using TBAOH as deprotecting agent. By changing the deprotection agent to TBAF, the compound was found to precipitate out of the solution, probably leaving the molecular wire inaccessible to the electrodes.

The sulfide bridged molecular wire **63** on the other hand did not show any molecular conductance plateaus within the available detection limit. As observed for the ether bridged wire, a decolorization after the probing was observed, indicating that the compound has formed aggregates that are inaccessible to the electrodes.

The results obtained by the MCBJ experiments do not ultimately imply that the molecules are inaccessible to break junction experiments, hence, another technique might provide molecular junction formation and therefore conductance data.

However, to investigate the transport properties of the redox active IMWs with respect to an applied gating voltage, a three-terminal setup has to be employed. We therefore collaborated with the research group of Prof. Dr. Thomas Wandlowski form the University of Bern.

EC-STM-BJ MEASUREMENTS

In order to investigate the electron transport characteristics under electrochemical gating of the ether bridged ferrocene **36** and sulfide bridged ferrocene **63**, *Electrochemical Scanning Tunneling Microscopy Break Junction* (EC-STM-BJ) experiments (schematic illustration in **FIGURE 39**) have been performed by Joseph Hamill from the group of Prof. Dr. Thomas Wandlowski at the University of Bern.

In general, STM experiments allow thousands of conductance curves to be measured within a much shorter time compared to MCBJ experiments, while having a more successful rate in forming the molecular junction.[147] The contacts are formed by driving the immersed gold tip repeatedly in and out of the gold substrate on which the molecules are immobilized. By setting a gating voltage during the junction formation the potential depending electron conductance curve can be recorded.
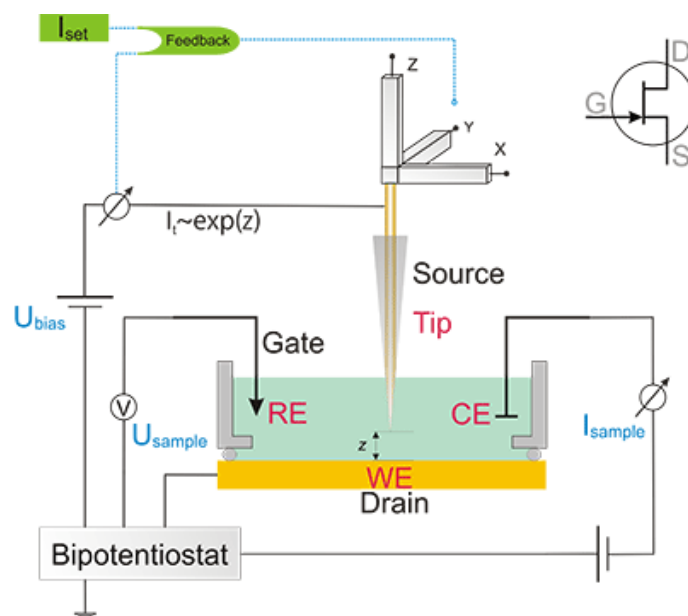
FIGURE 39 Schematic setup of a EC-STM device. The potential of the tip and sample must be controlled independently with respect to reference electrode, which requires a bipotentiostat. The STM tip must be isolated except of its very apex.[148]

The STM sample substrates were prepared with the macrocycles **36** and **63** by the immersion of a polycrystalic gold disc in a freshly prepared 0.2 mM solution of the IMW in THF for 12 h. *In-situ* cyclic voltammetry (**FIGURE 40**) in the EC-STM-BJ cell was performed using HMImPF$_6$ (1-Hexyl-3-methylimidazolium hexafluorophosphate) as electrolyte in order to assess the redox

potential and the substrate coverage of the individual IMWs. The electrochemical cell consists of two Pt wires, one as counter electrode and another as reference electrode that are connected to a bipotentiostat and the setup can be used as three-terminal gating device.

The integration of the anodic and cathodic peaks allows the estimation of the substrate coverage with the molecules (inset in **FIGURE 40**). The weak redox wave response for the ether bridged ferrocene **36**, indicates a moderate molecule coverage of the gold substrate. In contrary, the redox wave is well pronounced for the sulfide bridged ferrocene **63** that has better substrate coverage. This might be due to the gold affine sulfide bridge that additionally gets absorbed at the substrate. Both molecules **36** and **63** show a very similar redox potential at ~0.1 V vs. Pt.
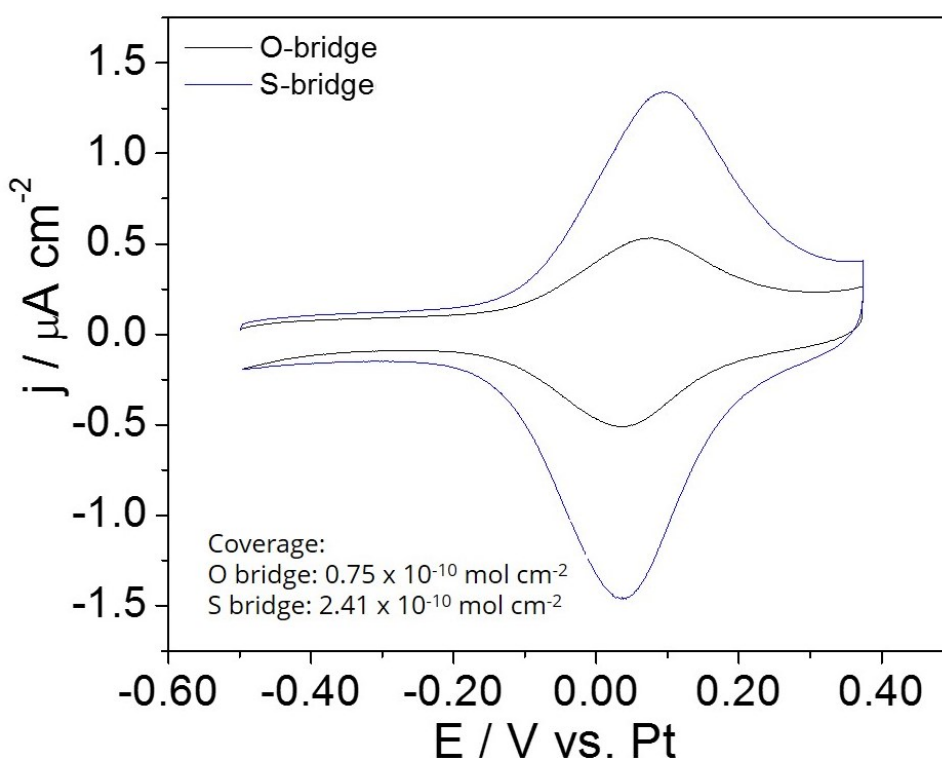
FIGURE 40 Cyclic Voltammetry of ether bridged ferrocene **36** (black line) and sulfide bridged ferrocene **63** (blue line) using $HMImPF_6$ as electrolyte sweeping from -0.5 V to 0.4 V vs. Pt at a scan rate of 10 mV/s.

For the conductance measurements, the STM tip was driven at a controlled rate of 87 nm/s towards the STM substrate when the upper current limit was reached. The tip was then withdrawn at a controlled rate from the substrate and the current was recorded between the STM gold tip and Au(111) substrate at constant bias voltage 100 mV at various electrochemical potential ranging from -0.3 to +0.3 V vs. Pt. This cycle was repeated thousands of times for each set of experimental condition. In **FIGURE 41** a–c, the 1D and 2D conductance histograms with CV insets of ether bridged ferrocene **36** are shown.
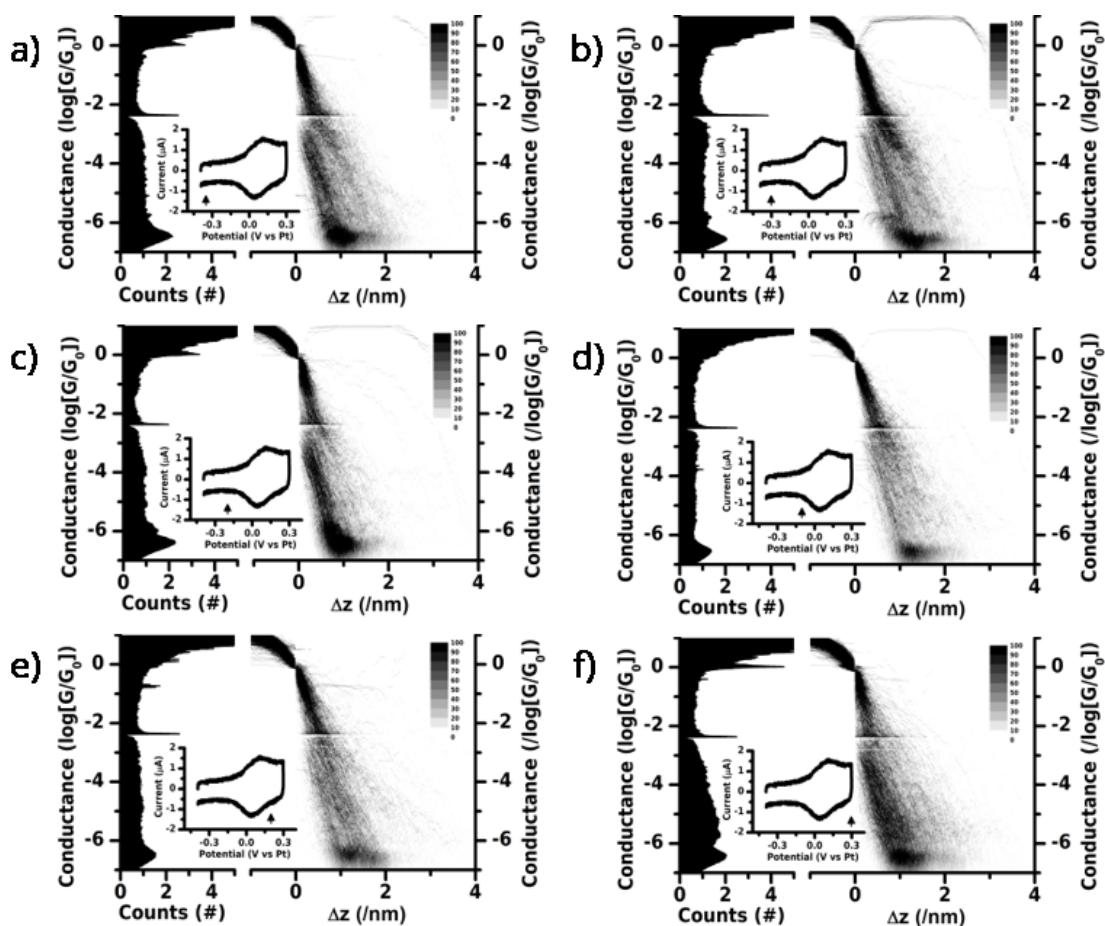
FIGURE 41 EC-STM-BJ histograms of **36** with a constant S-D bias voltage of 0.1 V. a) – f) 1D and 2D conductance histograms with various gating voltage (as CV curve inset).

For both redox states of ether bridged ferrocene **36**, the conductance traces decay exponentially without showing a conductance plateau. Based on these results, we conclude that the conductance of the neutral and oxidized form is below the detection limit of the EC-STM-BJ setup $(10^{-6.5}\ G/G_o)$.

The same experimental procedure was undertaken for the sulfide bridged ferrocene **63** and the results are shown in **FIGURE 42**. Likewise, we could not detect at any applied gating potential a reasonable conductance within the detection limit.
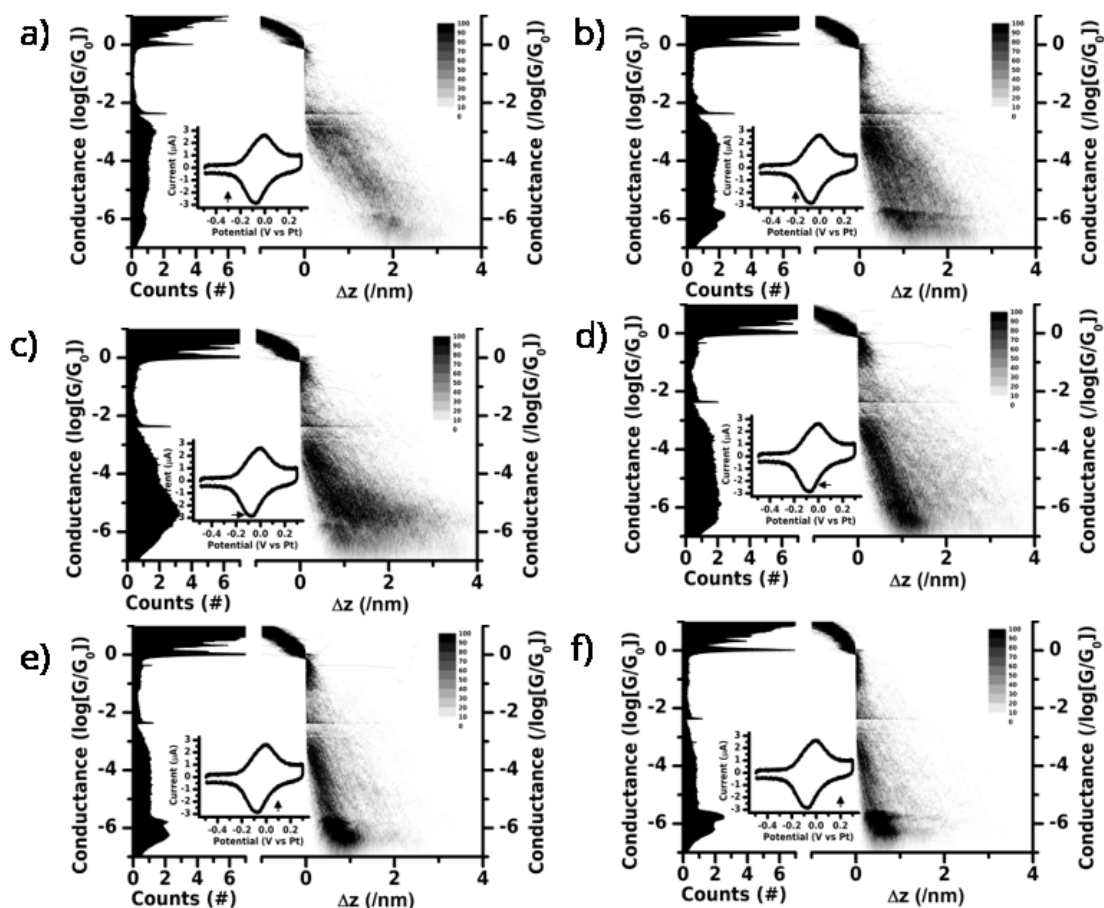
FIGURE 42 EC-STM-BJ histograms of **63** with a constant S-D bias voltage of 0.1 V. a) – f) 1D and 2D conductance histograms at different gate potentials, indicated with the arrow at CV curve inset.

In conclusion, no evidence for molecular junction formation was observed within the performed EC-STM-BJ experiments of both, the ether bridged ferrocene **36** (**FIGURE 41**) and the sulfide bridged ferrocene **63** (**FIGURE 42**). A possible explanation for this result is the length of the molecular wires employed here. In a recent study by Zhao et al.,[149] the length dependence of OPEs in MCBJ experiments was investigated and the conductance values for equally long compounds (~ 3 nm with 10^{-7} G/G_o) were found to be lower than the detection threshold (~$10^{-6.5}$ G/G_o) of the here employed device.

OUTLOOK AND CONCLUSION

In summary three interlinked molecular wires **36**, **63** and **65** with a central ferrocene unit have been synthesized (**FIGURE 43**). The molecules **36** and **63** have been fully characterized by means of spectroscopy, spectrometry and the formation of 1,3-buta-diyne bridged ferrocene **65** has been detected by mass spectrometry. The frontier orbitals for the three macrocycles has been studied by DFT-calculations and their accessibility for contacting experiments has been discussed. Their syntheses are all based on the functionalization of the 2-bromo-5-iodo-4-methoxyphenol **40** via substitution reaction and *Sonogashira* cross-coupling reaction. Furhermore, the introduction of ethylTMS protected ethynylphenyl thiol at an early stage improves the synthetic convergence of the strategy. Bis-aldehyde **53**, which is a common precursor of all three macrocycles, is an excellent synthon for the described macrocycles and in addition opens the synthetic door for other cyclization methods.
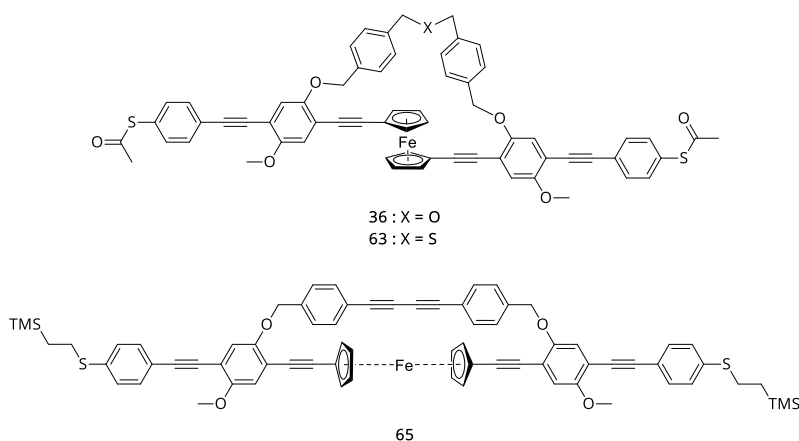
FIGURE 43 Synthesized interlinked molecular wires.

In the experiments presented in this work, the conductance characteristics of the compounds **36** and **63** were probed in an MCBJ and in an EC-STM-BJ setup. The motivation for these experiments was given by the significance of molecular wires as prospect functional materials for future application in molecular electronics. In this context, interlinked molecular wires display a very pragmatic approach to prevent the tendency of ferrocene grafted OPE wires for aromatic π-π stacking. Unfortunately, the experimental approach employed for the study of conductance characteristics does not provide reliable data for a deeper understanding of the structure-property relationship. A post measurement SEM of the MCBJ metallic substrate and the free-standing gold constrictions revealed that an agglomerate was dispersed on the surface of the substrate (**FIGURE 37**). The missing conductance plateau implies that the molecular wires **36** and **63** has been crushed out before molecular junctions could be formed. EC-STM-BJ experiments on the other hand suggest that the length of the molecular backbone exceeds the tunneling current regime. In other words, even if there is a conductance difference by changing the gate potential, the molecular conductance is below the detection limit of the device. To stay in

the tunneling regime, much shorter molecular wires have to be employed. The ferrocene grafting is still reasonable since the electrochemical stability and response of that function is superior to the alternative redox active compounds.[123,124,150] Hence, we suggest a short molecular backbone while being bridged with the here developed linker groups as depicted in **FIGURE 44**. The linker moiety in **pro-1** and **pro-2** is electronically decoupled of the molecular backbone while providing stiffness to the whole structure.
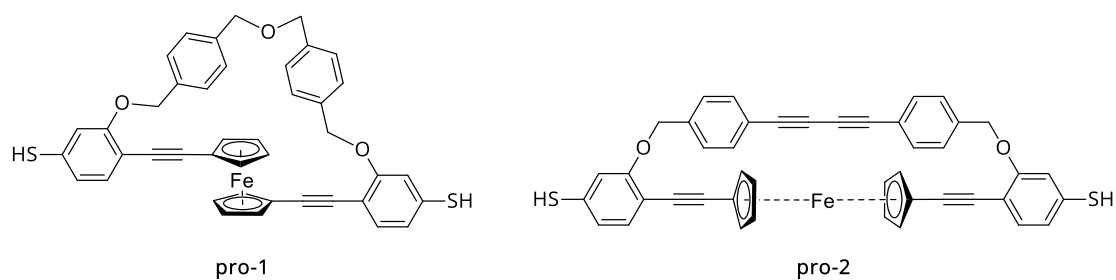
FIGURE 44 Prospect molecules for shorter and rigid molecular wires.

CHAPTER 3

DELTOID VERSUS RHOMBOID: CONTROLLING THE SHAPE OF BIS-FERROCENE MACROCYCLES BY THE BULKINESS OF THE SUBSTITUENTS
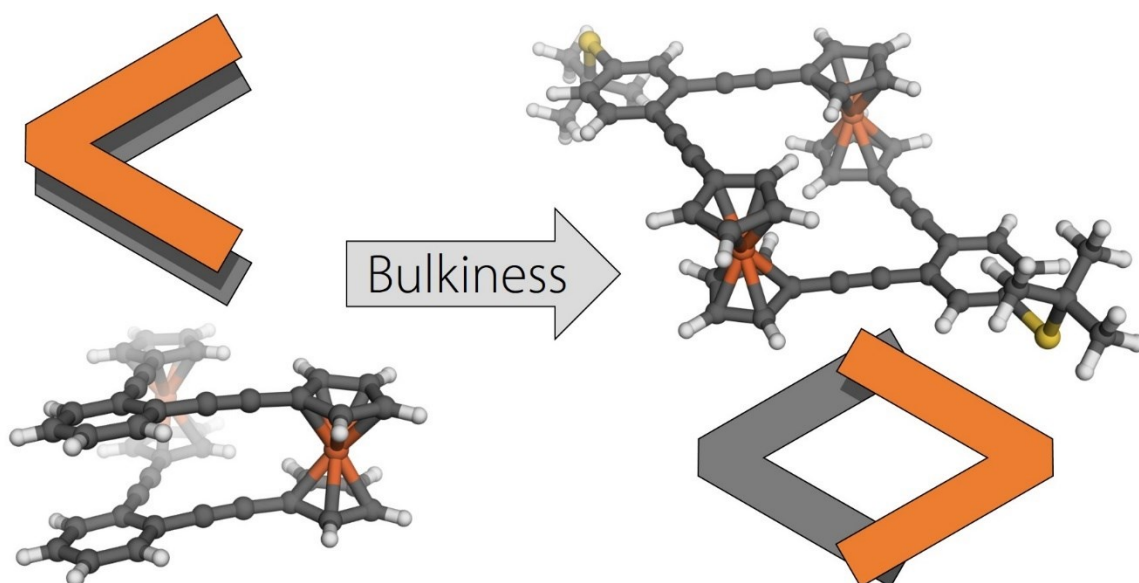
INTRODUCTION

MOLECULAR ELECTRONICS PARADIGM

Single-molecular electronics are an emerging frontier of research that frequently register substantial progress for 40 years. Steady improvement yields a deeper insight on what is required on the molecular side. This paradigm originates a high diversity of prospect molecules to be contacted in single molecular probing setups. They all are targeted to increase the functional density in circuits. Naturally such a progress generates very interesting and sometimes complementary approaches in terms of function principle.

Today, integrated circuits operate on *Complementary Metal-Oxide Semiconductor* (CMOS) technology that have been produced by electron beam lithography techniques. Without doubt, physics will set the boundary to this technology and further miniaturization following Moore's law will be limited. Already 40 years ago the scientific community has realized this issue, and therefore proclaimed a paradigm change.[82]

Consequently, new concepts need to be developed that are not exclusively based on "classical" CMOS technology. In the past decades, scientists have made great progress in designing hybrid semiconductor-molecular electronic ("CMOL") integrated circuits.[151–154] CMOL circuits are meant to be symbiotic constructs of well-established CMOS architectures with nanometer-sized molecules as functional units or connecting nanowires. Such applications aiming on a high functional density of devices on a circuit, employed in digital memories, logic circuits or neuromorphic networks[155,156]. For example, the CMOL concept is nicely demonstrated by the construction of a basic computer, consisting of circuits with carbon-nanotube FETs[157] that are build and implemented on a silicon platform (**FIGURE 45**). What makes this approach even more appealing, is that the employed fabrication and design techniques can be integrated into today's semiconductor fabrication facilities. On the other hand, the CMOL approach require high defect tolerance, due the size difference between the compartments. Nevertheless, there is strong indication that CMOL technology will dominate the field of nano-electronics for the next (few) decade(s)[158].

While CMOS transistor miniaturization will face a dead end from the lithographic point of view, further, device shrinking is accompanied with quantum effects and high power dissipation that will eventually render this technology inefficient. In this regard Craig Lent stated in a perspective article on molecular electronics that "If present transistors could be magically shrunk to the size of single molecules, a chip with phenomenal device density could be fabricated, but such a chip would melt as soon as it was turned on from the heat it generated"[159]
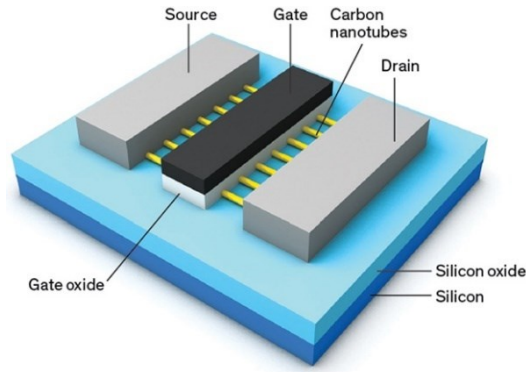
FIGURE 45 Schematic architecture of a CNFET build on a Silicon platform. Illustration from Jean-Luc Fortier, reprinted from IEEE Spectrum[160]

QUANTUM CELLULAR AUTOMATA

An alternative access towards molecular devices and circuits is the quantum-dot cellular automata (QDCA) paradigm, which was devised in the early 1990s by C. S. Lent and co-workers at Notre Dame University.[161] The concept has been derived by the classical cellular automaton paradigm, first proposed by von Neumann and Ulam, in the mid of 20th century[162]. Lent and co-workers envisaged to draft circuits and whole computing architectures based on QDCA arrays. A QDCA cell consist of at least four quantum dots that contain n/2 charges at antipodal positions in the cell. The two possible polarization states of the cell encode a binary logic '0' or '1'. If cells are brought in close proximity, the cell state can be influenced by the neighboring cell through Coulomb repulsion. Circuits would consist of an array of quantum-dot cells that are arranged properly to form wires, inverters and fulfill basic logic tasks, such as gating or data storing[163–165] (**FIGURE 46**). According to the authors, the possible technological benefits seem to be "revolutionary", as the QCA approach make ultra-high density computing possible, while being extremely power efficient as the computing is done with no current flow at the ground state of the molecule.
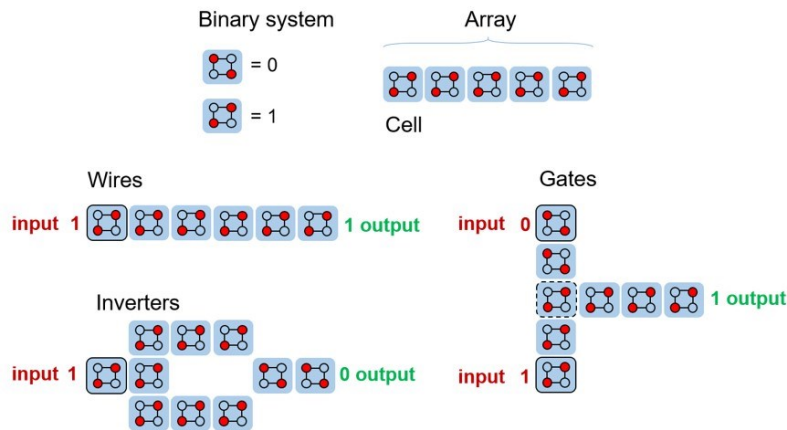
FIGURE 46 Top) cartoon is a schematic constitution of a QCA array, consisting of individual cells. Examples for wires, inverter and a "or" logic gate. The cells in darker squares are fixed to the input states. The cell in the dashed square is biased slightly toward the '1' state.

Aside from sheer hypothesis, the same authors have demonstrated the experimental realization of a functional cell with four metal dots for a quantum-dot cellular automata device.[166] The aluminum islands (60 by 60 nm square) were immobilized on an oxidized Si substrate by electron beam-lithography, and single electron transfer between the dots was achieved at cryogenic temperatures.

MOLECULAR QUANTUM CELLULAR AUTOMATA

While the experimental results were proving the conceptual rightness of the QDCA approach, a *molecular quantum cellular automata* (MQCA) interpretation would facilitate function at ambient temperatures. As one interpretation of such an approach, Qi et al. presented a vertically oriented two-dot MQCA that was bound on a Si surface. The authors could demonstrate the switching between ethynyl ferrocene and the Ru(II) complex, depending on the applied electric field (**FIGURE 47**).[167]
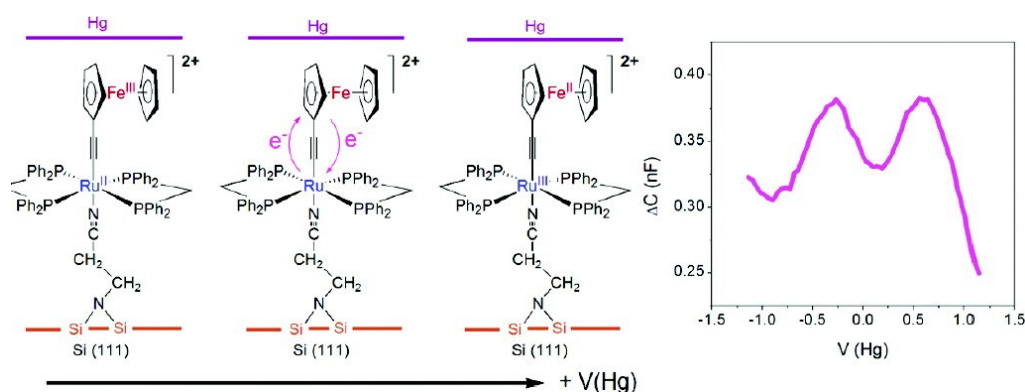
FIGURE 47 Oxidation of the bi-nuclear complex as a function of applied voltage that demonstrates the MQCA switching by an electric field. Reprinted from Qi et al.[167] Copyright © 2003, American Chemical Society.

The group of Fehlner, designed a di-mixed-valence metal complex consisting of two ferrocenes and two ferrocenium units linked to a cobalt(II) metallocene center (**FIGURE 48** a).[168] The dicationic four-dot square cell of a symmetric mixed-valence complex, can be organized in an array to form logic majority gates as depicted in **FIGURE 48** b. According to VT-Mössbauer and paramagnetic NMR spectroscopy, the charge localization, electron coupling and electron exchange properties are adequate to employ the structure as a molecular QCA building block. A similar approach, utilizing four interlinked iron bis-bipyridyne complexes was realized by Schneider et al.[169] in 2013. Both strategies suffer from missing linkage points to immobilize the molecules on a surface, which is a key requirement for the realization of a functional MQCA arrays. The predominant use of transition metal atoms emphasizes the preference and high potential, the community attribute to these structures for MQCA applications.
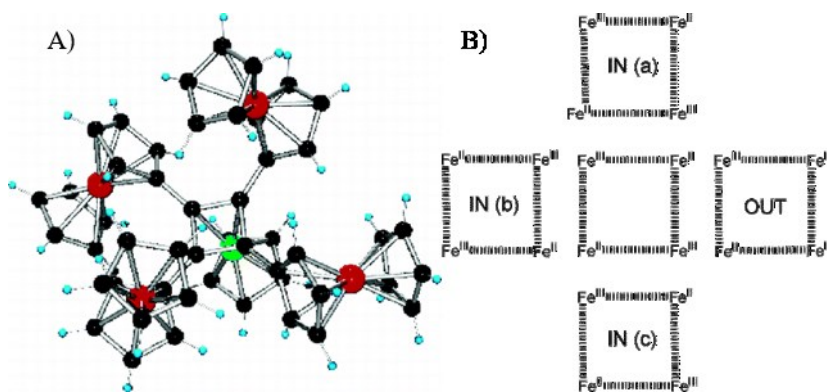
FIGURE 48 a) Molecular structure of four-dot cell b) schematic drawing of majority gate based on five cells. Reprinted with permission from Fehlner et al.[168] Copyright © 2005, American Chemical Society.

To recall the essentials of this paradigm, it is imperative to establish bi-stability with a localized charge and decorate the intended MQCA cell with an anchor group(s), in order to immobilize the cells on a substrate. Furthermore, it is required to arrange the molecules in a way that neighboring cells can interact electrostatically. An interesting approach to that issue is met in a recent proposal of Arima et al.[170]. The authors employed a carbazole linked bis-ferrocene that additionally bears an aliphatic thiol linker to contact a gold surface. The envisioned MQCA array would consist of two molecules per cell, with charge containers at the corners (**FIGURE 49** a). (It should be noted that the authors did not stated how the cells will be brought in their orientation). The cell encodes a binary state of '1' or '0' that could be set to 'Null' upon an applied clocking field. Neighboring cells should interact electrostatically and respond to the input cell by changing its value to the inverse. To assess the applicability, electrochemical properties of bis-ferrocene **67** in solution and in a solid-state film were investigated and compared with DFT calculations. The cyclic voltammetry (CV) of bis-ferrocene **67** showed a single two-electron redox event at $E_{1/2}$ = 0.35 V, in CH_2Cl_2/n-Bu_4NPF_6. The absent wave splitting approves the computational result that the electronic communication between the redox centers is negligible. Sadly, the authors did not perform CV experiments with weakly coordinating electrolytes that proof the electrostatic communication of the redox centers. However, their calculated results support that assumption. **FIGURE 49** b), illustrates the calculated charge localization whereat it is claimed that the compound exhibits a non-linear field polarization response. This is a very important feature, since charge propagation should be instant in MQCA arrays. STM measurements of self-assembled monolayers of racemic **67** and hexane-1,6-dithiol on Au(111) substrates (**FIGURE 49** c) revealed that even though the anchoring group is capable of attachment, the distribution is arbitrary and request patterning techniques to assemble the molecules in an aligned and controlled fashion. Moreover, the used mixture of diastereomers of **67** and the high flexibility of the ferrocene groups lead to irregular topologies of the SAMs (**FIGURE 49** c).
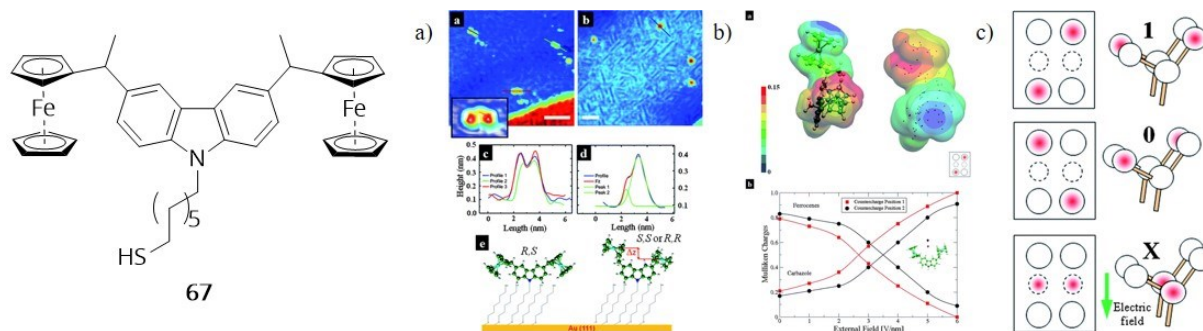
FIGURE 49 a) Schematic six-dot cell representation which allows three states, depending on charge localization; b) calculated electrostatic potential surface with a diagonal polarization and charge density at applied directed field; c) STM image and schematic representation of the height profile of the molecules. Reprinted permission from Arima et al. [170] Copyright © 2011, Royal Society of Chemistry.

This renders Arimas' approach limited in its applicability due to the conceptual design of the bis-ferrocene structure as the effective intra- and intermolecular coulombic antenna. The operative interaction is hampered by the varying ferrocene orientation. To exploit the properties of multi-ferrocene structures, it is necessary to understand their intrinsic behavior regarding their spatial separation and oxidation state.

ELECTRONIC AND ELECTROSTATIC COUPLING IN MULTI-FERROCENE COMPOUNDS

In 2011, the group of Astruc systematically investigated the electronic and electrostatic interaction between equivalent ferrocenyl groups in a molecule by cyclic voltammetry (CV).[171] By choosing the electrolyte media, either the electronic coupling or through-space electrostatic interaction between the redox sites can be investigated. Strong ion-pairing between the electrolyte anion (such as PF_6^-) and the oxidized cationic species, leave very little electrostatic communication between two equivalent redox centers. If a splitting in the CV wave of two equivalent redox centers is observed, the splitting roughly correlates to the electronic communication through a conjugated bridge. When a weakly coordinating anion such as tetrakis[3,5-bis(trifluoromethyl)phenyl]borate (BARF) is used, a through-space electrostatic effect may be visualized by the separation of the CV wave.

This was demonstrated by the following examples: Ferrocenes, directly connected to a central benzene unit only show electronic communication when they are conjugated via a *para*-substitution (compare structure **68** & **69** and corresponding half-wave potentials, **FIGURE 50** and **TABLE 9**), while the all *meta*-substituted 1,3,5-triferrocenylbenzene **68** had an absent wave splitting when n-Bu$_4$NPF$_6$ is employed as supporting electrolyte.
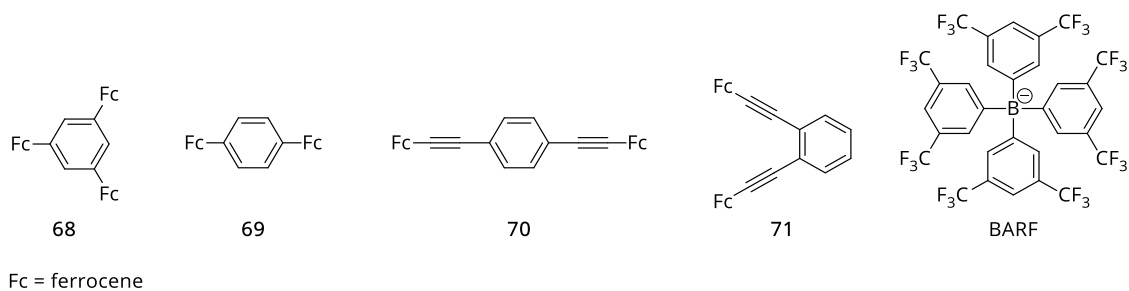
Fc = ferrocene

FIGURE 50 Selected bis- and tri-ferrocenyl compounds with different substitution patterns and the structure of BARF.[171]

On the other hand, both compounds showed substantial electrostatic interaction, within the equivalent redox centers when n-Bu$_4$NBARF is employed as supporting electrolyte. When the respective redox centers are further separated via multiple bonds, the electronic communication becomes insignificant (compare structure **70** & **71**, **FIGURE 50** and **TABLE 9**), while the electrostatic coupling is depending on the spatial separation.

TABLE 9 CV half-wave potentials of respective bis- and tri-ferrocenyl compounds with different supporting electrolyte in CH$_2$Cl$_2$. Reprinted from Diallo et al.[171]

Structure	$E_{1/2}$ in [V][a]	$E_{1/2}$ in [V][b]
68	0.68	0.62, 0.79, 0.98
69	0.54, 0.62	0.59, 0.80
70	0.68	0.75
71	0.68	0.72, 0.87

[a] in DCM with n-Bu$_4$NPF$_6$; [b] in DCM with n-Bu$_4$NBAr$^F_4$

Yet, another effect is accompanied with the translational variability of attached ferrocenyl groups. As depicted in **FIGURE 51**, ferrocenyl groups adopt opposing sides of a benzene ring, in order to minimize the Coulomb repulsion. This effect is called frustration and is especially pronounced when the dicationic or multiple chargerd form is present. Accordingly, bis-ferrocene **72** showed a lack of electronic and electrostatic interaction that renders the ferrocenyl groups independent, due to the frustration effect. If a third charge carrier was introduced (as in **73**), the CV experiment revealed three consecutive one-electron redox waves, displaying the electrostatic interaction between them.
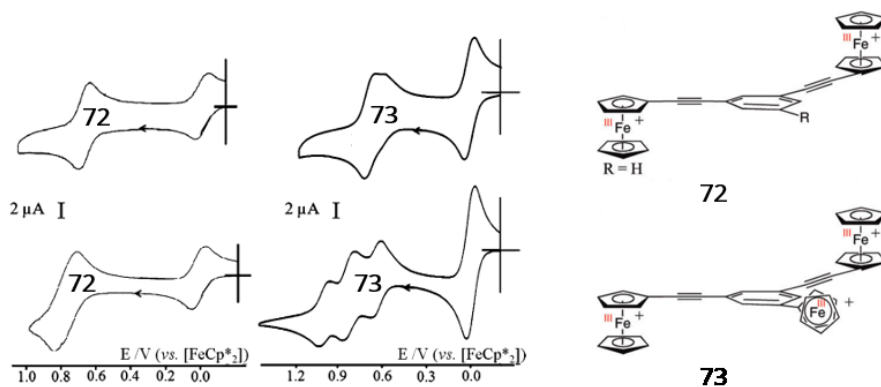
FIGURE 51 Comparison of the CVs of the *meta-* disubstituted and trisubstituted complexes of **72**, respectively, **73** showing the lack of electronic (with n-Bu$_4$NPF$_6$, top left) and electrostatic (with n-Bu$_4$NBArF$_4$, bottom left) interaction in **73** and the lack of significant electronic (with n-Bu$_4$NPF$_6$, top right), but electrostatic interaction (with n-Bu$_4$NBArF 4, bottom right) in **73**. Solvent: DCM; internal reference: Fc/Fc$^+$, Reprinted from Diallo et al.[171]

This phenomenon was also observed by comparing dendrimers with flexible tethers and rigid star shaped hexa(ferrocenyl)-arenes in terms of electron-transfer mechanisms and electrostatic effects. Furthermore, they observed a weak electrostatic coupling when structures, with long flexible tethers were used. In contrary, shorter rigid structures showed considerable electrostatic coupling.

In conclusion, spacing and orientation of the redox sites is ultimately displayed in the electrostatic and electronic communication of the individual units. However, effective intra- and intermolecular Coulomb interaction is hindered by varying ferrocene orientation as shown in the previous examples. Precise control over the spatial and relative orientation of the redox sites is a key prerequisite to construct molecules with electrostatic coupling. Yet, the field lacks from applicable structures, mainly due to the absence of suitable anchoring groups that facilitate an immobilization on a surface.

AIM OF THIS WORK

Precise construction of discrete and shape persistent ferrocene macrocycles is very challenging, as the high rotational mobility along the Cp-Fe-Cp axis permits many alterations. Owing to its extensive use in numerous areas of applied sciences, we became interested in the structural control over the embodied ferrocene units as part of the functional application. A macrocycle with two ferrocene units will increase the structural variation problematic, but on the other hand gives access to potentially mixed-valence compounds with exciting intramolecular redox properties. To minimize the structural diversity and to maximize the extent of Coulomb interactions between both ferrocene subunits, bis-Fc macrocycles consisting of small and rigid scaffolds moved into the focus of our interest. This motivated us to envisage the synthesis of macrocyclic bis-ferrocene **74** (**FIGURE 52**) with a rigid molecular backbone, unable to avoid the electrostatic repulsion when doubly oxidized. The C_i symmetric bis-ferrocene **74** further exhibits an electronic directionality for the *para*-substituted ferrocene units compared to a *meta*-substituted pair. This provides an independent addressability of the redox centers along the substitution axis. Thiol anchoring groups at antipodal positions of the molecule can form gold contacts in break junction experiments and further give access to investigate the structure-property relationship as a function of the applied potential. We were able to present the results in the scientific journal *"Organometallics"*.[172]
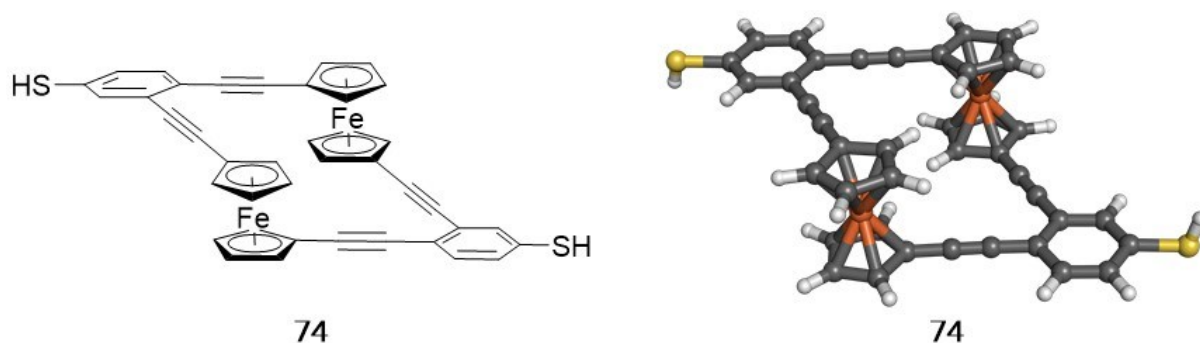
FIGURE 52 The synthetic goal of the project is a rhomboidal shaped bis-ferrocene macrocycle with antipodal thiol anchoring groups.

STRATEGY

From previously conducted experiments on the coupling of *ortho*-substituted bis-ethynylphenyl-ferrocene **75** with 1,1'-diiodoferrocene **22** we knew that the intramolecular oxidative homocoupling to form strained buta-1,3-diyne **76** is favored over the intermolecular cross-coupling to form bis-ferrocene **77** (**SCHEME 37**).[60] This led us to conclude that a stepwise repetitive coupling and deprotection strategy is inevitable to incorporate a second ferrocene functionality in a molecular backbone as shown in **SCHEME 38**.
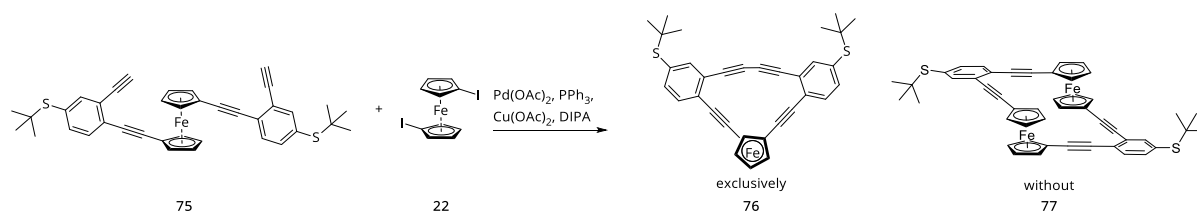
SCHEME 37 Attempts to form bis-ferrocene **77** exclusively gave the strained intramolecular reaction product **76**.

To assess this concept, we were first considering a model system that resembles the geometric identity of our target compound, while it is accessible in less synthetic effort. For this purpose, the unsubstituted phenyl analog of target structure **74** seemed appropriate. The assembly of the macrocycle and their precursors is based on a combination of acetylene scaffolding strategies[68] and the well-developed *Sonogashira*-type coupling chemistry with ferrocene building blocks.[73,128,173–175]

The first disconnection is the key step of the synthesis and made at one of the equivalent ferrocene-ethynyl single bonds in **78**. This is imperative although not appealing, but as we have seen that a statistical intermolecular approach yields a cyclic buta-1,3-diyn (**76** in **SCHEME 37**). Selective deprotection and coupling of the second ferrocene unit **R-6** will hence be the better choice.
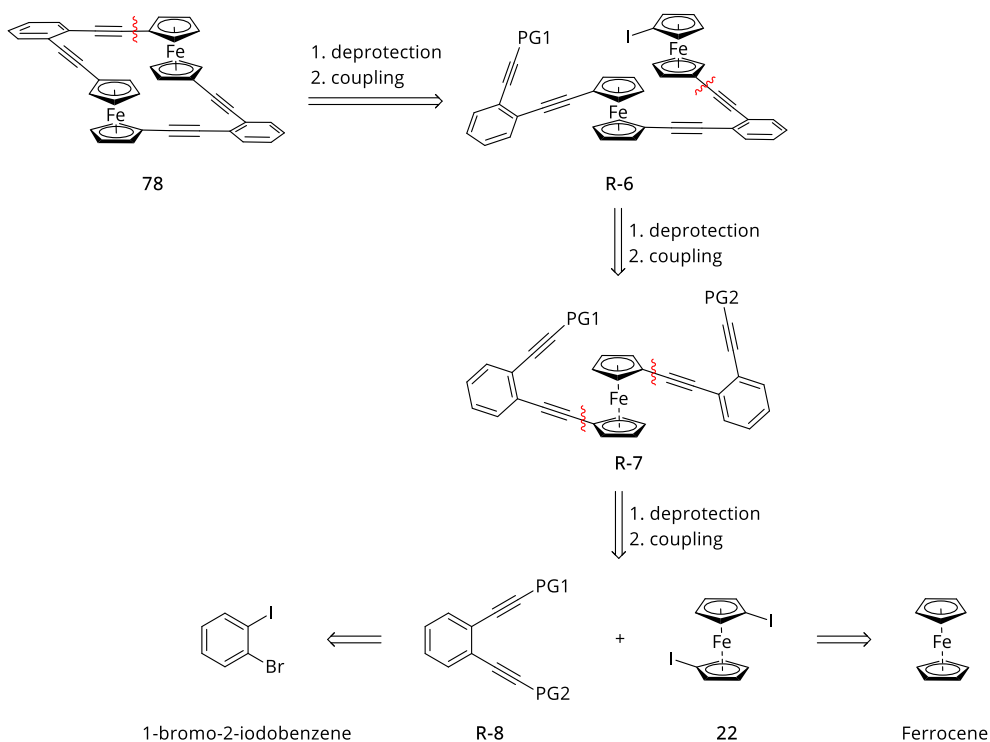
SCHEME 38 Retrosynthetic analysis of the model system.

Preferably, PG1 bears a higher polarity and can be dragged through the complete synthesis. Two consecutive coupling reactions with the corresponding bis-ethynylphenyl building block **R-8** will give the intermediate **R-7**. Therefore, orthogonally protected acetylene functionalities need to be installed and selectively removed. Building block **R-8** can be made by *Sonogashira* coupling of the corresponding acetylenes and 1-bromo-2-iodobenzene. 1,1'-diiodoferrocene **22** is accessible via two reaction steps in decent yields from ferrocene.

RESULTS AND DISCUSSION

SYNTHESIS PART 1

Following the outlined repetitive and straight forward strategy in assembling the molecular model structure **78**, the synthetic effort began as shown in **SCHEME 39**. 1,2-diethynylbenzene **79** was prepared by twofold palladium-catalyzed *Sonogashira* coupling of 1-bromo-2-iodobenzene with 2-methyl-3-butyn-2-ol and (triisopropylsilyl)acetylene. Thereby, the chemoselectivity of iodide over bromide in Pd[0]-catalysed cross-coupling reactions was exploited. The introduction of polar protected acetylenes is beneficial for the chromatographic purification. Removal of hydroxypropyl (HOP) gave **80** in 52% yield, using a 1 M solution of TBAOH in toluene at 80 °C, following Huang's protocol[69]. Alternatively, sodium hydride can be used for that purpose, but requests refluxing toluene at longer reaction time. Triisopropylsilane was cleanly removed after treating **79** with a 1 M TBAF solution in THF for 30 min. at room temperature to give **81** in 99% yield. Further, we found that the storage of the free acetylene was troublesome, as it forms buta-1,3-diyne dimers upon exposure to air. Thus, we used freshly deprotected building block for functionalization.
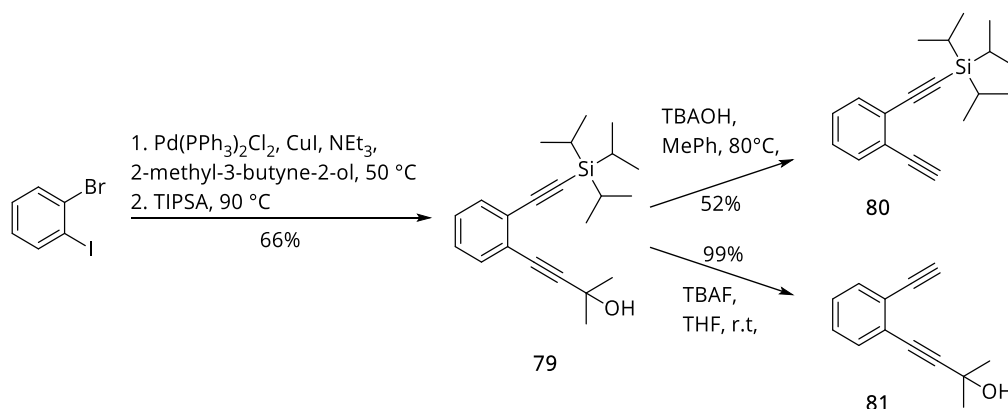
SCHEME 39 Synthesis of orthogonally protected building blocks **80** and **81**.

As in the previous chapters, we utilized the palladium/phosphine couple elaborated by Inkpen et al.[73,176]. However, for this synthetic work we changed to the corresponding air-stable trialkylphosphonium salt[177], as it showed comparable or better results (**TABLE 10**) while the handling and storage of the phosphonium salt is more convenient. Thus, we generally employed Pd(MeCN)$_2$Cl$_2$/[(t-Bu)$_3$PH]BF$_4$/CuI (1:2:1) in a freshly distilled and deoxygenated THF/DIPA mixture at 60 °C for 12 h. The reaction could be controlled via the ratio of acetylene:FcI$_2$. Using stoichiometric amounts of FcI$_2$ favors the mono-substituted product **82**, while a 3-fold excess of acetylene clearly pulls the outcome to the di-substituted product **83**. Due to the substantial polarity difference in **82** and **83**, the product mixture could easily be purified via flash column chromatography (FCC) on silica gel. 1-(phenylethynyl)-1'-iodoferrocene **82** was isolated as red oil, while **83** was an orange solid.
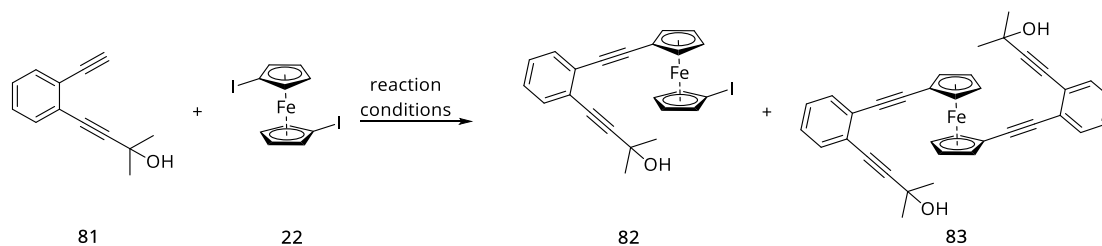
TABLE 10 Isolated yields of *Sonogashira* coupling of **81** and FcI$_2$.[a]

entry	**81**	FcI$_2$ (**22**)	phosphine	**82**	**83**
1	1 eq.	1 eq.	P(t-Bu)$_3$	27%	-
2	1 eq.	1.15 eq.	[(t-Bu)$_3$PH]BF$_4$	42%	15%
3	3 eq.	1 eq.	[(t-Bu)$_3$PH]BF$_4$	23%	47%

[a]Pd(MeCN)$_2$Cl$_2$ (6 mol-%), CuI (6 mol-%) and the respective phosphine (12 mol-%) were heated to 60 °C in a 1:3 mixture of DIPA/THF for 12 h.

Following the synthetic strategy to build up the molecular backbone in a stepwise manner, we attached the orthogonally protected ((2-ethynylphenyl)ethynyl)-tri-isopropylsilane **80** at the mono-functionalized ferrocene **82**, using a two-fold excess of the acetylene (see **SCHEME 40**). Subsequent removal of the TIPS group using a 1 M TBAF in THF at room temperature, according to standard procedure, gave the unsymmetric building block **85** in 48% over two steps. This pathway seemed to be inevitable, until we tried to statistically remove the HOP group. By using stoichiometric quantities of base and shorter reaction times, we could control the reaction and steer the output towards the product **85**. The reaction progress was monitored via TLC and stopped after no more starting material was observed, by pouring the cooled mixture on a saturated NH$_4$Cl solution. The product **85** was isolated after column chromatography as orange solid in 60%. As for the previous intermediates of terminal acetylenes it was necessary to perform the deprotection shortly before further coupling, as they tended to oxidatively dimerize upon standing even at temperatures below 4 °C and inert atmosphere. Hence, we routinely sonicated our glassware for 5 min. with sulfuric acid and 1 M NaOH, prior of deprotection and storing.
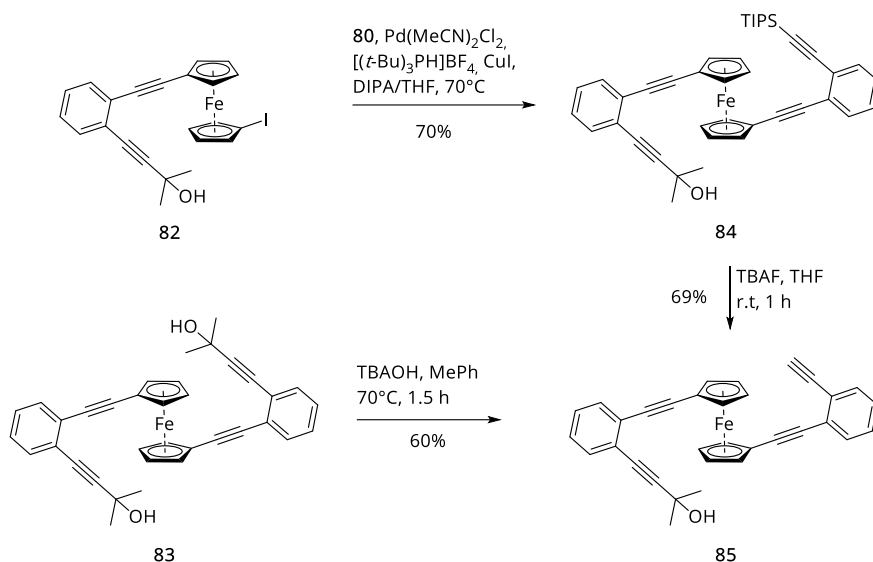
SCHEME 40 Two possible reaction pathways to the asymmetric acetylene **85**.

With the intermediate **85** in hand we were able to perform the subsequent *Sonogashira* reaction, utilizing the established conditions but with a 5-fold excess of FcI₂ that gave bis-ferrocene **86** in nearly 40 % yield (**SCHEME 41**). Despite extensive precaution of excluding all air from the reaction mixture, we could not prevent the formation of homo-coupled acetylene as a side product. We ascribe this formation to the activation cycle of the reactive Pd(0) species. Clean removal of the HOP protecting group was monitored after 2.5 h of treatment with 1 M TBAOH solution in degassed toluene at 70 °C. Acetylene **87** was isolated as orange solid in 84% yield. According to MALDI-TOF spectrometry, deprotection at 110 °C in toluene, afforded a side product with a m/z of 616 that is the molecular mass of target compound **78**. Out of curiosity, we repeated this procedure with elevated temperature, and indeed, we could isolate the pale orange solid with the product mass in poor 10% yield, plus that of the dehalogenated adduct with an m/z of 618 (**FIGURE 53**). We assume that the high temperature in combination with trace metal form the glassware, facilitate a nucleophilic substitution reaction forming the cyclic adduct.

To complete the outlined synthesis, we conducted the intramolecular *Sonogashira* reaction of compound **87**, in a 1.5 mM solution of DIPA/THF (1:3), and heated the reaction mixture to 60 °C for 12 h. After filtration over a short plug of celite, FCC and size exclusion chromatography we could isolate a poorly soluble pale orange solid, in 29% yield. One- and two-dimensional NMR spectroscopy suggested that only one species is prevalent. Crystals were grown by slow solvent evaporation from methylene chloride. The identity of **88** was revealed by the solid-state structure obtained by X-ray crystallography (**FIGURE 54**). To our surprise, crystal structure of both, the isolated product from the deprotection and the intramolecular cyclization product gave the stacked, deltoid conformer **88** and not the initially proposed anti- oriented conformation of **78**.
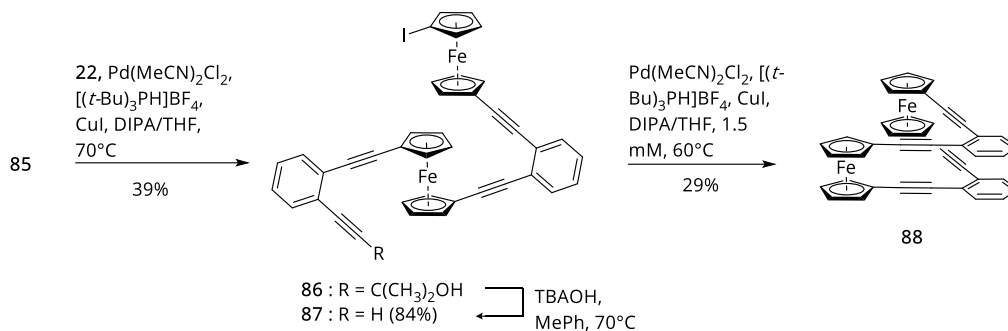
SCHEME 41 *Sonogashira* reaction with FcI₂, deprotection and intramolecular cyclization reaction formed the deltoid conformer **88**.
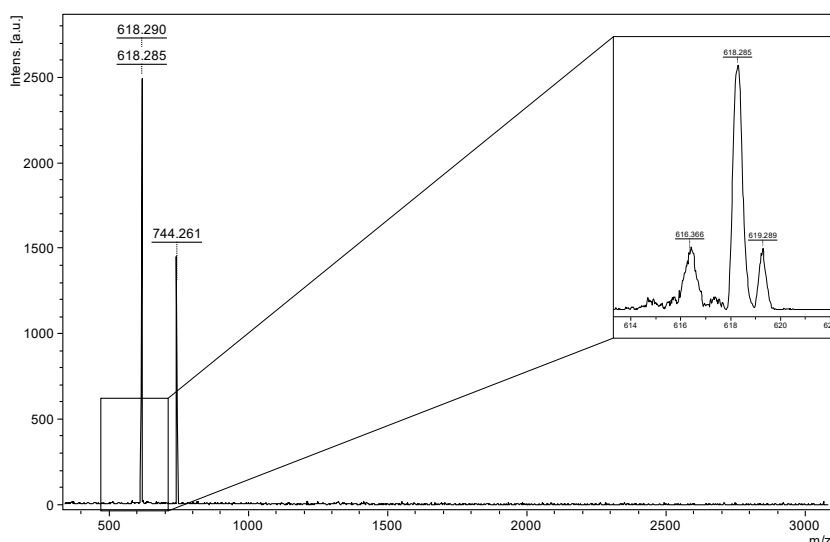
FIGURE 53 MALDI-ToF reaction control of deprotection with TBAOH in toluene at 110 °C after 3 h reveals the formation of the product **88** with a m/z of 616 amu and the dehalogenated analog with a m/z of 618 amu.

SOLID-STATE STRUCTURE

Diffraction-quality single crystals of bis-ferrocene **88** were grown by slow solvent evaporation of CH_2Cl_2 at ambient temperature. X-ray crystallography unambiguously resolved the structure displayed in **FIGURE 54**. Bis-ferrocene **88** has C_2 symmetry and resembles a deltoidal shaped molecule. The enclosed shank angles with deviations close to ideal are of 61.01° and 66.13°, respectively. This is caused by one ferrocene unit that is inclined with respect to the aryl plane by ~ 7°, while the other ferrocene is nearly in plane. Iron centers being almost coplanar, based on Cp centroid⋯Fe1⋯Fe2 enclosed angle of 89.32°, and separated by 7.116 Å only. The interplanar phenyl distance of 3.577 Å is slightly longer than the Cp-Cp distance (3.311 Å) that suggest considerable π-π interactions.
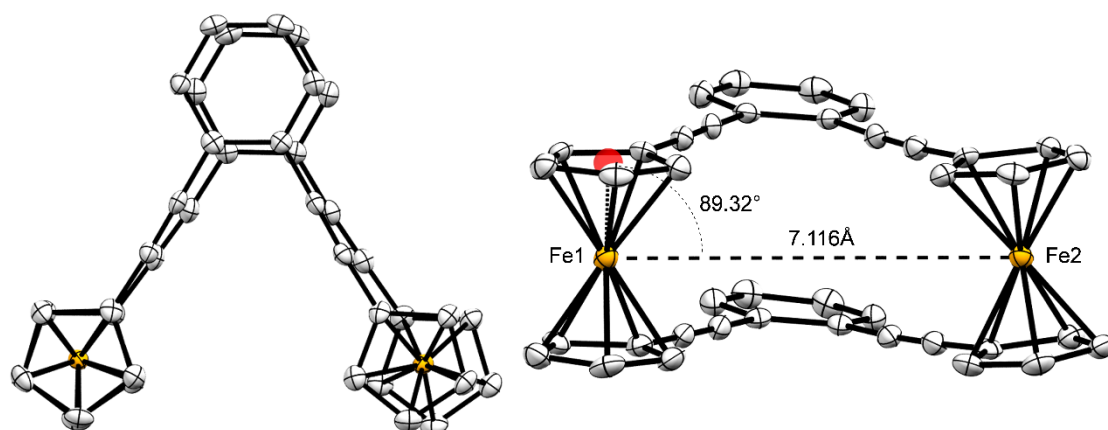
FIGURE 54 ORTEP plots of the solid-state structure of deltoid **88** with ellipsoids plotted at the 50% probability level.

The packing order of crystal structure **88**, reveals 4 molecules per unit cell (**FIGURE 55** and **FIGURE 56**) that are oriented perpendicular in an altering sequence, where two opposing molecules have parallel planes with a separation of roughly 3.23 Å.
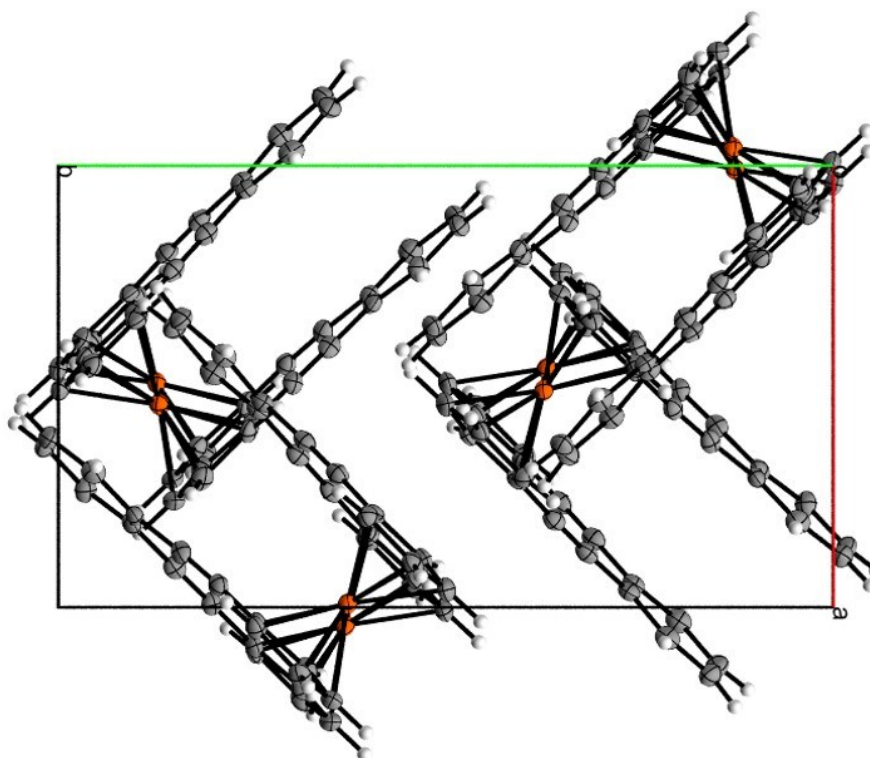
FIGURE 55 Orthorhombic unit cell of **88** with 9.3 Å x 15.9 Å x 18.3 Å cell length, where molecules being perpendicular oriented in an altering sequence. View along the C axis.
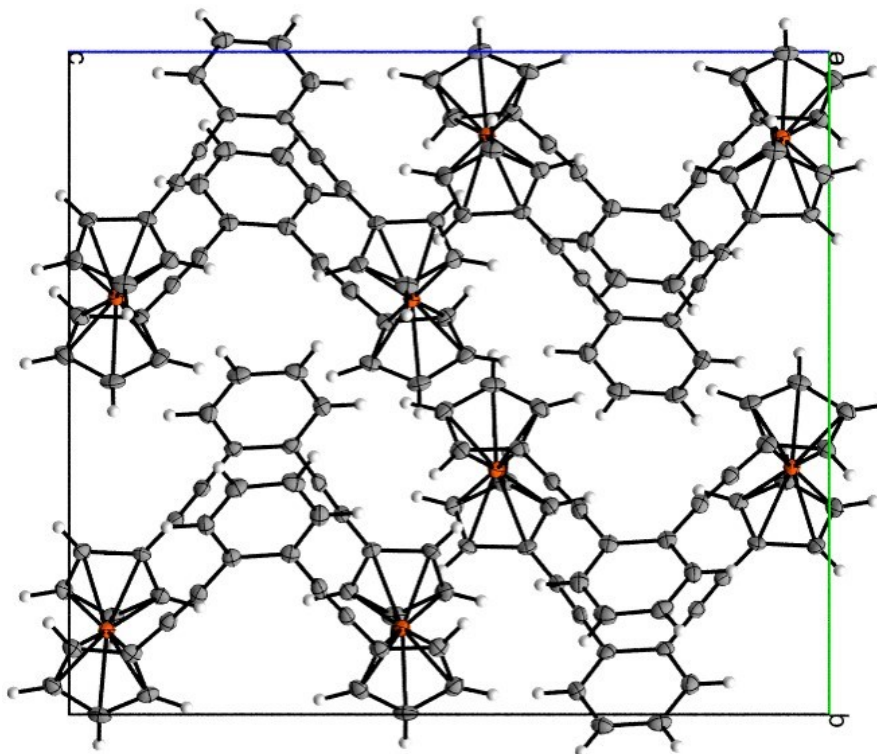
FIGURE 56 High packing order of **88** with the view along the A axis.

SYNTHESIS PART 2

We attribute the exclusive formation of deltoid **88** to the free rotation around the Cp-Fe-Cp axis and attractive π-π interactions between the phenyl rings and their influence and stabilization on transition states over the course of the bond formation (**SCHEME 42** left side). It is known in literature that free rotational motion along the ferrocene axis facilitates the formation of stacked conformers by π-π interaction of the opposing substituted rings.[128,178–180] Our result implies that an intrinsic determinant is imperative when the complementary result is wanted. We concluded that the introduction of bulky aliphatic groups (R in **SCHEME 42**) such as trityl, adamantyl or *tert*-butyl destabilizes the aromatic stacking interaction and increases the rotational energy barrier of the Cp rings around the coordination axis (**SCHEME 42** right side).[125] The comparable spacing between both phenyl rings and the Cp rings in the solid state structure of **88** suggested that substituents of comparable dimensions should be bulky enough to disfavor the syn-arrangement and steer the ring-closing reaction towards the rhomboidal anti- conformation.
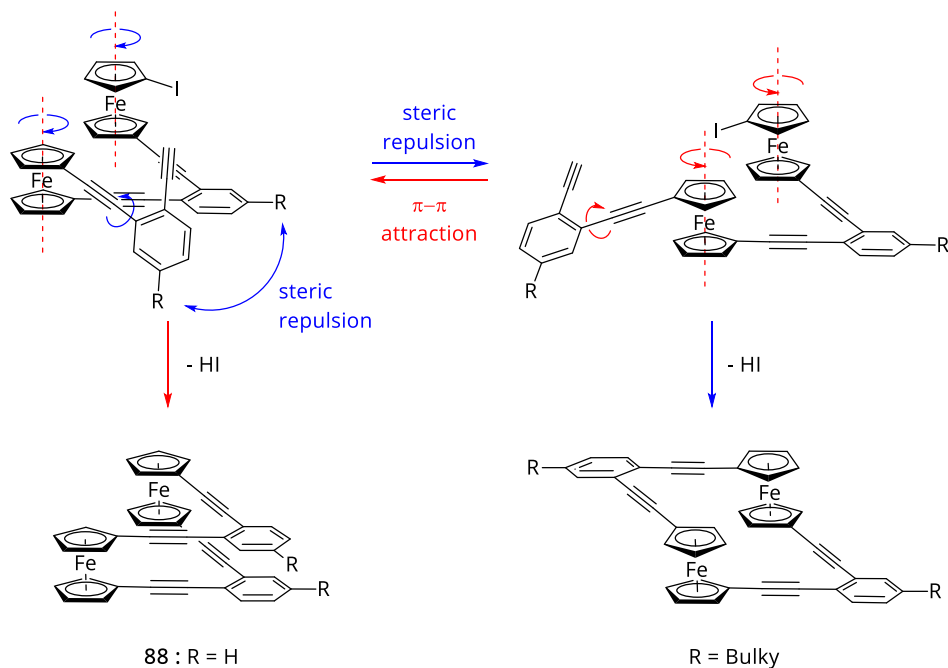
SCHEME 42 Free rotation around the ferrocene axis facilitates the deltoid **88** formation with two opposing planes, while introduction of bulky aliphatic groups destabilizes the aromatic stacking interaction and increases the rotational energy barrier of the Cp rings that leads to the opposite.

Consequently, we envisaged the phenyl building block to be decorated with very bulky trityl-groups. Not only their steric properties but also the removal seemed to be advantageous, as they are readily cleaved by treatment with trifluoroacetic acid and triethylsilane in DCM at room temperature.[181,182] Therefore, we became interested in an orthogonally protected di-ethynylphenyl tritylsulfane, as main building block. With that in mind, the step-wise assembling strategy could be followed and the bulky protecting groups would facilitate an elongated structure.

We started our efforts with a regioselective oxidative thiocyanation of 2-iodoaniline in *para*-position, using oxone and ammonium thiocyanate (**SCHEME 43**).[183] Aniline **89** could be sublimed in batch scales of up to 15 g in excellent yields. The aniline was then converted in a *Sandmeyer* reaction to the bromo derivate **90**, using anhydrous Cu(II) bromide and *tert*-butyl nitrite[184] in a 5:1 mixture of acetonitrile and methylene chloride. Reduction of the thiocyanate **90** using LAH or alternatively DIBAL gave the crude free thiol that was converted with tritylchloride and aluminum trichloride as Lewis acid in a S_N1 reaction to the tritylsulfane **91** in 85 % yield over two steps.
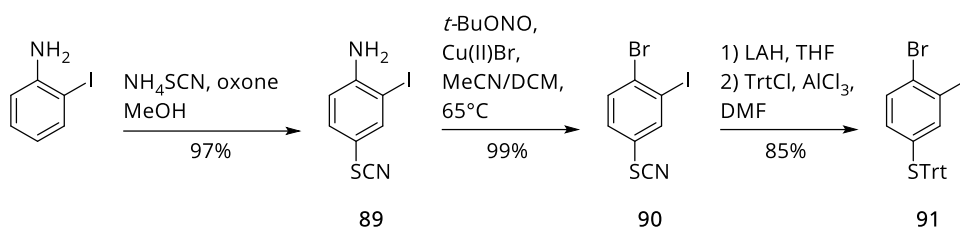
SCHEME 43 Synthesis of building block **91**

We first initiated double-fold one-pot *Sonogashira* reaction attempts, but could only isolate the mono-functionalized compound **93**. We then performed a step-wise approach to justify the reactivity of the substrate. Interestingly, TIPS-protected acetylene could not be introduced, while hydroxypropyl ethynylene was coupled with moderate success (**TABLE 11**). This result suggests that considerable sterically effects of the *meta*-substituted tritylsulfanyl are responsible for the low yield, as the less demanding HOP-acetylene could be introduced.

92 : R = C(CH$_3$)$_2$OH
93 : R = TIPS
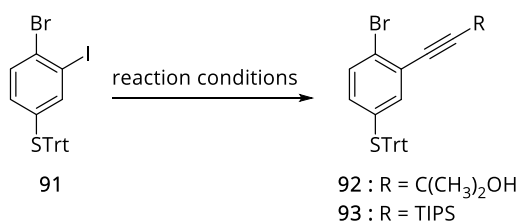
TABLE 11: *Sonogashira* reaction of aryl iodide **91**

entry	acetylene	catalyst	solvent	temperature	yield
1	TIPS-acetylene	Pd(PPh$_3$)$_2$Cl$_2$/CuI	THF/DIPA (3:1)	r.t – 50 °C	-
2	TIPS-acetylene	Pd(PPh$_3$)$_4$/CuI	THF/Et$_3$N (3:1)	r.t – 80 °C	-
3	2-methyl-3-butyn-2-ol	Pd(PPh$_3$)$_2$Cl$_2$/CuI	THF/DIPA (3:1)	r.t	55%

In the second coupling step, we triggered the aryl bromide with TIPS- and TMS protected acetylene (**TABLE 12TABLE 12**). Elongated reaction times and heating in the microwave reactor could not yield either product. We attribute this inaccessibility towards Pd(0)-catalyzed couplings to the deactivating effect caused by the steric and electronic nature of the tritylsulfanyl substituent. Attempts to convert the aryl bromide into an iodide via aromatic *Finkelstein* reaction could not facilitate a halogen exchange.
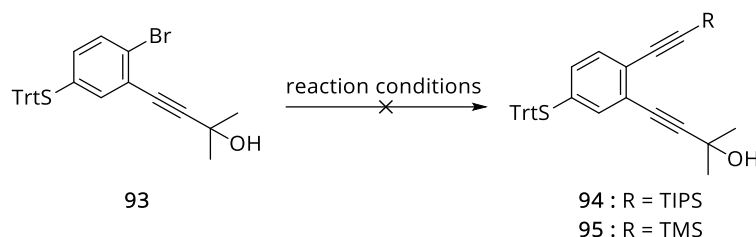
TABLE 12 Sonogashira reaction attempts with aryl bromide **93**.

entry	acetylene	catalyst	solvent	temperature
1	TIPS-acetylene	Pd(PPh$_3$)$_4$/CuI	THF/DIPA (3:1)	80 °C
2	TMS-acetylene	Pd(MeCN)$_2$Cl$_2$/P(*t*-Bu)$_3$/CuI	THF/DIPA (3:1)	80 °C
3	TMS-acetylene	Pd(MeCN)$_2$Cl$_2$/P(*t*-Bu)$_3$/CuI	THF/DIPA (3:1)	110 °C (MW)

We therefore switched to the synthesis of the less bulky *tert*-butylsulfanyl analog **96** depicted in **SCHEME 44**. *Tert*-butyl was introduced via reduction of thiocyanate and *Friedel-Crafts* alkylation of crude thiophenol with 2-chloro-2-methylpropane and aluminum chloride, in 76 % over two steps. Palladium-catalyzed *Sonogashira* coupling with 2-methyl-3-butyn-2-ol and (triisopropylsilyl)acetylene in degassed NEt$_3$ gave **97** in 81%.
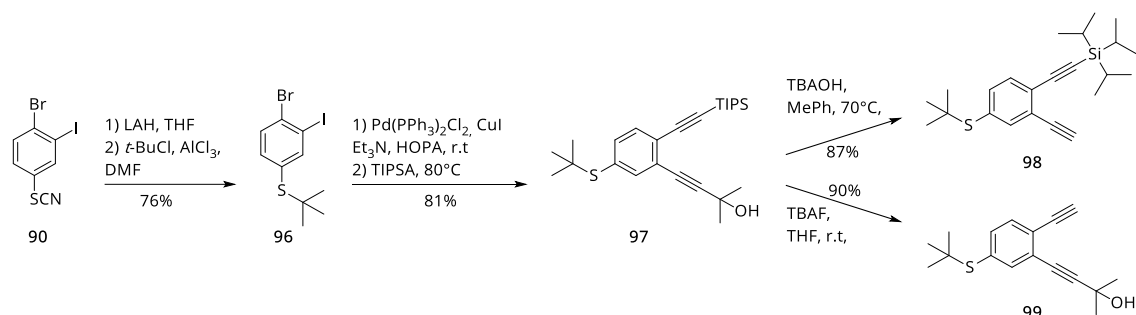
SCHEME 44 Synthesis of building block **98** and **99**.

Orthogonal protection groups allow either removal of triisopropylsilane or hydroxypropyl and consequently control over *para-* or *meta*-addressability of building block **97**. This is also important as double-fold substitution of either acetylene **98** or **99** would eventually lead to a C_2 symmetric rhomboid shaped structure instead of C_i symmetric one, and consequently a structure with both *tert*-butylsulfanyl groups pointing to the same ferrocene unit. Under this premise, the mono-substituted 1,1'-ferrocene **100** is the intended substitution order.
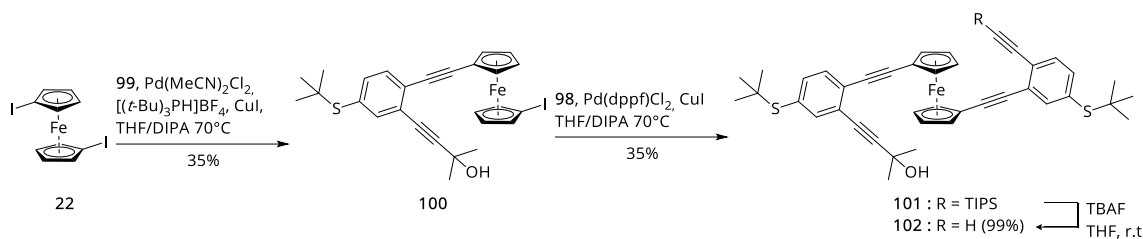
SCHEME 45 Assembly of the rhomboid scaffold by stepwise introduction of the orthogonally protected di-ethynylphenyl building blocks.

For this, we employed Pd(MeCN)$_2$Cl$_2$/[(*t*-Bu)$_3$PH]BF$_4$ and CuI as catalyst system, a 3-fold excess of FcI$_2$ **22** at 70 °C for 12 h (**SCHEME 45**). The mono-substituted iodoferrocene **100** was isolated in moderate 37% yield. In contrast to our prior experience with this catalytic system, the reaction progress was very slow and we observed notable quantities of dehalogenated ferrocene substituent. In the hope to improve the yield, we switched to Pd(dppf)Cl$_2$ with copper(I) iodide and added arylacetylene **98** in a slight excess to a mixture of **100** dissolved in DIPA/THF and heated for 12 h at 70 °C. Although the reaction yield could not be improved (35%), we observed within 60 minutes a considerable product formation by MALDI-ToF mass spectrometry. Desilylation of ferrocene complex **101** was cleanly performed using a 1 M TBAF solution in THF at room temperature and free acetylene **102** was isolated in 99% yield.

We consequently converted the terminal acetylene **102** with a 3-fold excess of FcI$_2$ (**SCHEME 46**). When all starting material was consumed after 1.5 h at 50 °C, bis-ferrocene **103** was isolated after chromatography on silica gel as red solid in 38%. However, considerable quantities (23%) of acetylene **102** were lost in the formation of homo-coupled dimers and oligomers observed by MALDI-ToF (**FIGURE 57**), although the reaction solution was extensively degassed beforehand.
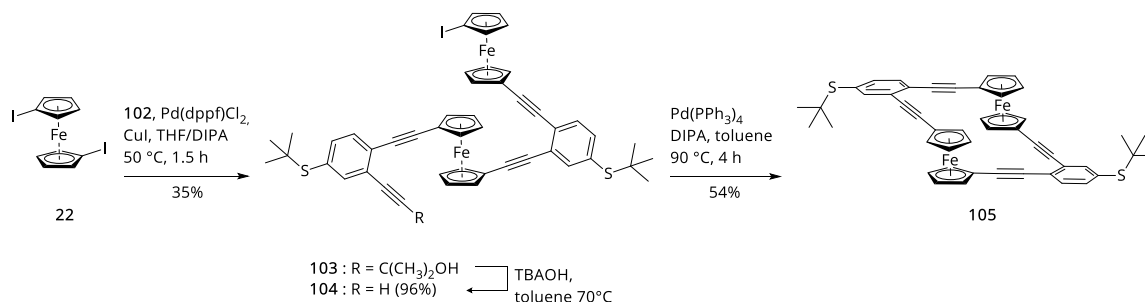
SCHEME 46 Consecutive build up and deprotection formed **104** that was then intramolecularly cyclized to the rhomboid **105**.
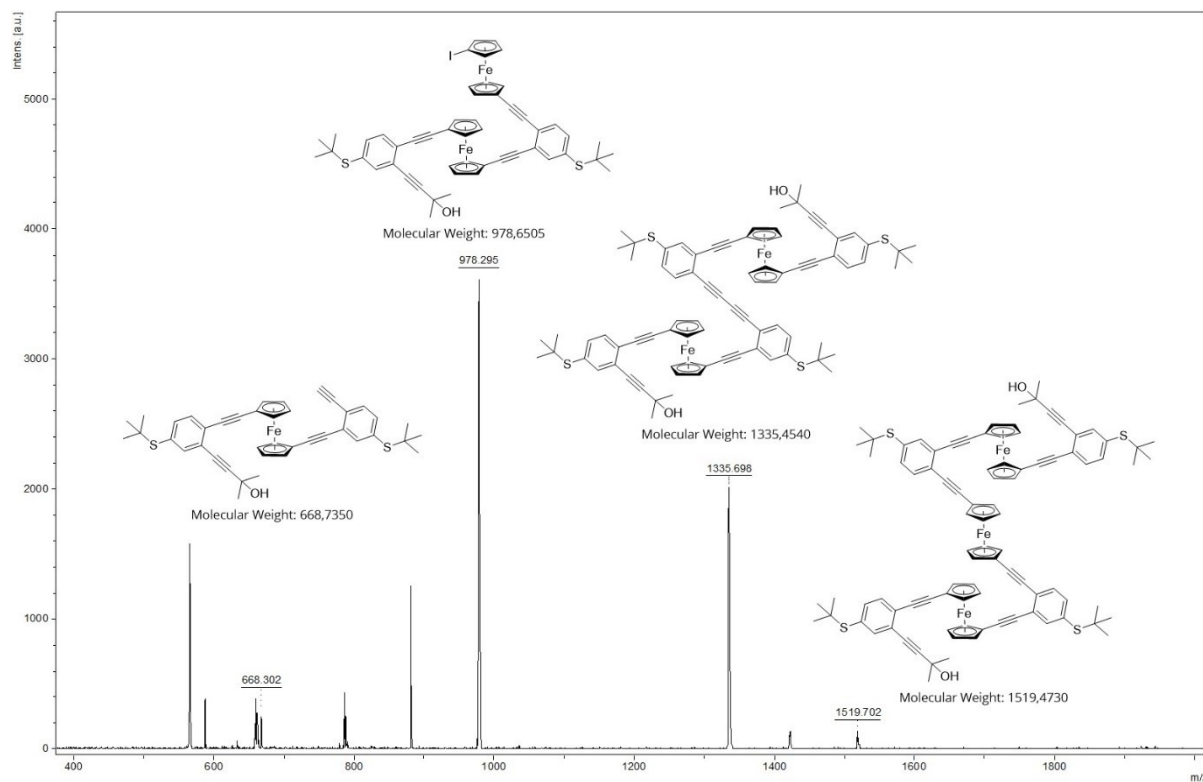
FIGURE 57 MALDI-ToF reaction progress control after 1 hour at 50 °C. No more FcI₂ is detected and only very little starting material **102** was observed. Instead homo-coupled adduct and higher oligomer were formed.

For the last deprotection in this sequence (**SCHEME 46**), bis-ferrocene **103** was treated with a 1 M TBAOH solution in degassed toluene at 70 °C and the reaction was monitored with MALDI-ToF. After 3 h the reaction was complete. Acetylene **104** was isolated after column chromatography in 96% yield as red solid. To favor intramolecular macrocyclisation over intermolecular acetylene homo-coupling and cross-coupling reactions, we tested several cyclization conditions. By far the best result was achieved with Pd(PPh₃)₄ and DIPA in toluene without additional copper(I) salt (**TABLE 13**, entry 5). Completion was achieved after 4 h at 90 °C in a previously degassed 0.1 mM toluene solution. To our delight, the reaction was not hampered by competitive dimer formation (**FIGURE 58**). None of the prior used *Sonogashira* reaction conditions showed product formation, but formed homo-coupled reaction product at best. Rhomboidal shaped bis-ferrocene complex **105** was isolated as bright orange solid after column chromatography in 54% yield.
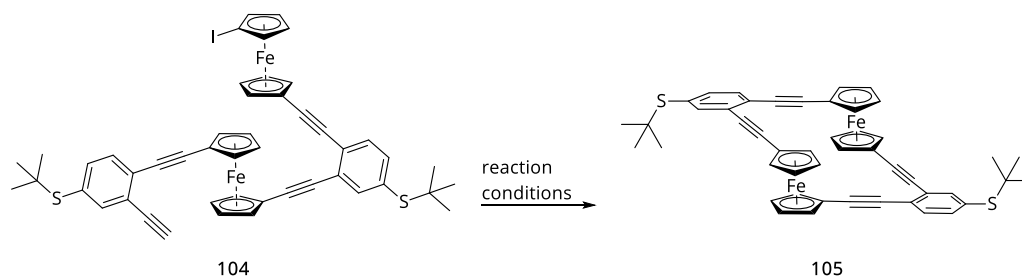
TABLE 13 Intramolecular cyclization reaction of **104** were conducted in a 0.1 mM solution and the output was justified via MALDI-TOF mass spectroscopy. [a/b]

entry	solvent	catalyst	base	temp.	time	output
1	THF	Pd(dppf)$_2$Cl$_2$/CuI[a]	DIPA	70 °C	12 h	dimer
2	toluene	-	-	110 °C	12 h	-
3	toluene	-	TBAOH	110 °C	12 h	-
4	toluene	-	NaH	110 °C	12 h	-
5	toluene	Pd(PPh$_3$)$_4$ [b]	DIPA	90 °C	4 h	full consumption

[a] 6 mol-% Pd(II) and 10 mol-% Cu(I) catalyst loading; [b] 3 mol-% Pd(0) catalyst loading

FIGURE 58 MALDI-TOF reaction control after 2 hour at 90 °C. **105** was formed cleanly, no dimer formation was observed and most of the starting material was consumed.

UV-Vis Spectroscopy

The electronic absorption spectra of bis-ferrocene structures **88** and **105** were measured, and tested for their chemical redox reversibility. UV-Vis spectra of both ferrocenes in neutral, fully oxidized and back-reduced state were recorded and compared (**Figure 59** & **Figure 60**). Therefore, a 10^{-4} M solution of **88** and a 10^{-6} M solution of **105** in methylene chloride was prepared and recorded at room temperature (black lines). Then, an equally concentrated solution of $AgBF_4$ in DCM was added, until no more change was observed. For both complexes, saturation was monitored after the addition of 4 eq. $AgBF_4$ dissolved in CH_2Cl_2 (red lines). To evaluate the reversibility, the oxidized species were treated with grain portions of sodium dithionite, until the former spectra was resembled (dotted lines).

Figure 59 Left) Electronic spectra of deltoid **88** in CH_2Cl_2 at 25 °C (black curve). The red curve shows the fully oxidized species. Dotted line displays the spectra of back-reduced **88**. Right) Qualitative MO-diagram of ferrocene with D_{5h} symmetry.

Transitions in **88** were assigned according to the MO-diagram (**Figure 59**). We observed a strong short-wavelength absorption band ranging from the lower limit of 230 nm to 350 nm with a plateau ending at ~254 nm, and a vertex at λ_{max} = 279 nm. The absorption band can be ascribed to transannular π-π interactions between the stacked phenyl rings that resembles the geometric situation (in terms of orientation and interplanar distance) in [2,2]-paracyclophanes.[185,186] The plateau, can be attributed to a charge-transfer arising from π-d* transitions ($e^*_{1g} \leftarrow e_{1u}$) that can be classified as Ligand-Metal Charge Transfer (LMCT). The LMCT transition is both, spin and Laporte allowed, hence of high intensity. The band at λ_{max} =

279 nm is most likely a metal centered MLCT, arising from the d-π absorption ($e_{2u} \leftarrow e_{2g}$). The absorptions at ~300 nm and ~370 nm, which appear as shoulders are probably Laporte-forbidden d-d transitions arising from ($e^*_{1g} \leftarrow e_{2g}$) and ($e^*_{1g} \leftarrow a'_{1g}$) respectively. The latter transition with an onset of λ_{onset} = 420 nm that is in the visible part of the spectrum and responsible for the pale orange color of the compound. Upon oxidation (**FIGURE 59**, red line), the intensity of phenyl centered short-wavelength band decreases, most likely due to the electron withdrawing effect on the phenyl backbone caused by the positively charged ferrocenes. At the same time, the LMCT plateau red-shifts by ~15 nm (Δ = 0.28 eV), which can be correlated to the transition into a half-filled metal d (a'_{1g}, e_{2g}) orbital that is of lower energy than the e^*_{1g} orbital. The MLCT band at λ_{max} = 279 nm decreases in intensity while no bathochromic effect is observed, this suggests that the relative energy of the ligand-centered e_{2u} orbital is not effect by the oxidation. Further, a new weak transition is observed at λ_{max} = 385 nm that is most likely from Laporte and spin forbidden d-d ($a'_{1g} \leftarrow e_{2g}$) transitions. The red-shift of λ_{onset} = 475 nm of the oxidized species correlates with the observed brown color of the solution.
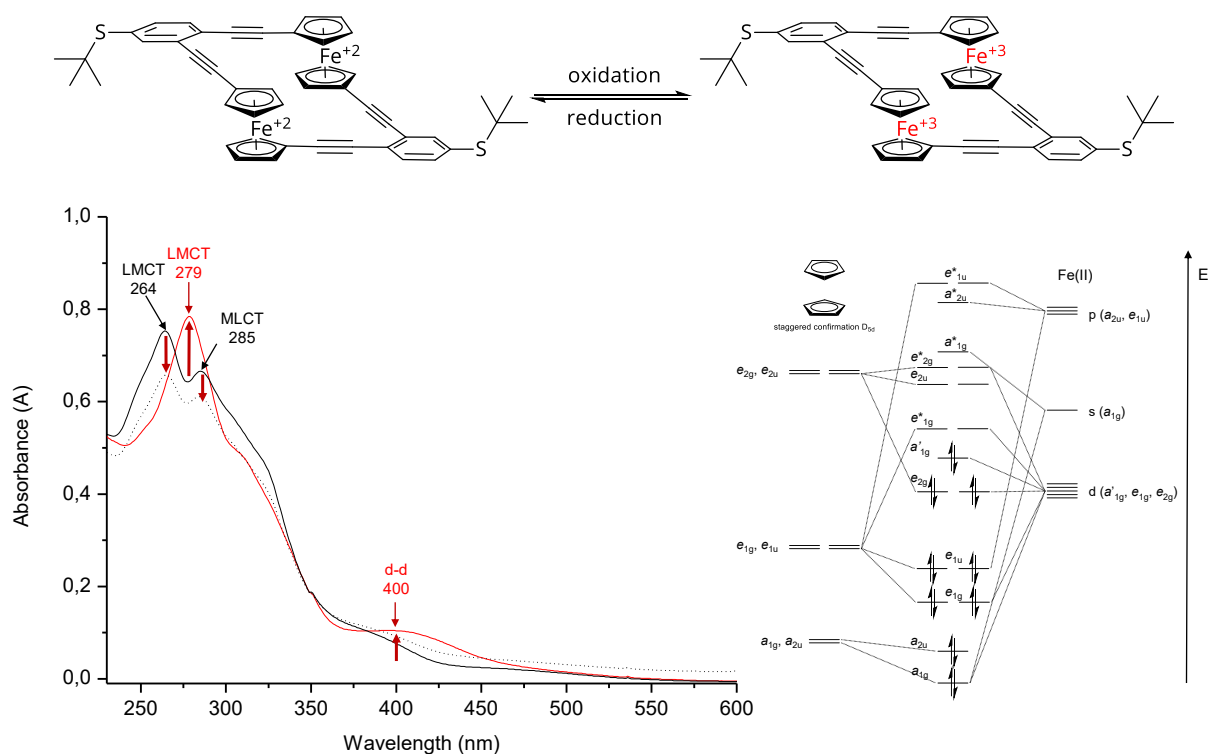
FIGURE 60 Left) Electronic spectra of rhomboid **105** in CH₂Cl₂ at 25 °C (black curve). The red curve shows the fully oxidized species. Dotted line displays the spectra of back-reduced **105**. Right) Qualitative MO-diagram of ferrocene with D_{5d} symmetry.

The electronic spectra of neutral and oxidized bis-ferrocene **105** is depicted in **FIGURE 60** and highlights some of the features we have observed in the electronic spectra of bis-ferrocene **88**. This is not surprising, as there is very little difference in electronic states of ferrocene with D_{5h} and D_{5d} symmetry. However, the main difference is the missing transannular interaction absorption in the deep UV region. That missing feature is a tentative argument for the elongated

structure. More strikingly, LMCT ($e^*_{1g} \leftarrow e_{1u}$) and MLCT ($e_{2u} \leftarrow e_{2g}$) transitions are not overlapped by the strong short-wavelength transitions. They show little red shift compared to the former structure at λ_{max} = 264 nm and λ_{max} = 285 nm respectively. Weak d-d transitions appearing as shoulder in the near UV region and the onset at λ_{onset} = 425 nm gives the orange color of the solution. Successive addition of AgBF$_4$ gave the spectra of the doubly charged **105** (**FIGURE 60**, red line). Again, we could observe a new absorption band at λ_{max} = 279 nm that we account as ($a'_{1g} \leftarrow e_{1u}$) LMCT absorption, being red-shifted (energy difference of 0.25 eV) and of higher intensity. The MLCT band disappeared or is masked by the LMCT absorption, while the d-d ($a'_{1g} \leftarrow e_{2g}$) transition in the blue region arises at λ_{max} = 400 nm. The red-shift of λ_{onset} = 500 nm of the oxidized species correlates with the observed brown color of the solution.

NMR SPECTROSCOPY

While the successful formation of macrocyclic bis-ferrocene **105** was verified by mass spectrometry of the isolated compound, the proposed structure was further identified by 2-dimensional and dynamic NMR spectroscopy. **FIGURE 61** displays a NOESY spectra of the aromatic region. The plot is showing the nuclear *Overhauser* cross relaxation between nuclear spins that are spatially close. A stacked conformation as it is shown in the inset, would possibly facilitate an NOE effect of opposing H$_A$ and H$_C$ phenyl protons that are brought into proximity at about 4.1 Å according to DFT calculations. The missing resonances (red squares) indicate that there is no spatial coupling between those two nuclei, which is an indication for the elongated structure (black box).
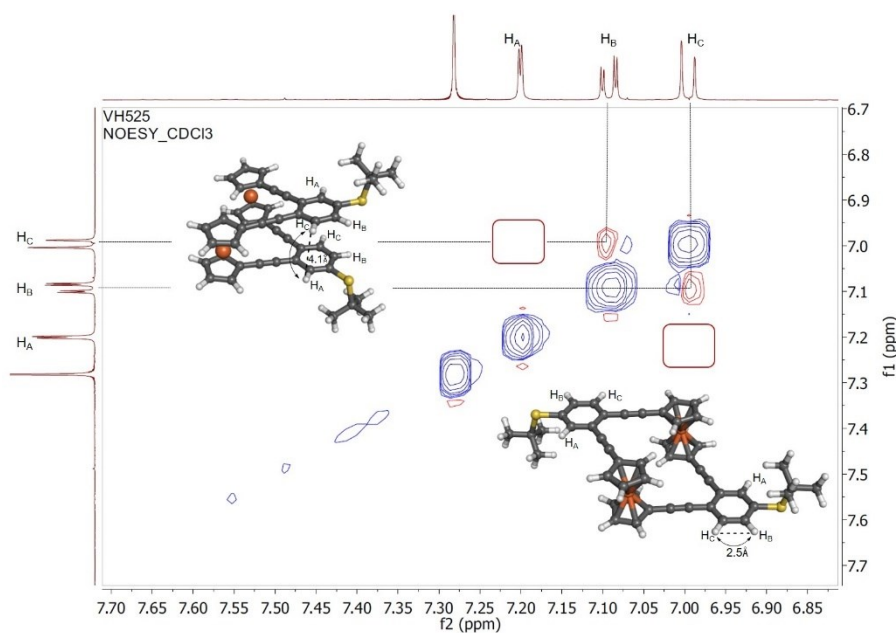
FIGURE 61 Two-dimensional correlated NOESY of bis-ferrocene **105** in the aromatic region (500 MHz, CDCl$_3$, 25 °C). The red boxes, shape the missing resonance for a stacked structure.

Another significant aspect that gives perception over the actual structure of bis-ferrocene **105** are chemical shift changes as a consequence of magnetic anisotropy effects of protons facing the interior or exterior of an elongated macrocycle. However, we observed an average resonance for both sets of α- and β ferrocene protons (**FIGURE 62**). Under the premise of an elongated structure, this indicates that an interconversion of α & β interior to α & β exterior protons must occur at a timescale that is faster than the NMR timescale.
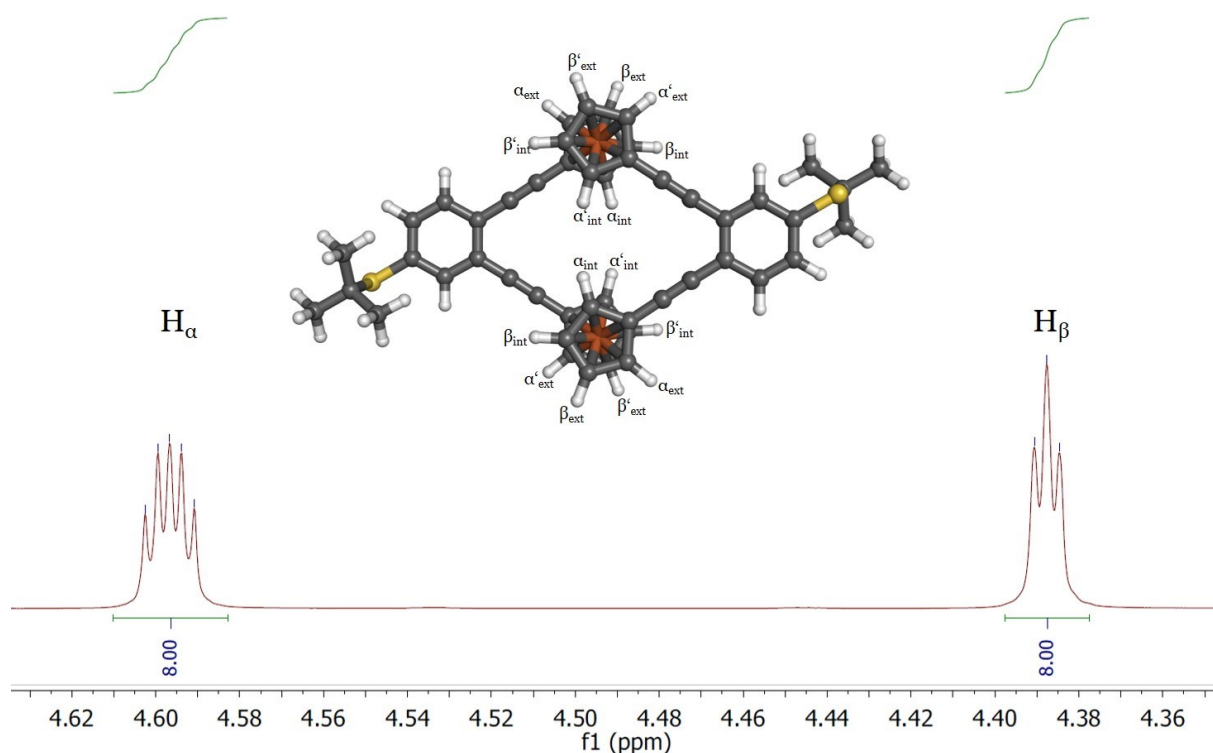
FIGURE 62 ^{1}H-NMR of bis-ferrocene 105 of the Fc resonance section recorded in CD$_2$Cl$_2$ at 25 °C.

A rotation of a freely suspended single ferrocene unit by 180° will give a chiral helical conformer with pseudo C_2 symmetry that interconverts the interior into exterior protons (**FIGURE 63**). In contrast, a stacked structure as in bis-ferrocene **88** could not facilitate such a conformational change.
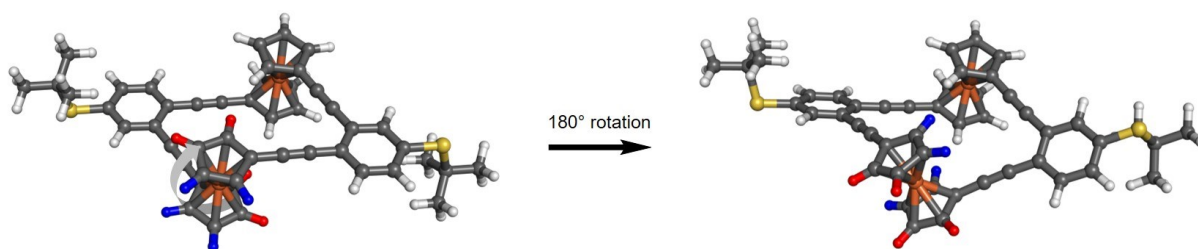
FIGURE 63 Elongated structure of bis-ferrocene **105** could facilitate a full rotation about a ferrocene unit, thereby ferrocene protons interconvert from interior to exterior, and vice versa. Here, only one Fc unit is colored.

It is noteworthy to define the term "pseudo" with respect to the symmetry description that is only correct if exclusively the macrocyclic structure is considered and the two peripheral *tert*-butylsulfanyl substituents are ignored. Another 180° rotation of the second ferrocene unit renders the initial conformer (**FIGURE 64** a).

To test this hypothesis, we recorded the NMR spectra of **105** at 25 °C and successively cooled the sample to -100 °C. The respective spectra are displayed in decreasing temperature from top to bottom in **FIGURE 64** b. At room temperature, we observe two overlapping high-order multiplets, one for the 4 Cp α-protons (Cp ring in para-position) and the 4 Cp α'-protons (Cp ring in meta-position) that resonate at δ = 4.59 ppm, and a further high-order multiplet for 8 Cp β-protons at δ = 4.39 ppm. The observed spectrum reflects the averaged conformation in fast exchange at the NMR time scale. Gradual lowering of the temperature forces the revolving motion of the ferrocene joints to match the NMR time scale and hence differentiate the protons from interior and exterior position, in which all α-protons become anisochronous δ ($\alpha_{int} \neq \alpha_{ext} \neq \alpha'_{int} \neq \alpha'_{ext}$). Likewise, β-protons diverge into two signals with different chemical shift δ ($\beta_{int} = \beta'_{int}$) $\neq \delta$ ($\beta_{ext} = \beta'_{ext}$). This splitting can be explained by the magnetic inequivalence of the two Cp-rings due to the different substitution at the asymmetric phenyl ring and the spatial variance of protons facing the exterior or interior of the macrocycle.
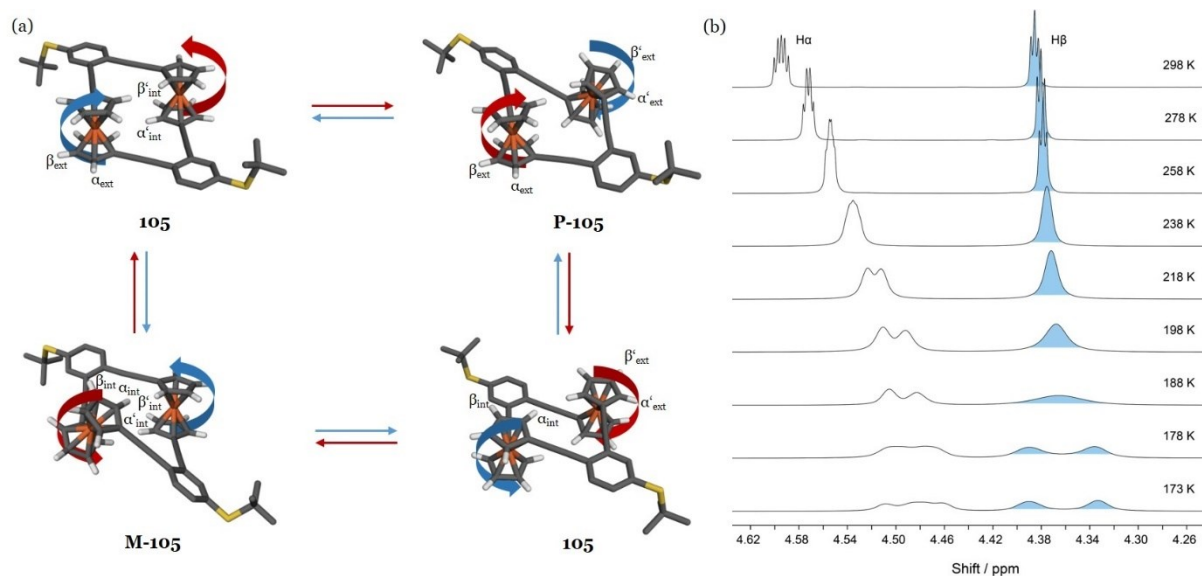
FIGURE 64 a) Equilibrium between the different conformers of **105** accessible via rotational motion of a ferrocene subunit within the macrocycle's framework. Exclusively the α and β ferrocene protons are labelled for visibility. The helical chirality descriptors *P* and *M* refer exclusively to the arrangement of the macrocycle and ignore the peripheral *t*BuS-substituent. b) Region of the ferrocene signals of the recorded ^{1}H-NMR spectra of **105** in CD$_2$Cl$_2$ in a temperature range from 298 to 173 K. The signals of the β ferrocene protons were used for LSA and are highlighted in light blue.

The coalescence temperature (T_c = 186.7 ± 0.5 °K) was identified by line shape analysis (LSA) of β-protons and used to determine the rate constant of interconversion $k_{eTc} \approx$ 71.0 s^{-1} with an

activation energy of $\Delta G^{\ddagger}_{eTc} = 38.5 \pm 2.2$ kJ mol^{-1}. Thermodynamic parameters were extracted from Eyring plot regression (**FIGURE 65**) with reaction enthalpy of $\Delta H^{\ddagger}_{e} = 44.8 \pm 2.0$ kJ mol^{-1} and a positive entropy term of $\Delta S^{\ddagger}_{e} = 34.0 \pm 1.6$ J K^{-1} mol^{-1} was found. The positive entropic term indicates an increase of microscopic configurations and consequently that suggests a transition state with reduced symmetry, in respect to both, coplanar and helical configuration. The emerging line splitting upon sample cooling, is a strong evidence for the proposed elongated structure. Only an elongated structure can facilitate a conformational change with a low barrier of interconversion. In contrast a stacked structure is not able to perform a ferrocene rotation without breaking at least one C-C bond.
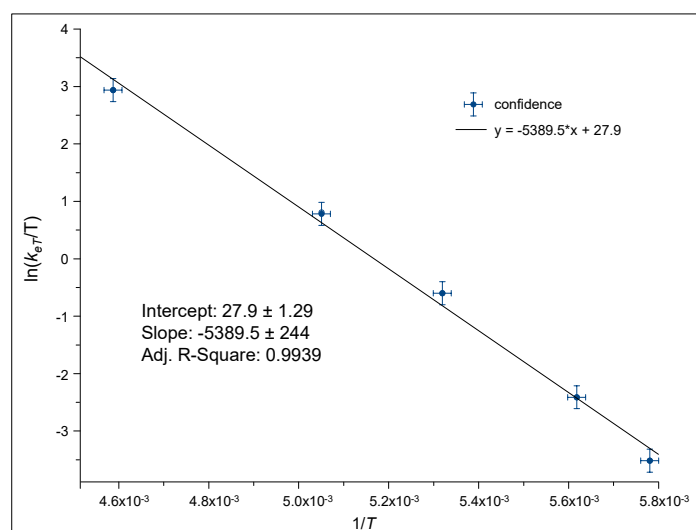
FIGURE 65 Eyring plot of the rates as determined by LSA. The subsequent linear regression y = ax + b yields slope a = −5389 ± 244 and intercept b = 27.9 ± 1.29. Error bars indicate the standard deviation at each temperature.

In this respect, it is worth mentioning that only one example for a dangling ferrocene moiety was observed and analyzed so far. In 2008, Stępień et al. [187] reported activation enthalpies ranging from 70 to 100 kJ/mol for helical ferrocene porphyrinoids. However, neither does this analysis give a quantitative result over the population of the conformers involved nor does it give insight in the energy of the traversed transition state that must be trespassed in the rotation.

ELECTROCHEMISTRY

In order to estimate electronic states and redox reversibility of bis-ferrocene molecules **88** & **105** potentio-dynamic electrochemical investigation had to be performed. Further, the electronic and electrostatic communication between the redox centers of the molecules can be evaluated, by utilizing either strong or weakly coordinating supporting electrolytes.

We performed cyclic voltammetry (CV) and square wave voltammetry (SWV) in CH_2Cl_2 at room temperature, using a single-compartment three electrode, all-glass cell with a volume of 7 mL. The results are summarized in **TABLE 14**. As working electrode, we utilized a glassy carbon disk (Ø 2 mm), a Pt wire as counter electrode and referenced to a saturated potassium calomel electrode (SCE) with a scan rate of 100 mV/s. An electrochemical reaction is considered of Nernstian behavior, when the two oxidation states are stable in the time of the experiment and the wave shape is approximately the same. Further, the potential difference between the cathodic (E_{pc}) and anodic (E_{pa}) peaks should be about 57 mV per transferred electron. The ratio of the peak currents of a redox couple, is equal to one ($i_{pa}/i_{pc} = 1$) and the peak currents are proportional to the square root of the scan rate ($i_p \propto v_s^{1/2}$).

FIGURE 66 shows the CV and SWV scans of bis-ferrocene molecules **88** & **105** recorded in a 0.1 M n-Bu$_4$NPF$_6$ solution of DCM. For compound **88**, a single and reversible ($i_{pa}/i_{pc} \approx 1$, $i_p \propto v_s^{1/2}$) oxidation wave at $E_{1/2}$ = 0.63 V vs. SCE was observed in a sweeping range from -0.1 V to 1.4 V and formally attributed to the overlapping simultaneous two-electron oxidation of Fe^{II} centres to Fe^{III}. In the case of bis-ferrocene **105**, two irreversible oxidation waves were observed at E_{1pa} = 0.63 V and E_{2pa} = 1.68 V vs. SCE when scanning up to 1.8 V (**FIGURE 66** b). Such reversibility challenges are well known from studies on multi-ferrocenyl compounds when n-Bu$_4$NPF$_6$ in CH_2Cl_2 is used.[188] Sweeping up to 1.4 V vs. SCE only a single, reversible, simultaneous two-electron oxidation wave was detected with half-wave potential at $E_{1/2}$ = 0.63 V vs. SCE (**FIGURE 66** c). In literature, single-step multiple-electron transfers are common for multi-ferrocenyl complexes when a [PF$_6$]$^-$ salt is employed.[170,189–192] Diallo et. al deduced thereof that strong ion-pairing as facilitated by nucleophilic [PF$_6$]$^-$ ions, shield the electrostatic interaction between two redox centers and hence low electronic coupling between those redox centers leads to independent response. Consequently, if a single redox wave is observed, low electronic through-bond communication between the redox centers can be assumed. This is in accordance with the single redox wave recorded for fully conjugated 1,2-bis-(ferrocenylethynyl)-benzene, when n-Bu$_4$NPF$_6$ in CH_2Cl_2 is used.[171] An increase of electronic coupling between the individual redox sites should go hand in hand with increasing thermodynamic stabilization of the mixed-valence state. As a measure of the stabilization energy, the potential splitting $\Delta E_{1/2}$ is directly correlated.[193] In other words, the higher the potential splitting the larger the thermodynamic stability of the mixed-valence intermediate.

FIGURE 66 CV and SWV (dashed lines) curves of bis-ferrocenes **88** (a) & **105** (b, c), using SCE as reference, GC as working electrode and a Pt wire as counter electrode. Scan rates were at 100 mV/s and conducted with a 0.1 M n-Bu$_4$NPF$_6$ solution in DCM at room temperature. The curve in b) further displays the irreversible behavior of **105** when a wide potential window is exploited. The current response is plotted as a function of the applied potential.

Barrière and Geiger reported that using perfluorinated electrolytes such as BARF (**FIGURE 50**) weakens ion-pairing effects and favors the observation of electrostatic through-space communication.[194] Consequently, we recorded CV and SWV voltammograms of deltoid **88** and rhomboid **105**, with 0.005 M NaBARF in CH$_2$Cl$_2$ as supporting electrolyte (**FIGURE 67**). Each redox event exhibits reversible behavior ($i_{pa}/i_{pc} \approx 1$, $i_p \propto v_s^{1/2}$) and voltammograms of deltoid **88** displays a broad wave, with a lowered half-wave potential at $E_{1/2} = 0.53$ V vs. SCE.

In the case of rhomboid **105** a well-resolved two one-electron redox curve was recorded with half-wave potentials at $E_{1/2} = 0.13$ V and $E_{1/2} = 0.41$ V vs. SCE. This seemingly complementary characteristic can be explained with the structure of **88** and **105**. In the neutral form, the two ferrocenes in **88** are relaxed and have no motivation to obtain opposing sides. When the redox centers are getting oxidized, the Coulomb repulsion between the two Fe^{III} atoms, forces them to turn out of plane. Obviously, the rigid structure of deltoid **88** doesn't facilitate free rotation along the Cp-sp single bonds. Twisting comes along with high conformational stress and thermodynamic destabilization slows down the electron transfer rate, and consequently broadens the redox wave. In contrast, rhomboidal bis-ferrocene **105** showed to have highly flexible ferrocene joints that can freely twist, thereby reducing electrostatic repulsion when oxidized, which permits fast sequential oxidation. These results allow to tentatively conclude that: First, the electronic through-bond communication between the two ferrocenes in **88** and **105** is insignificant. That consequently provides a framework capable of supporting charge localization, evident by absent wave splitting in a [PF$_6$]$^-$ electrolyte media. Second, the large half-wave potential split in rhomboid **105** of $\Delta E_{1/2} = 280$ mV and the broadened redox wave in deltoid **88** suggest considerable through-space communication when BARF is employed as electrolyte.

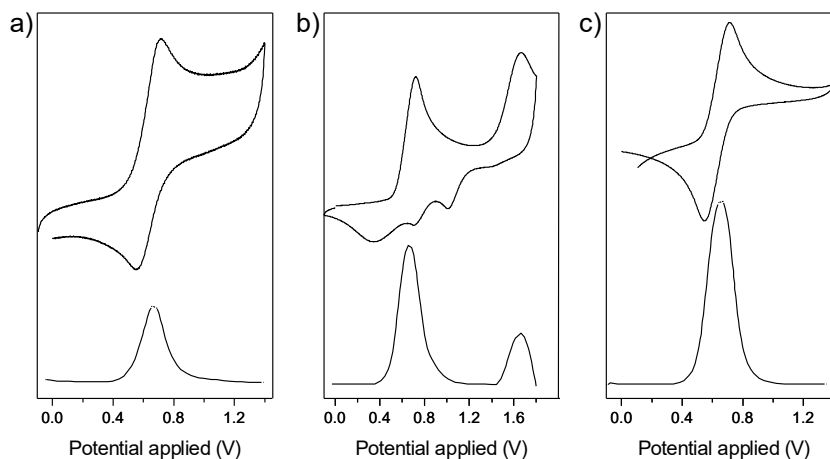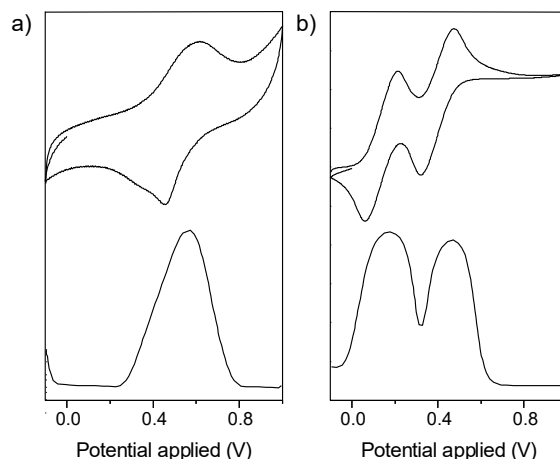**FIGURE 67** CV (solid lines) and SWV (dashed lines) curves of bis-ferrocenes **88** & **105**, using SCE as reference, GC as working electrode and a Pt wire as counter electrode. Scan rates were at 100 mV/s and conducted with a 0.005 M NaBARF solution in CH_2Cl_2 at room temperature. The current response is plotted as a function of the applied potential.

TABLE 14 CV and (SWV) potentials of bis-ferrocene complex **88** and **105** in CH_2Cl_2 at room temperature, using 0.1 M TBAPF$_6$ and 0.005 M NaBARF, respectively as supporting electrolyte.[a]

complex	$E_{1/2}$ n-Bu$_4$NPF$_6$	$E_{1/2}$ NaBARF	$E_{1/2}$ NaBARF	E_{HOMO}[b] (eV)	E_{LUMO}[c] (eV)
88	0.63 (0.67)	0.54 (0.56)	-	- 5.02	- 2,07
105	0.63 (0.66)	0.13 (0.18)	0.41 (0.46)	- 5.02	- 2,10

[a]$E_{1/2} = (E_{pa} - E_{pc})/2$ Potentials in [V] vs SCE with scan rates of 100 mV s^{-1}. [b]Energy vacuum correction for $E_{1/2}$ [V] measured in CV with TBAPF$_6$ as electrolyte vs SCE. [c]LUMO energy level obtained from optical energy by adding the optical energy gap ($E_g = 1240/\lambda_{onset}$), ($E_{LUMO} = E_{HOMO} + E_g$).

The redox potentials and the frontier orbital energies are correlated and can be estimated, according to a vacuum energy correction factor that was found empirically.[195] This is because, the required minimum energy to remove or add an electron from/to a molecule in solution is related to the energy of the HOMO/LUMO orbital, located in the gas phase. Therefore, the HOMO energy levels of **88** and **105** can be estimated after correction of the vacuum energy levels, by adding 4.4 eV (Fermi level vs. SCE) to the onset potential of the oxidation current i_{pa} (see **TABLE 14**).

DFT-CALCULATIONS

In the preceding section, VT-NMR investigations on bis-ferrocene **105** gave the Gibbs' free energy of activation $\Delta G^{\ddagger}$ = 38.5 kJ mol^{-1} that is the activation barrier needed for the interconversion of one conformer (coplanar or helical) into the other. Consequently, this suggests that the equilibrium energies of the existing conformers of rhomboid **105**, are of similar energy and that the transition state is transcended very rapidly at room temperature. To assess the relative energies of the conformers, geometry optimization calculations and transition state search were performed in collaboration with Oliver Unke from the research group of Prof. Dr. Markus Meuwly. Calculations were carried out using the Gaussian09 suite of codes[196], on the B3LYP level of

theory using a mixed basis set. C, H, S atoms were treated with 6-31G** whereas Fe, was treated with the LANL2DZ basis set.[197,198] The transition state (TS) was located using the *Synchronous Transit-Guided Quasi-Newton* (STQN) method.[199] The QST2 method does not require a guess for the transition structure, instead the start and end structures are the input geometries. This approach did not work and thus the QST3 process was subjected, thereby a guess structure for the transition state was provided.

The quantum mechanical findings are compared with experimental results and are displayed in the **FIGURE 68**. The calculations propose that the energy difference between the coplanar (**FIGURE 68,** left bottom) and the helical (**FIGURE 68,** right bottom) structure **105** is of only ΔH = 3.6 kJ mol^{-1}, whereas the coplanar conformation has the lower energy content. In regard of the experimental activation barrier $\Delta G_{eTc}^{\ddagger}$ = 38.5 kJ mol^{-1} (**FIGURE 68,** central red bar), the calculated activation energy for the TS (**FIGURE 68,** central structure and bar) is $\Delta E^{\ddagger}$ = 70.1 kJ mol^{-1} and of the same order of magnitude as the experimentally determined. The lower value obtained in the experiment, might be explained by the solvation of the transition state in the VT NMR, which is not considered in the DFT calculation.
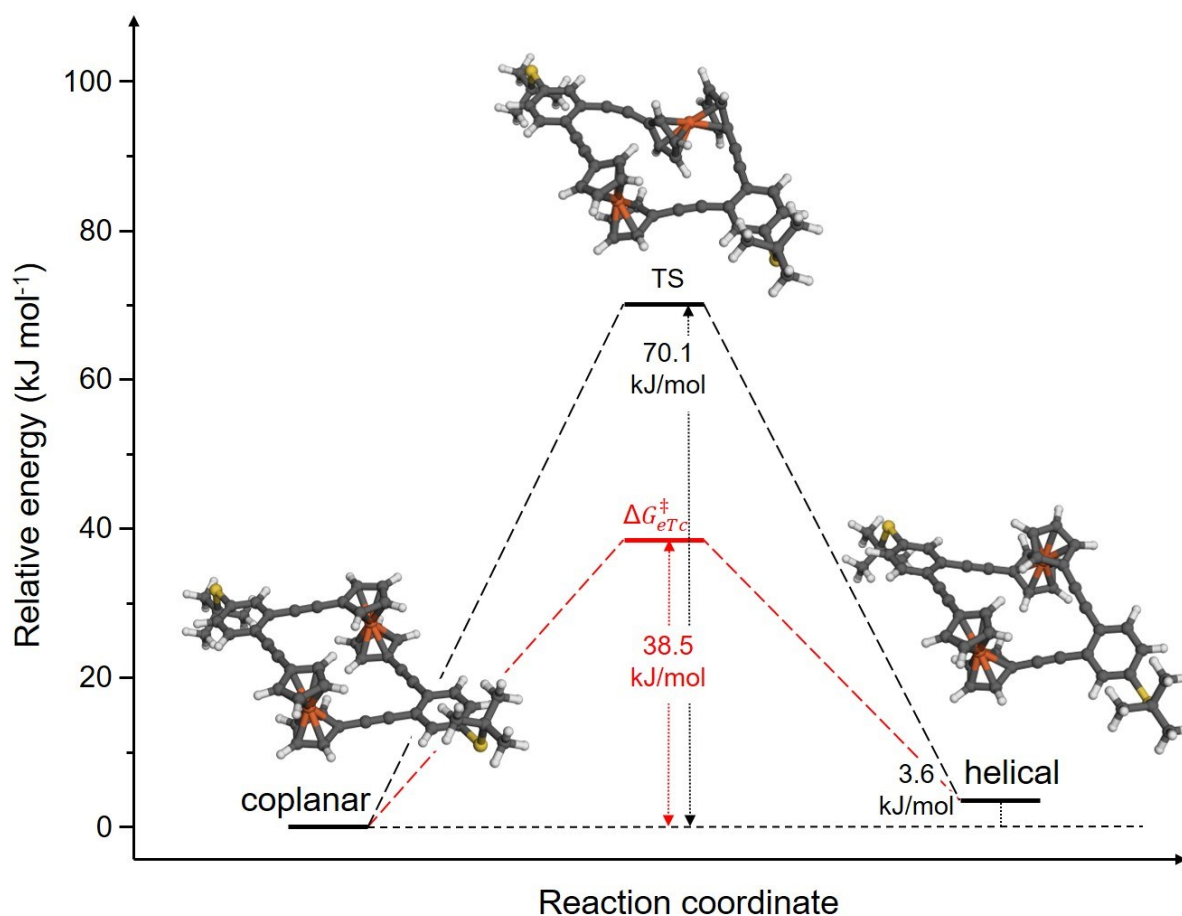
FIGURE 68 Relative energy diagram of the calculated conformers of the macrocycle **105** together with the Gibbs' free energy of the transition state obtained by the VT NMR experiment in red.

The electrochemical investigations discussed in the previous section, suggested approximations for the HOMO/LUMO energy level extrapolated from oxidation potentials of bis-ferrocene **105** (**TABLE 14**). In order to compare these findings and validate their correctness, DFT calculations were performed.

The ground state molecular orbital representation of the conformers of **105** in gas phase as obtained by the DFT calculations using B3LYP functional with mixed basis set (6-31G** for C, H, S and LANL2DZ for Fe) within the SPARTAN'10 software package (Wavefunction, Inc., USA) are reproduced in **FIGURE 69** and summarized in **TABLE 15**.

For the coplanar and helical conformers of **105**, the HOMO and HOMO^{-1} orbitals are predominantly distributed over the ferrocenyl units with little contribution of adjacent ethynyl sp-carbons, while the HOMO of the TS is located on the coplanar ferrocenyl unit and the HOMO^{-1} lobe is found on the inclined ferrocenyl unit.

The LUMO and LUMO^{+1} lobes of the coplanar and helical conformer in **105**, are almost even distributed over the conjugated molecular backbone including the sulfur atom connected to the phenyl rings. The LUMO and LUMO^{+1} orbitals in the transition state conformer are found unilateral on the coplanar side, distributed from one sulfur to the other.
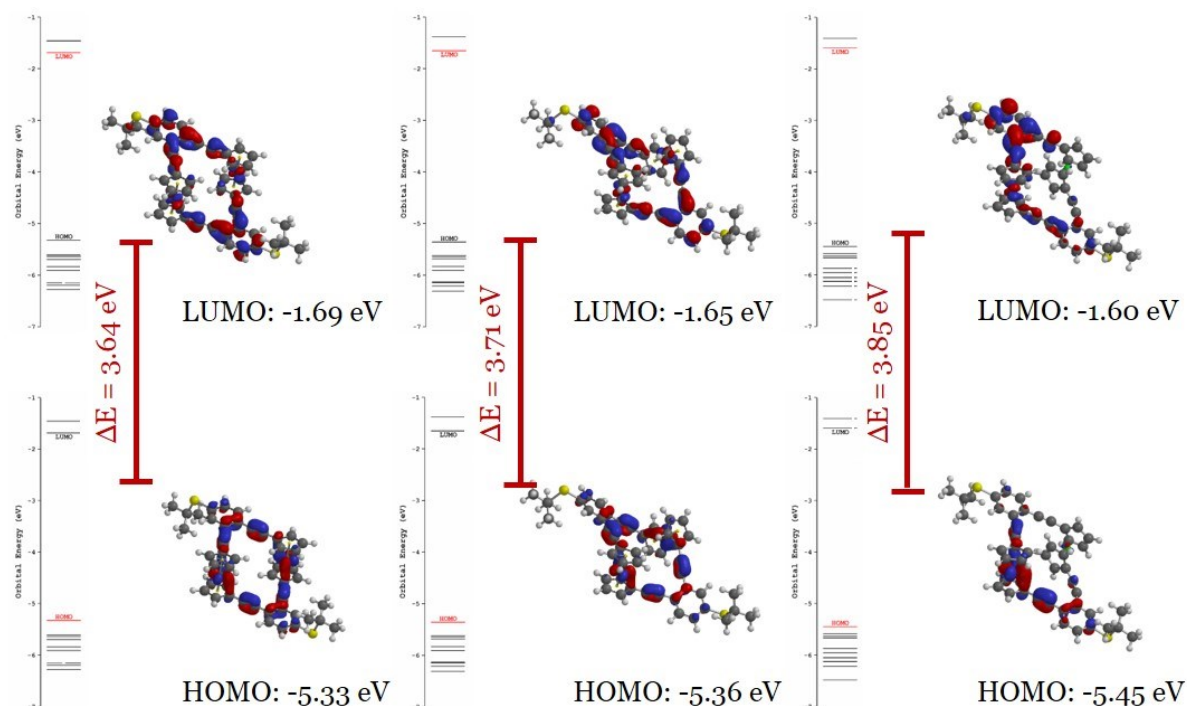
FIGURE 69 HOMO-LUMO orbital energy representation of rhomboidal structure **105** in coplanar (left), helical (middle) and of determined transition state (right) conformation.

The DFT calculations show that the HOMO energies for all three conformers are as expected: very similar and being the closest molecular energy levels to the fermi level of the gold contacts

in a gold-gold nanojunction at zero bias voltage (E_F = - 5.0 eV, work function of gold-gold nanojunctions was experimentally determined by Trouborst et al.[144]).

Therefore, it can be expected that conductance channels would be governed by the electron transport involving the HOMO orbitals and conductance would be directly influenced by an applied gating voltage.

TABLE 15 Molecular orbital energies and the HOMO-LUMO gap calculated for **105** DFT B3LYP method and compared with the experimentally extracted values.

conformer	E_{HOMO} eV	E_{LUMO} eV	E_Δ eV
coplanar 105	-5.33	-1.69	3.64
helical 105	-5.36	-1.65	3.71
TS 105	-5.45	-1.60	3.85
105	-5.02[a]	-2.10[b]	2.92

[a]HOMO energy extracted from electrochemistry and vacuum energy corrected. [b]LUMO energy level obtained from optical energy by adding the optical energy gap (E_g = 1240/λ_{onset}), (E_{LUMO} = E_{HOMO} + E_g).

Further, the structural influence of sequential oxidation on the rhomboidal bis-ferrocene **105** was investigated by DFT calculations. Geometry optimization calculations with a total charge of +1 and +2, respectively were performed. Thereby the B3LYP functional with mixed basis set (6-31G** for C, H, S and LANL2DZ for Fe) within the SPARTAN'10 software package (Wavefunction, Inc., USA) was used and the results are summarized in **TABLE 16**.

In the neutral form, the Fe-Fe gap in **105** is 7.123 Å in the coplanar, and 6.874 Å in the helical conformation. The end to end (S-S) distance of the conformers is by the same extend (roughly 0.2 Å) shorter for the coplanar than for the helical. When the molecule is oxidized sequentially, the Fe-Fe distance is enlarged for both conformers by about 10% (for the dicationic species). Interestingly, the S-S distance is reduced for the coplanar conformer by (0.2 Å), but remaining almost constant in the helical representation. The corresponding conformational stress that is accompanied by stretching the Fe-Fe distance while holding the S-S distance constant, is reflected in the increasing energy difference between the conformers. In the quantum chemical treatment, charge is not localized on one iron center, but rather evenly distributed between both centers, as the molecular symmetry suggests. Thus, the Fe-Fe distance is gradually increasing from neutral to cationic and dicationic, rather than abruptly, as it could be expected for charge localized systems.
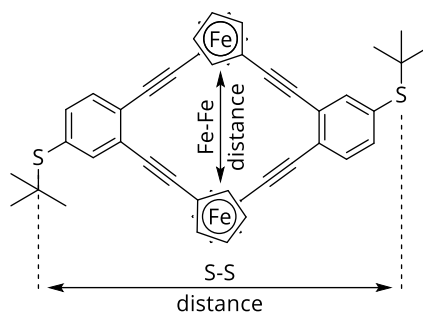
TABLE 16 Calculated Fe-Fe and S-S (in parentheses) distances upon sequential oxidation and the corresponding energy difference in kJ/mol.

Fe-Fe (S-S) distance in	neutral	cationic	dicationic
coplanar **105**	7.120 (17.8) Å	7.324 (17.8) Å	7.843 (17.6) Å
helical **105**	6.870 (18.0) Å	6.958 (18.1) Å	7.545 (18.0) Å
ΔE in kJ/mol	4.04[a]	5.02[a]	10.03[a]

[a]ΔE of coplanar and helical conformer, whereby the coplanar is of lower energy.

STM-BJ MEASUREMENTS

In order to investigate the electron transport characteristics of the bis-ferrocene **105**, *Scanning Tunneling Microscopy Break Junction* (STM-BJ) experiments (schematic in **FIGURE 70**) have been performed in collaboration with the group of Prof. Dr. Magdalena Hromadova at the ASCR in Prague.
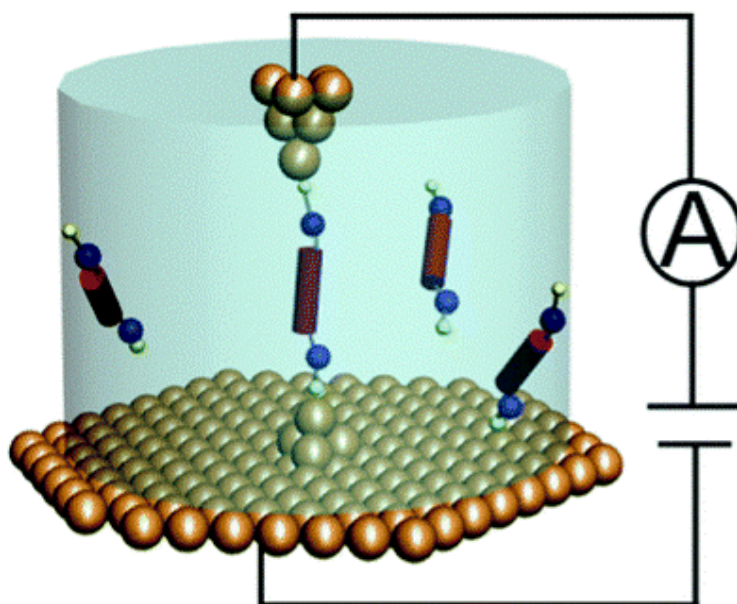
FIGURE 70 Schematic representation of the gold–molecule–gold STM-BJ. Reprinted with permission from ref.[200] Copyright © 2014 Royal Society of Chemistry.

The measurements were performed in solution and the break junctions were generated by driving the immersed gold tip repeatedly in and out of the molecule containing solution on the gold substrate. Different solvents (H_2O, EtOH and mesitylene) were used to probe single molecule conductance.

First, the charge transport of **105** was inspected in water containing 10 vol% EtOH and the result is displayed in **FIGURE 71**. The low solubility of bis-ferrocene **105** is arguably the cause that no molecular plateaus were detected in 1D and 2D histogram, suggesting that molecular junctions could not have been formed.
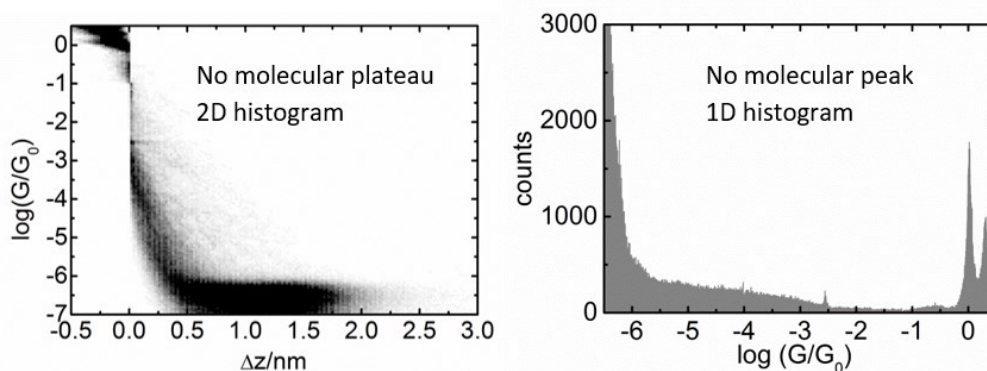
FIGURE 71 Left) 2D right) 1D logarithmic conductance histogram of **105** in H_2O with10 vol% EtOH. Virtually no molecular plateaus/peaks were observed (insulated tip).

The experiment in polar solvent is of great interest, since electrochemical investigations with an additional gating electrode require a polar solvent and insulated gold tips (in order to minimize Faradaic current). Organic solvent on the other hand promise good solubility of the molecule, but render setup limitation in terms of charge mobility and tip insulation stability (such a tip does not withstand nonpolar solvents like mesitylene). However, the STM-BJ measurements using a non-insulated gold tip in organic solvent were tested (summarized in **FIGURE 72**, top). Bis-ferrocene **105** showed limited solubility in EtOH, and good solubility in mesitylene. The 2D conductance histograms show plateaus at $\sim 10^{-2.5}$ G_0 for bis-ferrocene **105** in both organic solvents that imply molecular junctions. However, the plateau is more distinct in mesitylene, the corresponding plateau length analysis shows two values (0.57 and 0.98 nm) that cannot be associated with the length of the molecular junction directly. It is more likely the molecular junction is formed with no preferred molecular orientation, caused by the very bulky *tert*-butyl thiol anchor groups that effectively prevent chemisorption, so that the molecule will be physisorbed instead, leading to weak coupling with the electrodes. A very similar result is gained from the experiment in EtOH with the insulated tip. The plateau is weakly pronounced, but found with the same conductance. From all the stretching curves, the plateau lengths are comparable with that from the values found in mesitylene.
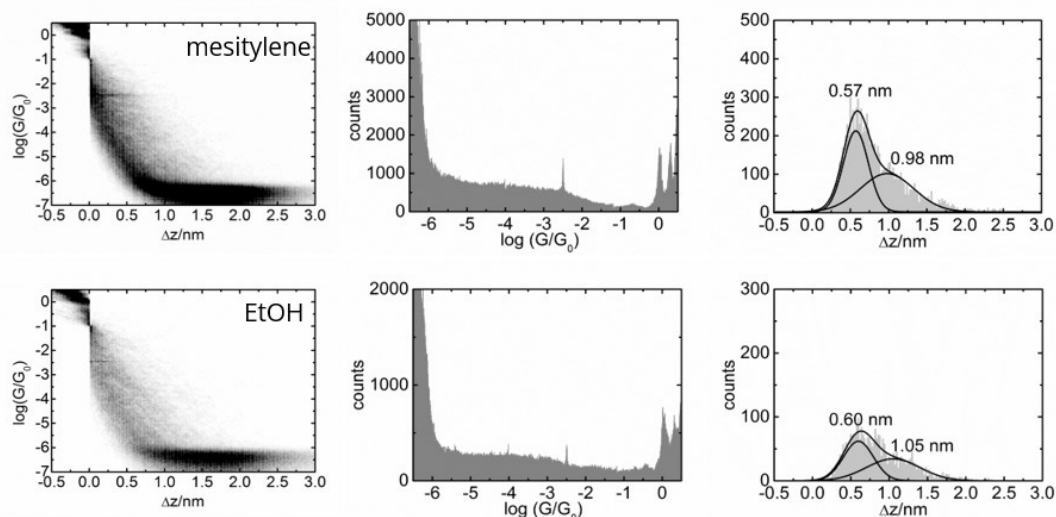
FIGURE 72 STM BJ measurements of **105**. Top) 2D, 1D logarithmic conductance and displacement distributions in mesitylene (non-insulated tip); Bottom) 2D, 1D logarithmic conductance and displacement distributions in EtOH (with insulated tip). The stretching distance of the molecular junction is determined from the conductance region set between the breaking of the electrode contact and the end of the molecular plateau.

It can be assumed that the protecting groups of the terminal thiol do effectively prevent binding to the gold tips. As a consequence, the molecular junctions were formed with low probability and no preferable orientation. It is noteworthy that ferrocene itself is used to form molecule-gold contacts in STM measurements[201] and in mesa nanojunctions[130]. This tentatively implies that the observed junction distance of ~0.6 nm could correspond to gold-ferrocene contacts as the Fe-Fe distance in coplanar bis-ferrocene **105** is 0.71 nm and 0.69 nm in the helical conformer.

Contacting of the molecule was hampered by the protected thiol anchoring group. To gain results that can be validated statistically, stable junctions needed to be formed. Consequently, molecule-electrode contacts have to be established with either free thiols, amines and pyridines that possess strong electrode coupling characteristics.[200,202]

OUTLOOK AND CONCLUSION

We have demonstrated the design, syntheses and characterization of two complementary, simple, yet aesthetic bis-ferrocene macrocycles (**FIGURE 73**). While the crystal structure of **88** shows that the bis-ferrocene obtains a rigid and nearly ideal isosceles deltoidal shape, rhomboid **105** features a unique structural flexibility, which results from a low rotational energy barrier of $\Delta G^{\ddagger} = 38.5$ kJ mol^{-1} observed by VT NMR studies. Consequently, bis-ferrocene **105** can form helical structures with varying relative orientation that were confirmed by DFT calculations.

Electrochemical investigation on both macrocycles **88** and **105** have revealed that although fully conjugated throughout the molecular backbone, electronic communication between the redox centers is neglectable. Further, bis-ferrocene **105** shows two well resolved one-electron redox waves when BARF is employed as supporting electrolyte, while **88** displays one broadened redox wave. This suggests that the redox centers interact electrostatically in both macrocycles. These features deliver the essentials for field-coupled applications in material science.[161,169,170] In this respect, the effect of an applied magnetic field on the Coulomb repulsion and charge localization of a mono- and twofold oxidized bis-ferrocene **105** would be very interesting.
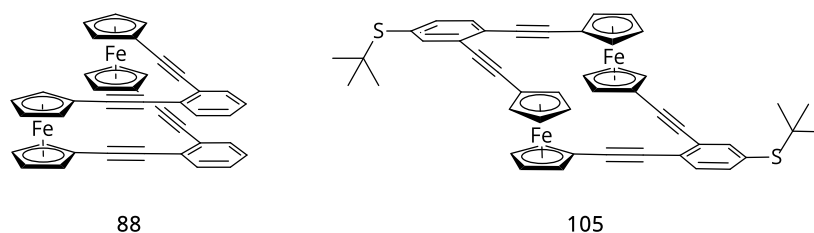
FIGURE 73 Two complementary bis-ferrocene macrocycles were synthesized and characterized.

In addition, macrocycle **105** was investigated in a STM-BJ experiment. The measurements reveal that although *tert*-butylsulfanyl groups are present at antipodal positions, the electrode coupling is not sufficient and no molecular plateau can be observed. Deprotection of the *tert*-butylsulfanyl groups with the standard conditions would be accompanied with decomposition of the compound. Hence, further investigations on alternative deprotection conditions or replacement of the protecting group needs to be performed. However, we are highly interested in wiring the rhomboidal shaped bis-ferrocene structure in a junction experiment in order to extract conductance values. Moreover, the conductance and directionality as a function of the oxidation state of the bis-ferrocene structure **105** could give detailed insight in the electron transport mechanism of a molecular wire with two redox addressable units. To make this happen, a new synthetic route towards an orthogonally protected rhomboidal bis-ferrocene needs to be devised.

One possibility is to adapt the existing route (**SCHEME 47**) by using a thiol protecting group PG3 that is sterically demanding and orthogonal to PG1 and PG2 while being cleaved at reductive

conditions. Hydroxypropyl (HOP) and triisopropylsilyl (TIPS) as PG1 and PG2 have been successfully utilized in the shown synthesis and proved their suitability as reliable PGs that can be cleaved cleanly. *S*-Benzyl thioether and other benzyl derivatives thereof (PMB, BOM) as PG3 might facilitate the formation rhomboidal structure while being cleaved off at reductive conditions such as Na/NH$_3$ or at acidic conditions (TFA).[181] Another variant of the promoted route is to replace the PG3 in **R-9**, after the ferrocenyl moieties are installed with a more sterically demanding PG such as trityl. Trityl could not be used as initial PG3, because the group is deactivating the Pd-catalysed *Sonogashira* coupling at the attached aryl system as evaluated in Table 12. A late step trans-protection might bypass the deactivation issue and allows the cleavage with TFA/Et$_3$SiH after the rhomboid has been formed.
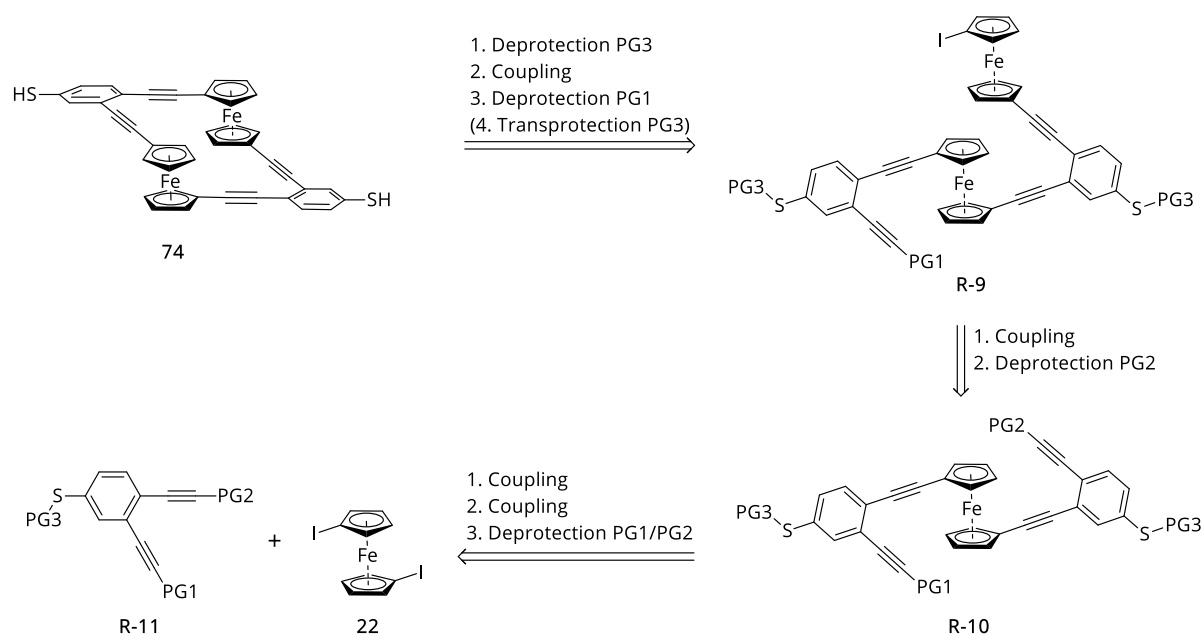
SCHEME 47 Retrosynthetic plan with three orthogonal protecting groups.

CHAPTER 4

EXPERIMENTAL

GENERAL REMARKS

All commercially available compounds were purchased from Sigma−Aldrich, Acros, ApolloScientific, Alfa Aesar, and Fluorochem, and were used as purchased. Dry solvents were purchased from Sigma−Aldrich and Acros and stored over molecular sieves (4 Å). $PdCl_2(MeCN)_2$ was synthesized by refluxing $PdCl_2$ in acetonitrile for 1 hr. The resulting solution was filtered through Celite and concentrated to crystallize the product, which was washed with acetonitrile and diethyl ether before drying in air.[73] THF and DCM were distilled from CaH_2 for 6 h in an argon atmosphere. DIPA was distilled and stored over activated 4Å molecular sieve. The reaction flasks used for acetylene deprotection were washed successively with concentrated sulfuric acid, aqueous 1 M NaOH solution and deionized water, then heated under vacuum prior to use. HPLC purification was achieved on a Shimadzu LC-20 AB machine using a Reprosil 100Å Si, 5 μm, 250 x 16 mm column from Dr.Maisch with HPLC grade 2-propanol from Biosolve and hexane form Baker. For column chromatography, usually silica gel P60 (40−63 μm) from Silicycle™ was used and solvents were of technical grade. TLC was performed on silica gel 60 F254 glass plates with a thickness of 0.25 mm purchased from Merck. ^{1}H NMR and ^{13}C NMR spectra were recorded with a Bruker DPX NMR spectrometer operating at 400 and 101 MHz or a Bruker BZH NMR at 250 and 63 MHz. The chemical shifts are reported in parts per million (ppm) relative to tetramethylsilane or a residual solvent peak, and the J values are given in Hz (±0.1 Hz). High-resolution mass spectra (HRMS) were measured as HR-ESI-ToF-MS with a Maxis 4G instrument from Bruker or were recorded with a Bruker solariX spectrometer with a MALDI source. MALDI-TOF mass spectra were recorded with a Bruker Microflex LRF spectrometer and were calibrated by using CsI_3 clusters.[203] DCTB {trans-2-[3-(4-tert-butylphenyl)-2-methyl-2-propenylidene]malononitrile} was used as matrix if needed.[204] GC-MS was performed on a Shimadzu GCMS-2020 SE equipped with a Zebron 5 MS Inferno column which allowed achieving temperatures up to 350 °C. Elemental analyses were measured with an Elementar Vario Micro Cube instrument.

SYNTHESIS AND ANALYTICAL DATA

4-(bromomethyl)benzaldehyde 16
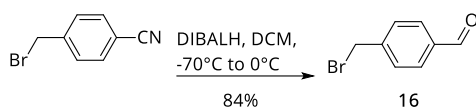
An oven-dried two-necked round-bottomed flask was purged with argon and charged with 4-(bromomethyl)benzonitrile (5.00 g, 24.2 mmol) and dissolved in dry dichloromethane (100 mL). The solution was cooled to -70 °C and then a solution of DIBAL-H (1 M in hexane, 26.7 ml, 26.7 mmol) was added via a dropping funnel. After the addition, the mixture was allowed to warm to 0 °C over a period of 1 h. Then, the mixture was slowly quenched by adding 10 ml of aqueous 1 M HCl solution and then warmed to room temperature. The mixture was eluted with toluene (250 mL) and washed subsequently with aqueous 1 M HCl solution, 1 M NaOH solution, 2 x water and brine. The organic phase was separated, dried over $MgSO_4$, filtered and concentrated under reduced pressure. The crude product was purified by FCC on silica using EtOAc/c-hexane (1:5) as eluent. Upon evaporation of the solvent, 4-(bromomethyl)benzaldehyde 16 was obtained as an off white solid. **Analytical Data for 16**: Yield: 84% (4.22 g, 21.3 mmol). ^{1}H NMR (400 MHz, $CDCl_3$, 25 °C): δ_H = 10.01 (s, 1H), 7.93 – 7.81 (m, 2H), 7.61 – 7.50 (m, 2H), 4.51 (s, 2H) ppm. ^{13}C NMR (101 MHz, $CDCl_3$, 25 °C): δ_C = 191.47, 144.24, 136.14, 130.16, 129.66, 31.94 ppm. MS (EI$^+$, 70eV): m/z (%) = 198 (4), 119 (100), 91 (75), 63 (20). EA: C_8H_7BrO (197.97): calcd. C 48.27, H 3.54; found C 48.25, H 3.81.

2-(4-(bromomethyl)phenyl)-1,3-dioxolane 17
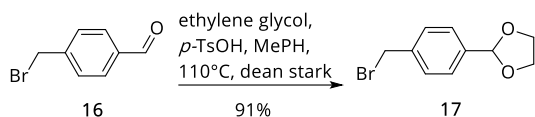
A round-bottomed flask was charged with 4-(bromomethyl)benzaldehyde 16 (4.10 g, 22.9 mmol), and dissolved in toluene (80 mL). To the solution, ethylene glycol (2.55 ml, 45.7 mmol) and a catalytic amount of p-toluenesulfonic acid (10 mol-%) were added and the mixture was refluxed with the aid of a Dean Stark trap for 12 h. After no more water was segregated, the reaction was stopped and eluted with toluene (100 mL). Then, the mixture was washed with water (2 x 150 mL) and brine. The organic phase was separated, dried over $MgSO_4$, filtered and concentrated under reduced pressure. The product was purified via FCC on silica using EtOAc/c-hexane (1:5) as eluent. Upon evaporation of the solvent, 2-(4-(bromomethyl)phenyl)-1,3-dioxolane 17 was obtained as a colourless liquid which solidifies upon standing. **Analytical Data for 17**: Yield 91% (5.04 g, 20.8 mmol). ^{1}H NMR (400 MHz, $CDCl_3$, 25 °C): δ_H = 7.48 – 7.44 (m, 2H), 7.43 – 7.38 (m, 2H), 5.81 (s, 1H), 4.49 (s, 2H), 4.17 – 3.98 (m, 4H) ppm. ^{13}C NMR (63 MHz, $CDCl_3$, 25 °C): δ_C = 138.77, 138.34, 129.16, 126.99, 103.34, 65.41, 33.12 ppm. MS (EI$^+$,

70 eV): m/z (%) = 241 (9), 163 (100), 91 (70), 73 (23). EA: $C_{10}H_{11}BrO_2$ (241.99): calcd. C 49.41, H 4.56; found C 49.31, H 4.28, N 0.4.

2-(4-((2-bromophenoxy)methyl)phenyl)-1,3-dioxolane **18**
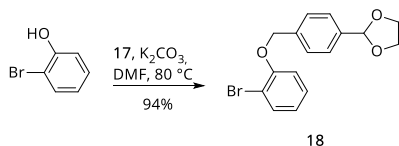
A round-bottomed flask was charged with 2-bromophenol (581 mg, 3.29 mmol) and was dissolved in dry DMF (20 mL). To that solution, 2-(4-(bromomethyl)phenyl)-1,3-dioxolane **17** (800 mg, 3.29 mmol) and potassium carbonate (919 mg, 6.58 mmol) were added. The mixture was stirred over night at 80 °C. After the reaction was completed, the reaction mixture was poured onto a sat. sol. of aqueous NH$_4$Cl (100 mL). The aqueous phase was extracted with 3 portions of toluene (50 mL). The organic phases combined and washed with water (2 x 100 mL) and brine. The organic phase was dried over MgSO$_4$, filtered and the volatiles were removed under reduced pressure. The crude product was purified by FCC on silica gel using EtOAc/c-hexane (1:5) as eluent. Upon evaporation of the volatiles the title compound was isolated as an off white solid. **Analytical Data for 18**: Yield 94% (1.05 g, 3.14 mmol). ^{1}H NMR (400 MHz, CDCl$_3$, 25 °C): δ_H = 7.56 (dd, $^3J_{H,H}$ = 7.9 Hz, $^4J_{H,H}$ = 1.6 Hz, 1H), 7.53 − 7.47 (m, 4H), 6.91 (dd, $^3J_{H,H}$ = 8.3 Hz, $^4J_{H,H}$ = 1.4 Hz, 1H), 6.84 (dd, $^3J_{H,H}$ = 7.9 Hz, $^4J_{H,H}$ = 1.4 Hz, 1H), 5.83 (s, 1H), 5.18 (s, 2H), 4.19 − 3.96 (m, 4H) ppm. ^{13}C NMR (63 MHz, CDCl$_3$, 25 °C): δ_C = 155.07, 137.80, 137.75, 133.59, 128.53, 127.11, 126.88, 122.34, 114.04, 112.64, 103.65, 70.61, 65.47 ppm. MS (EI$^+$, 70 eV): m/z (%) = 334 (1.5), 163 (67), 119 (15), 91 (100). EA: $C_{16}H_{15}BrO_3$ (335.02): calcd. C 57.33, H 4.51; found C 57.07, H 4.63.

4-(2-((4-(1,3-dioxolan-2-yl)benzyl)oxy)phenyl)-2-methylbut-3-yn-2-ol **19**
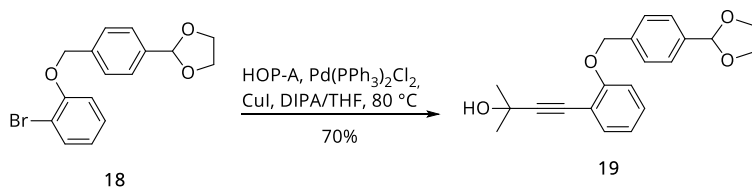
An oven-dried 25 mL Schlenk tube was purged with argon and charged under the positive pressure of argon with CuI (136 mg, 0.712 mmol, 10 mol-%), Pd(PPh$_3$)$_2$Cl$_2$ (303 mg, 0.427 mmol, 6 mol-%) and aryl bromide **18** (2.72 g, 7.12 mmol). The mixture was suspended in a previously deoxygenated mixture of THF and diisopropylamine (15 ml, 3:1). Then, 2-methyl-3-butyn-2-ol (3.55 ml, 35.6 mmol) was added drop wise via a syringe and the reaction was heated to 80 °C for 15 h. After the reaction was completed, the mixture was suspended on celite, eluting with DCM. The volatiles were removed and the dry powder was subjected to a flash column chromatography on silica gel using EtOAc/cyclohexane (1:3 to 1:1). The solvent was removed under re-

duced pressure and afforded the title compound as colorless oil. **Analytical Data for 19**: Yield 70% (1.65 g, 4.98 mmol). ^{1}H NMR (400 MHz, CDCl$_3$, 25 °C): δ_H = 7.51 − 7.43 (m, 4H), 7.37 (dd, $^3J_{H,H}$ = 7.5 Hz, $^4J_{H,H}$ = 1.7 Hz, 1H), 7.20 (td, $^3J_{H,H}$ = 7.7 Hz, $^4J_{H,H}$ = 1.5 Hz, 1H), 6.88 (d, $^3J_{H,H}$ = 7.5 Hz, 1 H), 6.84 (d, $^3J_{H,H}$ = 8.5 Hz, 1H), 5.79 (s, 1H), 5.09 (s, 2H), 4.14 − 3.94 (m, 4H), 2.83 (s, 1H), 1.60 (s, 6H) ppm. ^{13}C NMR (63 MHz, CDCl$_3$, 25 °C): δ_C = 159.10, 138.10, 137.36, 133.38, 129.59, 126.70, 126.64, 120.91, 112.90, 112.74, 103.51, 98.46, 78.33, 77.21, 69.94, 65.58, 65.28, 31.56, 31.06 ppm. HRMS (ESI-ToF): calcd. for [C$_{21}$H$_{22}$O$_4$ + Na]$^+$ 361.1410; found 361.1418.

2-(4-((2-ethynylphenoxy)methyl)phenyl)-1,3-dioxolane **20**
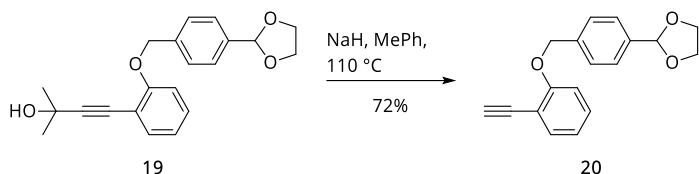
An oven-dried 50 ml round-bottomed flask was equipped with a reflux condenser, purged with argon and charged with hydroxypropyl **19** (1.17 g, 3.46 mmol) and dissolved in previously deoxygenated dry toluene (30 mL). Then, NaH (60% dispersion in mineral oil, 85.2 mg, 2.13 mmol) was added in one portion and the resulting mixture was heated to reflux overnight (12 h). After the reaction was completed, the mixture was eluted with toluene (50 mL) and washed with water (2 x 100 mL) and brine. The organic phase was dried over MgSO$_4$, filtered and the volatiles were removed under reduced pressure. The crude product was purified by column chromatography on silica gel using EtOAc/c-hexane (1:5) as eluent. Upon evaporation of the volatiles the title compound was isolated as pale yellow oil. **Analytical Data for 20**: Yield 72% (694 mg, 2.48 mmol) ^{1}H NMR (400 MHz, CDCl$_3$, 25 °C): δ_H = 7.52 - 7.46 (m, 5H), 7.28- 7.21 (m, 1H), 6.91 (td, $^3J_{H,H}$ = 7.5 Hz, $^4J_{H,H}$ = 1.0 Hz, 1H), 6.89 - 6.85 (m, 1H), 5.82 (s, 1H), 5.20 (s, 2H), 4.20 - 3.98 (m, 4H), 3.31 (s, 1H) ppm. ^{13}C-NMR (63 MHz, CDCl3, 25 °C): δ_C = 159.65, 137.92, 137.48, 134.17, 130.11, 126.86, 126.71, 120.82, 112.70, 112.04, 103.54, 81.36, 80.03, 70.09, 65.33 ppm. MS (EI$^+$, 70 eV): m/z (%) = 279 (6), 208 (11), 163 (36), 91 (100). EA: C$_{18}$H$_{16}$O$_3$ (280.11): calcd. C 77.12, H 5.75; found: C 77.35, H 5.87.

1,1-bis-(tri-n-butylstannyl) ferrocene **21**
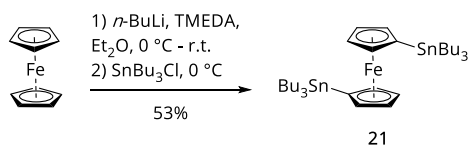
A 500 ml three-necked round bottom flask was purged with argon and charged with TMEDA (11.4 mL, 75 mmol) and dry diethylether (10 mL). The mixture was cooled to 0 °C and n-BuLi (2.5 M in hexane, 30 mL, 75 mmol) was added via syringe. The mixture was allowed to warmed to room temperature before ferrocene (5.7 g, 30 mmol) dissolved in 250 mL Et$_2$O was transfer

cannulated to it. The reaction mixture was stirred overnight at room temperature. The resulting slurry was cooled with an ice bath and tri-n-butyltin chloride (22.9 g, 63.3 mmol) was added. The reaction mixture was warmed to room temperature and stirred overnight. After TLC control showed no more conversion, the half quantity of reaction solvent was distilled off. The mixture was transferred into a 1 L separator funnel, diluted with tBME (100 mL) and washed with water (250 mL), 100 mL of a 1 M NaOH solution (removal of residual stannyl chloride), water (250 mL) and brine (200 mL). The organic phase was dried over MgSO$_4$ and concentrated under reduced pressure to afford the crude product as a brown oil. The crude product was pre-purified portion wise (3x) via a short column (Al$_2$O$_3$, n-hexane). Then, the solvent was evaporated and the tri-n-butylstannyl ferrocene was removed via vacuum distillation at the Kugelrohr apparatus (235 – 250 °C at 3 x 10^{-2} mbar) to afford the bis-tri-n-butylstannyl ferrocene as a golden oil.

Analytical Data for 21: Yield 53% (12.2 g, 15.9 mmol). ^{1}H NMR (400 MHz, CDCl$_3$, 25 °C) δ_H = 4.24 (pseudo-t, J = 1.7 Hz, 4H), 3.97 (pseudo-t, J = 1.7 Hz, 4H), 1.64 – 1.49 (m, 12H), 1.43 – 1.29 (m, 12H), 1.07 – 0.98 (m, 12H), 0.92 (t, $^3J_{HH}$ = 7.3 Hz, 18H) ppm. ^{13}C NMR (101 MHz, CDCl$_3$, 25 °C) δ_C = 74.21, 70.44, 68.73, 29.23, 27.43, 13.71, 10.25 ppm. MALDI-ToF: m/z (%)= 756.497 (3), 757.454 (3), 758.696 (17), 759.679 (25), 760.690 (58), 761.623 (66), 762.556 (91), 763.491 (91), 764.478 (100), 765.439 (88), 766.453 (92), 767.364 (62), 768.431 (50), 769.395 (24), 770.412 (24), 771.325 (10), 772.395 (4).

1,1-diiodoferrocene **22**
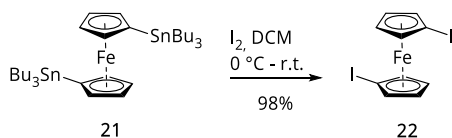
A 100 mL round-bottomed flask was purged with argon and charged with 1,1'-bis(tri-n-butylstannyl) ferrocene **21** (2.00 g, 2.63 mmol) and dry DCM (50 mL). The solution was degassed for 10 min and cooled to 0 °C, before iodine flakes (1.46 g, 5.78 mmol) were added in one portion. After the addition, the mixture was allowed to warm to room temperature and stirred for 2 h. Then, the reaction mixture was eluted with tBME, washed with 1 M thiosulfate solution (2 x 100 mL), concentrated and filtered through a short pad of neutral AlO$_2$, eluting with tBME. The solvent was removed and the remaining oil was washed with KF (20 g) dissolved in MeOH (100 mL). The solution was concentrated and was extracted with several portions of diethyl ether. The solvent was removed to a convenient amount and the crude product filtered through a neutral pad of Al$_2$O$_3$. The filtrate was concentrated and yielded the title compound as red oil.

Analytical Data for 22: Yield 98% (1.13 g, 2.58 mmol). ^{1}H NMR (400 MHz, CDCl$_3$, 25 °C) δ_H = 4.39 – 4.36 (m, 4H), 4.19 – 4.17 (m, 4H) ppm. ^{13}C NMR (101 MHz, CDCl$_3$, 25 °C) δ_C = 77.59, 72.29, 40.34 ppm. MALDI-ToF: m/z (%) = 435.821 (4), 437.819 (100), 438.800 (15), 439.802 (1).

Bis-acetal 23
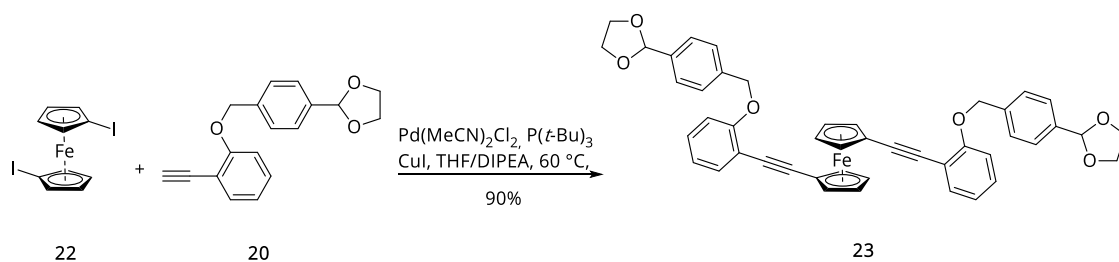
An oven-dried 15 ml Schlenk tube was purged with argon and charged with Pd(MeCN)$_2$Cl$_2$ (12.9 mg, 0.049mmol, 6 mol-%), copper iodide (15.7 mg, 0.08mmol, 10 mol-%) and 1,1´-diiodoferrocene **22** (359 mg, 0.82 mmol) under the positive pressure of argon. Then, freshly distilled and deoxygenated THF (9 mL) together with the ligand P(t-Bu)$_3$ (24.8 µL, 0.09 mmol, 12 mol-%) was added. Phenylacetylene **20** (690 mg, 2.46 mmol) was dissolved in freshly distilled and deoxygenated DIPA (3 ml) and added to the reaction mixture. The oil bath was heated to 60 °C and the mixture was stirred overnight (20 h). The black reaction mixture was suspended on celite, eluting with DCM. The volatiles were removed and the dry powder was subjected to a flash column chromatography on silica gel using EtOAc/c-hexane (1:5) as eluent to isolate the mono- and disubstituted **23** ferrocene derivative as red oil. **Analytical Data for 23**: Yield 90% (550 mg, 0.74 mmol).^{1}H NMR (400 MHz, CDCl$_3$, 25 °C): δ_H = 7.59 - 7.47 (m, 8H), 7.41 - 7.37 (m, 2H), 7.23 - 7.17 (m, 2H), 6.89 - 6.83 (m, 4H), 5.81 (s, 2H), 4.52 (pseudo-t, $^3J_{H,H}$ = 1.9 Hz, 4H), 4.26 (pseudo-t, $^3J_{H,H}$ = 1.9 Hz, 4H), 4.10 - 3.98 (m, 8H) ppm. ^{13}C NMR (63 MHz, CDCl$_3$, 25 °C): δ_C = 158.98, 138.16, 137.50, 133.16, 128.92, 126.94, 126.60, 120.85, 113.98, 112.65, 103.50, 91.71, 82.63, 72.86, 71.33, 70.00, 67.03, 65.25 ppm. HRMS (MALDI/ESI): calcd. for [C$_{46}$H$_{38}$FeO$_6$]$^+$ 742.2013; found 742.2013.

Bis-aldehyde 14
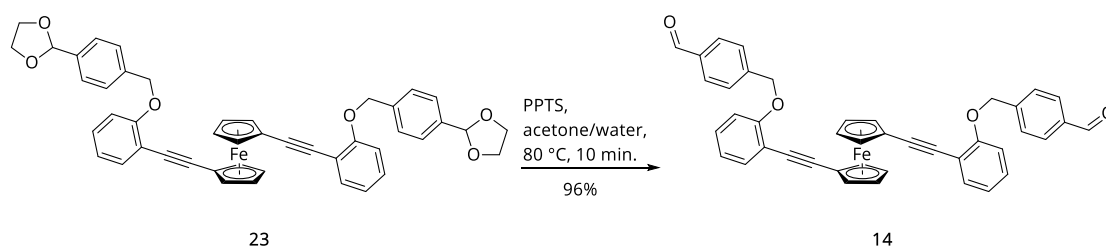
A 20 mL oven-dried argon flushed microwave vial was charged with bis-acetal **23** (163 mg, 0.219 mmol) and pyridinium p-toluenesulfonate (226 mg, 0.262 mmol) and suspended in a solvent mixture of absolute acetone (12 mL) and water (2 mL). The microwave vial was sealed and heated in the microwave for 10 min at 80 °C. After the vial was cooled to room temperature, the solvent was removed in vacuum and the remaining substance was dissolved in tBME (80 mL) and washed with aqueous NaHCO$_3$ (2 x 50 mL), water and brine. The organic phase was dried over MgSO$_4$ and concentrated in vacuum to afford the title compound as a red solid. **Analytical Data for 14**: Yield 96% (125 mg, 0.190 mmol).^{1}H NMR (400 MHz, CDCl$_3$, 25 °C): δ_H = 9.90 (s,

2H), 7.84 (d, $^3J_{H,H}$ = 8,1, 4H), 7.67 (d, $^3J_{H,H}$ = 7.8 Hz, 4H), 7.38 - 7.34 (m, 2H), 7.22 - 7.16 (m, 2H), 6.88 - 6.82 (m, 2H), 6.78 - 6.73 (m, 2H), 5.01 (s, 4H), 4.57 - 5.50 (m, 4H), 4.36 - 4.31 (m, 4H) ppm. ^{13}C NMR (63 MHz, CDCl$_3$, 25 °C): δ_C = 191.90, 158.52, 144.06, 135.76, 133.07, 129.87, 129.00, 126.98, 121.17, 113.97, 112.32, 91.78, 82.93, 73.00, 70.96, 69.23, 67.50 ppm. HRMS (MALDI/ESI): calcd. for [C$_{42}$H$_{30}$FeO$_4$]$^+$ 654.1489; found 654.1489.

Bis-alcohol **15**
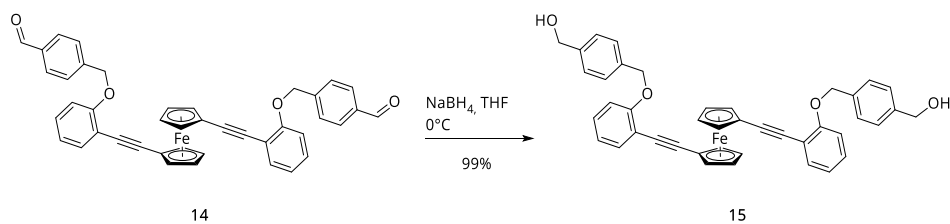
An oven-dried, argon flushed 50 mL round-bottomed flask was charged with bis-aldehyde **14** (0.191 mol, 125 mg) and dissolved in dry THF (20 ml). To the clear bright orange solution, NaBH$_4$ (30 mg) was added in one portion. The reaction was stirred for 45 min at room temperature, when TLC showed full conversion. The reaction mixture was cooled down to 0 °C and aq. NH$_4$Cl (20%, 20 ml) was slowly added. After extraction with *t*BME the combined organic phases were washed with water and brine. After drying over anhydrous MgSO$_4$ the solvent was removed in vacuum. The residue was purified by flash column chromatography (SiO$_2$, EtOAc/cyclohexane, 1:1) to isolate the bis-alcohol **15** as a bright red/orange solid. **Analytical Data for 15**: Yield 99% (120 mg, 0.190 mol) ^{1}H NMR (400 MHz, CDCl$_3$, 25 °C): δ_H = 7.52 (d, $^3J_{H,H}$ = 7.7 Hz, 3H), 7.39 (dd, $^3J_{H,H}$ = 7.8 Hz, $^4J_{H,H}$ = 1.7 Hz, 2H), 7.35 (d, $^3J_{H,H}$ = 7.9 Hz, 2H), 7.25 − 7.19 (m, 2H), 6.90 - 6.84 (m, 4H), 5.07 (s, 4H), 4.61 (s, 4H), 4.49 (pseudo-t, J = 1.9, 4H), 4.24 (pseudo-t, J = 1.9, 4H), 1.80 (s, 2H) ppm. ^{13}C NMR (63 MHz, CDCl$_3$, 25 °C): δ_C = 159.21, 140.63, 136.85, 133.28, 129.12, 127.52, 127.30, 120.98, 114.04, 112.64, 100.12, 91.74, 82.85, 72.99, 71.47, 70.21, 65.21 ppm. HRMS (MALDI/ESI): calcd. for [C$_{42}$H$_{34}$FeO$_4$]$^+$ 658.1802; found 658.1802.

Mono-bromomethyl **27**
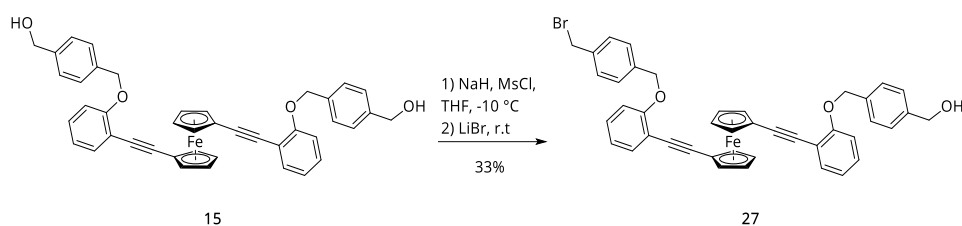
An oven-dried 10 ml round-bottomed flask was flushed with argon and charged with bis-alcohol **15** (15 mg, 22.8 µmol) dissolved in 5 mL freshly distilled and deoxygenated THF. To the mixture, NaH (60% dispersion in mineral oil, 18.2 mg, 456 µmol) was added at -10 °C and the resulting suspension was stirred for 20 min, then methanesulfonyl chloride (5.3 µL, 45.6 µmol) was added at -10 °C. The reaction mixture was allowed to warm to room temperature overnight. To the reaction mixture, LiBr (39.6 mg, 456 µmol) was added and the reaction was stirred at room temperature for 2 h. After the reaction was finished, the reaction mixture was poured onto water and extracted with EtOAc (2 x 50 ml). The organic phase was washed with water (2 x 50 mL) and brine (50 mL), dried over MgSO$_4$, filtered and concentrated under reduced pressure. The crude was purified by flash column chromatography over a silica gel using DCM/cyclohexane, 1:5 to elute the bis-bromo adduct **28** (40%) then EtOAc/cyclohexane, 1:5 was utilized to elute the title compound **27** and EtOAc/cyclohexane, 1:1 was used to wash out the starting material **15** (21%). The solvent was removed under reduced pressure and afforded the mono-bromomethyl **27** as orange solid. **Analytical Data for 27**: Yield 33% (5.5 mg, 7.28 µmol). ^{1}H NMR (600 MHz, CDCl$_3$, 25 °C): δ_H = 7.54 − 7.52 (m, 2H), 7.51 (d, $^3J_{H,H}$ = 8.1 Hz, 2H), 7.41 − 7.38 (m, 4H), 7.37 (d, $^3J_{H,H}$ = 8.0 Hz, 2H), 7.25 − 7.21 (m, 2H), 6.90 − 6.85 (m, 4H), 5.09 (s, 2H), 5.08 (s, 2H), 4.64 (s, 2H), 4.49 (pseudo-t, J = 1.9 Hz, 2H), 4.46 (pseudo-t, J = 1.8 Hz, 2H), 4.44 (s, 2H), 4.24 (pseudo-dt, J = 4.9 Hz, 1.9 Hz, 4H) ppm. ^{13}C NMR (151 MHz, CDCl$_3$, 25 °C): δ_C = 159.05, 158.94, 140.49, 137.43, 137.29, 136.47, 133.16, 133.16, 129.19, 128.99, 128.96, 127.40, 127.16, 120.95, 120.83, 113.96, 113.87, 112.58, 112.50, 91.76, 91.60, 82.65, 82.60, 72.87, 72.85, 71.26, 71.23, 70.06, 69.87, 67.12, 67.02, 65.12, 33.27 ppm. HRMS (ESI-ToF): calcd. for [C$_{42}$H$_{33}$BrFeO$_3$]$^+$ 720.0959; found 720.0956.

Ether bridged macrocycle **24**
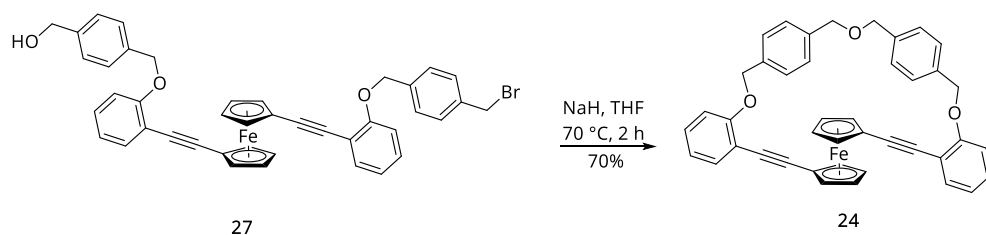
An oven-dried 20 ml round-bottomed microwave vial was flushed with argon, charged with NaH (60% dispersion in mineral oil, 10 mg, 251 µmol) and compound **27** (5.50 mg, 7.69 µmol) and dispensed in 15 mL freshly distilled and deoxygenated THF. The suspension was heated to70 °C

for 2 h when MALDI-ToF mass control indicated complete consumption of the starting material. The reaction mixture was cooled to room temperature, before it was transferred to an Erlenmeyer flask and quenched by dropwise addition of water (50 mL). The organic phase was eluted with ethylacetate and washed with water (2 x 50 mL) and brine (50 mL), dried over MgSO$_4$, filtered and concentrated under reduced pressure. The crude was purified by column chromatography over a silica gel using with EtOAc/c-hexane (1:3). The solvent was removed under reduced pressure and afforded ether bridged ferrocene **24** as orange oil. **Analytical Data for 24**: Yield 70% (3.40 mg, 5.34 μmol). ^{1}H NMR (600 MHz, CDCl$_3$, 25 °C): δ_H = 7.67 (d, $^3J_{H,H}$ = 7.9 Hz, 4H), 7.50 − 7.44 (m, 6H), 7.35 − 7.28 (m, 2H), 7.01 (dd, $^3J_{H,H}$ = 8.3 Hz, $^4J_{H,H}$ = 1.1 Hz, 2H), 6.96 (td, $^3J_{H,H}$ = 7.5 Hz, $^4J_{H,H}$ = 1.0, 2H), 5.14 (s, 4H), 4.61 (pseudo-t, J = 1.8 Hz, 4H), 4.58 (s, 4H), 4.30 (pseudo-t, J = 1.8 Hz, 4H) ppm. ^{13}C NMR (151 MHz, CDCl$_3$, 25 °C): δ_C = 159.22, 137.78, 136.60, 132.65, 129.04, 128.00, 127.21, 120.94, 114.02, 112.19, 92.06, 82.67, 72.52, 72.41, 70.62, 70.03, 65.82 ppm. HRMS (MALDI/ESI): calcd. for [C$_{42}$H$_{32}$FeO$_3$]$^+$ 640.1696; found 640.1696.

Bis-bromomethyl **28**

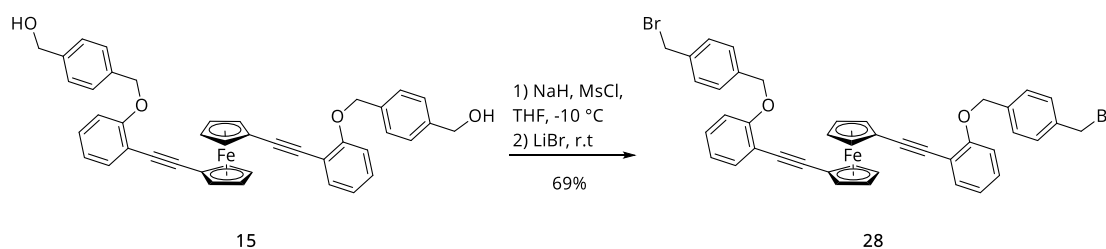A dried 5 ml round-bottomed flask was flushed with argon and charged with bis-alcohol **15** (50 mg, 75.6 μmol) dissolved in 5 mL freshly distilled and deoxygenated THF. To the mixture, NaH (60% dispersion in mineral oil, 152 mg, 37 mmol) was added and the reaction mixture was stirred for 20 min, then methanesulfonyl chloride (58 μL, 152 μmol) was added at -10 °C. The reaction was allowed to warm slowly to r.t. overnight. To the reaction mixture, LiBr (133 mg, 1.5 mmol) was added and the reaction was stirred at r.t. for 2 h. After the reaction was finished, the reaction mixture was poured onto water and extracted with EtOAc (2 x 50 ml). The organic phase was washed with water (2 x 50 mL) and brine (50 mL), dried over MgSO$_4$, filtered and concentrated under reduced pressure. The crude was purified by filtration over a silica gel plug using DCM/c-hexane (1:5). The solvent was removed under reduced pressure and afforded the bis-bromomethyl **28** as orange oil that solidified upon standing at 4 °C. **Analytical Data for 28**: Yield 69% (41 mg, 0.052 mmol). ^{1}H NMR (400 MHz, CDCl$_3$, 25 °C): δ_H = 7.51 (d, $^3J_{H,H}$ = 8.1 Hz, 4H), 7.43 − 7.37 (m, 6H), 7.26 − 7.20 (m, 2H), 6.91 − 6.84 (m, 4H), 5.08 (s, 4H), 4.50 (pseudo-t, J = 1.9 Hz, 4H), 4.45 (s, 4H), 4.27 (pseudo-t, J = 1.9 Hz, 4H) ppm. ^{13}C NMR (101 MHz, CDCl$_3$, 25 °C): δ_C = 159.21, 140.63, 136.58, 133.28, 129.12, 127.52, 127.30, 120.98, 114.04, 112.64, 100.12, 91.74, 82.85, 72.99, 71.47, 70.21, 65.21 ppm. HRMS (MALDI/ESI): calcd. for [C$_{42}$H$_{32}$Br$_2$FeO$_2$]$^+$ 782.0113; found 782.0111.

Bis-allyl **31**

28 → 31
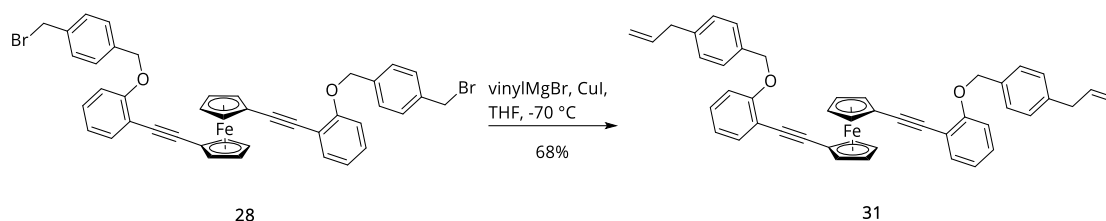
A heat gun-dried 5 ml round-bottomed flask was purged with argon and charged with vinyl-magnesium bromide (0.7 M solution in THF, 1.5 mL, 1.04 mmol (clear, light brown solution) and CuI (10 mg, 52 umol) and cooled to -78 °C. To the stirred suspension, bis-bromomethyl **28** (41 mg, 52 umol) dissolved in freshly distilled and deoxygenated THF (5 ml) was added and the mixture was allowed to reach r.t. overnight. After the reaction was complete, the suspension was poured onto a saturated aqueous NH_4Cl solution (100 mL) and extracted with EtOAc (2 x 50 mL). The combined organic phases were washed with water (2 x 50 mL) and brine (50 mL) then dried over $MgSO_4$, filtered and the volatiles were removed under reduced pressure. The crude was purified by flash column chromatography on silica gel using DCM/cyclohexane (1:10). The solvent was removed under reduced pressure and afforded the bis-allyl **31** as orange oil. **Analytical Data for 31**: Yield 68% (24 mg, 0.035 mmol). ^{1}H NMR (400 MHz, CDCl$_3$, 25 °C): δ_H = 7.47 (d, $^3J_{H,H}$ = 8.0, 4H), 7.41 (dd, J = 7.5, 1.7, 2H), 7.25 − 7.18 (m, 6H), 6.94 − 6.84 (m, 4H), 5.94 (ddt, $^3J_{H,H}$ = 16.9 Hz, $^3J_{H,H}$ = 10.2 Hz, $^3J_{H,H}$ = 6.7 Hz, 2H), 5.13 − 5.01 (m, 8H), 4.49 (pseudo-t, J = 1.9 Hz, 4H), 4.22 (pseudo-t, J = 1.9 Hz, 4H), 3.37 (d, $^3J_{H,H}$ = 6.7 Hz, 4H) ppm. ^{13}C NMR (63 MHz, CDCl$_3$, 25 °C): δ_C = 159.21, 139.69, 137.37, 134.82, 133.18, 128.96, 128.73, 127.38, 120.77, 115.84, 113.97, 112.68, 91.68, 82.59, 72.80, 71.42, 70.32, 66.94, 39.94 ppm. HRMS (MALDI/ESI): calcd. for $[C_{46}H_{38}FeO_2]^+$ 678.2217; found 678.2215.

Butene bridged macrocycle **32E/Z**

31 → 32E/Z
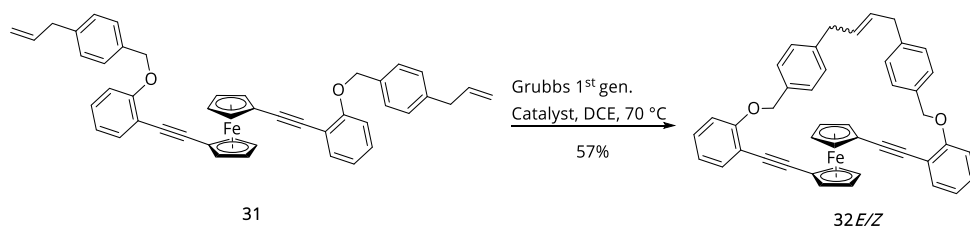
An oven-dried 50 ml Schlenk flask was purged with argon and charged with a solution of diene 23 (20 mg, 295 µmol) in freshly distilled dichloroethane (27 mL) and a solution of Grubbs Catalyst, 1st Generation (3.46 mg, 15 mol-%) in dichloroethane (3 mL). The reaction mixture was degassed by bubbling argon for 15 min. Then, the flask was closed with a rubber septum and heated to 70 °C for 16 h. After the reaction was complete, the mixture was cooled to room temperature and diluted with EtOAc (50 mL). The crude mixture was concentrated and purified by flash column chromatography on silica gel using dichloromethane/cyclohexane (1:10). The solvent was removed under reduced pressure to provide the macrocycle 2 as an orange solid (a mixture of *E/Z*-isomers [73:27]). **Analytical Data for 32**: Yield 57% (11 mg, 0.017 mmol). ^{1}H

NMR (600 MHz, CDCl$_3$, 25 °C): δ_H = 7.57 − 7.52 (m, 4H overlapping signals of *E/Z*), 7.47 − 7.42 (m, 2H, overlapping signals of *E/Z*), 7.32 − 7.25 (m, 4H overlapping signals of *E/Z*), 7.02 − 6.97 (m, 2H, overlapping signals of *E/Z*), 6.97 − 6.90 (m, 2H, overlapping signals of *E/Z*), 5.73 − 5.65 (m, 2H, overlapping signals of *E/Z*), 5.16 − 5.13 (m, 4H, overlapping signals of *E/Z*), 4.63 (pseudo-t, J = 1.8 Hz, 4H, *Z* isomer), 4.61 (pseudo-t, J = 1.9 Hz, 4H, *E* isomer), 4.33 (pseudo-t, J = 1.8 Hz, 4H, *Z* isomer), 4.29 (pseudo-t, J = 1.8 Hz, 4H, *E* isomer), 3.54 (d, $^3J_{H,H}$ = 5.1 Hz, 4H, *Z* isomer), 3.46 − 3.38 (m, 4H, *E* isomer) ppm. Only proton bound carbons are reported; ^{13}C NMR (151 MHz, CDCl$_3$, 25 °C): δ_C = 127.22, 132.72, 128.98, 112.71, 121.00, 130.49, 129.07, 70.20, 72.51, 72.50, 72.51, 72.67, 33.37, 38.70 ppm. HRMS (MALDI/ESI): calcd. for $[C_{44}H_{34}FeO_2]^+$ 650.1904; found 650.1903.

Allyl-ether **33**
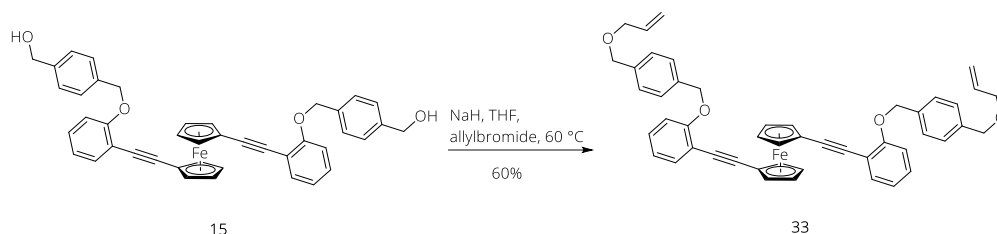
A 100 mL round-bottomed flask was purged with argon and charged with bis-alcohol **15** (30 mg, 0.045 mmol) and dissolved in freshly distilled THF (50 ml). To the stirred solution, NaH (7.28 mg, 0.18 mmol) was added in one portion at room temperature. After no more gas was produced, allyl bromide (0.016 ml, 0.182 mmol) was added to the mixture and the reaction was heated to 60 °C for 5 h. After the reaction was complete, the mixture was quenched with water (50 mL), washed with NaHCO$_3$ (50 mL) and brine (75 mL). The organic layer was dried over Na$_2$SO$_4$, filtered and concentrated under reduced pressure. The crude product was purified via column chromatography over silica gel using EtOAc/cyclohexane (1:5). The solvent was removed under reduced pressure to afford the title compound **33** as an orange solid. **Analytical Data for 33**: Yield 60% (20 mg, 0.03 mmol). ^{1}H NMR (400 MHz, CDCl$_3$, 25 °C): δ_H = 7.54 − 7.49 (m, 4H), 7.42 − 7.38 (m, 2H), 7.38 − 7.34 (m, 4H), 7.25 − 7.19 (m, 2H), 6.91 − 6.83 (m, 4H), 5.93 (ddt, $^3J_{H,H}$ = 17.2 Hz, $^3J_{H,H}$ = 10.4 Hz, $^3J_{H,H}$ = 5.6 Hz, 2H), 5.29 (dq, $^3J_{H,H}$ = 17.3 Hz, $^4J_{H,H}$ = 1.7 Hz, 2H), 5.19 (dq, $^3J_{H,H}$ = 10.4 Hz, $^4J_{H,H}$ = 1.3 Hz, 2H), 5.11 (s, 4H), 4.52 − 4.47 (m, 8H), 4.24 (pseudo-t, J = 1.9 Hz, 4H), 3.99 (pseudo-dt, J = 5.6 Hz, J = 1.4 Hz, 4H) ppm. ^{13}C NMR (63 MHz, CDCl$_3$, 25 °C): δ_C = 159.10, 137.91, 136.46, 134.73, 133.18, 128.95, 127.86, 127.16, 120.82, 117.12, 113.97, 112.67, 91.67, 82.65, 72.84, 71.84, 71.34, 71.10, 70.18, 67.04 ppm. HRMS (MALDI/ESI): calcd. for $[C_{48}H_{42}FeO_4]^+$ 738.2428; found 738.2425.

Allyl-ether macrocycle **34*E/Z***

An oven-dried 100 mL Schlenk flask was purged with argon and charged with a solution of allyl ether **33** (29 mg, 393 µmol) in freshly distille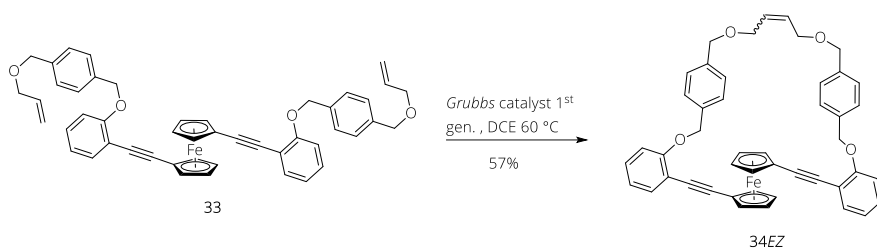d and deoxygenated dichloroethane (29 mL) and a solution of Grubbs Catalyst, 1st Generation (2.4 mg, 7.5 mol-%) in dichloroethane (3 mL). The reaction mixture was degassed by bubbling argon for 15 min. Then, the flask was closed with a rubber septum and heated to 70 °C overnight. After the reaction was complete, the mixture was cooled to r.t., concentrated and purified by column chromatography over silica gel using EtOAc/cyclohexane (1:5). The solvent was removed under reduced pressure and afforded the title compound 3 as an orange solid (a mixture of *E/Z*-isomers [73:27]) which were separated by HPLC (silica 100 Å, 2-propanol/hexane [95:5], isocratic elution with 8 mL/min). **Analytical Data for 34**: Yield 57% (16 mg, 0.027 mmol). *E*-isomer of **34**: ^{1}H NMR (600 MHz, CDCl$_3$, 25 °C): δ_H = 7.58 (d, $^3J_{H,H}$ = 7.8 Hz, 4H), 7.44 (dd, $^3J_{H,H}$ = 7.6 Hz, 1.7 Hz, 2H), 7.42 – 7.39 (m, 4H), 7.30 – 7.26 (m, 2H), 6.97 (pseudo-d, $^3J_{H,H}$ = 8.4 Hz, 2H), 6.93 (pseudo-t, $^3J_{H,H}$ = 7.5 Hz, 2H), 5.90 – 5.85 (m, 2H), 5.09 (s, 4H), 4.56 (s, 4H), 4.55 (pseudo-t, J = 1.9 Hz, 4H), 4.21 (pseudo-t, J = 1.8 Hz, 4H), 4.08 – 4.04 (m, 4H) ppm. Only proton bound carbons are reported; ^{13}C NMR (151 MHz, CDCl$_3$, 25 °C): δ_C = 127.29, 132.98, 127.71, 129.05, 112.37, 120.96, 129.53, 69.38, 71.78, 72.47, 69.94 ppm; *Z*-isomer of **34**: ^{1}H NMR (600 MHz, CDCl$_3$, 25 °C): δ_H = 7.50 (d, $^3J_{H,H}$ = 7.8 Hz, 4H), 7.37 – 7.33 (m, 2H), 7.29 (d, $^3J_{H,H}$ = 7.8 Hz, 4H), 7.24 – 7.20 (m, 2H), 6.87 (pseudo-d, $^3J_{H,H}$ = 8.3 Hz, 2H), 6.84 (pseudo-t, $^3J_{H,H}$ = 7.5 Hz, 2H), 5.80 – 5.77 (m, 2H), 5.03 (s, 4H), 4.52 – 4.48 (m, 4H), 4.43 (s, 4H), 4.23 – 4.18 (m, 4H), 3.94 (d, $^3J_{H,H}$ = 4.2 Hz, 4H) ppm. Only proton bound carbons are reported; ^{13}C NMR (151 MHz, CDCl$_3$, 25 °C): δ_C = 127.32, 133.04, 128.05, 112.50, 120.90, 129.73, 70.17, 72.61, 71.68, 71.21, 65.06 ppm. HRMS (MALDI/ESI): calcd. for [C$_{46}$H$_{38}$FeO$_4$]$^+$ 710.2115, found 710.2113.
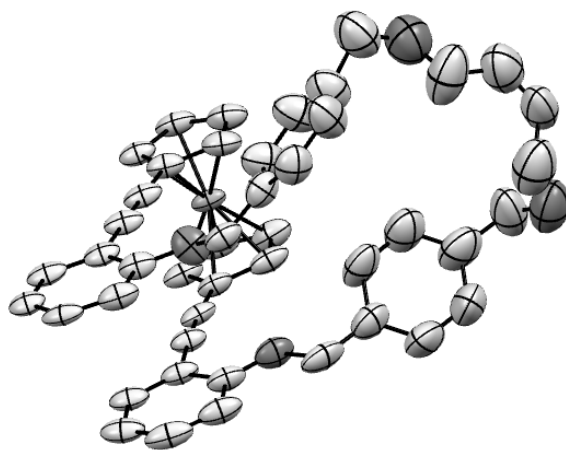
Structure Determination by Single-Crystal X-ray Analysis: The intensity data for suitably sized crystals of compound **34Z** with the formula $C_{46}H_{38}Fe_1O_4$, M = 710.65 g was collected with a Stoe StadiVari diffractometer at 123K using Ga-K_α radiation with λ = 1.34143 Å. The STOE X-AREA suite has been used for data collection and integration. The structure 3Z was solved by the charge flipping method using the program Superflip to reveal the atomic positions. Least-squares refinement against F was carried out on all non-hydrogen atoms using the program CRYSTALS, and Chebychev polynomial weights were used to complete the refinement. Plots were produced using Mercury. Crystallographic data (excluding structure factors) for compound XX has been deposited with the Cambridge Crystallographic Data Center, the deposition number is CCDC-1453128. Copies of the data can be obtained, free of charge, on application to the CCDC, 12 Union Road, Cambridge CB2 1EZ, UK [fax: +44-1223-336033 or e-mail: deposit@ccdc.cam.ac.uk].

4-Methoxyphenyl *p*-Toluenesulfonate **37**
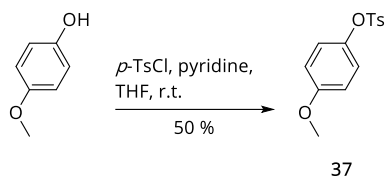
A 250 mL round-bottomed flask was purged with argon and charged with 4-methoxyphenol (15.0 g, 119 mmol), *p*-toluenesulfonyl chloride (22.9 g, 119 mmol) and dry THF (100 ml). Pyridine (9.72 ml, 119 mmol) was added and the reaction mixture was stirred for 12 h at room temperature. After the reaction was complete, the mixture was poured into a mixture of water (100 mL) and diethyl ether (600 mL). The organic layer was separated and washed with 1 M aqueous sodium hydroxide (4 x 100 mL), washed with water (210 mL) and brine (100 mL). The organic layer was dried over MgSO$_4$, filtered and concentrated under reduced pressure. The residue was recrystallized from methanol to afford the desired compound as a white solid. **Analytic Data for 37**: Yield 50% (16.6 g, 59.6 mmol). ^{1}H NMR (400 MHz, CDCl$_3$, 25 °C): δ_H = 7.68 (d, $^3J_{H,H}$ = 8.3 Hz, 2H), 7.30 (d, $^3J_{H,H}$ = 8.0 Hz, 2H), 6.91 – 6.83 (m, 2H), 6.81 – 6.72 (m, 2H), 3.76 (s, 3H), 2.44 (s, 3H) ppm. ^{13}C NMR (101 MHz, CDCl$_3$, 25 °C): δ_C = 158.28, 145.36, 143.17, 132.42, 129.82, 128.68, 123.47, 114.56, 55.67, 21.84 ppm. HRMS (ESI-ToF): calcd. for [C$_{14}$H$_{14}$O$_4$SNa]$^+$ 301.0505; found 301.0508.

3-iodo-4-methoxyphenyl *p*-Toluenesulfonate **38**
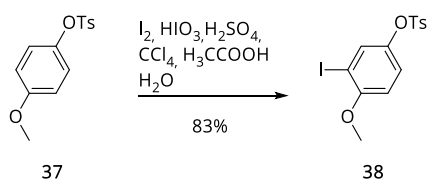
A mixture of 4-methoxyphenyl *p*-toluenesulfonate **37** (17.61 g, 63.0 mmol), iodine (12,5 g, 50.6 mmol), iodic acid (4.45 g, 25.3 mmol), 2.6 mL sulfuric acid and 15 mL of CCl4, 30 ml of acetic acid and 15 mL of water was refluxed for 4 days. After cooling to room temperature, the reaction

mixture was poured into 100 mL of water and 100 mL of EtOAc. The organic layer was washed successively with water (50 mL), aqueous sodium thiosulfate (4 x 50 mL), 1 M aqueous sodium hydroxide solution (50 mL) and brine (50 mL). The organic layer was dried over MgSO$_4$, filtered and the volatiles removed in vacuo. The remaining yellow solid was recrystallized from methanol to the title compound as a colorless solid. **Analytic Data for 38:** Yield 83 % (21.3 g, 52.7 mmol). ^{1}H NMR (400 MHz, CDCl$_3$, 25 °C): δ_H = 7.69 (d, $^3J_{H,H}$ = 8.4 Hz, 2H), 7.37 − 7.29 (m, 3H), 7.00 − 6.90 (m, 1H), 6.68 (d, $^3J_{H,H}$ = 8.9 Hz, 1H), 3.84 (s, 3H), 2.46 (s, 3H) ppm. ^{13}C NMR (101 MHz, CDCl$_3$, 25 °C): δ_C = 157.03, 145.60, 143.02, 133.21, 131.96, 129.82, 128.58, 123.25, 110.40, 85.04, 56.71, 21.76 ppm. EA: C$_{14}$H$_{13}$IO$_4$S (403.95): calcd. C 41.60, H 3.24; found C 41.38, H 3.29.

3-Iodo-4-methoxyphenol **39**
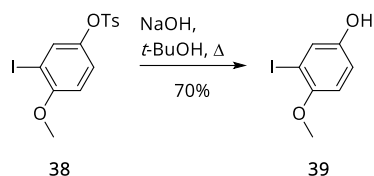
Sodium hydroxide (10.0 g) was dissolved in H$_2$O (40 mL) and degassed for 10 min. 3-Iodo-4-methoxyphenyl-p-toluenesulfonate **38** (20 g, 49.5 mmol) was dissolved in t-BuOH (100 mL) and degassed for 10 min. The sodium hydroxide solution was added dropwise and the reaction was heated to reflux for 16 h. The mixture was cooled to room temperature, acidified with aq. HCl (10%, 50 mL) and poured into a mixture of tBME (50 mL) and H$_2$O (100 mL). The aqueous phase was separated and the org. layer was extracted with NaOH (1 M, 4 x 50 mL). The aqueous layers were combined, acidified with aq. HCl (37%, 20 mL) and extracted with tBME (4 x 50 mL). The combined org. layers were washed with brine (100 mL), dried over MgSO$_4$, filtered and concentrated under reduced pressure to afford the desired compound after recrystallization from chloroform as colorless needles. **Analytic Data for 39:** Yield 70% (8.65 g, 34.6 mmol). ^{1}H NMR (400 MHz, CDCl$_3$, 25 °C): δ_H = 7.29 (d, $^3J_{H,H}$ = 2.9 Hz, 1H), 6.81 (dd, $^3J_{H,H}$ = 8.8, 2.9 Hz, 1H), 6.71 (d, $^3J_{H,H}$ = 8.8 Hz, 1H), 4.71 (s, 1H), 3.82 (s, 3H) ppm. ^{13}C NMR (101 MHz, CDCl$_3$, 25 °C): δ_C = 152.81, 149.98, 126.30, 116.01, 111.80, 85.98, 57.05 ppm. HRMS (ESI-ToF): calcd. for [C$_7$H$_6$IO$_2$]$^+$ 248.9418; found 248.9415.

2-Bromo-5-iodo-4-methoxyphenol **40**
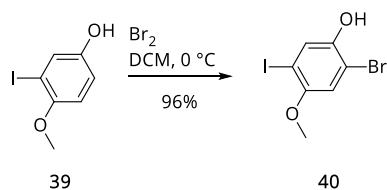
Bromine (1.78 mL, 34.6 mmol) was dissolved in 20 mL of CH$_2$Cl$_2$ and was added dropwise to a solution of 3-iodo-4-methoxyphenol **39** (8.65 g, 34.6 mmol) in CH$_2$Cl$_2$ (70 mL) at 0 °C and

stirred at this temperature for an additional 30 min. The reaction mixture was poured into 150 mL of water and 200 mL of ether, and the organic layer was washed with water (two times, each 100 mL), aqueous sodium thiosulfate (two times, each 100 mL), and 100 mL of brine. After the organic phase was dried over MgSO$_4$, filtered, and evaporated, the remaining brown solid was purified by silica-gel column chromatography (SiO$_2$, EtOAc/cyclohexane, 1:5). **Analytic Data for 40:** Yield 96% (10.9 g, 33.7 mmol). ^{1}H NMR (400 MHz, CDCl$_3$, 25 °C): δ_H = 7.46 (s, 1H), 6.89 (s, 1H), 5.10 (s, 1H), 3.82 (s, 6H) ppm. ^{13}C NMR (101 MHz, CDCl$_3$, 25 °C): δ_C = 152.81, 147.13, 126.15, 113.95, 109.71, 85.34, 57.17 ppm. HRMS (ESI-ToF): calcd. for [C$_7$H$_5$BrIO$_2$]$^+$ 326.8523; found 326.8525.

1,3-dioxolane **41**
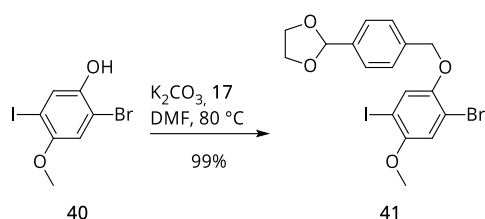
To a solution of 2-Bromo-5-iodomethoxy phenol **40** (2.55 g, 7.75 mmol) in 60 mL dry DMF, 2-(4-(bromomethyl)phenyl)-1,3-dioxolane **17** (1883 mg, 7.75 mmol) and potassium carbonate (2.16 g, 15.5 mmol) were added and the resulting mixture was first degassed with argon for 15 min. then heated at 80 °C for 12 h. After completion was monitored by TLC, the reaction mixture was poured onto a saturated solution of aqueous NH$_4$Cl (150 mL) and extracted with toluene. The phases were separated and the organic layer was washed with water and brine, dried over MgSO$_4$ and the volatiles were evaporated under reduced pressure. The crude product was purified via FCC (SiO$_2$, EtOAc/cyclohexane, 1:10) to afford the product as colorless solid. **Analytic Data for 41**: Yield 99% (3.75 g, 7.65 mmol). ^{1}H NMR (400 MHz, CDCl$_3$, 25 °C): δ_H = 7.54 − 7.45 (m, 4H), 7.35 (s, 1H), 7.02 (s, 1H), 5.83 (s, 1H), 5.08 (s, 2H), 4.20 − 3.98 (m, 4H), 3.83 (s, 3H) ppm. ^{13}C NMR (101 MHz, CDCl$_3$, 25 °C): δ_C = 153.55, 150.07, 137.97, 137.40, 127.41, 126.88, 125.23, 115.96, 113.15, 103.63, 83.99, 71.89, 65.47, 57.26 ppm. HRMS (ESI-ToF): calcd. for [C$_{17}$H$_{16}$BrINaO$_4$]$^+$ 512.9169; found 512.9177.

TMS-acetylene **47**
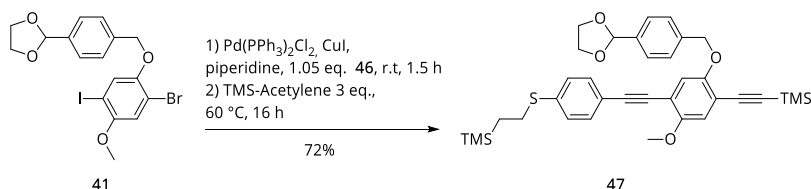
A 25 mL Schlenk tube was purged with argon and charged with **41** (1.00 g, 2.04 mmol), bis-(triphenylphosphine) palladium(II) chloride (72 mg, 5 mol-%), CuI (39 mg, 10 mol-%) and piperidine (10 mL). The mixture was degassed with argon for 15 min. then acetylene **46** (478 mg, 2.04 mmol) was added and the reaction mixture was stirred for 1.5 h at room temperature. After TLC control showed full consumption, TMS-acetylene (0.87 mL, 6.12 mmol) was added and the mix-

ture was stirred over night at 60 °C. The mixture was concentrated and eluted with DCM (50 mL) and again concentrated on Hyflo. The crude product was then purified via flash column chromatography (SiO$_2$, EtOAc/cyclohexane, 1:20) to afford the title compound. **Analytic Data for 47.** Yield 67% (839 mg, 1.37 mmol). ^{1}H NMR (400 MHz, CDCl$_3$, 25 °C): δ_H = 7.52 (q, $^3J_{H,H}$ = 8.3 Hz, 4H), 7.46 (d, $^3J_{H,H}$ = 8.3 Hz, 2H), 7.24 (d, $^3J_{H,H}$ = 8.4 Hz, 2H), 7.06 (s, 1H), 6.98 (s, 1H), 5.84 (s, 1H), 5.12 (s, 2H), 4.17 − 3.98 (m, 4H), 3.87 (s, 3H), 3.03 − 2.94 (m, 2H), 0.99 − 0.89 (m, 2H), 0.29 (s, 9H), 0.06 (s, 9H) ppm. ^{13}C NMR (101 MHz, CDCl$_3$, 25 °C): δ_C = 154.22, 153.66, 138.65, 138.12, 137.51, 132.04, 127.83, 126.85, 126.59, 120.01, 118.04, 115.69, 114.30, 113.81, 103.62, 101.12, 100.76, 95.14, 85.86, 70.95, 65.35, 56.48, 29.00, 16.73, 0.09, -1.64 ppm. MALDI-ToF (DCTB): m/z (%) = 614.28 (100), 615.26 (44), 616.24 (17), 617.22 (3).

Ethynyl **48**

A 50 mL round bottom flask was charged with TMS-acetylene **47** (830 mg, 1.35 mmol), and dissolved in methanol (20 mL + a few drops of water) and DCM (5 mL). The mixture was degassed for 15 min, then potassium carbonate (188 mg, 1.56 mmol) was added. The mixture was stirred for 45 min. at room temperature. The mixture was concentrated then dissolved in EtOAc and washed with water and brine. The organic phase was dried over MgSO$_4$, filtered and concentrated under reduced pressure. The crude product was purified by FCC (SiO$_2$, EtOAc/cyclohexane, 1:5) to give the title compound as a yellow solid. **Analytical data for 48.** Yield 79% (577 mg, 1.06 mmol). ^{1}H NMR (400 MHz, CDCl$_3$, 25 °C): δ_H = 7.49 (s, 4H), 7.45 (d, $^3J_{HH}$ = 8.5 Hz, 2H), 7.23 (d, $^3J_{HH}$ = 8.5 Hz, 2H), 7.03 (s, 1H), 6.99 (s, 1H), 5.82 (s, 1H), 5.15 (s, 2H), 4.17 − 3.97 (m, 4H), 3.86 (s, 3H), 3.39 (s, 1H), 2.98 (m, 2H), 0.94 (m, 2H), 0.05 (s, 9H) ppm. ^{13}C NMR (101 MHz, CDCl$_3$, 25 °C): δ_C = 154.20, 153.76, 138.73, 137.94, 137.69, 132.11, 127.85, 127.18, 126.81, 119.96, 117.98, 116.19, 114.24, 113.09, 103.67, 95.21, 85.67, 82.97, 80.02, 71.15, 65.45, 56.56, 29.03, 16.76, -1.62 ppm. MALDI-ToF (DCTB): m/z (%) = 542.19 (100), 543.17 (37), 544.15 (12), 545.23 (2).

Bis-oxolane ferrocene 52

48 : R = (CH$_2$)$_2$TMS

52 : R = (CH$_2$)$_2$TMS
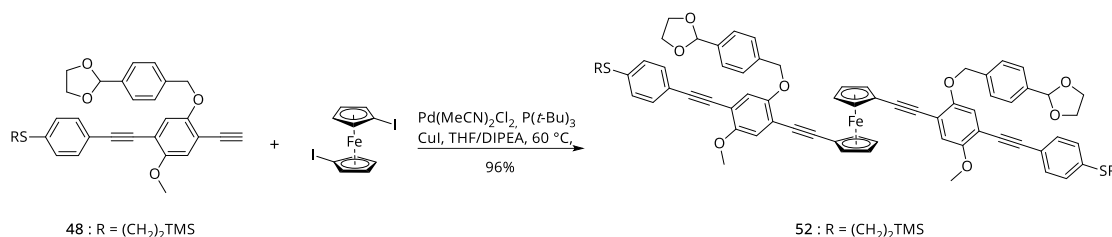
An oven-dried 25 mL Schlenk flask was purged with argon and charged with Pd(MeCN)$_2$Cl$_2$ (12.1 mg, 10 mol-%) CuI (8.8 mg, 10 mol-%) and 1,1'-diiodoferrocene (244 mg, 0.55 mmol). The reaction vessel was evacuated and backfilled with argon three times and suspended in a previously degassed and freshly distilled solvent mixture of THF/DIPA (4:3 mL). To the resulting reaction mixture, a stock solution of P(t-Bu)$_3$ (1 M in THF, 100 µl, 20 mol-%) was added and the reaction mixture was degassed for 15 min. Then, acetylene 48 (750 mg, 1.38 mmol) dissolved in 2 mL freshly distilled and deoxygenated THF was added and the mixture heated to 65 °C for 12 h. After the reaction was complete, the mixture was eluted with EtOAc and concentrated on silica. The volatiles were evaporated and the remaining silica powder subjected to flash column chromatography (SiO$_2$, EtOAc/cyclohexane 1:3), to isolate the disubstituted product 52 as a red solid. **Analytical data for ferrocene 52.** Yield 96% (680 mg, 0.54 mmol). ^{1}H NMR (400 MHz, CDCl$_3$, 25 °C): δ_H = 7.60 − 7.49 (m, 8H), 7.43 (d, $^3J_{HH}$ = 8.0 Hz, 4H), 7.20 (d, $^3J_{HH}$ = 8.1 Hz, 4H), 6.97 (s, 2H), 6.87 (s, 2H), 5.82 (s, 2H), 5.04 (s, 4H), 4.59 − 4.50 (m, 4H), 4.37 − 4.25 (m, 4H), 4.16 − 3.94 (m, 8H), 3.77 (s, 6H), 3.03 − 2.94 (m, 4H), 0.99 − 0.89 (m, 4H), 0.06 (s, 18H) ppm. ^{13}C NMR (101 MHz, CDCl$_3$, 25 °C): δ_C = 154.31, 152.94, 138.46, 138.31, 137.64, 132.08, 127.85, 127.08, 126.71, 120.23, 117.79, 115.19, 115.07, 112.71, 103.64, 94.81, 93.62, 86.17, 83.24, 73.04, 71.42, 70.88, 67.20, 65.40, 56.45, 29.06, 16.78, 0.15 ppm. HRMS (ESI-ToF): calcd. for [C$_{74}$H$_{74}$FeO$_8$S$_2$Si$_2$]$^+$ 1266.3710; found 1266.3697.

Bis-aldehyde 53

52 : R = (CH$_2$)$_2$TMS

53 : R = (CH$_2$)$_2$TMS
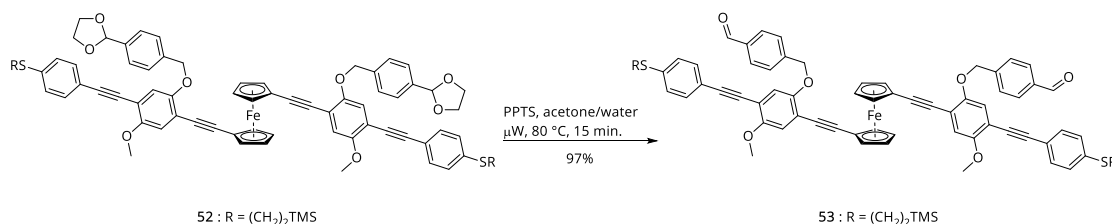
A 100 mL round bottom flask was charged with dioxolane 52 (680 mg, 0.54 mmol) in acetone (25 mL), 5 mL DCM and PPTS (109 mg, 0.43 mmol). Then, 5 mL water was added and the mixture was degassed for 15 min. The mixture was heated to 80 °C for 4 h. The solvent was removed in vacuum and the remaining substance was diluted with DCM and washed with 1 M HCl, NaHCO$_3$, water and brine. The organic phase was dried over MgSO$_4$ and concentrated under reduced presure to afford the target compound sufficiently pure as orange solid. **Analytical Data for 53**. Yield 97% (613 mg, 0.52 mmol). ^{1}H NMR (400 MHz, CDCl$_3$, 25 °C): δ_H = 9.98 (s, 2H), 7.93 − 7.85 (m, 4H), 7.70 (d, $^3J_{HH}$ = 7.9, 4H), 7.46 − 7.39 (m, 4H), 7.22 − 7.16 (m, 4H), 6.90 (s, 2H),

6.83 (s, 2H), 5.00 (s, 4H), 4.55 (pseudo-t, $^3J_{HH}$ = 1.9 Hz, 4H), 4.35 (pseudo-t, $^3J_{HH}$ = 1.9 Hz, 4H), 3.76 (s, 6H), 3.05 – 2.94 (m, 4H), 0.99 – 0.91 (m, 4H), 0.06 (s, 18H). ^{13}C NMR (101 MHz, CDCl$_3$, 25 °C): δ_C = 192.00, 154.50, 152.51, 144.24, 138.68, 135.96, 132.08, 129.98, 127.83, 127.17, 120.10, 117.50, 115.15, 114.99, 112.81, 95.04, 93.65, 85.98, 83.39, 73.12, 71.12, 70.24, 67.49, 56.44, 29.05, 16.80, -1.58. HRMS (ESI-ToF): calcd. for [C$_{70}$H$_{66}$FeO$_6$S$_2$Si$_2$]$^+$ 1182.3499; found 1182.3487.

Bis-alcohol **54**

53 : R = (CH$_2$)$_2$TMS   54 : R = (CH$_2$)$_2$TMS
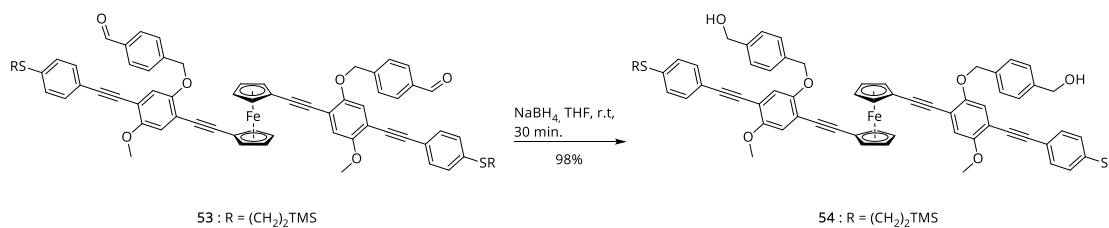
Bis-aldehyde **53** (613 mg, 0.52 mmol) was dissolved in dry and deoxygenated THF (50 mL) and NaBH$_4$ (205 mg, 5.20 mmol) was added portion wise. The reaction was stirred for 15 min at room temperature, when TLC showed full conversion. The reaction mixture was cooled down to 0 °C and aq. NH$_4$Cl (20%, 50 ml) was slowly added. After extraction with EtOAc, the combined organic phases were washed with water and brine. Drying over MgSO$_4$, filtration and removal of the solvent, the remaining orange residue was purified by column chromatography (SiO$_2$, EtOAc/cyclohexane, 1:1) to give the desired product as red-orange solid. **Analytical Data for 54**. Yield 98% (602 mg, 0.51 mmol). ^{1}H NMR (400 MHz, CDCl$_3$, 25 °C): δ_H = 7.51 (d, $^3J_{HH}$ = 8.1 Hz, 4H), 7.44 (d, $^3J_{HH}$ = 8.4 Hz, 4H), 7.35 (d, $^3J_{HH}$ = 8.0 Hz, 4H), 7.23 – 7.18 (m, 4H), 6.98 (s, 2H), 6.88 (s, 2H), 5.01 (s, 4H), 4.63 (s, 4H), 4.51 (pseudo-t, J = 1.9 Hz, 4H), 4.29 (pseudo-t, J = 1.9 Hz, 4H), 3.79 (s, 6H), 3.03 – 2.93 (m, 4H), 1.89 (s, 2H), 0.99 – 0.91 (m, 4H), 0.06 (s, 18H) ppm. ^{13}C NMR (101 MHz, CDCl$_3$, 25 °C): δ_C = 154.29, 153.04, 140.63, 138.55, 136.58, 132.08, 127.84, 127.47, 127.22, 120.16, 117.80, 115.13, 115.08, 112.78, 94.88, 93.56, 86.11, 83.24, 77.36, 77.16, 73.09, 71.37, 71.02, 67.18, 65.22, 56.46, 29.04, 16.77, 0.15, -1.59 ppm. HRMS (ESI-ToF): calcd. for [C$_{70}$H$_{70}$Fe O$_6$S$_2$Si$_2$]$^+$ 1178.3196; found 1178.3196.

Mono- and bis-bromo **58/59**

54 : R = (CH$_2$)$_2$TMS   58 : R = (CH$_2$)$_2$TMS, R' = OH, R' = Br
                                        59 : R = (CH$_2$)$_2$TMS, R' = R' = Br

A dried 20 mL round-bottomed flask was purged with argon and charged with bis-alcohol **54** (50 mg, 0.04 mmol) and dissolved in freshly distilled and desoxygenated THF (10 mL). The

Flask was placed in a Dewar filled with salt/ice and cooled to approx. -18 °C. Then, NaH (168 mg, 4.2 mmol) was added and the mixture was stirred for 10 min, before methanesulfonyl chloride (14.6 mg dissolved in freshly distilled THF (100 µL, 1.2 M, 0.13 mmol) was added and the mixture stirred for 16 h (MALDI-ToF control), after all reagent was consumed, LiBr (73 mg, 0.84 mmol) was added and the reaction mixture was stirred for 2 h at room temperature. When the reaction was finished, the mixture was diluted with EtOAc (50 mL) and quenched, by dropwise addition of water (10 mL). The aqueous phase was extracted with EtOAc (2 x 50 mL). The organic phase was washed with water and brine, dried over $MgSO_4$, filtered and the solvent was removed under reduced pressure. The crude product was subject to column chromatography. (SiO_2, DCM/cyclohexane, 1:5 then EtOAc/cyclohexane, 1:5 to EtOAc/cyclohexane 1:1). **Analytical Data for Bis-bromo 59**: Yield 24% (13 mg, 0.01 mmol). ^{1}H NMR (400 MHz, $CDCl_3$, 25 °C): δ_H = 7.52 (d, $^3J_{HH}$ = 8.1 Hz, 4H), 7.46 – 7.38 (m, 8H), 7.20 (d, 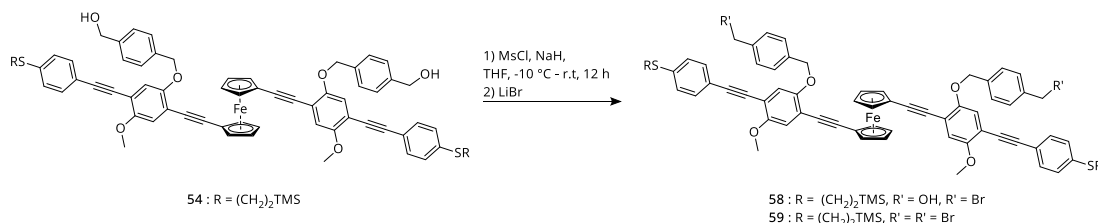$^3J_{HH}$ = 8.4, 4H), 6.97 (s, 2H), 6.86 (s, 2H), 5.00 (s, 4H), 4.51 (pseudo-t, J = 1.8 Hz, 4H), 4.48 (s, 4H), 4.30 (pseudo-t, J = 1.9 Hz, 4H), 3.78 (s, 6H), 3.03 – 2.94 (m, 4H), 0.99 – 0.91 (m, 4H), 0.06 (s, 18H) ppm. ^{13}C NMR (101 MHz, $CDCl_3$, 25 °C): δ_C = 154.35, 152.91, 138.56, 137.62, 137.47, 132.08, 129.31, 127.81, 127.58, 120.14, 117.81, 115.16, 115.03, 112.75, 94.89, 93.66, 86.08, 83.22, 73.05, 71.38, 70.80, 67.19, 56.45, 33.45, 29.03, 16.76, -1.59 ppm. HRMS (ESI-ToF): calcd. for $[C_{70}H_{68}Br_2FeNaO_4S_2Si_2]^+$ 1329.1706; found 1329.1697. **Analytical Data for Mono-bromo 58**: Yield 42% (22 mg, 0.02 mmol). ^{1}H NMR (500 MHz, $CDCl_3$, 25 °C): δ_H = 7.56 – 7.49 (m, 4H), 7.46 – 7.40 (m, 4H), 7.42 – 7.39 (m, 2H), 7.39 – 7.35 (m, 2H), 7.23 – 7.19 (m, 4H), 6.98 (s, 1H), 6.97 (s, 1H), 6.88 (s, 1H), 6.87 (s, 1H), 5.02 (s, 2H), 5.01 (s, 2H), 4.66 (d, $^3J_{HH}$ = 5.5 Hz, 2H), 4.52 (pseudo-t, J = 1.9 Hz, 2H), 4.49 (pseudo-t, J = 1.9 Hz, 2H), 4.47 (s, 2H), 4.29 (q, $^4J_{HH}$ = 1.7 Hz, 4H), 3.79 (s, 3H), 3.78 (s, 3H), 3.01 – 2.96 (m, 4H), 0.97 – 0.92 (m, 4H), 0.06 (s, 18H) ppm. ^{13}C NMR (151 MHz, $CDCl_3$, 25 °C): δ_C = 154.37, 154.30, 153.03, 152.93, 140.66, 138.58, 138.55, 137.61, 137.48, 136.63, 132.09, 129.32, 127.84, 127.84, 127.60, 127.51, 127.26, 120.17, 120.13, 117.87, 117.83, 115.19, 115.12, 115.09, 112.80, 112.77, 94.93, 94.86, 93.72, 93.59, 86.12, 86.05, 83.21, 83.16, 73.12, 73.10, 71.41, 71.38, 71.03, 70.87, 67.18, 67.10, 65.29, 56.48, 56.46, 43.53, 40.51, 33.44, 32.08, 30.31, 29.85, 29.81, 16.78, 14.28, -1.58 ppm. HRMS (ESI-ToF): calcd. for $[C_{70}H_{69}BrFeNaO_5S_2Si_2]^+$ 1267.2554; found 1267.2548.

Ether bridged ferrocene **55**

58 : R = (CH₂)₂TMS   NaH, THF, 50 °C   55 : R = (CH₂)₂TMS
                                    45%
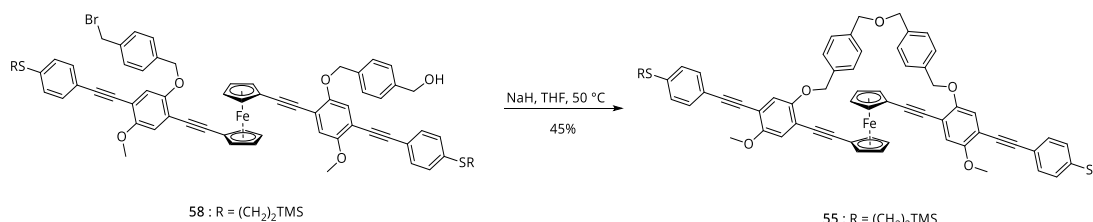
A dried, 50 mL round-bottomed flask was purged with argon and charged with mono-bromo **58** (26.0 mg, 0,02 mmol) and dissolved in freshly distilled and desoxygenated THF (20 mL, 1 mM). NaH (42 mg, 1.00 mmol) was added and the mixture stirred for 2 h at 50 °C, after all starting material was consumed (MALDI-ToF control), the reaction mixture was quenched with water (5 mL). The aqueous phase was extracted with EtOAc (2 x 25 mL) and the combined organic phas-

es were washed with water and brine, dried over MgSO4, filtered and volatiles were removed under reduced pressure. The crude product was subject to column chromatography (SiO$_2$, DCM/cyclohexane, 1:5) to afford the title compound as red-orange solid. **Analytical Data for 55:** Yield 45% (11.0 mg, 9.44 μmol). ^{1}H NMR (400 MHz, Chloroform-d) δ = 7.65 (d, $^3J_{HH}$ = 7.8 Hz, 4H), 7.51 – 7.43 (m, 8H), 7.24 (s, 2H), 7.15 (s, 2H), 6.98 (s, 2H), 5.11 (s, 4H), 4.62 (pseudo-t, J = 1.9 Hz, 4H), 4.59 (s, 4H), 4.34 (pseudo-t, J = 1.8 Hz, 4H), 3.91 (s, 6H), 3.03 – 2.96 (m, 4H), 0.99 – 0.92 (m, 4H), 0.06 (s, 18H) ppm. ^{13}C NMR (101 MHz, CDCl3) δ 154.46, 153.32, 138.62, 138.04, 136.72, 132.08, 128.15, 127.94, 127.48, 120.20, 117.60, 115.22, 114.90, 112.86, 94.97, 94.12, 86.15, 83.09, 72.87, 72.73, 71.22, 70.86, 65.63, 56.62, 29.09, 16.81, -1.60 ppm. HRMS (ESI-ToF): calcd. for [C$_{70}$H$_{70}$FeNaO$_6$S$_2$Si$_2$]$^+$ 1205.3396; found 1205.3395.

Ferrocene 36

55 : R = (CH$_2$)$_2$TMS   36
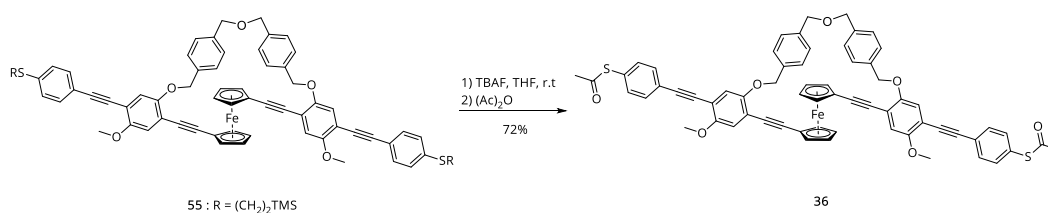
A 15 mL oven-dried round-bottomed flask was flushed with argon and charged with ether bridged ferrocene **55** (9 mg, 7.72 μmol) and dissolved in 5 mL freshly distilled and deoxygenated THF. To the mixture, TBAF (1 M in THF, 77.0 μL, 77.0 μmol) was added at room temperature. The reaction mixture was stirred for 45 min, then acetic anhydride (73.0 μL, 772 μmol) was added at 0 °C. After stirring for 15 min at 0 °C, the reaction mixture was quenched with ice and extracted with CH$_2$Cl$_2$. The aqueous phase was washed twice with CH$_2$Cl$_2$. The combined organic phases were washed twice with water and brine, dried with MgSO$_4$ and the solvent was evaporated. The crude was purified by filtration over a silica plug eluting with CH$_2$Cl$_2$. Affording the product as orange solid. **Analytical Data for 36:** Yield 72% (5.8 mg, 6.0 μmol). ^{1}H NMR (400 MHz, CDCl$_3$, 25 °C): δ_H = 7.62 (d, $^3J_{HH}$ = 7.9 Hz, 4H), 7.59 (d, $^3J_{HH}$ = 8.3 Hz, 4H), 7.46 (d, $^3J_{HH}$ = 7.8 Hz, 4H), 7.43 – 7.38 (m, 4H), 7.14 (s, 2H), 6.95 (s, 2H), 5.10 (s, 4H), 4.75 (brs, 4H), 4.59 (s, 4H), 4.47 (brs, 4H), 3.90 (s, 6H), 2.44 (s, 6H) ppm. ^{13}C NMR (101 MHz, CDCl3) δ = 193.61, 154.61, 153.24, 138.03, 136.65, 134.30, 132.31, 131.02, 128.13, 117.60, 114.89, 112.35, 94.22, 72.86, 72.74, 71.18, 70.86, 68.27, 65.56, 65.45, 58.60, 56.59 ppm. HRMS (ESI-ToF): calcd. for [C$_{64}$H$_{48}$FeNaO$_7$S$_2$]$^+$ 1071.2085; found 1071.2077.

Bis-mesylate 57

54 : R = (CH$_2$)$_2$TMS   57 : R = (CH$_2$)$_2$TMS
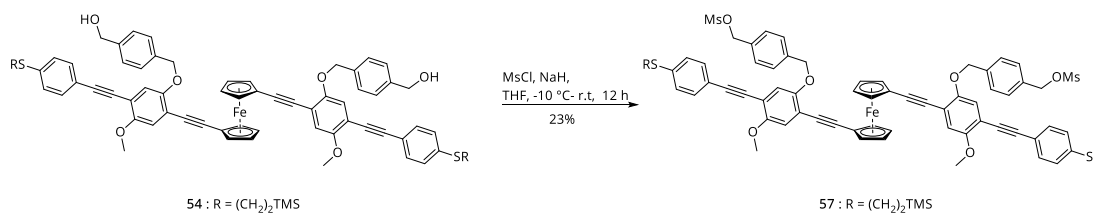
An oven-dried 25 ml Schlenk tube was purged with argon and charged with bis-alcohol **54** (73.0 mg, 0,06 mmol) and dissolved in freshly distilled THF 20 mL, the solution was cooled to -10 °C

and NaH (41.0 mg, 1.23 mmol) was added. The mixture was stirred for 10 min, before methanesulfonyl chloride (41.1 µL, 0.61 mmol) was added and the mixture stirred for overnight. After all reagent was consumed (MALDI-ToF control), the reaction was quenched, by dropwise addition of 10 mL water. The suspension was separated and the aq. phase extracted with EtOAc. The organic phase was washed with water, brine and dried over $MgSO_4$. The extract was filtered and concentrated under reduced pressure to afford the crude product was purified by FCC (SiO_2, EtOAc/cyclohexane, 1:5) as orange solid. **Analytical Data for 57** Yield 23% (18.7 mg, 14.0 µmol). ^{1}H NMR (400 MHz, $CDCl_3$, 25 °C): δ_H = 7.58 (d, $^3J_{HH}$ = 8.0 Hz, 4H), 7.47 − 7.39 (m, 8H), 7.21 (d, $^3J_{HH}$ = 8.4 Hz, 3H), 6.96 (s, 2H), 6.88 (s, 2H), 5.20 (s, 4H), 5.02 (s, 4H), 4.51 (pseudo-t, J = 1.9 Hz, 4H), 4.32 (pseudo-t, J = 1.9 Hz, 4H), 3.79 (s, 6H), 3.02 − 2.95 (m, 4H), 2.88 (s, 6H), 0.99 − 0.91 (m, 4H), 0.06 (s, 18H) ppm. ^{13}C NMR (101 MHz, $CDCl_3$, 25 °C): δ_C = 154.41, 152.79, 138.65, 133.04, 132.06, 129.15, 127.81, 127.61, 120.05, 117.79, 115.11, 112.84, 94.99, 93.63, 86.00, 83.20, 77.36, 73.12, 71.34, 70.67, 56.46, 38.48, 29.01, 16.76, 0.14, -1.59 ppm. MALDI-ToF (DCTB): m/z (%)= 1338.248 (100), 1339.221 (87), 1340.194 (55), 1341.056 (22), 1342.055 (5).

Sulfide bridged ferrocene 62

57 : R = (CH$_2$)$_2$TMS

62 : R = (CH$_2$)$_2$TMS

An oven-dried round-bottomed flask was purged with argon and charged with sodium sulfide nonahydrate (3.28 mg, 13.4 µmol) dissolved in ethanol/toluene (1:1, 10 mL) to the solution, bis-mesylate **57** (18 mg, 13.4 µmol) dissolved in toluene (10 mL) was added over a period of 1 h and the mixture was stirred for 5 h. After the the reaction was finished (MALDI-ToF), the solvent was removed under reduced pressure and the crude product was subject to column chromatography (SiO_2, CH_2Cl_2/cyclohexane, 1:5) to afford sulfide **62** as orange solid. **Analytical Data for 62**: Yield 49% (7.8 mg, 4 µmol). ^{1}H NMR (400 MHz, $CDCl_3$, 25 °C): δ_H = 7.62 (d, $^3J_{HH}$ = 7.8 Hz, 4H), 7.47 (d, $^3J_{HH}$ = 8.4 Hz, 4H), 7.40 (d, $^3J_{HH}$ = 8.1 Hz, 4H), 7.24 (d, $^3J_{HH}$ = 8.4 Hz, 4H), 7.14 (s, 2H), 6.99 (s, 2H), 5.11 (s, 4H), 4.70 (pseudo-t, J = 1.9, 4H), 4.46 − 4.41 (m, 4H), 3.91 (s, 6H), 3.54 (s, 4H), 3.04 − 2.95 (m, 4H), 1.00 − 0.91 (m, 4H), 0.06 (s, 18H) ppm. ^{13}C NMR (101 MHz, CD_2Cl_2, 25 °C): δ_C = 154.85, 153.43, 139.51, 138.40, 136.38, 132.29, 129.75, 128.03, 127.52, 120.30, 117.85, 115.45, 115.32, 113.13, 95.07, 93.91, 86.56, 83.72, 73.10, 72.97, 71.35, 66.73, 56.91, 34.60, 29.21, 17.09, -1.58 ppm. HRMS (ESI-ToF): calcd. for $[C_{70}H_{68}FeNaO_4S_3Si_2]^+$ 1203.3062; found 1203.3056.

Sulfide bridged ferrocene 63

62 : R = (CH$_2$)$_2$TMS

1) TBAF, THF, r.t
2) (Ac)$_2$O

60%

63
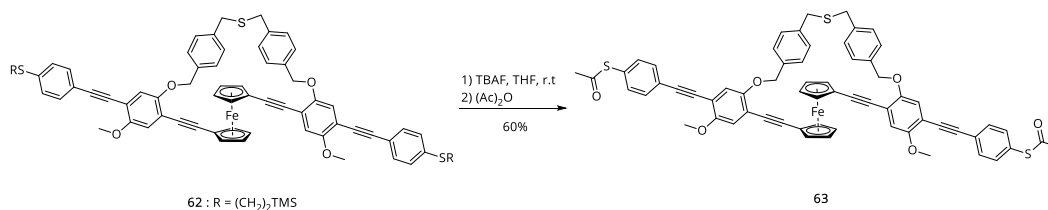
A 5 mL dried round-bottomed microwave-vial was flushed with argon and charged with thi-oether bridged ferrocene **62** (9.6 mg, 8.1 μmol) and dissolved in 5 mL freshly distilled and deoxygenated THF. To the Mixture TBAF (1 M in THF, 325 μL, 325 μmol) was added at room temperature. The reaction mixture was stirred for 45 min, then acetic anhydride (168 μL, 16.2 mmol) was added at 0 °C. After stirring for 15 min at 0 °C, the reaction mixture was quenched with ice and extracted with CH$_2$Cl$_2$. The aqueous phase was washed twice with DCM. The combined organic phases were washed twice with water and brine, dried with MgSO$_4$ and the solvents were evaporated. The crude was purified by filtration over a silica plug (in a Pasteur pipette) eluting with DCM to isolate the product as orange solid. **Analytical Data for 63**: Yield 60% (5.2 mg, 5.0 μmol). ^{1}H NMR (400 MHz, CDCl$_3$, 25 °C): δ_H = 7.62 − 7.55 (m, 8H), 7.42 − 7.34 (m, 8H), 7.13 (s, 2H), 6.95 (s, 2H), 5.10 (s, 4H), 4.81 (brs, 4H), 4.53 (brs, 4H), 3.91 (s, 6H), 3.55 (s, 4H), 2.44 (s, 6H) ppm. ^{13}C NMR (101 MHz, CDCl$_3$, 25 °C): δ_C = 193.61, 154.61, 153.01, 137.81, 135.92, 134.30, 132.35, 129.42, 128.24, 127.05, 124.69, 117.57, 115.50, 115.05, 112.45, 94.28, 93.94, 87.61, 72.61, 70.92, 56.60 ppm. HRMS (ESI-ToF): calcd. for [C$_{64}$H$_{48}$FeNaO$_6$S$_3$]$^+$ 1087.1856; found 1087.1853.

Bis-ethynyl 64

53 : R = (CH$_2$)$_2$TMS

B-O-R, Cs$_2$CO$_3$,
THF/MeOH, r.t

78%

64 : R = (CH$_2$)$_2$TMS
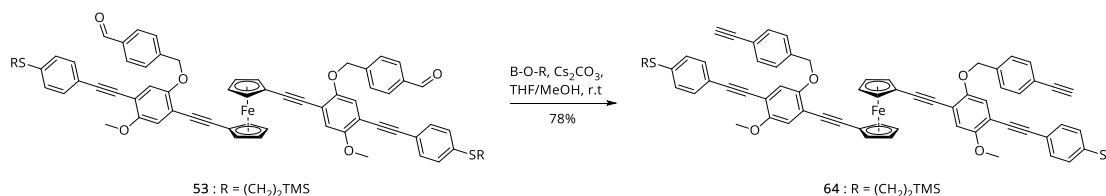
An oven-dried round-bottomed 50 mL flask was charged with bis-aldehyde **53** (130 mg, 0.11 mmol) and Cs$_2$CO$_3$ (179 mg, 0.55 mmol) in a mixture of absolute methanol (10 mL) and freshly distilled THF (10 mL). The mixture was degassed for 15 min, before the Bestmann-Ohira Reagent (40.8 μL, 0.26 mmol) was added to the heterogenous mixture. The mixture was stirred at r.t. for 4 h under an argon atmosphere. After MALDI control indicated full conversion, the crude mixture was filtered through a short pad of Celite eluting with CH$_2$Cl$_2$. The organic solvent was removed under reduced pressure and the residue was dissolved in CH$_2$Cl$_2$, washed with NaHCO$_3$, water and brine. The org. phase was dried over MgSO$_4$, filtered and the solvent removed in vacuo, to give the target compound sufficiently pure as orange solid. **Analytical Data for 64:** Yield 78% (100 mg, 85.0 μmol). ^{1}H NMR (400 MHz, CDCl$_3$, 25 °C): δ_H = 7.41 − 7.32 (m, 8H), 7.22 − 7.17 (m, 4H), 7.06 − 7.01 (m, 4H), 6.77 (s, 2H), 6.68 (s, 2H), 4.81 (s, 4H), 4.39 (pseudo-t, J = 1.9 Hz, 4H), 4.17 (pseudo-t, J = 1.9 Hz, 4H), 3.61 (s, 6H), 3.10 (s, 2H), 2.86 − 2.80 (m, 4H), 0.79 (m, 4H), -0.10 (s, 18H) ppm. ^{13}C NMR (101 MHz, CDCl$_3$, 25 °C): δ_C = 154.37, 152.76, 138.16, 132.33, 132.09, 129.87, 128.18, 127.83, 126.90, 121.55, 120.18, 117.69, 114.96,

112.71, 94.88, 93.57, 86.10, 83.69, 83.39, 73.03, 71.24, 70.59, 67.44, 60.55, 56.43, 29.85, 16.79, 14.36, -1.58 ppm. HRMS (ESI-ToF): calcd. for $[C_{72}H_{66}FeNaO_4S_2Si_2]^+$ 1193.3185; found 1193.3182.
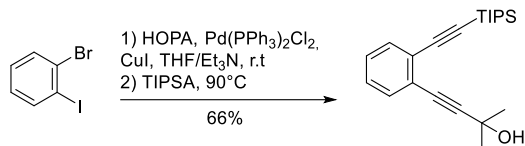
2-methyl-4-(2-((triisopropylsilyl)ethynyl)phenyl)but-3-yn-2-ol 79

An oven-dried round-bottomed flask was purged with argon and charged with 1-bromo-2-iodobenzene (5.0 g, 17.7 mmol), copper(I)iodide (206 mg, 6 mol-%) and $PdCl_2(PPh_3)_2$ (627 mg, 5 mol-%) were dissolved in a 3:1 mixture of THF/NEt_3. The solution was degassed for 20 min. with a stream of argon. To the mixture, 2-methyl-3-butyn-2-ol (1.85 mL, 18.6 mmol) was added dropwise and the mixture was stirred for 3 h at 50 °C. After full consumption, (triisopropylsilyl)acetylene (16.4 ml, 70.8 mmol) was added under argon atmosphere, and the reaction mixture was stirred for 12 h at 90°C. After the mixture was cooled to room temperature, the solvent was removed under reduced pressure, and the remaining slurry dissolved in methylene chloride and concentrated on Hyflo. The residue was purified by column chromatography (SiO_2, c-Hex/EtOAc, 5:1). The product was isolated as colorless oil. **Analytic Data for 79**: Yield 66% (3.99 g, 11.7 mmol). ^{1}H NMR (400 MHz, CDCl$_3$, 25 °C): δ_H = 7.51 − 7.44 (m, 1H), 7.44 − 7.38 (m, 1H), 7.25 − 7.21 (m, 2H), 2.08 (s, 1H), 1.62 (s, 6H), 1.15 (s, 21H) ppm. ^{13}C NMR (101 MHz, CDCl$_3$, 25 °C): δ_C = 133.17, 132.44, 128.07, 127.96, 125.75, 125.15, 105.51, 97.65, 94.75, 81.15, 65.82, 31.54, 18.90, 11.45 ppm. HRMS (ESI-ToF): calcd. for $[C_{22}H_{33}OSi]^+$ 341.2295; found 341.2297.

4-(2-ethynylphenyl)-2-methylbut-3-yn-2-ol 81
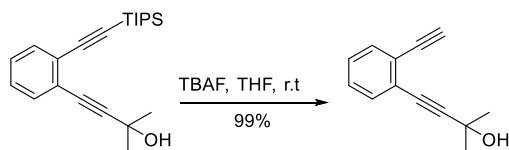
A 100-mL round-bottomed flask was purged with argon and charged with TIPS protected acetylene 79 (1.50 g, 1.4 mmol) dissolved in 50 mL THF. The solution was degassed for 15 min. with an argon stream. Then, a TBAF solution (1 M in THF, 4.84 ml, 4.84 mmol) was added and the mixture was stirred for 1 h at room temperature. After all starting material was consumed, the reaction was quenched with water (10 mL) and extracted with EtOAc (3 x 50 mL). The organic phase was washed with water (50 mL) and brine (50 mL) and dried over MgSO$_4$. The extract was filtered and concentrated under reduced pressure to afford the crude product. The remaining white solid was washed with MeOH, filtered and dried under vaccum to give the product as white solid. **Analytical data for 81**: Yield 99% (810 mg, 4.40 mmol). ^{1}H NMR (400 MHz, CDCl$_3$, 25 °C): δ_H = 7.51 − 7.47 (m, 1H), 7.45 − 7.39 (m, 1H), 7.32 − 7.22 (m, 2H), 7.26 (s, 1H), 3.30 (s, 1H), 1.89 − 1.71 (s, 1H), 1.64 (s, 6H) ppm. ^{13}C NMR (101 MHz, CDCl$_3$, 25 °C): δ_C =

132.46, 131.71, 128.47, 127.97, 125.73, 124.78, 98.00, 82.07, 80.88, 80.64, 65.74, 31.40 ppm. HRMS (ESI-ToF): calcd. for $[C_{13}H_{12}NaO]^+$ 207.0780; found 207.0779.

1,1`-bis((2-ethynylphenyl)2-methylbut-3-yn-ol)-ferrocene **83**
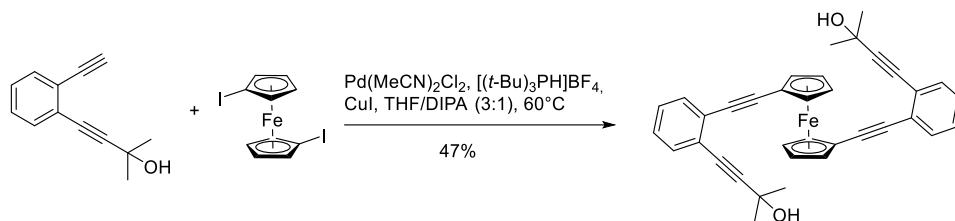
An oven-dried two-necked round-bottomed flask was purged with argon and charged with $Pd(MeCN)_2Cl_2$ (22.2 mg, 6 mol-%), $[(t\text{-}Bu)_3PH]BF_4$ (50 mg, 12 mol-%), CuI (16.2 mg, 6 mol-%) and 1,1´-diiodoferrocene (617 mg, 1.41 mmol). The flask was evacuated and backfilled with argon, before freshly distilled and deoxygenated THF (15 ml) was added. Then acetylene **81** (779 mg, 4.23 mmol) dissolved in DIPA (5 ml) was added and the mixture was degassed with a stream of argon for 15 min. The mixture was heated to 60 °C for 12 h. When all starting material was consumed, the reaction mixture was diluted with DCM and concentrated on Hyflo. The remaining powder was subjected to a FCC (SiO_2, c-Hex/EtOAc, 5:1 then 3:1) to elute the mono substituted product **7** as highly viscous red oil and the disubstituted product **83** as red-orange powder. **Analytical Data for 83**: Yield 47% (365 mg, 0.66 mmol). ^1H NMR (400 MHz, $CDCl_3$, 25 °C): δ_H = 7.34 − 7.30 (m, 2H), 7.30 − 7.27 (m, 2H), 7.16 (td, $^3J_{H,H}$ = 7.6 Hz, $^4J_{H,H}$ = 1.5 Hz, 2H), 7.10 (td, $^3J_{H,H}$ = 7.5 Hz, $^4J_{H,H}$ = 1.5 Hz, 2H), 4.59 (pseudo-t, $J_{H,H}$ = 1.9 Hz, 4H), 4.34 (pseudo-t, J = 1.9 Hz, 4H), 2.51 (s, 2H), 1.65 (s, 12H) ppm. ^{13}C NMR (101 MHz, $CDCl_3$, 25 °C): δ_C = 131.77, 131.57, 127.96, 127.20, 126.65, 124.69, 97.83, 91.15, 86.05, 81.46, 72.98, 71.07, 67.58, 65.82, 31.74 ppm. HRMS (ESI-ToF): calcd. for $[C_{36}H_{30}FeNaO_2]^+$ 573.1488; found 573.1486.

1-((2-ethynylphenyl)2-methylbut-3-yn-ol),1'-((2-ethynylphenyl)ethynyl)-ferrocene **85**
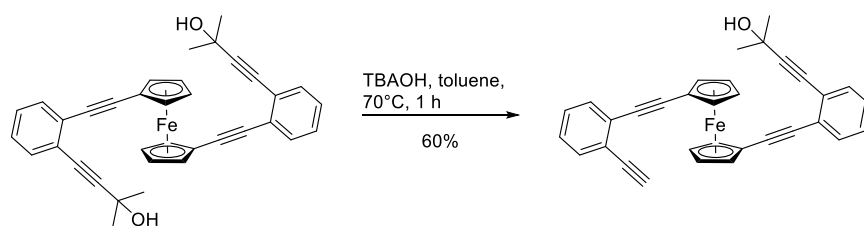
A 100-mL round-bottomed flask was charged with **83** (100 mg, 0.18 mmol) and dissolved anhydrous toluene (50 mL). The solution was degassed for 30 min. then TBAOH (1 M in methanol, 182 μL, 0.18 mmol) was added and the mixture heated to 70 °C for 1 h. The progress was controlled via TLC and stopped when no more starting material was observed. After cooling down to room temperature, the mixture was washed successively with NH_4Cl (25 mL), water (25 mL) and brine, dried over $MgSO_4$, filtered and concentrated in vacuum. The crude product was then purified by column chromatography (SiO_2, c-Hex/EtOAc, 5:1) to afford the product as orange solid. **Analytical Data for 85**: Yield 60% (54 mg, 0.11 mmol). ^1H NMR (400 MHz, $CDCl_3$, 25 °C): δ_H = 7.53 − 7.31 (m, 4H), 7.25 − 7.17 (m, 4H), 4.59 (pseudo-q, J = 1.7 Hz, 4H), 4.37 (pseu-

do-dt, J = 4.9, 1.9 Hz, 4H), 3.37 (s, 1H), 2.19 (s, 1H), 1.67 (s, 6H) ppm. ^{13}C NMR (101 MHz, CDCl$_3$, 25 °C): δ_C = 132.60, 131.89, 131.74, 131.72, 128.56, 128.07, 127.44, 127.37, 126.95, 126.61, 97.77, 91.84, 91.59, 85.57, 85.14, 82.75, 81.36, 81.21, 73.39, 73.34, 71.54, 67.08, 66.88, 65.86, 31.74, 29.84 ppm. HRMS (ESI-ToF): calcd. for [C$_{33}$H$_{24}$FeNaO]$^+$ 515.1069; found 515.1068.

Bis-ferrocene **86**
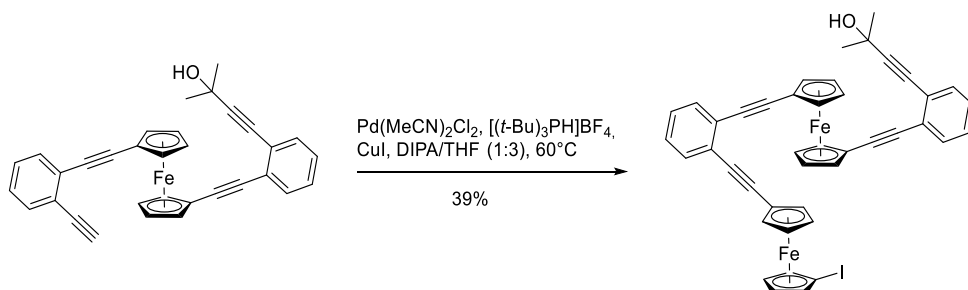
An oven-dried Schlenk flask was purged with argon and charged with Pd(MeCN)$_2$Cl$_2$ (10.8 mg, 10 mol-%), [(t-Bu)$_3$PH]BF$_4$ (24.1 mg, 20 mol-%), CuI (7.89 mg, 10 mol-%) and 1,1′-diiodoferrocene (902 mg, 2.06 mmol). The flask was evacuated and backfilled with argon, before freshly distilled and deoxygenated THF (18 mL) was added. Then, acetylene **85** (203 mg, 0.41 mmol) dissolved in DIPA (6 mL) was added and the mixture degassed with a stream of argon for 15 min. The mixture was heated to 60 °C for 12 h. When all starting material was consumed, the reaction mixture was diluted with CH$_2$Cl$_2$ and concentrated on Hyflo. The remaining powder was subjected to a FCC (SiO$_2$, c-Hex/EtOAc, 5:1) to isolate the bis-ferrocene **86** as a red solid. **Analytical Data for 86**: Yield 39% (129 mg, 0.16 mmol). ^{1}H NMR (400 MHz, CDCl$_3$, 25 °C): δ_H = 7.51 − 7.46 (m, 1H), 7.45 − 7.33 (m, 3H), 7.25 − 7.13 (m, 4H), 4.63 (pseudo-t, J = 1.9 Hz, 2H), 4.59 (pseudo-t, J = 1.9 Hz, 2H), 4.54 (pseudo-t, J = 1.9 Hz, 2H), 4.45 (pseudo-t, J = 1.8 Hz, 2H), 4.37 (pseudo-t, J = 1.9 Hz, 2H), 4.35 (pseudo-t, J = 1.9 Hz, 2H), 4.25 (pseudo-t, J = 1.9 Hz, 2H), 4.22 (pseudo-t, J = 1.8 Hz, 2H), 2.18 (s, 1H), 1.67 (s, 6H) ppm. ^{13}C NMR (101 MHz, CDCl$_3$, 25 °C): δ_C = 131.88, 131.83, 131.73, 128.04, 127.54, 127.47, 127.34, 126.62, 126.06, 125.97, 124.78, 97.79, 91.49, 91.35, 91.25, 86.13, 86.05, 85.71, 81.37, 76.46, 74.20, 73.14, 73.11, 72.60, 71.59, 71.50, 71.46, 67.48, 67.23, 67.04, 65.83, 40.87, 31.76 ppm. HRMS (ESI-ToF): calcd. for [C$_{43}$H$_{31}$Fe$_2$INaO]$^+$ 825.0012; found 825.0009.

Bis-ferrocene **87**
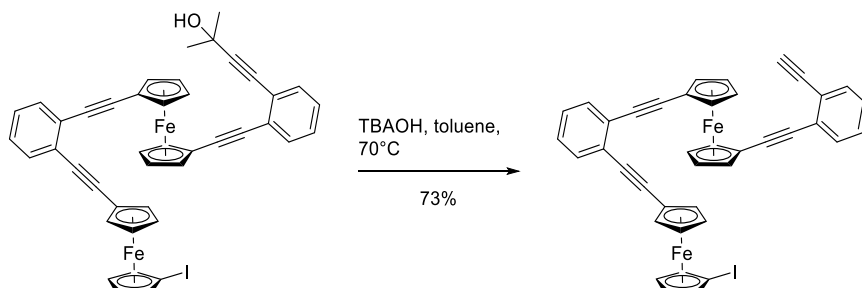
Bis-ferrocene **86** (25 mg, 31 µmol) was dissolved in anhydrous toluene (12 mL) and degassed for 15 min. then, TBAOH (1 M in methanol, 31.0 µL, 31.0 µmol) was added and the mixture was heated to 70 °C for 3 h. After cooling down to room temperature, the mixture was washed suc-

cessively with NH_4Cl, water and brine. The organic phase was dried over $MgSO_4$, filtered and concentrated under reduced pressure. The crude product was then purified by column chromatography (SiO_2, c-Hex/EtOAc, 5:1) to isolate the bis-ferrocene **87** as red solid. **Analytical Data for 87**: Yield 73% (17 mg, 23 µmol). ^{1}H NMR (400 MHz, $CDCl_3$, 25 °C): δ_H = 7.53 − 7.43 (m, 4H), 7.29 − 7.19 (m, 4H), 4.62 (pseudo-t, J = 1.9 Hz, 2H), 4.58 (pseudo-t, J = 1.9 Hz, 2H), 4.54 (pseudo-t, J = 1.9 Hz, 2H), 4.45 (pseudo-t, J = 1.9 Hz, 2H), 4.39 (pseudo-t, J = 1.9 Hz, 2H), 4.35 (pseudo-t, J = 1.9 Hz, 2H), 4.25 (pseudo-t, J = 1.9 Hz, 2H), 4.22 (pseudo-t, J = 1.9 Hz, 2H), 3.37 (s, 1H) ppm. ^{13}C NMR (101 MHz, $CDCl_3$, 25 °C): δ_C = 132.66, 131.97, 131.94, 131.85, 128.60, 127.63, 127.57, 127.52, 127.00, 126.10, 126.05, 124.51, 92.00, 91.63, 91.26, 86.10, 85.77, 85.00, 82.66, 81.26, 76.49, 74.24, 73.47, 72.60, 71.69, 71.67, 71.50, 67.53, 66.99, 66.61, 40.90 ppm. HRMS (ESI-ToF): calcd. for $[C_{40}H_{25}Fe_2INa]^+$ 766.9593; found 766.9594.

Bis-ferrocene **88**
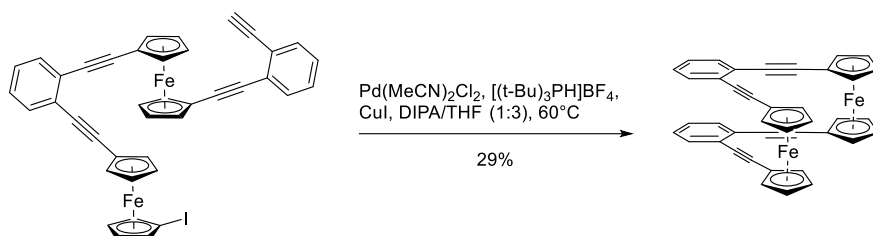
An oven-dried Schlenk flask was purged with argon and charged with bis-ferrocene **87** (17 mg, 22.8 µmol), $Pd(MeCN)_2Cl_2$ (2.99 mg, 11.4 µmol), CuI (2.18 mg, 11.4 µmol,) tri-*tert*-butylphosphonium tetrafluoroborate (6.68 mg, 22.8 µmol) and freshly distilled and deoxygenated THF (9 ml) and DIPA (3 mL) were added, the mixture was degassed for 10 min with an argon stream. Then the mixture was heated to 60 °C and stirred for 24 h. After all starting material was consumed, the mixture was diluted with CH_2Cl_2 and concentrated on Hyflo, then purified via column chromatography (SiO_2, 1:5 DCM/cHex) and size exclusion chromatography ($CHCl_3$) to isolate the product as a pale orange solid. **Analytical Data for 88**: Yield 29% (4 mg, 6.5 µmol). ^{1}H NMR (400 MHz, $CDCl_3$, 25 °C): δ_H = 7.03 (dd, $^3J_{H,H}$ = 5.8 Hz, $^4J_{H,H}$ = 3.3 Hz, 4H), 6.87 (dd, $^3J_{H,H}$ = 5.8 Hz, $^3J_{H,H}$ = 3.3 Hz, 4H), 4.60 (pseudo-t, J = 1.8 Hz, 8H), 4.34 (pseudo-t, J = 1.8 Hz, 8H) ppm. ^{13}C NMR (101 MHz, $CDCl_3$, 25°C): ^{13}C NMR from HMBC (151 MHz, $C_6D_4Cl_2$, 25 °C) δ_C = 127.24, 127.26, 72.03, 69.67, 70.15, 70.18, 69.68, 72.04 ppm. MALDI-MS: m/z (%) = 614.602(4), 615.408(5), 616.302 (100), 617.258(36), 618.192(6).

Crystals of **88** were grown from dichloromethane under slow evaporation at room temperature. Measured crystals were prepared under inert conditions immersed in perfluoropolyether as protecting oil for manipulation. The crystal was measured on a Bruker Kappa Apex2 diffractometer at 123K using graphitemonochromated Cu Kα-radiation with λ = 1.54178 Å, Θmax = 70.139°. Minimal/maximal transmission 0.59/0.77, µ = 8.851 mm-1. The Apex2 suite has been used for data collection and integration. From a total of 12826 reflections, 4571 were independent (merging r = 0.039). From these, 4571 were considered

as observed (I>2.0σ(I)) and were used to refine 380 parameters. The structure was solved by direct methods using the program SIR92. Least-squares refinement against Fsqd was carried

out on all nonhydrogen atoms using the program CRYSTALS. R = 0.0328 (observed data), wR = 0.0812 (all data), GOF = 0.8648. Minimal/maximal residual electron density = -0.23/0.53 e Å^{-3}. Chebychev polynomial weights were used to complete the refinement. Plots were produced using CAMERON. Crystallographic data (excluding structure factors) for the structure in this paper have been deposited with the Cambridge Crystallographic Data Center, the deposition number is (1515120). Copies of the data can be obtained, free of charge, on application to the CCDC, 12 Union Road, Cambridge CB2 1EZ, UK [fax: +44-1223- 336033 or e-mail: deposit@ccdc.cam.ac.uk].
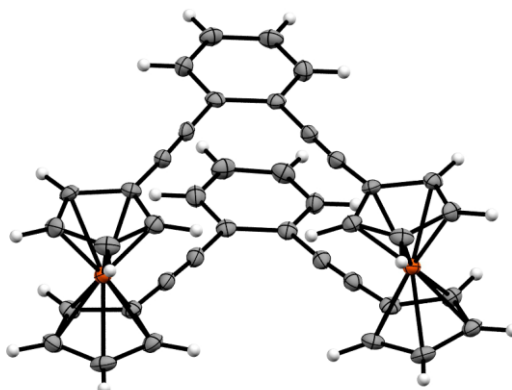
2-iodo-4-thiocyanatoaniline 89
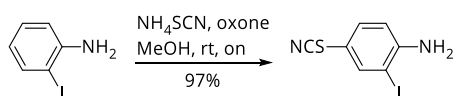
A 500 mL round-bottomed flask was charged with 2-iodoaniline (12.5 g, 55.9 mmol) and NH_4SCN (6.38 g, 83.9 mmol) and suspended in previously degassed methanol (350 mL). To this Oxone (25.8 g, 83.9 mmol) was added and stirred for 12 h at room temperature. As full conversion was observed, water (100 mL) was added and the aqueous phase was extracted with methylene chloride (3 x 250 mL). The combined organic layers were dried over $MgSO_4$, filtered and solvent was removed under reduced pressure. The crude solid was transferred into a sublimation flask and sublimed for 6 h at 110 °C with a pressure of 2.5 x 10^{-2} mbar. The product was isolated as a white crystalline solid. **Analytic Data for 89**: Yield 97% (15 g, 54.3 mmol). ^{1}H NMR (400 MHz, CDCl$_3$, 25 °C): δ_H = 7.86 (d, $^4J_{H,H}$ = 2.1 Hz, 1H), 7.36 (dd, $^3J_{H,H}$ = 8.5 Hz, $^4J_{H,H}$ = 2.2 Hz, 1H), 6.74 (d, $^3J_{H,H}$ = 8.5 Hz, 1H), 4.43 (s, 2H) ppm. ^{13}C NMR (101 MHz, CDCl$_3$, 25 °C): δ_C = 149.01, 143.12, 134.15, 115.00, 111.69, 110.71, 83.49 ppm. EA: C$_7$H$_5$IN$_2$S (276.09): calcd. C 30.45, H 1.83, I 45.96, N 10.15, S 11.61; found C 30.28, H 1.97, N 9.97.

1-bromo-2-iodo-4-thiocyanatobenzene 90
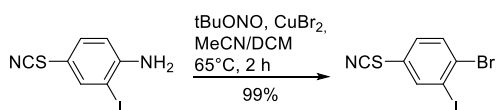
Anhydrous copper(II) bromide (2.92 g, 13.1 mmol) and *tert*-butyl nitrite (1.96 ml, 16.3 mmol) were suspended in anhydrous acetonitrile (270 mL) in a two-necked round-bottomed flask

equipped with a reflux condenser and a septum. The rapidly stirred mixture was heated to 65 °C and the amine **89** (3.01 g, 10.9 mmol) dissolved in CH_2Cl_2 (50 mL) was then slowly added via syringe. After TLC control showed full consumption, the reaction mixture was diluted with a sat. aqueous NH_4Cl solution and extracted with EtOAc (3 x 50 mL). The organic phase was washed with water (50 mL) and brine (50 mL). The combined organic phases were dried over $MgSO_4$, filtered and concentrated under reduced pressure. The residue was purified via FCC (SiO_2, cyclohexane/EtOAc, 10:1) to afford the title compound as off-white solid. **Analytic Data for 90:** Yield 99% (3.68 g, 10.8 mmol). ^{1}H NMR (400 MHz, $CDCl_3$, 25 °C): δ_H = 7.98 (d, $^4J_{H,H}$ = 2.3 Hz, 1H), 7.67 (d, $^3J_{H,H}$ = 8.4 Hz, 1H), 7.37 (dd, $^3J_{H,H}$ = 8.4 Hz, $^4J_{H,H}$ = 2.3 Hz, 1H) ppm. ^{13}C NMR (101 MHz, $CDCl_3$, 25 °C): δ_C = 140.69, 133.95, 131.82, 130.62, 124.70, 109.27, 102.86 ppm. EA: C_7H_3BrINS (339.97): calcd. C 24.73, H 0.89, Br 23.50, I 37.33, N 4.12, S 9.43; found C 25.13, H 1.10, N 4.37.

(4-bromo-3-iodophenyl)(*tert*-butyl)sulfane **96**

1-bromo-2-iodo-4-thiocyanatobenzene **90** (1.0 g, 2.93 mmol) was placed in an oven-dried argon flushed 100-mL round-bottomed flask and dissolved in dry THF (50 mL). To the clear solution LAH (1 M in THF, 3.08 ml, 3.08 mmol) was added dropwise at room temperature. After full conversion, a mixture of ice and THF followed by water was added ca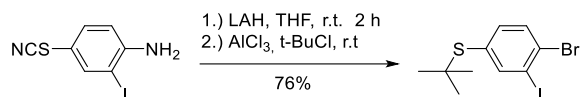refully to the reaction mixture. The product was extracted with methylene chlroide (3 x 70 mL) and successively washed with aq. HCl (1 M, 50 mL), water and brine. The organic layer was dried over $MgSO_4$, filtered and solvent was removed at vacuum. The crude thiol was placed in a 2-necked oven-dried argon flushed 50 mL round-bottomed flask equipped with a washing flask containing an aq. 1 M NaOH solution. 2-Chloro-2-methylpropane (2.51 mL, 22.9 mmol) was added followed by $AlCl_3$ (20.0 mg, 5 mol-%). After gas evolution, has stopped, methylene chloride (100 mL) was added and reaction mixture was quenched with aq. sat $NaHCO_3$ (50 mL). The crude product was extracted with methylene chloride (2 x 50 mL) and washed with brine (1 x 50 mL). The combined organic layers were dried over $MgSO_4$ and solvent was removed under reduced pressure. The residue was purified by column chromatography (SiO_2, c-Hex/EtOAc, 20:1) giving the product as a white solid. **Analytic Data for 96:** Yield 76% (830 mg, 2.24 mmol). ^{1}H NMR (250 MHz, $CDCl_3$, 25 °C): δ_H = 8.03 (d, $^4J_{H,H}$ = 2.1 Hz, 1H), 7.56 (d, $^3J_{H,H}$ = 8.2 Hz, 1H), 7.33 (dd, $^3J_{H,H}$ = 8.2 Hz, $^4J_{H,H}$ = 2.1 Hz, 1H), 1.28 (s, 9H) ppm. ^{13}C NMR (63 MHz, $CDCl_3$, 25 °C): δ_C = 148.19, 138.16, 133.71, 132.46, 130.73, 101.11, 46.73, 31.02 ppm. EA: $C_{10}H_{12}BrIS$ (371.07): calcd. C 33.37, H 3.26, Br 21.53, I 34.20, S 8.64; found C 32.32, H 3.31.

4-(5-(tert-butylthio)-2-((triisopropylsilyl)ethynyl)phenyl)-2-methylbut-3-yn-2-ol **97**
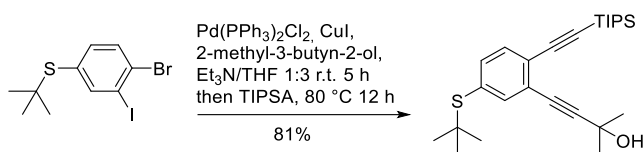
An oven-dried Schlenk tube was purged with argon and charged with $Pd(PPh_3)_2Cl_2$ (19.0 mg, 10 mol-%) CuI (5.23 mg, 10 mol-%) and **96** (100 mg, 0.27 mmol). The flask was evacuated and backfilled with argon before suspending in 20 mL of a 3:1 mixture of THF/NEt_3. The mixture was degassed with an argon stream for 20 min, then 2-methyl-3-butyn-2-ol (28.0 μl, 0.28 mmol) was added and the mixture was stirred for 5 h at room temperature. After all starting material was consumed (TLC control), (triisopropylsilyl)acetylene (250 μL, 1.08 mmol) was added and the mixture was heated to 80 °C for 16 h. After the reaction was complete, the mixture was concentrated on Hyflo which was subjected to flash column chromatography (SiO_2, cyclohexane/EtOAc, 1:5) to isolate the title compound as yellow oil. **Analytic Data for 97:** Yield 81% (93 mg, 0.22 mmol). ¹H NMR (400 MHz, $CDCl_3$, 25 °C): δ_H = 7.58 (d, $^4J_{H,H}$ = 1.7 Hz, 1H), 7.43 (d, $^3J_{H,H}$ = 8.0 Hz, 1H), 7.39 (dd, $^3J_{H,H}$ = 8.0 Hz, $^4J_{H,H}$ = 1.7 Hz, 1H), 2.02 (s, 1H), 1.62 (s, 6H), 1.15 (s, 21H) ppm. ¹³C NMR (101 MHz, $CDCl_3$, 25 °C): δ_C = 140.83, 136.79, 133.30, 133.01, 125.97, 125.35, 105.01, 98.09, 96.55, 80.65, 65.83, 46.83, 31.51, 31.15, 18.90, 11.44 ppm. HRMS (ESI-ToF): calcd. for $[C_{26}H_{40}NaOSSi]^+$ 451.2461; found 451.2463.

((4-(tert-butylthio)-2-ethynylphenyl)ethynyl)triisopropylsilane **98**
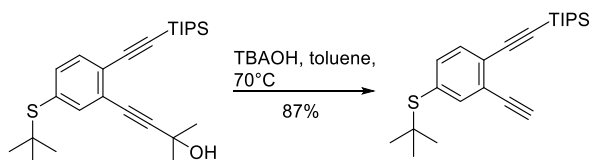
A 50 mL round-bottomed flask was evacuated and backfilled with argon, when hydroxypropyl protected acetylene **97** (93 mg, 0.217 mmol) was dissolved in anhydrous toluene (15 mL) and degassed for 15 min. To the solution TBAOH (1 M in MeOH, 141 uL, 0.217 mmol) was added and the mixture was heated to 70 °C for 3 h. After cooling down to room temperature, the mixture was washed successively with water, a saturated NH_4Cl solution and brine. The organic phase was dried over $MgSO_4$, filtered and concentrated in vacuum. The crude product was then purified by column chromatography (SiO_2, cyclohexane/EtOAc, 10:1) to afford the product as colorless oil. **Analytic Data for 98:** Yield 87% (70 mg, 0.19 mmol). ¹H NMR (400 MHz, $CDCl_3$, 25 °C): δ_H = 7.66 − 7.64 (m, 1H), 7.45 − 7.42 (m, 2H), 3.28 (s, 1H), 1.28 (s, 9H), 1.14 (s, 21H). ¹³C NMR (101 MHz, $CDCl_3$, 25 °C): δ_C = 140.94, 137.34, 133.28, 132.39, 126.99, 125.26, 104.44, 97.28, 81.88, 81.68, 46.87, 31.11, 18.83, 11.43. HRMS (MPT): calcd. for $[C_{23}H_{35}SSi]^+$ 371,2223; found 371.2220.

4-(5-(tert-butylthio)-2-ethynylphenyl)-2-methylbut-3-yn-2-ol **99**
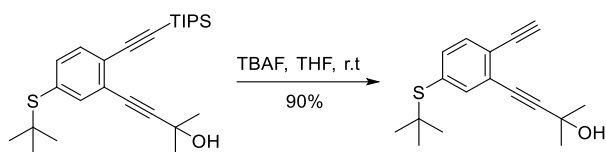
A 50-ml oven-dried round-bottomed flask was flushed with argon and charged with TIPS pro-tected acetylene **97** (104 mg, 0.24 mmol) and dissolved in 20 mL freshly distilled and deoxygenated THF. To the mixture, TBAF (1 M in THF, 2.42 mL, 2.42 mmol) was added at room temperature. The reaction mixture was stirred for 30 min, when MALDI-ToF MS showed complete cleavage of silane. The reaction mixture was quenched with water and extracted with CH_2Cl_2 50 mL. The aqueous phase was extracted twice with CH_2Cl_2 20 mL. The combined organ-ic phases were washed twice with water and brine, dried over $MgSO_4$, filtered and the solvents evaporated. The crude was purified by flash column chromatography (SiO_2, cyclohexane/EtOAc, 3:1) affording the title compound as colorless solid. **Analytik data 99**: Yield 90% (60 mg, 0.22 mmol). ^1H NMR (400 MHz, $CDCl_3$, 25 °C): δ_H = (ppm) 7.58 (dd, J=1.6, 0.7 Hz, 1H), 7.44 (dd, J=8.0, 0.7 Hz, 1H), 7.42 (d, J=1.6 Hz, 1H), 3.36 (s, 1H), 2.16 (s, 1H), 1.64 (s, 6H), 1.29 (s, 9H) ppm. ^{13}C NMR (101 MHz, $CDCl_3$, 25 °C): δ_C = 140.14, 136.84, 134.03, 132.40, 126.05, 125.11, 98.62, 82.38, 81.78, 80.26, 65.86, 46.88, 31.50, 31.15, 27.05 ppm. HRMS (ESI-ToF): calcd. for $[C_{17}H_{20}NaOS]^+$ 295.1127; found 295.1130.

Ferrocene **100**
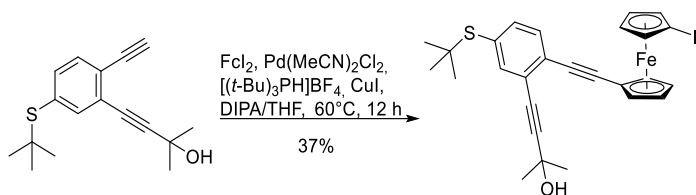
A 25 mL Schlenk flask was purged with argon and charged with $Pd(MeCN)_2Cl_2$ (9.62 mg, 10 mol-%) CuI (4.21 mg, 6 mol-%), $[(t\text{-}Bu)_3PH]BF_4$ (21.7 mg, 20 mol-%), 1,1´-diiodoferrocene (482 mg, 1.10 mmol). The flask was evacuated and backfilled with argon, then freshly distilled and deoxygenated THF (9 ml) and DIPA (3 mL) was added. To the mixture, the ethynylphenyl **99** (100 mg, 0.36 mmol) was added and the mixture was heated to 60 °C for 12 h. After the reaction was complete, the mixture was diluted with CH_2Cl_2 and concentrated on Hyflo, then purified via silica gel column (SiO_2, cyclohexane/EtOAc, 5:1) to isolate the monosubstitutued product as orange solid. **Analytic Data for 100:** Yield 37% (78 mg, 0.13 mmol). ^1H NMR (400 MHz, $CDCl_3$, 25 °C): δ_H = 7.59 (dd, $^4J_{H,H}$ = 1.8 Hz, $^5J_{H,H}$ = 0.6 Hz, 1H), 7.46 (dd, $^3J_{H,H}$ = 8.1 Hz, $^5J_{H,H}$ = 0.6 Hz, 1H), 7.41 (dd, $^3J_{H,H}$ = 8.1 Hz, $^4J_{H,H}$ = 1.7 Hz, 1H), 4.50 (pseudo-t, J = 1.9 Hz, 2H), 4.46 (pseudo-t, J = 1.8 Hz, 2H), 4.31 − 4.27 (m, 2H), 4.27 − 4.24 (m, 2H), 2.15 (s, 1H), 1.69 (s, 6H), 1.30 (s, 9H) ppm. ^{13}C NMR (101 MHz, $CDCl_3$, 25 °C): δ_C = 140.39, 137.03, 132.53, 131.57, 126.87, 124.98, 98.21, 93.05, 85.49, 80.91, 76.49, 74.22, 72.65, 71.30, 67.19, 65.91, 46.78, 41.09, 31.77, 31.17 ppm. HRMS (ESI-ToF): calcd. for $[C_{27}H_{27}FeINaOS]^+$ 605.0074; found 605.0069.

Ferrocene **101**
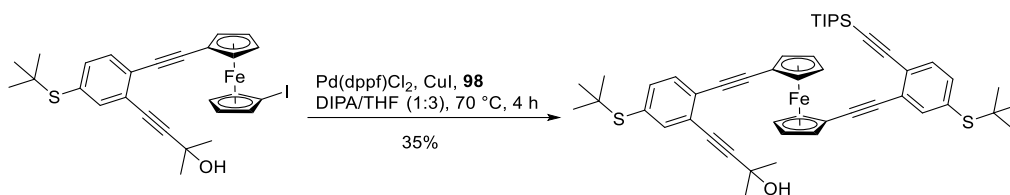
An oven-dried 25 mL Schlenk flask was purged with argon and charged with Pd(dppf)Cl$_2$ (15.1 mg, 6 mol-%) and CuI (3.94 mg, 6 mol-%). The flask was evacuated and backfilled with argon, then freshly distilled and deoxygenated THF (9 ml) and DIPA (3 mL) was added together with iodo-ferrocene **100** (200 mg, 0.34 mmol). To the mixture, ethynylphenyl **98** (178 mg, 0.48 mmol) was added and the mixture was degassed for 10 min before it was heated to 70 °C for 4 h. Full conversion was monitored by TLC, and the mixture was diluted with CH$_2$Cl$_2$ and concentrated on Hyflo, then purified by silica gel column (SiO$_2$, cyclohexane/EtOAc, 10:1) to isolate the product as orange oil. **Analytic Data for 101:** Yield 35% (100 mg, 0.13 mmol). ^{1}H NMR (400 MHz, CDCl$_3$, 25 °C): δ_H = 7.59 (dd, $^4J_{H,H}$ = 1.8 Hz, $^5J_{H,H}$ = 0.6 Hz, 1H), 7.46 (dd, $^3J_{H,H}$ = 8.1, $^5J_{H,H}$ = 0.6 Hz, 1H), 7.41 (dd, $^3J_{H,H}$ = 8.1, $^4J_{H,H}$ = 1.7 Hz, 1H), 4.50 (pseudo-t, J = 1.9 Hz, 2H), 4.46 (pseudo-t, J = 1.8 Hz, 2H), 4.31 – 4.27 (m, 2H), 4.27 – 4.24 (m, 2H), 2.15 (s, 1H), 1.69 (s, 6H), 1.30 (s, 9H) ppm. ^{13}C NMR (101 MHz, CDCl$_3$, 25 °C): δ_C = 140.39, 137.03, 132.53, 131.57, 126.87, 124.98, 98.21, 93.05, 85.49, 80.91, 76.49, 74.22, 72.65, 71.30, 67.19, 65.91, 46.78, 41.09, 31.77, 31.17 ppm. HRMS (ESI-ToF): calcd. for [C$_{50}$H$_{60}$FeNaOS$_2$Si]$^+$ 847.3091; found 847.3098.
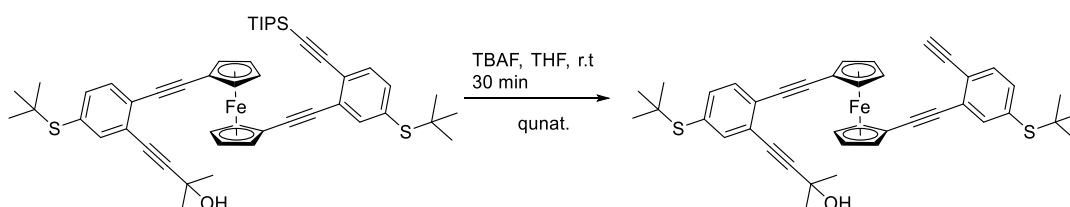
Ferrocene **102**

An oven-dried 50 mL round-bottomed flask was flushed with argon and charged with TIPS protected ferrocene **101** (100 mg, 0.12 mmol) and dissolved in 20 mL freshly distilled and deoxygenated THF. To the mixture, TBAF (1 M in THF, 2.42 mL, 2.42 mmol) was added at room temperature. The reaction mixture was stirred for 30 min at room temperature, when MALDI-MS showed complete cleavage of the silane. The reaction mixture was quenched with ice and extracted with CH$_2$Cl$_2$ (2 x 50 mL). The aqueous phase was extracted twice with small portions of CH$_2$Cl$_2$. The combined organic phases were washed twice with water and brine, dried over MgSO$_4$, filtered and the volatiles removed under reduced pressure. The crude was purified by flash column chromatography (SiO$_2$, cyclohexane/EtOAc, 5:1) affording the title compound quantitatively as orange solid. **Analytic Data for 102:** Yield 99% (81 mg, 0.12 mmol). ^{1}H NMR (400 MHz, CDCl$_3$, 25 °C): δ_H = 7.60 (dd, $^4J_{HH}$ = 1.7 Hz, $^5J_{HH}$ = 0.7 Hz, 1H), 7.51 (dd, $^4J_{H,H}$ = 1.6 Hz, $^5J_{H,H}$ = 0.8 Hz, 1H), 7.44 – 7.31 (m, 4H), 4.60 – 4.57 (m, 4H), 4.38 (pseudo-t, J = 1.9 Hz, 2H), 4.36 (pseudo-t, J = 1.9 Hz, 2H) , 3.44 (s, 1H), 2.37 (s, 1H), 1.68 (s, 6H), 1.29 (s, 9H), 1.29

(s, 9H) ppm. ^{13}C NMR (101 MHz, CDCl$_3$, 25 °C): δ_C = 140.28, 139.96, 136.93, 136.17, 133.89, 132.39, 132.29, 131.43, 127.11, 126.81, 124.86, 124.55, 98.21, 93.16, 92.37, 85.26, 84.68, 82.52, 82.29, 80.83, 73.39, 73.35, 71.64, 66.76, 66.60, 65.78, 46.80, 46.66, 31.70, 31.14, 31.13 ppm. HRMS (ESI-ToF): calcd. for [C$_{41}$H$_{40}$FeNaOS$_2$]$^+$ 691.1756; found 691.1763.

Bis-ferrocene **103**

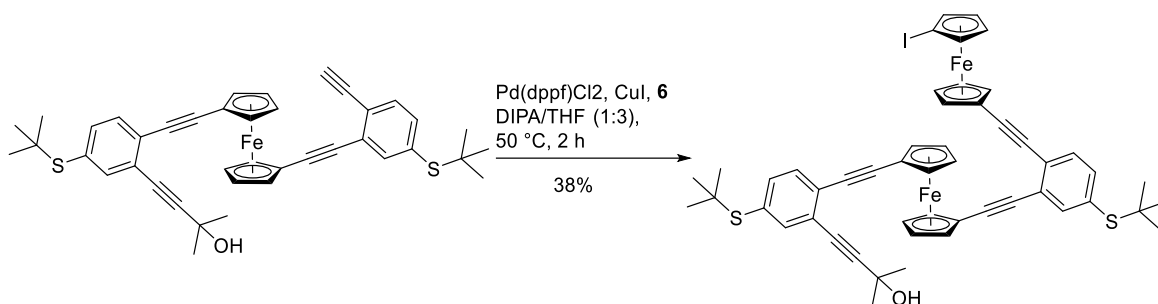
An oven-dried 50 ml Schlenk flask was purged with argon and charged with Pd(dppf)Cl$_2$ (6.10 mg, 6 mol-%) and CuI (2.30 mg, 10 mol-%) and 1,1'-diiodoferrocene (183 mg, 0.42 mmol), before the reaction vessel was evacuated and back-filled with argon. Then, freshly distilled THF (6 ml) and DIPA (3 mL) were added and the mixture was degassed for 10 min. Acetylene **102** (93 mg, 139 µmol) dissolved in 3 mL dry and deoxygenated THF was added to the mixture, and the reaction vessel was heated for 2 h at 50 °C. The reaction progress was monitored by MALDI MS and after the reaction was completed, the mixture was diluted with DCM and concentrated on silica gel, then purified via flash column chromatography (SiO$_2$, cyclohexane/EtOAc, 10:1) to isolate the product as red solid. **Analytic Data for 103:** Yield 38% (51 mg, 52 µmol). ^{1}H NMR (400 MHz, CDCl$_3$, 25 °C): δ_H = 7.62 (dd, $^4J_{HH}$ = 1.7 Hz, $^5J_{HH}$ = 0.7 Hz, 1H), 7.50 (dd, $^4J_{HH}$ = 1.6 Hz, $^5J_{HH}$ = 0.7 Hz, 1H), 7.40 (dd, $^3J_{HH}$ = 8.0 Hz, $^5J_{HH}$ = 0.7 Hz, 1H), 7.37 (dd, $^3J_{HH}$ = 8.1 Hz, $^4J_{HH}$ = 1.6 Hz, 1H), 7.36 (dd, $^3J_{HH}$ = 8.0 Hz, $^5J_{HH}$ = 0.6 Hz, 1H), 7.33 (dd, $^3J_{HH}$ = 8.1 Hz, $^4J_{HH}$ = 1.6 Hz, 1H), 4.63 (pseudo-t, J = 1.9 Hz, 2H), 4.58 (pseudo-t, J = 1.9 Hz, 2H), 4.53 (pseudo-t, J = 1.9 Hz, 2H), 4.45 (pseudo-t, J = 1.8 Hz, 2H), 4.38 (pseudo-t, J = 1.9 Hz, 2H), 4.35 (pseudo-t, J = 1.8 Hz, 2H), 4.27 (pseudo-t, J = 1.9 Hz, 2H), 4.23 (pseudo-t, J = 1.8 Hz, 2H), 2.27 (s, 1H), 1.66 (s, 6H), 1.31 (s, 9H), 1.29 (s, 9H) ppm. ^{13}C NMR (101 MHz, CDCl$_3$, 25 °C): δ_C = 140.24, 140.23, 136.93, 136.33, 132.47, 132.25, 131.61, 131.49, 126.82, 126.22, 124.87, 98.21, 93.02, 92.90, 91.84, 85.75, 85.60, 85.42, 80.88, 76.51, 74.27, 73.20, 73.18, 72.70, 71.72, 71.56, 71.50, 67.22, 67.04, 66.82, 65.80, 46.74, 46.69, 40.84, 31.73, 31.18, 31.16 ppm. HRMS (ESI-ToF): calcd. for [C$_{51}$H$_{47}$Fe$_2$INaOS$_2$]$^+$ 1001.0710; found 1001.0706.

Bis-ferrocene **104**
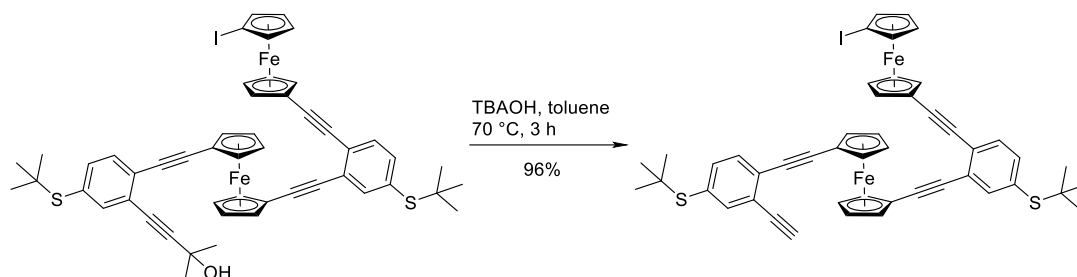
A sulfuric acid washed, dried round-bottomed flask was evacuated and backfilled with argon, before bis-ferrocene **104** (51 mg, 52 µmol) was dissolved in anhydrous toluene (15 mL) and degassed for 15 min with a stream of argon. To the solution TBAOH (1 M in MeOH, 40 µL, 52 µmol) was added and the mixture was heated to 70 °C for 2 h. After cooling down to room temperature, the mixture was washed successively with NH_4Cl and brine, dried over $MgSO_4$, and concentrated in vacuum. The crude product was then purified by column chromatography (SiO_2, cyclohexane/EtOAc 10:1) to afford the product as red oil. **Analytic Data for 104 :** Yield 96% (46 mg, 50 µmol). ^{1}H NMR (400 MHz, $CDCl_3$, 25 °C): δ_H = 7.66 − 7.63 (m, 2H), 7.45 (d, $^3J_{HH}$ = 8.0 Hz, 1H), 7.42 − 7.37 (m, 3H), 4.62 (pseudo-t, J = 1.9 Hz, 2H), 4.58 (pseudo-t, J = 1.9 Hz, 2H), 4.54 (pseudo-t, J = 1.9 Hz, 2H), 4.45 (pseudo-t, J = 1.8 Hz, 2H), 4.39 (pseudo-t, J = 2.0 Hz, 2H), 4.36 (pseudo-t, J = 2.0 Hz, 2H), 4.26 (pseudo-t, J = 1.9 Hz, 2H), 4.22 (pseudo-t, J = 1.9 Hz, 2H), 3.39 (s, 1H), 1.31 (s, 9H), 1.29 (s, 9H) ppm. ^{13}C NMR (101 MHz, $CDCl_3$, 25 °C): δ_C = 141.03, 140.27, 137.47, 136.42, 132.61, 132.55, 131.73, 131.62, 127.20, 126.30, 126.24, 124.65, 93.61, 92.94, 92.14, 85.73, 85.32, 84.69, 82.11, 81.71, 76.52, 74.29, 73.53, 73.51, 72.69, 71.80, 71.75, 71.48, 67.23, 66.78, 66.38, 46.79, 46.75, 40.88, 31.19, 31.14 ppm. HRMS (ESI-ToF): calcd. for $[C_{48}H_{41}Fe_2INaS_2]^+$ 943.0287; found 943.0293.

Bis-ferrocene **105**
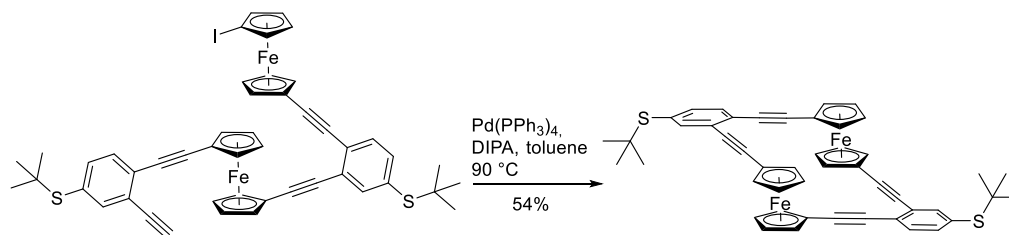
A 250 ml round-bottomed flask was charged with $Pd(PPh_3)_4$ (0.5 mg, 3 mol-%), 150 mL absolute toluene and 2 ml dry DIPA. The mixture was degassed for 10 min, then *bis*-ferrocene **104** (14 mg, 15 µmol) was added and the mixture was heated for 4 h at 90 °C. After completion, the reaction mixture was concentrated on silica and subjected to a flash column chromatography (SiO_2, cyclohexane/DCM, 3:1) to isolate the product as a red/orange solid. **Analytic Data for 105:** Yield 54% (6.5 mg, 8 µmol). ^{1}H NMR (400 MHz, $CDCl_3$, 25 °C): δ_H = 7.20 (dd, $^4J_{HH}$ = 1.8 Hz, $^5J_{HH}$ = 0.5 Hz, 2H), 7.09 (dd, $^3J_{HH}$ = 8.0 Hz, $^4J_{HH}$ = 1.8 Hz, 2H), 7.00 (dd, $^3J_{HH}$ = 8.0 Hz, $^5J_{HH}$ = 0.5 Hz, 2H), 4.61 (pseudo-dt, J = 4.0 Hz, J = 1.9 Hz, 8H), 4.37 (pseudo-t, J = 1.8 Hz, 8H), 1.27

(s, 18H) ppm. ^{13}C NMR (101 MHz, CDCl$_3$, 25°C): δ_C = 139.69, 135.49, 131.00, 130.71, 125.74, 125.60, 90.34, 89.11, 87.50, 87.42, 72.09, 72.04, 69.90, 69.70, 69.68, 69.63, 46.28, 31.03 ppm. HRMS (ESI-ToF): calcd. for [C$_{48}$H$_{40}$Fe$_2$NaS$_2$]$^+$ 815.1164; found 815.1161.

BIBLIOGRAPHY

[1]   "Press Release: The 1973 Nobel Prize in Chemistry," can be found under
        https://www.nobelprize.org/nobel_prizes/chemistry/laureates/1973/press.html, **n.d.**
[2]   T. J. Kealy, P. L. Pauson, *Nature* **1951**, *168*, 1039–1040.
[3]   S. A. Miller, J. A. Tebboth, J. F. Tremaine, *J. Chem. Soc.* **1952**, 632–635.
[4]   E. O. Fischer, W. Pfab, *ZfN* **1952**, *7b*, 377–379.
[5]   G. Wilkinson, M. Rosenblum, M. C. Whiting, R. B. Woodward, *J. Am. Chem. Soc.* **1952**,
        74, 2125–2126.
[6]   J. D. Dunitz, L. E. Orgel, *Nature* **1953**, *171*, 121–122.
[7]   P. F. Eiland, R. Pepinsky, *J. Am. Chem. Soc.* **1952**, *74*, 4971–4971.
[8]   P. L. Pauson, *J. Organomet. Chem.* **2001**, *637–639*, 3–6.
[9]   A. Haaland, J. E. Nilsson, T. Olson, T. Norin, *Acta Chem. Scand.* **1968**, *22*, 2653–2670.
[10]   P. D. rer nat C. Elschenbroich, in *Organometallchemie*, Vieweg+Teubner, **2008**, pp.
        367–540.
[11]   M. D. Rausch, E. O. Fischer, H. Grubert, *J. Am. Chem. Soc.* **1960**, *82*, 76–82.
[12]   in *Organomet. Chem. Catal.*, Springer Berlin Heidelberg, **2007**, pp. 251–288.
[13]   J. P. Hurvois, C. Moinet, *J. Organomet. Chem.* **2005**, *690*, 1829–1839.
[14]   J. Chen, A. K. Burrell, G. E. Collis, D. L. Officer, G. F. Swiegers, C. O. Too, G. G. Wallace,
        Electrochimica Acta **2002**, *47*, 2715–2724.
[15]   P. D. Beer, *Acc. Chem. Res.* **1998**, *31*, 71–80.
[16]   K. Schlögl, in *Top. Stereochem.* (Eds.: N.L. Allinger, E.L. Eliel), John Wiley & Sons, Inc.,
        1967, pp. 39–91.
[17]   D. Marquarding, H. Klusacek, G. Gokel, P. Hoffmann, I. Ugi, *J. Am. Chem. Soc.* **1970**, *92*,
        5389–5393.
[18]   D. Marquarding, H. Klusacek, G. Gokel, P. Hoffmann, I. Ugi, *Angew. Chem.* **1970**, *82*,
        360–361.
[19]   D. Schaarschmidt, H. Lang, *Organometallics* **2013**, *32*, 5668–5704.
[20]   H.-U. Blaser, B. Pugin, F. Spindler, *J. Mol. Catal. Chem.* **2005**, *231*, 1–20.
[21]   M. E. Wright, E. G. Toplikar, *Macromolecules* **1992**, *25*, 6050–6054.
[22]   S. R. Marder, J. W. Perry, B. G. Tiemann, W. P. Schaefer, *Organometallics* **1991**, *10*,
        1896–1901.
[23]   S. Celedón, V. Dorcet, T. Roisnel, A. Singh, I. Ledoux-Rak, J.-R. Hamon, D. Carrillo, C.
        Manzur, *Eur. J. Inorg. Chem.* **2014**, *2014*, 4984–4993.
[24]   C. Manzur, M. Fuentealba, J.-R. Hamon, D. Carrillo, *Coord. Chem. Rev.* **2010**, *254*, 765–
        780.
[25]   A. Trujillo, M. Fuentealba, D. Carrillo, C. Manzur, I. Ledoux-Rak, J.-R. Hamon, J.-Y. Sail-
        lard, *Inorg. Chem.* **2010**, *49*, 2750–2764.
[26]   N. Novoa, T. Roisnel, P. Hamon, S. Kahlal, C. Manzur, H. M. Ngo, I. Ledoux-Rak, J.-Y.
        Saillard, D. Carrillo, J.-R. Hamon, *Dalton Trans.* **2015**, *44*, 18019–18037.
[27]   S. Celedón, M. Fuentealba, T. Roisnel, I. Ledoux-Rak, J.-R. Hamon, D. Carrillo, C. Man-
        zur, *Eur. J. Inorg. Chem.* **2016**, *2016*, 3012–3023.
[28]   S. Fery-Forgues, B. Delavaux-Nicot, *J. Photochem. Photobiol. Chem.* **2000**, *132*, 137–159.
[29]   J. Cisterna, V. Dorcet, C. Manzur, I. Ledoux-Rak, J.-R. Hamon, D. Carrillo, *Inorganica
        Chim. Acta* **2015**, *430*, 82–90.
[30]   M. L. H. Green, S. R. Marder, M. E. Thompson, J. A. Bandy, D. Bloor, P. V. Kolinsky, R. J.
        Jones, *Nature* **1987**, *330*, 360–362.
[31]   W.-Y. Wang, N.-N. Ma, S.-L. Sun, Y.-Q. Qiu, *Phys. Chem. Chem. Phys.* **2014**, *16*, 4900–
        4910.
[32]   J. Elbert, M. Gallei, C. Rüttiger, A. Brunsen, H. Didzoleit, B. Stühn, M. Rehahn, *Organo-
        metallics* **2013**, *32*, 5873–5878.
[33]   R. Pietschnig, *Chem. Soc. Rev.* **2016**, *45*, 5216–5231.
[34]   L. Peng, H. Zhang, A. Feng, M. Huo, Z. Wang, J. Hu, W. Gao, J. Yuan, *Polym. Chem.*
        2015, *6*, 3652–3659.
[35]   G. V. Dubacheva, A. Van Der Heyden, P. Dumy, O. Kaftan, R. Auzély-Velty, L. Coche-
        Guerente, P. Labbé, *Langmuir* **2010**, *26*, 13976–13986.
[36]   L. Q. Xu, D. Wan, H. F. Gong, K.-G. Neoh, E.-T. Kang, G. D. Fu, *Langmuir* **2010**, *26*,
        15376–15382.
[37]   Y. Ahn, Y. Jang, N. Selvapalam, G. Yun, K. Kim, *Angew. Chem. Int. Ed.* **2013**, n/a–n/a.
[38]   P. D. Beer, Z. Chen, A. J. Goulden, A. Graydon, S. E. Stokes, T. Wear, *J. Chem. Soc.,
        Chem. Commun.* **1993**, 1834–1836.

[39]   P. D. Beer, Z. Chen, M. G. B. Drew, A. O. M. Johnsona, D. K. Smith, P. Spencer, *Inorganica Chim. Acta* **1996**, *246*, 143–150.

[40]   T. Yamamoto, K.-I. Sanechika, A. Yamamoto, M. Katada, I. Motoyama, H. Sano, *Inorganica Chim. Acta* **1983**, *73*, 75–82.

[41]   D. O. Cowan, J. Park, C. U. Pittman, Y. Sasaki, T. K. Mukherjee, N. A. Diamond, *J. Am. Chem. Soc.* **1972**, *94*, 5110–5112.

[42]   K.-S. Park, S. B. Schougaard, J. B. Goodenough, *Adv. Mater.* **2007**, *19*, 848–851.

[43]   H. Zhong, G. Wang, Z. Song, X. Li, H. Tang, Y. Zhou, H. Zhan, *Chem. Commun.* **2014**, *50*, 6768–6770.

[44]   C. Su, L. Ji, L. Xu, X. Zhu, H. He, Y. Lv, M. Ouyang, C. Zhang, *RSC Adv.* **2015**, *5*, 14053–14060.

[45]   J. Xiang, R. Burges, B. Häupler, A. Wild, U. S. Schubert, C.-L. Ho, W.-Y. Wong, *Polymer* **2015**, *68*, 328–334.

[46]   Y. Zhao, Y. Ding, J. Song, G. Li, G. Dong, J. B. Goodenough, G. Yu, *Angew. Chem. Int. Ed.* **2014**, *53*, 11036–11040.

[47]   Y. Ding, Y. Zhao, G. Yu, *Nano Lett.* **2015**, *15*, 4108–4113.

[48]   X. Xiao, D. Brune, J. He, S. Lindsay, C. B. Gorman, N. Tao, *Chem. Phys.* **2006**, *326*, 138–143.

[49]   E. D. Mentovich, N. Rosenberg-Shraga, I. Kalifa, M. Gozin, V. Mujica, T. Hansen, S. Richter, *J. Phys. Chem. C* **2013**, *117*, 8468–8474.

[50]   K. Kanthasamy, M. Ring, D. Nettelroth, C. Tegenkamp, H. Butenschön, F. Pauly, H. Pfnür, *Small* **2016**, *12*, 4849–4856.

[51]   S. A. Getty, C. Engtrakul, L. Wang, R. Liu, S.-H. Ke, H. U. Baranger, W. Yang, M. S. Fuhrer, L. R. Sita, *Phys. Rev. B* **2005**, *71*, 241401.

[52]   Q. Lu, C. Yao, X. Wang, F. Wang, *J. Phys. Chem. C* **2012**, *116*, 17853–17861.

[53]   T. Muraoka, K. Kinbara, Y. Kobayashi, T. Aida, *J. Am. Chem. Soc.* **2003**, *125*, 5612–5613.

[54]   C. F. R. A. C. Lima, A. M. Fernandes, A. Melo, L. M. Gonçalves, A. M. S. Silva, L. M. N. B. F. Santos, *Phys. Chem. Chem. Phys.* **2015**, *17*, 23917–23923.

[55]   T. Ikeda, S. Shinkai, K. Sada, M. Takeuchi, *Tetrahedron Lett.* **2009**, *50*, 2006–2009.

[56]   T. Fukino, N. Fujita, T. Aida, *Org. Lett.* **2010**, *12*, 3074–3077.

[57]   T. J. Katz, J. Pesti, *J. Am. Chem. Soc.* **1982**, *104*, 346–347.

[58]   J. Y. C. Lim, M. J. Cunningham, J. J. Davis, P. D. Beer, *Chem. Commun.* **2015**, *51*, 14640–14643.

[59]   X. Xiao, D. Brune, J. He, S. Lindsay, C. B. Gorman, N. Tao, *Chem. Phys.* **2006**, *326*, 138–143.

[60]   Ni. Jenny, Synthesis of New Functional Molecules for Molecular Electronics. 2012, PhD Thesis, University of Basel, Faculty of Science, Basel, **2012**.

[61]   V. Hoffmann, N. Jenny, D. Häussinger, M. Neuburger, M. Mayor, *Eur. J. Org. Chem.* **2016**, *2016*, 2187–2199.

[62]   J. E. Baldwin, *J. Chem. Soc. Chem. Commun.* **1976**, 734–736.

[63]   D. R. Buckle, C. J. M. Rockell, *J. Chem. Soc. [Perkin 1]* **1985**, 2443–2446.

[64]   P. Babin, J. Dunogues, M. Petraud, *Tetrahedron* **1981**, *37*, 1131–1139.

[65]   W. Y. Lee, C. H. Park, Y. D. Kim, *J. Org. Chem.* **1992**, *57*, 4074–4079.

[66]   R. Sterzycki, *Synthesis* **1979**, *1979*, 724–725.

[67]   J. Claffey, H. Müller-Bunz, M. Tacke, *J. Organomet. Chem.* **2010**, *695*, 2105–2117.

[68]   N. M. Jenny, M. Mayor, T. R. Eaton, *Eur. J. Org. Chem.* **2011**, *2011*, 4965–4983.

[69]   J. Li, P. Huang, *Beilstein J. Org. Chem.* **2011**, *7*, 426–431.

[70]   J. K. Pudelski, M. R. Callstrom, *Organometallics* **1994**, *13*, 3095–3109.

[71]   I. R. Butler, S. B. Wilkes, S. J. McDonald, L. J. Hobson, A. Taralp, C. P. Wilde, *Polyhedron* **1993**, *12*, 129–131.

[72]   T. Hundertmark, A. F. Littke, S. L. Buchwald, G. C. Fu, *Org. Lett.* **2000**, *2*, 1729–1731.

[73]   M. S. Inkpen, A. J. P. White, T. Albrecht, N. J. Long, *Chem. Commun.* **2013**, *49*, 5663–5665.

[74]   Y. He, M. Johansson, O. Sterner, *Synth. Commun.* **2004**, *34*, 4153–4158.

[75]   G. Cahiez, O. Gager, A. Moyeux, T. Delacroix, *Adv. Synth. Catal.* **2012**, *354*, 1519–1528.

[76]   A. K. Chatterjee, T.-L. Choi, D. P. Sanders, R. H. Grubbs, *J. Am. Chem. Soc.* **2003**, *125*, 11360–11370.

[77]   P. Sabila, *Univers. J. Chem.* **2015**, *3*, 87–90.

[78]   F. Derguini-Boumechal, G. Linstrumelle, *Tetrahedron Lett.* **1976**, *17*, 3225–3226.

[79]   R. Rossi, A. Carpita, M. G. Quirici, C. A. Veracini, *Tetrahedron* **1982**, *38*, 639–644.

[80]   R. P. Feynman, *Eng. Sci.* **1960**, *23*, 22–36.

[81]   B. Mann, H. Kuhn, *J. Appl. Phys.* **1971**, *42*, 4398–4405.

[82] A. Aviram, M. A. Ratner, *Chem. Phys. Lett.* **1974**, *29*, 277–283.

[83] "Press Release: The 1986 Nobel Prize in Physics," can be found under http://www.nobelprize.org/nobel_prizes/physics/laureates/1986/press.html, **n.d.**

[84] G. Binning, H. Rohrer, *IBM J. Res. Dev.* **1986**, *4*, 355–369.

[85] M. A. Reed, C. Zhou, C. J. Muller, T. P. Burgin, J. M. Tour, *Science* **1997**, *278*, 252–254.

[86] R. Landauer, *Phys. Scr.* **1992**, *1992*, 110.

[87] R. Landauer, *Philos. Mag.* **1970**, *21*, 863–867.

[88] N. Agrait, A. L. Yeyati, J. M. van Ruitenbeek, *Phys. Rep.* **2003**, *377*, 81–279.

[89] H. Ohnishi, Y. Kondo, K. Takayanagi, *Nature* **1998**, *395*, 780–783.

[90] C. Huang, A. V. Rudnev, W. Hong, T. Wandlowski, *Chem. Soc. Rev.* **2015**, *44*, 889–901.

[91] C. Huang, A. V. Rudnev, W. Hong, T. Wandlowski, *Chem. Soc. Rev.* **2015**, *44*, 889–901.

[92] J. Ulrich, D. Esrail, W. Pontius, L. Venkataraman, D. Millar, L. H. Doerrer, *J. Phys. Chem. B* **2006**, *110*, 2462–2466.

[93] V. Kaliginedi, P. Moreno-García, H. Valkenier, W. Hong, V. M. García-Suárez, P. Buiter, J. L. H. Otten, J. C. Hummelen, C. J. Lambert, T. Wandlowski, *J. Am. Chem. Soc.* **2012**, *134*, 5262–5275.

[94] T. Kim, H. Vázquez, M. S. Hybertsen, L. Venkataraman, *Nano Lett.* **2013**, *13*, 3358–3364.

[95] C.-H. Ko, M.-J. Huang, M.-D. Fu, C. Chen, *J. Am. Chem. Soc.* **2010**, *132*, 756–764.

[96] C. Jia, B. Ma, N. Xin, X. Guo, *Acc. Chem. Res.* **2015**, *48*, 2565–2575.

[97] S. Y. Quek, K. H. Khoo, *Acc. Chem. Res.* **2014**, *47*, 3250–3257.

[98] E. Lörtscher, V. Geskin, B. Gotsmann, J. Fock, J. K. Sørensen, T. Bjørnholm, J. Cornil, H. S. J. van der Zant, H. Riel, *Small* **2013**, *9*, 332–332.

[99] E. Leary, M. T. González, C. van der Pol, M. R. Bryce, S. Filippone, N. Martín, G. Rubio-Bollinger, N. Agraït, *Nano Lett.* **2011**, *11*, 2236–2241.

[100] C. A. Martin, D. Ding, J. K. Sørensen, T. Bjørnholm, J. M. van Ruitenbeek, H. S. J. van der Zant, *J. Am. Chem. Soc.* **2008**, *130*, 13198–13199.

[101] B. Xu, X. Xiao, N. J. Tao, *J. Am. Chem. Soc.* **2003**, *125*, 16164–16165.

[102] S. Yasuda, S. Yoshida, J. Sasaki, Y. Okutsu, T. Nakamura, A. Taninaka, O. Takeuchi, H. Shigekawa, *J. Am. Chem. Soc.* **2006**, *128*, 7746–7747.

[103] R. S. Klausen, J. R. Widawsky, T. A. Su, H. Li, Q. Chen, M. L. Steigerwald, L. Venkataraman, C. Nuckolls, *Chem. Sci.* **2014**, *5*, 1561–1564.

[104] A. Ulman, *Chem. Rev.* **1996**, *96*, 1533–1554.

[105] S. K. Yee, J. Sun, P. Darancet, T. D. Tilley, A. Majumdar, J. B. Neaton, R. A. Segalman, *ACS Nano* **2011**, *5*, 9256–9263.

[106] C. Li, I. Pobelov, T. Wandlowski, A. Bagrets, A. Arnold, F. Evers, *J. Am. Chem. Soc.* **2008**, *130*, 318–326.

[107] J. C. Love, L. A. Estroff, J. K. Kriebel, R. G. Nuzzo, G. M. Whitesides, *Chem. Rev.* **2005**, *105*, 1103–1170.

[108] L. A. Zotti, T. Kirchner, J.-C. Cuevas, F. Pauly, T. Huhn, E. Scheer, A. Erbe, *Small* **2010**, *6*, 1529–1535.

[109] F. Chen, X. Li, J. Hihath, Z. Huang, N. Tao, *J. Am. Chem. Soc.* **2006**, *128*, 15874–15881.

[110] M. S. Hybertsen, L. Venkataraman, J. E. Klare, A. C. Whalley, M. L. Steigerwald, Colin Nuckolls, *J. Phys. Condens. Matter* **2008**, *20*, 374115.

[111] L. Venkataraman, J. E. Klare, I. W. Tam, C. Nuckolls, M. S. Hybertsen, M. L. Steigerwald, *Nano Lett.* **2006**, *6*, 458–462.

[112] Y. S. Park, A. C. Whalley, M. Kamenetska, M. L. Steigerwald, M. S. Hybertsen, C. Nuckolls, L. Venkataraman, *J. Am. Chem. Soc.* **2007**, *129*, 15768–15769.

[113] S. Y. Quek, M. Kamenetska, M. L. Steigerwald, H. J. Choi, S. G. Louie, M. S. Hybertsen, J. B. Neaton, L. Venkataraman, *Nat. Nanotechnol.* **2009**, *4*, 230–234.

[114] *J. Chem. Phys.* **1997**, *106*, 584–598.

[115] S. H. Choi, B. Kim, C. D. Frisbie, *Science* **2008**, *320*, 1482–1486.

[116] C. Huang, S. Chen, K. Baruël Ørnsø, D. Reber, M. Baghernejad, Y. Fu, T. Wandlowski, S. Decurtins, W. Hong, K. S. Thygesen, et al., *Angew. Chem. Int. Ed.* **2015**, *54*, 14304–14307.

[117] F. Chen, N. J. Tao, *Acc. Chem. Res.* **2009**, *42*, 429–438.

[118] C. Huang, A. V. Rudnev, W. Hong, T. Wandlowski, *Chem. Soc. Rev.* **2015**, *44*, 889–901.

[119] G. C. Solomon, C. Herrmann, T. Hansen, V. Mujica, M. A. Ratner, *Nat. Chem.* **2010**, *2*, 223–228.

[120] C. J. Lambert, *Chem. Soc. Rev.* **2015**, *44*, 875–888.

[121] H. Valkenier, C. M. Guédon, T. Markussen, K. S. Thygesen, S. J. van der Molen, J. C. Hummelen, *Phys. Chem. Chem. Phys.* **2013**, *16*, 653–662.

[122] L. Venkataraman, J. E. Klare, C. Nuckolls, M. S. Hybertsen, M. L. Steigerwald, *Nature* **2006**, *442*, 904–907.

[123] N. J. Kay, S. J. Higgins, J. O. Jeppesen, E. Leary, J. Lycoops, J. Ulstrup, R. J. Nichols, *J. Am. Chem. Soc.* **2012**, *134*, 16817–16826.

[124] N. Darwish, I. Díez-Pérez, P. Da Silva, N. Tao, J. J. Gooding, M. N. Paddon-Row, *Angew. Chem. Int. Ed.* **2012**, *51*, 3203–3206.

[125] E. W. Abel, N. J. Long, K. G. Orrell, A. G. Osborne, V. Šik, *J. Organomet. Chem.* **1991**, *403*, 195–208.

[126] N. Krauße, H. Butenschön, *Eur. J. Org. Chem.* **2014**, *2014*, 6686–6695.

[127] I. Baumgardt, H. Butenschön, *Eur. J. Org. Chem.* **2010**, *2010*, 1076–1087.

[128] M. S. Inkpen, A. J. P. White, T. Albrecht, N. J. Long, *Dalton Trans.* **2014**, *43*, 15287–15290.

[129] S. Wu, M. T. González, R. Huber, S. Grunder, M. Mayor, C. Schönenberger, M. Calame, *Nat. Nanotechnol.* **2008**, *3*, 569–574.

[130] S. Karmakar, S. Kumar, P. Marzo, E. Primiceri, R. D. Corato, R. Rinaldi, P. G. Cozzi, A. P. Bramanti, G. Maruccio, *Nanoscale* **2012**, *4*, 2311–2316.

[131] Q. Lu, C. Yao, X. Wang, F. Wang, *J. Phys. Chem. C* **2012**, *116*, 17853–17861.

[132] C. Engtrakul, L. R. Sita, *Organometallics* **2008**, *27*, 927–937.

[133] S. Höger, *Liebigs Ann.* **1997**, *1997*, 273–277.

[134] S. Creager, C. J. Yu, C. Bamdad, S. O'Connor, T. MacLean, E. Lam, Y. Chong, G. T. Olsen, J. Luo, M. Gozin, et al., *J. Am. Chem. Soc.* **1999**, *121*, 1059–1064.

[135] C. J. Yu, Y. Chong, J. F. Kayyem, M. Gozin, *J. Org. Chem.* **1999**, *64*, 2070–2079.

[136] *Org. Synth.* **1977**, *57*, 53.

[137] V. Boekelheide, R. A. Hollins, *J. Am. Chem. Soc.* **1973**, *95*, 3201–3208.

[138] K. Nagasawa, A. Yoneta, *Chem. Pharm. Bull. (Tokyo)* **1985**, *33*, 5048–5052.

[139] D. F. Taber, S. Bai, P. Guo, *Tetrahedron Lett.* **2008**, *49*, 6904–6906.

[140] T. Gibtner, F. Hampel, J.-P. Gisselbrecht, A. Hirsch, *Chem. – Eur. J.* **2002**, *8*, 408–432.

[141] K. Balaraman, V. Kesavan, *Synthesis* **2010**, *2010*, 3461–3466.

[142] X. Feng, Z. Zhao, F. Yang, T. Jin, Y. Ma, M. Bao, *J. Organomet. Chem.* **2011**, *696*, 1479–1482.

[143] J. Yan, J. Wu, H. Jin, *J. Organomet. Chem.* **2007**, *692*, 3636–3639.

[144] M. L. Trouwborst, E. H. Huisman, F. L. Bakker, S. J. van der Molen, B. J. van Wees, *Phys. Rev. Lett.* **2008**, *100*, 175502.

[145] S. H. Choi, B. Kim, C. D. Frisbie, *Science* **2008**, *320*, 1482–1486.

[146] L. Grüter, M. T. González, R. Huber, M. Calame, C. Schönenberger, *Small* **2005**, *1*, 1067–1070.

[147] J.-H. Tian, Y. Yang, X.-S. Zhou, B. Schöllhorn, E. Maisonhaute, Z.-B. Chen, F.-Z. Yang, Y. Chen, C. Amatore, B.-W. Mao, et al., *Chemphyschem Eur. J. Chem. Phys. Phys. Chem.* **2010**, *11*, 2745–2755.

[148] "Electrochemical NanoScience Group | Research | Methodological and Instrumental Developments | STM," can be found under http://wandlowski.dcb.unibe.ch/research/equipment/stm.html, **n.d.**

[149] X. Zhao, C. Huang, M. Gulcur, A. S. Batsanov, M. Baghernejad, W. Hong, M. R. Bryce, T. Wandlowski, *Chem. Mater.* **2013**, *25*, 4340–4347.

[150] M. Baghernejad, X. Zhao, K. Baruël Ørnsø, M. Füeg, P. Moreno-García, A. V. Rudnev, V. Kaliginedi, S. Vesztergom, C. Huang, W. Hong, et al., *J. Am. Chem. Soc.* **2014**, *136*, 17922–17925.

[151] G. Snider, P. Kuekes, R. S. Williams, *Nanotechnology* **2004**, *15*, 881.

[152] Y. Chen, G.-Y. Jung, D. A. A. Ohlberg, X. Li, D. R. Stewart, J. O. Jeppesen, K. A. Nielsen, J. F. Stoddart, R. S. Williams, *Nanotechnology* **2003**, *14*, 462.

[153] Z. Zhong, D. Wang, Y. Cui, M. W. Bockrath, C. M. Lieber, *Science* **2003**, *302*, 1377–1379.

[154] C. Li, W. Fan, B. Lei, D. Zhang, S. Han, T. Tang, X. Liu, Z. Liu, S. Asano, M. Meyyappan, et al., *Appl. Phys. Lett.* **2004**, *84*, 1949–1951.

[155] Ö. Türel, K. Likharev, *Int. J. Circuit Theory Appl.* **2003**, *31*, 37–53.

[156] K. Likharev, A. Mayr, I. Muckra, O. Türel, *Ann. N. Y. Acad. Sci.* **2003**, *1006*, 146–163.

[157] M. M. Shulaker, G. Hills, N. Patil, H. Wei, H.-Y. Chen, H.-S. P. Wong, S. Mitra, *Nature* **2013**, *501*, 526–530.

[158] G. Cuniberti, G. Fagas, K. Richter, in *Introd. Mol. Electron.* (Eds.: G. Cuniberti, K. Richter, G. Fagas), Springer Berlin Heidelberg, **2006**, pp. 1–10.

[159] C. S. Lent, *Science* **2000**, *288*, 1597–1599.

[160] M. S. Mitra H. S.Philip Wong and Subhasish, "How We'll Put a Carbon Nanotube Computer in Your Hand," can be found under

http://spectrum.ieee.org/semiconductors/devices/how-well-put-a-carbon-nanotube-computer-in-your-hand, **2016**.

[161] C. S. Lent, P. D. Tougaw, W. Porod, G. H. Bernstein, *Nanotechnology* **1993**, *4*, 49.

[162] D. P. Waters, *Biosemiotics* **2011**, *5*, 5–15.

[163] A. Pulimeno, M. Graziano, D. Demarchi, G. Piccinini, *Solid-State Electron.* **2012**, *77*, 101–107.

[164] S. Bandyopadhyay, B. Das, A. E. Miller, *Nanotechnology* **1994**, *5*, 113.

[165] K. Walus, A. Wetteth, G. A. Jullien, V. S. Dimitrov, *Nanotech* **2003**, 160–163.

[166] A. O. Orlov, I. Amlani, G. H. Bernstein, C. S. Lent, G. L. Snider, *Science* **1997**, *277*, 928–930.

[167] H. Qi, S. Sharma, Z. Li, G. L. Snider, A. O. Orlov, C. S. Lent, T. P. Fehlner, *J. Am. Chem. Soc.* **2003**, *125*, 15250–15259.

[168] J. Jiao, G. J. Long, L. Rebbouh, F. Grandjean, A. M. Beatty, T. P. Fehlner, *J. Am. Chem. Soc.* **2005**, *127*, 17819–17831.

[169] B. Schneider, S. Demeshko, S. Neudeck, S. Dechert, F. Meyer, *Inorg. Chem.* **2013**, *52*, 13230–13237.

[170] V. Arima, M. Iurlo, L. Zoli, S. Kumar, M. Piacenza, F. D. Sala, F. Matino, G. Maruccio, R. Rinaldi, F. Paolucci, et al., *Nanoscale* **2012**, *4*, 813–823.

[171] A. K. Diallo, C. Absalon, J. Ruiz, D. Astruc, *J. Am. Chem. Soc.* **2011**, *133*, 629–641.

[172] V. Hoffmann, L. le Pleux, D. Häussinger, O. T. Unke, A. Prescimone, M. Mayor, *Organometallics* **2017**, DOI 10.1021/acs.organomet.6b00909.

[173] A. K. Diallo, C. Absalon, J. Ruiz, D. Astruc, *J. Am. Chem. Soc.* **2011**, *133*, 629–641.

[174] I. Baumgardt, H. Butenschön, *Eur. J. Org. Chem.* **2010**, *2010*, 1076–1087.

[175] J. Ma, N. Krauße, H. Butenschön, *Eur. J. Org. Chem.* **2015**, *2015*, 4510–4518.

[176] T. Hundertmark, A. F. Littke, S. L. Buchwald, G. C. Fu, *Org. Lett.* **2000**, *2*, 1729–1731.

[177] M. R. Netherton, G. C. Fu, *Org. Lett.* **2001**, *3*, 4295–4298.

[178] J. Ma, N. Krauße, H. Butenschön, *Eur. J. Org. Chem.* **2015**, n/a-n/a.

[179] I. Baumgardt, H. Butenschön, *Eur. J. Org. Chem.* **2010**, *2010*, 1076–1087.

[180] S. L. Ingham, M. S. Khan, J. Lewis, N. J. Long, P. R. Raithby, *J. Organomet. Chem.* **1994**, *470*, 153–159.

[181] P. G. M. Wuts, T. W. Greene, in *Greenes Prot. Groups Org. Synth.*, John Wiley & Sons, Inc., **2006**, pp. 647–695.

[182] T. Peterle, A. Leifert, J. Timper, A. Sologubenko, U. Simon, M. Mayor, **2008**, 3438–3440.

[183] G. Wu, Q. Liu, Y. Shen, W. Wu, L. Wu, *Tetrahedron Lett.* **2005**, *46*, 5831–5834.

[184] M. P. Doyle, B. Siegfried, J. F. Dellaria, *J. Org. Chem.* **1977**, *42*, 2426–2431.

[185] D. J. Cram, N. L. Allinger, H. Steinberg, *J. Am. Chem. Soc.* **1954**, *76*, 6132–6141.

[186] M. Shibahara, M. Watanabe, T. Iwanaga, T. Matsumoto, K. Ideta, T. Shinmyozu, *J. Org. Chem.* **2008**, *73*, 4433–4442.

[187] M. Stępień, I. Simkowa, L. Latos-Grażyński, *Eur. J. Org. Chem.* **2008**, *2008*, 2601–2611.

[188] M. S. Inkpen, S. Scheerer, M. Linseis, A. J. P. White, R. F. Winter, T. Albrecht, N. J. Long, *Nat. Chem.* **2016**, *advance online publication*, DOI 10.1038/nchem.2553.

[189] J.-K. Ou-Yang, L.-J. Chen, L. Xu, C.-H. Wang, H.-B. Yang, *Chin. Chem. Lett.* **2013**, *24*, 471–474.

[190] N. Das, A. M. Arif, P. J. Stang, M. Sieger, B. Sarkar, W. Kaim, J. Fiedler, *Inorg. Chem.* **2005**, *44*, 5798–5804.

[191] J.-L. Fillaut, D. Astruc, J. Linares, *Angew. Chem. Int. Ed. Engl.* **1995**, *33*, 2460–2462.

[192] V. J. Chebny, D. Dhar, S. V. Lindeman, R. Rathore, *Org. Lett.* **2006**, *8*, 5041–5044.

[193] R. F. Winter, *Organometallics* **2014**, *33*, 4517–4536.

[194] F. Barrière, W. E. Geiger, *J. Am. Chem. Soc.* **2006**, *128*, 3980–3989.

[195] C. M. Cardona, W. Li, A. E. Kaifer, D. Stockdale, G. C. Bazan, *Adv. Mater.* **2011**, *23*, 2367–2371.

[196] M. J. Frisch, G. W. Trucks, H. B. Schlegel, G. E. Scuseria, M. A. Robb, J. R. Cheeseman, G. Scalmani, V. Barone, B. Mennucci, G. A. Petersson, H. Nakatsuji, M. Caricato, X. Li, H. P. Hratchian, A. F. Izmaylov, J. Bloino, G. Zheng, J. L. Sonnenberg, M. Hada, M. Ehara, K. Toyota, R. Fukuda, J. Hasegawa, M. Ishida, T. Nakajima, Y. Honda, O. Kitao, H. Nakai, T. Vreven, J. A. Montgomery, Jr., J. E. Peralta, F. Ogliaro, M. Bearpark, J. J. Heyd, E. Brothers, K. N. Kudin, V. N. Staroverov, R. Kobayashi, J. Normand, K. Raghavachari, A. Rendell, J. C. Burant, S. S. Iyengar, J. Tomasi, M. Cossi, N. Rega, J. M. Millam, M. Klene, J. E. Knox, J. B. Cross, V. Bakken, C. Adamo, J. Jaramillo, R. Gomperts, R. E. Stratmann, O. Yazyev, A. J. Austin, R. Cammi, C. Pomelli, J. W. Ochterski, R. L. Martin, K. Morokuma, V. G. Zakrzewski, G. A. Voth, P. Salvador, J. J. Dannenberg, S. Dapprich, A. D. Dan-

iels, Ö. Farkas, J. B. Foresman, J. V. Ortiz, J. Cioslowski, and D. J. Fox, *Gaussian 09*, Gaussian Inc., Wellington, CT, **2009**.

[197] R. Ditchfield, W. J. Hehre, J. A. Pople, *J. Chem. Phys.* **1971**, *54*, 724–728.

[198] P. J. Hay, W. R. Wadt, *J. Chem. Phys.* **1985**, *82*, 299–310.

[199] C. Peng, H. Bernhard Schlegel, *Isr. J. Chem.* **1993**, *33*, 449–454.

[200] V. Kaliginedi, A. V. Rudnev, P. Moreno-García, M. Baghernejad, C. Huang, W. Hong, T. Wandlowski, *Phys. Chem. Chem. Phys.* **2014**, *16*, 23529–23539.

[201] J. J. Davis, B. Peters, W. Xi, J. Appel, A. Kros, T. J. Aartsma, R. Stan, G. W. Canters, *J. Phys. Chem. Lett.* **2010**, *1*, 1541–1546.

[202] K. Moth-Poulsen, T. Bjørnholm, *Nat. Nanotechnol.* **2009**, *4*, 551–556.

[203] X. Lou, J. L. J. van Dongen, E. W. Meijer, *J. Am. Soc. Mass Spectrom.* **2011**, *21*, 1223–1226.

[204] J. D. Winter, G. Deshayes, F. Boon, O. Coulembier, P. Dubois, P. Gerbaux, *J. Mass Spectrom.* **2011**, *46*, 237–246.

APPENDIX

ABBREVIATIONS

Å	Ångström
AFM	Atomic force microscope
AQ	Anthraquinone
aq.	Aqueous
Ar	Aryl
BARF	Tetrakis[3,5-bis(trifluoromethyl)phenyl]borate
BOM-SR	Benzyloxymethyl thioether
CE	Counter electrode
CIP	Cahn–Ingold–Prelog convention
CMOL	Semiconductor/molecular integrated circuits
CMOS	Complementary metal-oxide-semiconductor
COSY	Correlation spectroscopy
Cp	Cyclopentadienyl
CV	Cyclic voltammetry
D-A	Donor-Acceptor
DCM	Dichloromethane
DIBALH	Diisobutylaluminium hydride
DFT	Desnsity functional theory
DIPEA	Diisopropylethylamine
DIBALH	Diisobutylaluminium hydride
DMF	N,N'-dimethylforamide
EA	Elemental analysis
EC-STM	Electrochemical Scanning tunneling microscope
EI	Electron impact
Equiv.	Equivalent
Fc	Ferrocene
FCC	Flash column chromatography
FET	Field effective transistor
FcI$_2$	1,1-Diiodoferrocene
HMBC	Heteronuclear multiple bond coherence
HMImPF6	1-Hexyl-3-methylimidazolium hexafluorophosphate
HMQC	Heteronuclear multiple quantum coherence
HOMO	Highest occupied molecular orbital
HOP	Hydroxypropyl
ICs	Integrated circuits
LDA	Lithium diisopropylamine
IMW	Interlinked molecular wire
LUMO	Lowest unoccupied molecular orbital
m/z	Mass over charge
MALDI-ToF	Matrix-assisted laser desorption ionization-time of flight
MCBJ	Mechanically controlled break junction
MeCN	Acetonitrile
MS	Mass spectrometry
MQCA	Molecular quantum-cellular automata
nBuLi	n-Butyl lithium
NLO	Nonlinear optics
NMR	Nuclear magnetic resonance
NOESY	Nuclear Overhauser effect spectroscopy
OPE	Oligo-phenylene ethynylene
PG	Protecting group
Ph	Phenyl
PhMe	Toluene
PMP-SR	Para-methoxybenzyl thioether
ppm	Parts per million
PPTS	Pyridinium para-toluenesulfonate
pTsOH	Para-toluenesulfonic acid
pTTF	Pyrrolo-tetrathiafulvalene
PVFc	Polyvinyl ferrocene

QCA	Quantum-cellular automata
QI	Quantum interference
quant.	Quantitative
RCM	Ring closing metathesis
RE	Reference electrode
SEM	Scanning electron microscope
STM-BJ	Scanning tunneling microscopy break junction
TBAF	Tetrabutylammonium fluoride
TBAOH	Tetrabutylammonium hydroxide
TBAPF$_6$	Tetrabutylammonium hexafluorophosphate
TFA	Trifluoromethyl acetic acid
THF	Tetrahydrofuran
TIPS	Triisopropylsilyl
TLC	Thin layer chromatography
*t*BME	Tert-butylmethyl ether
TMEDA	*N,N,N',N'*-tetramethylethylenediamine
TMS	Trimethylsilyl
Trt	Trityl
UV-Vis	Ultraviolate-visible
VT NMR	Variable temperature NMR
WE	Working electrode
X-ray	X-ray spectroscopy

CURRICULUM VITAE

Viktor Hoffmann

Basler Strasse 42; 79540 Lörrach, Germany; +49 (0) 163 835 385 7;

Viktor.Hoffmann@unibas.ch

Education

09/2012 – 12/2016

        PhD in Organic Chemistry, University of Basel.

        Supervisor: Prof. Dr. Marcel Mayor, University of Basel

        Co-referee: Prof. Dr. Thomas Ward, University of Basel

02/2011 - 07/2012

        M.Sc. in Chemistry, University of Basel.

        Master thesis*: Synthesis of Photocleavable Halo-SNAP Chemical Inducer of Dimerization*.

        Supervisor: Prof. Dr. Matthias Wymann

09/2007 – 01/2011

        B.Sc. in Chemistry, University of Basel

2003 – 2006

        Abitur: Biotechnologisches Gymnasium Lörrach, Germany

Oral presentations

- Viktor Hoffmann, Marcel Mayor *Controlling the Shape of bis-Ferrocene Macrocycles by the Bulkiness of the Substituents*, Statusworkshop der Baden Württemberg Stiftung "Funktionelle Nanostrukturen", Bad Herrenalb 2016, Germany, oral and poster presention

Teaching Experience

03/2014 – 03/2016

        Organization, supervision and teaching of the "Blockkurs Nanochemistry" in organic chemistry for undergraduate students in NanoScience, Department of Chemistry, University of Basel

03/2014 – 09/2015

        Supervision and tutoring of two successfully completed Master Theses in organic chemistry, Department of Chemistry, University of Basel

03/2013 – 03/2015

        Teaching Assistant in the organic laboratory course for chemistry, biology and pharmacy undergraduate students, Department of Chemistry, University of Basel

LIST OF PUBLICATIONS

- Hoffmann, V; Le Pleux L.; Häussinger D.; Unke O.; Prescimone A. and Mayor M., *Organometallics*, **2017**, *36*, 858–866.

- Hoffmann, V.; Jenny, N.; Häussinger, D.; Neuburger, M.; Mayor, M. *Eur. J. Org. Chem.* **2016**, 2016 (12), 2187–2199.

- Zimmermann, M.; Cal, R.; Janett, E.; Hoffmann, V.; Bochet, C. G.; Constable, E.; Beaufils, F.; Wymann, M. P. *Angew. Chem. Int. Ed.* **2014**, 53 (18), 4717–4720.

SYNTHESIZED COMPOUNDS IN ORDER OF APPEARANCE